Systematic Study of Azimuthal Anisotropy for Charged Hadron in Relativistic Nucleus-Nucleus Collisions at RHIC-PHENIX

Maya SHIMOMURA

October 2009

Systematic Study of Azimuthal Anisotropy
for Charged Hadron in Relativistic
Nucleus-Nucleus Collisions at RHIC-PHENIX

Maya SHIMOMURA

Submitted to the Graduate School of
Pure and Applied Sciences
in Partial Fulfillment of the Requirements
for the Degree of Doctor of Philosophy in
Science

at the
University of Tsukuba

Abstract

On Earth, relativistic heavy ion collisions have been considered as a unique way to create the quark-gluon plasma (QGP), which is the phase in quantum chromodynamics (QCD) matter of deconfined quarks and gluons. Relativistic Heavy Ion Collider (RHIC) at Brookhaven National Laboratory was constructed to create and study QGP.

Azimuthal anisotropy of particles produced in relativistic heavy ion collisions is a powerful probe for investigating the characteristics of the QGP. Especially the strength of the elliptic anisotropy (v_2), which is defined by the second harmonics of Fourier expansion for the azimuthal distribution of produced particles with respect to the reaction plane, is expected to be sensitive to the early stage of heavy ion collisions. The anisotropy in the momentum phase space is transferred from the geometrical anisotropy of the initial collisional region because of the pressure gradient. Thus, the measured v_2 reflects the equation of state of the dense matter such as QGP, produced in the collisions.

One of the most remarkable findings at RHIC is that the strength of v_2 is much larger than what is expected from hadronic scenario in Au+Au collisions at the energy of $\sqrt{s_{\mathrm{NN}}} = 200$ GeV. It has been reported that the observed v_2 for hadrons on the transverse momentum agree with predictions from hydrodynamical model including hadron mass dependence in the low transverse momentum region ($p_{\mathrm{T}} \leq 1$ GeV/c). Moreover, a universal scaling of v_2 in the intermediate transverse momentum region ($p_{\mathrm{T}} = 1$ - 4 GeV/c), suggestive of quark-like degrees of freedom has also been reported for a broad range of particle species produced in Au+Au at $\sqrt{s_{\mathrm{NN}}} = 200$ GeV. In addition, from the comparison of v_2 measured at the various collision energies such as $\sqrt{s_{\mathrm{NN}}} = 17.2$ GeV, 62.4 GeV, 130 GeV and 200 GeV, it has been found higher collision energy provides larger v_2 up to $\sqrt{s_{\mathrm{NN}}} = 62.4$ GeV, while v_2 seems to be saturated above $\sqrt{s_{\mathrm{NN}}} = 62.4$ GeV collision energies up to $\sqrt{s_{\mathrm{NN}}} = 200$ GeV. It has been considered that this saturation indicates that formation of QGP, namely above $\sqrt{s_{\mathrm{NN}}} = 62.4$ GeV.

For a more comprehensive understanding of v_2, we have carried out systematic measurements of v_2. We have studied the dependence on collision energy, species and centrality. These data were taken at PHENIX. The v_2 has been measured by the event plane method. The event plane is determined from azimuthal anisotropy observed by the Beam-Beam Counter (BBC) while the central arm spectrometers detect the particle tracks and measure the azimuthal distribution with respect to the reaction plane. The large rapidity gap ($| \eta | \sim 3$) between the BBC and the central arm spectrometers reduces non-flow effects which can be the major background of v_2 measurement. A particle identification, namely a separation of pion/kaon/proton is performed by the mass square which are calculated from the time of flight and the momentum for each particle. To measure the time of flight, we newly used the Electro-Magnetic Calorimeter (EMCal) in addition to the Time-of-Flight counter (TOF). TOF provides better timing resolution while Electromagnetic Calorimeter (EMCal) gives much more statistics. Combining the TOF and EMCal measurement brings the detailed study for centrality dependence.

We have compared the v_2 for inclusive charged hadrons in Au+Au and Cu+Cu at $\sqrt{s_{\mathrm{NN}}} = 200$ GeV and 62.4 GeV as a function of the transverse momentum for a broad range of centrality selection. Consequently, we found the following features,

- The values of v_2 are the same between $\sqrt{s_{\mathrm{NN}}} = 200$ GeV and 62.4 GeV in Au+Au at the same momentum and centrality while there may be difference between $\sqrt{s_{\mathrm{NN}}} = 200$ GeV and 62.4 GeV in Cu+Cu.

- The magnitude of v_2 can be scaled by the geometrical eccentricity ($\varepsilon_{\mathrm{part}}$) of initial participants of collision between Au+Au and Cu+Cu at same N_{part} (Eccentricity scaling).

- The v_2 divided by the eccentricity proportionally increases with the number of the participants (N_{part}) to the $\frac{1}{3}$ power ($N_{\mathrm{part}}^{1/3}$ scaling).

These features indicate that the produced matter reaches the local thermal equilibrium. We have also measured the v_2 for pion/kaon/proton for the two data sets, in Au+Au at $\sqrt{s_{\mathrm{NN}}} = 62.4$ GeV and in Cu+Cu at $\sqrt{s_{\mathrm{NN}}} = 200$ GeV. We obtained that

- The v_2 divided by the number of constitute quarks as a function of the KE_{T} ($= \sqrt{(p_{\mathrm{T}}^2 + m_0^2)} - m_0$) is independent of the quark species (Quark number scaling and KE_{T} scaling).

All measurements of hadron v_2 at RHIC energy are consistent with quark recombination/ coalescence models, which assume the production of QGP and quark level flow after the collision, as same as the previous measurement in Au+Au at $\sqrt{s_{\mathrm{NN}}} = 200$GeV. Taking all scaling such as $N_{\mathrm{part}}^{1/3}$, eccentricity, quark number and KE_{T} scalings into account, it is newly found that there is a universal scaling for v_2 with different energies and collision sizes.

To understand how the N_{part} effects on the v_2 value, we have examined the blast-wave model fitting, which is based on hydrodynamical model, with the v_2 together with p_{T} spectra to extract dynamical properties of the matter especially at the freeze-out. From this fitting, thermal freeze-out temperature (T_{fo}) and radial flow velocity (β_{T}) are obtained in plane and out-of plane separately. As a result, we have newly observed the following two important aspects.

- β_{T} is clearly different between in and out-of plane, and $\beta_{\mathrm{T}2}$, which is the amplitude of β_{T} in azimuthal distribution, is proportional to $\varepsilon_{\mathrm{part}}$ at $N_{\mathrm{part}} \geq 40$.

- The blast wave model can reproduce the KE_{T} scaling.

In the blast-wave frame work, the $\beta_{\mathrm{T}2}$ is proportional to v_2 when the other parameters are all fixed. The measurement results that $\varepsilon_{\mathrm{part}}$ determines the $\beta_{\mathrm{T}2}$. However, since v_2 is not proportional to $\varepsilon_{\mathrm{part}}$ on the experimental results, v_2 is not determined only by $\beta_{\mathrm{T}2}$, but also other parameter, T_{fo}. T_{fo} is smaller at more central collisions, and smaller T_{fo} makes slope of p_{T} spectra steeper which makes v_2 larger. Assuming the simple adiabatic expansion model with β_{T} and T_{fo} obtained by the blast-wave fitting, it was found that a thermal freeze-out time is longer with larger collision system. The longer freeze out time makes the system colder at freeze out. Thus, the size dependence of v_2 can be understood as thermal nature of produced particles based on hydrodynamical behavior, which is different from that of chemical freeze-out. Additionally, we conform that the KE_{T} scaling can also be explained by hydrodynamical nature as the effect of radial flow. The result of this systematic study indicates the matter reaches thermal equilibrium and the QGP is created at RHIC energy.

Acknowledgments

First of all, I would love to express my deepest gratitude to all the people who assist me to accomplish this thesis. I especially bless my supervisor Prof. Y. Miake, who introduced this fantastic physics field to me. He also gave me a lot of useful advices about my analysis and even my life for many years. I am also very grateful to Prof. S. Esumi for his continuous encouragement, plenty of valuable advices and beneficial discussions to advance my research. He triggered my interest in this analysis and always conduct me to next steps. I have learned a lot about being a physicist from his attitude to physics. I appreciate that Prof. T. Chujo gave me many useful advices for the analysis of this thesis and for the work at experiment. I would like to thank Prof. M. Inaba for his professional advices especially about detector and electronics work. I am obliged to Mr. S. Kato for management of comfortable computing system at Tsukuba. I also grateful to Prof. T. Hirano for giving me valuable theoretical advices and having fruitful discussion with me about flow analysis.

I acknowledge for all the collaboration members of the PHENIX experiment. I think I am a very lucky person since I belong to PHENIX as my first experiment in my life. I am grateful to the spokespersons, Prof. W. A. Zajc and Prof. B. V. Jacak for their various arrangements, advices and encouragement for my activities at BNL.

I am very obliged to Prof. R. Lacey for his many effective advices, kind helps, useful discussions and very patient encouragement for my analysis and life at PHENIX. I am also very grateful to Dr. A. Taranenko for his friendship, very patient encouragement and a lot of useful advices for all my works such as analysis, computing, writing thesis and writing English. I would like to thank Prof. J. Jia for his friendship, encouragement and many effective advices for analysis at PHENIX. I am grateful to Dr. M. Chiu for his friendship, encouragement, useful advices and a lot of helps for analysis, computing, detector works, writing English and etc, etc... Without them, I would have never complete this thesis. Also I have learned how fun being a physicist is from them.

I would like to express my thanks to Dr. J. S. Haggerty, Prof. C. Y. Chi, Mr. M. Lenz, Dr. E. Kistenev, Dr. S. Huang, Prof. D. Winter, Dr. C. Vale, Mr. R. Wei, Prof. S. V. Greene, Prof. M. Grosse Perdekamp, Prof. T. K. Hemmick, Prof. J. G. Lajoie, Dr. M. J. Tannenbaum, Prof. J. Velkovska, Dr. C. L. Woody, Dr. C. Aidala, Prof. J. C. Hill, Prof. A. Litvinenko, Dr. J. T. Mitchell, Dr. B. M. Johnson, Dr. W. Holzmann, Dr. M. L. Purschke, Dr. C. Pinkenburg, Dr. J. E. Frantz, Dr. M. Issah, Mr. S. Boose, Dr. S. Bathe, Mr. J. L. Bounty, Dr. D. P. Morrison, Prof. J. L. Nagle, Dr. E. O'Brien, Prof. V. Pantuev, Dr. V. Riabov, Dr. H. Buesching, Prof. M. Rosati, Prof. R. Seto, Dr. C. L. Silva, Dr. S. P. Stoll, Prof. H. Pereira, Dr. C. Zhang and Dr. S. Batsouli ! I really appreciate their friendship and that they gave me a lot of useful advices and help for detector works, physics analysis, English and wonderful life at BNL.

I also wish to acknowledge for all the PHENIX-j members. I would like to thank Prof. H. Hama-

The PHENIX Collaboration

Contents

List of Figures

List of Tables

Chapter 1

INTRODUCTION

The hadrons, which compose our beautiful universe, take a state such that quarks and gluons are confined, and quantum chromodynamics (QCD) describes the state of the quarks and gluons. Under extreme condition such as high temperature and density, QCD calculations performed on the lattice (LQCD) predicts a phase transition from hadron matter into plasma of quarks and gluons so called Quark-Gluon plasma(QGP), where quarks and gluons are deconfined. On the earth, ultra-relativistic heavy ion collisions have been considered to be the only way which can provide the opportunity to create and study the QGP. Relativistic Heavy Ion Collider (RHIC) at Brookhaven National Laboratory (BNL) has been constructed for this purpose, and nuclei as heavy as gold (Au) are accelerated to $\sqrt{s_{\mathrm{NN}}} = 200$ GeV.

In this chapter, QGP, QCD which is the theory to describe the QGP are briefly introduced, and previous studies at RHIC followed by the thesis motivation.

1.1   Quantum Chromodynamics and Quark-Gluon Plasma

As well known, a matter is composed of molecules. A molecule consists of more than one atom and, an atom is formed by a nucleus and electrons surrounding the nucleus. A nucleus is made of nucleons such as protons and neutrons. Mesons are binding the nucleons together. A nucleon consists of three quarks bound by gluons. A meson is made up of a pair of a quark and an anti-quark bound by gluons. All compound particles made of quarks and gluons are termed hadrons. A theory of the strong force describing the interactions of the quarks and gluons is so-called Quantum chromodynamics (QCD). QCD is a quantum field theory of a special kind called non-Abelian or Yang-Mills gauge theory. It is an important part of the Standard Model of particle physics. The quarks in hadrons interact with each other through strong interactions. The medium particles, gluon, mediate this strong force and the fact that the gluons themselves interacts each other makes the QCD calculations complex. The gluon is like an elastic string between quarks; smaller interaction when the quark distance is shorter while larger separation between quarks brings greater attractive force between them. The attempt to extract one quark or gluon from hadron needs infinite energy. In fact, quark has not been observed in many attempts. They appear either as pairs of quark and anti-quark in the form of mesons or bound groups of three quarks in the form of baryons. The names assigned to them, up, down, strange, charm, bottom, top, are only mnemonic symbols to identify the different species [1] . The quark confinement is a consequence of the nonperturbative structure of the vacuum and this vacuum structure is considered to be

modified at high temperatures and/or densities where quarks and gluons are free from individual hadrons. These expectations suggest that QCD is a fundamental theory of nature containing a phase transition that may be accessible to experimental investigation.

While the development of QCD, it was noted in 1975 that the decrease of the coupling constant at small distances indicated that the dense matter at the center of neutron stars would consist of deconfined quarks and gluons [2] . The paper focused on the high-density, with low-temperature condition of QCD, but additionally it is noted that similar arguments might apply to the high temperatures present in the early universe. In 1980, Shuryak has examined the high-temperature phase called quark-gluon plasma (QGP) in detail as a first time [3] . The only occasion that such conditions have existed in the History of Universe is during a short time interval of a fraction of a second after the big bang that gave a birth to the Universe. For this reason, the topic is of interest to cosmology as well. The same condition is also important to QCD because there is the possibility of freeing quarks from their confined state inside hadrons and transform them into a new phase in which many quarks and gluons are present in a plasma-like state.

Simple dimensional calculation suffice to indicate both the critical energy density $\varepsilon \sim 1$ GeV/fm^3 and the associated critical temperature $T_{\mathrm{C}} \sim 170$ MeV to provide the deconfining phase transition in hadronic matter. These values imply that the transition occurs in a regime where the QCD coupling constant , α_s, becomes large, therefore the perturbative method is no longer used. Instead, lattice formulation could be used to study phase transition phenomena, and it has led to detailed investigations of the thermodynamic properties of quarks and gluons [48] .

Lattice QCD predicts that a phase transition from hadrons to QGP occurs at a temperature of approximately $T \approx 170$ MeV $\approx 10^{12}$ K as shown in Figure 1.1 [4] . The temperature of this phase transition corresponds to an energy density $\varepsilon \approx 1$ GeV/fm^3, and this is nearly an order of magnitude larger than that of normal nuclear matter.

In the limit of massless non-interacting particles, each bosonic degree of freedom contributes $\frac{\pi^2}{30}T^4$ to the energy density; each fermionic degree of freedom contributes $\frac{7}{8}$ this value. The corresponding "Stefan-Boltzmann" limits of the energy density $\varepsilon_{\mathrm{SB}}$ for the cases of 2 and 3 active flavor quark-gluon plasma is then

$$\varepsilon_{\mathrm{SB}}^2 = \{2_f \cdot 2_s \cdot 2_q \cdot 3_c \frac{7}{8} + 2_s \cdot 8_c\}\frac{\pi^2}{30}T^4 = 37\frac{\pi^2}{30}T^4, \tag{1.1}$$

$$\varepsilon_{\mathrm{SB}}^3 = \{3_f \cdot 2_s \cdot 2_q \cdot 3_c \frac{7}{8} + 2_s \cdot 8_c\}\frac{\pi^2}{30}T^4 = 47.5\frac{\pi^2}{30}T^4, \tag{1.2}$$

after summing over the appropriate flavor, spin, quark/anti-quark and color factors for quarks and spin times color factors for gluons. The large numerical coefficients (37 and 47.5) stand in stark contrast to the value of ~ 3 expected for a hadron gas with temperature $T < T_{\mathrm{C}}$, in which case the degrees of freedom are dominated by the three pion species $\pi^-/\pi^0/\pi^+$.

1.2   Relativistic Heavy Ion Collisions

The ultra-relativistic heavy ion collision has been suggested as a unique way to create and study such a hot and dense matter at high temperature and density.
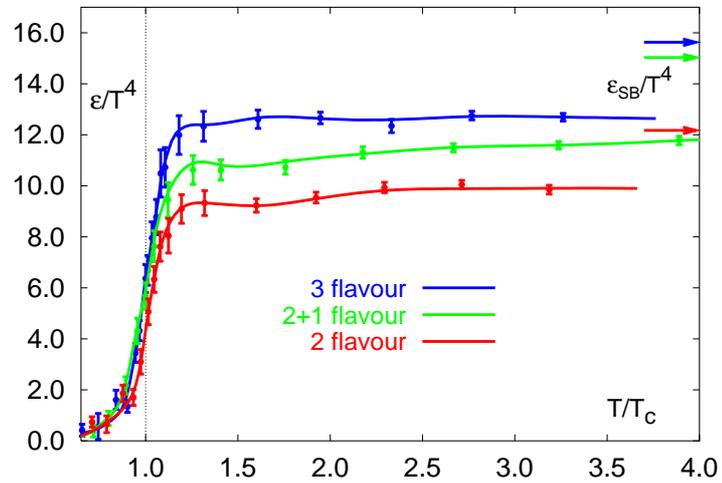
Figure 1.1: Lattice QCD results [4] for the energy density/T^4 as a function of the temperature scaled by the critical temperature T_C. Note the arrows on the right side indicating the values for the Stefan-Boltzmann limit.
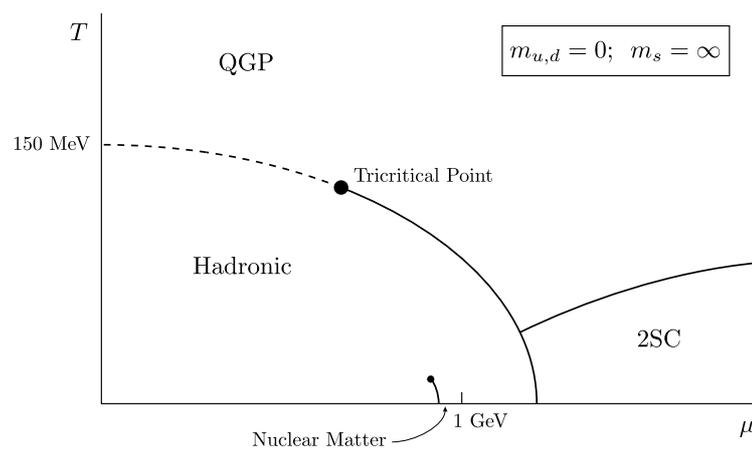
Figure 1.2: Theoretical phase diagram of nuclear matter for two massless quarks as a function of temperature T and baryon chemical potential μ [47].

1.2.1 Relativistic Heavy Ion Colliders

Relativistic heavy ion colliders have been built for the heavy ion colliding experiments at Brookhaven National Laboratory (BNL) and European Organization for Nuclear Research (CERN). The parameters of these accelerators are summarized in Table 1.1 . At RHIC as shown in Figure 1.3, four experiments, BRAHMS, PHENIX, PHOBOS and STAR, are operating to investigate collisions ranging from p+p to Au+Au. The data presented in this thesis were taken at PHENIX. PHENIX, "the Pioneering High Energy Nuclear Interaction eXperiment", is one of the largest experiments currently taking data at RHIC. It is carried out by a collaboration of about 500 physicists and engineers from 54 participating institutions in 13 countries. Measuring leptons and photons probes the QGP phase directly. While studying the copiously produced hadron spectra gives information on the later hadronization of the QGP, measuring the hadron v_2 also reflects the early stage of the collision. The primary goal of PHENIX is to discover QGP and study its properties. The bird's view photograph of the PHENIX detector is shown in Figure 1.4. The detail of the PHENIX experiment is explained in Chapter 2.

Table 1.1: Heavy ion collider facilities with the ion beams, and the center of mass energy.

Collider	Location	beam	$\sqrt{s_{\mathrm{NN}}}$ [GeV]	Year
AGS	BNL	^{16}O, ^{28}Si	5.4	1986
		^{197}Au	4.8	1992
SPS	CERN	^{16}O, ^{32}S	19.4	1986
		^{208}Pb	17.4	1994
RHIC	BNL	^{197}Au	130	2000
		^{197}Au	200	2001
		d+^{197}Au	200	2003
		^{197}Au	200	2004
		^{197}Au	62.4	2004
		$^{63.5}$Cu	200	2005
		$^{63.5}$Cu	62.4	2005

1.2.2 Participant Spectator Picture

Since a nucleus is extended, the geometrical aspect has an important role in the dynamics of the high energy heavy ion collision. With extreme velocity of Lorentz contracted nucleus much faster than Fermi motion, the nucleus-nucleus collision is separated into two parts; "participants" which is in the overlapped region and "spectators" which is the rest. In this picture, the spectators are going through the collision region keeping the velocity of its own along the original beam direction while a lot of produced particles from participants are emitted in the mid-rapidity. Figure 1.5 shows this participant-spectator picture of symmetric Lorentz contracted nuclei in the center of mass frame. As is shown in this figure, the size of the participants/spectators is determined by the collision impact parameter, b, which is defined by the distance between the center of nuclei in the collision. There is anti-correlation between the size of participants and that of spectators. The number of participant nucleons (N_{part}) and the number of nucleon-nucleon collisions (N_{coll})
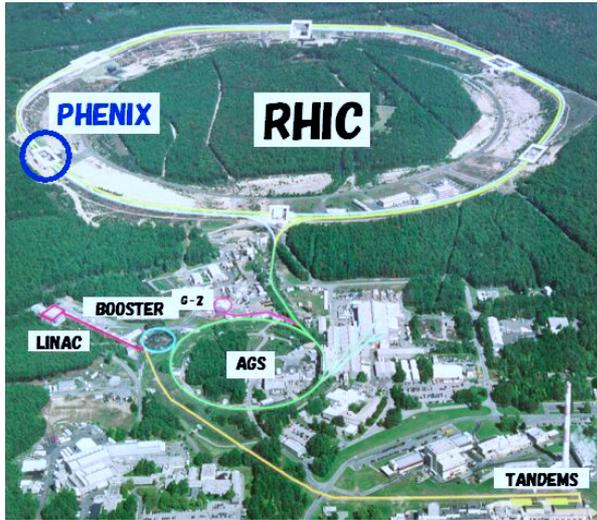
Figure 1.3: Aerial photograph of the RHIC and PHENIX.

Figure 1.4: Bird's view photograph of the PHENIX detector viewed from north to south. The central arms are visible on the right(west) and left(east) sides.

related to the given b are calculated by using Glauber Model (See Section 3.5.1).

Based on this participant-spectator picture, the centralities of the nucleus-nucleus collision can be defined by the information of the energy deposit of neutrons in spectator on the calorimeter located at zero-degree and the information of charge sum measured by beam-line detectors (See Section 2).
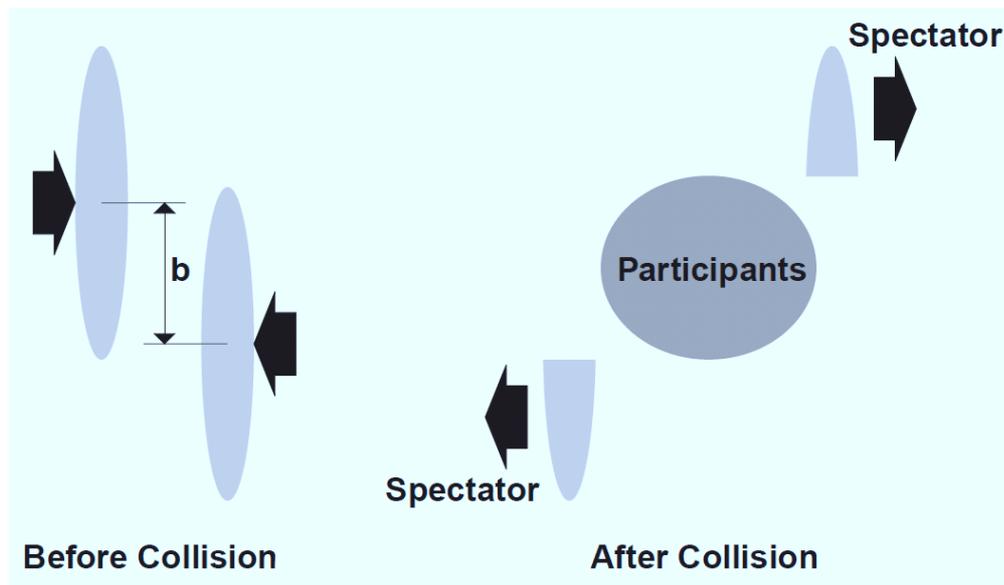
Figure 1.5: The sketch of the colliding nuclei with impact parameter (b). On the left, the two incoming nuclei in the center of mass frame are shown. On the right, the nucleons are separated to participants, projectile spectators and target spectators after the collision.

1.2.3   Space-Time Evolution of Collision

The matter produced in the high energy heavy ion collision is expected to undergo several stages from the initial hard scattering to the final hadron emission. J. D. Bjorken illustrated the space-time evolution of the high energy heavy ion collision based on hydrodynamic [25]. In the Bjorken's picture with high energy limit, the space-time evolution is separated into four individual phases which are characterized by a proper time $\tau = \sqrt{t^2 + z^2}$. Figure 1.6 shows the picture of the light-cone diagram for the space-time evolution of these phases in the heavy ion collision. The value of the proper times τ in Figure 1.6 are described in [26]. In this picture, passing along the longitudinal (z) axis, the two Lorentz contracted nuclei being "disks" collide at $z = 0$ and time (t) $= 0$ in the center of mass frame. The thickness of the disk represents $\Delta L \approx 1$ fm. After the collision, the disks recede from the overlap region with a large amount of baryon number. In the overlap region, the hard scatterings between partons, quarks and gluons, occur which can be described by perturbative QCD following parton cascade, and then a huge amount of energy is deposited in the matter. This initial phase is named as pre-equilibrium phase.

The multiple scatterings of partons continue and the partons share their momentum with in short time, so that the matter would reach the local thermal equilibrium which is so-called QGP phase. The time to form the QGP phase is called as "formation time" τ_0. Once the matter reaches local equilibrium, the QGP matter would expand hydrodynamically until the matter cools down to the critical temperature T_c where the QGP phase transition ($T_c \approx 180$ MeV) occurs.

At T_c, the QGP matter begins to hadronize so that quarks and gluons are confined into color singlet hadrons. If the phase transition between the QGP to the hadron phase is the first order phase transition, a mixture of QGP and hadronic matter would appear during the transition. In this mixed phase, the volume fraction of hadronic matter in the QGP phase increases with expansion. The temperature in the system stays at T_c because the hadronic matter releases latent heat during the transition.

The system finishes to hadronize and the produced hadrons interact with each other until the system temperature drops to freeze-out temperature ($T_f \approx 100$ MeV). This is called as "Hadron Gas phase". The hadronic matter expands and the system size becomes larger than the mean free path of the interacting hadrons. Eventually the hadrons freely move away from the hadronic matter under T_f and those are detected in our measurement at approximately infinite distance.

1.2.4   Energy Density

The formation of QGP requires a sufficiently large energy density. The density is expected to be order of 1 GeV/fm^3 This is about 10 times larger than that of normal nucleus (≈ 0.14 MeV/fm^3). It is interesting how much energy density can be reached at the formation time (τ_0) of QGP.

In Bjorken's picture, the expansion of the system is one dimensional expansion along with z. Also, the matter is cylindrically symmetry until the time reaches τ_0. The volume of the system at τ_0 is written as $\Delta V = \pi R^2 dz$ where R is a radius of the colliding nucleus. Energy (E) in the volume is written as following;

$$E = \langle m_T \rangle \frac{dN}{dy} \delta y = \frac{dE_T}{dy} \delta y \tag{1.3}$$

where $m_T = \sqrt{p_T^2 + m^2}$ is a transverse energy of the produced hadrons (transverse mass), and dN/dy is rapidity density of particle multiplicity. y is rapidity defined as following;
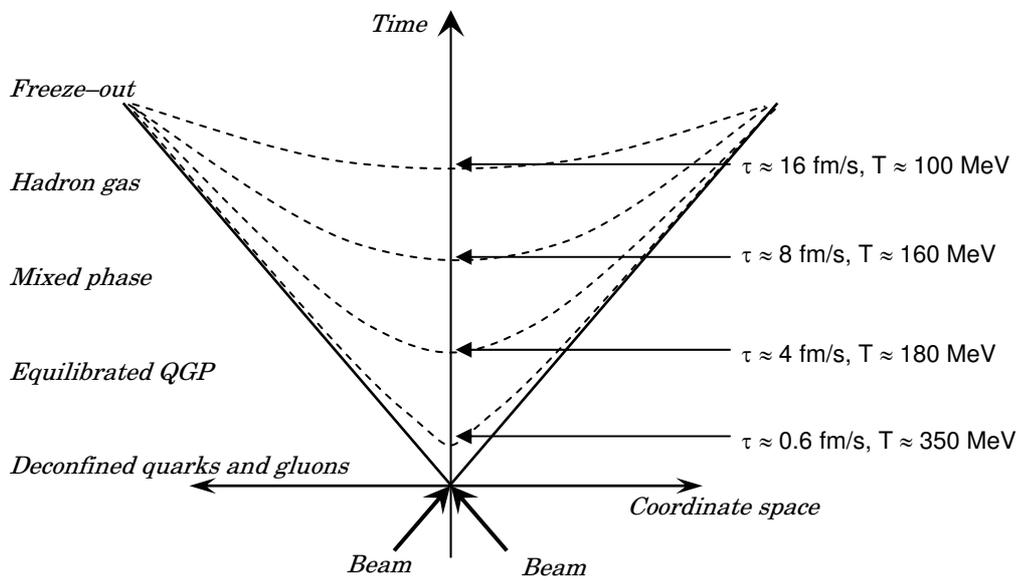
Figure 1.6: The light-cone diagram of space time evolution in high energy heavy ion collisions. The values of the time and the temperature for each phases are taken from [26]. The mixed phase exists if the phase transition is first order.

$$y = \frac{1}{2} \ln \left(\frac{t+z}{t-z} \right). \tag{1.4}$$

Using both the volume ΔV and the energy (E by Equation 1.3), the energy density (ε_0) of the system at τ_0 can be expressed as following;

$$\varepsilon_0 = \frac{\Delta E}{\Delta V} \tag{1.5}$$

$$= \frac{\langle m_{\rm T} \rangle}{\pi R^2} \frac{{\rm d}N(\tau_0)}{{\rm d}z} = \frac{\langle m_{\rm T} \rangle}{\pi R^2 \tau_0} \frac{{\rm d}N(\tau_0)}{{\rm d}y} \tag{1.6}$$

$$= \frac{1}{\pi R^2 \tau_0} \frac{{\rm d}E_{\rm T}(\tau_0)}{{\rm d}y} \tag{1.7}$$

where $E_{\rm T}$ is total energy and $dz = \tau dy$ at central rapidity ($y = 0$). We equated $\langle m_{\rm T} \rangle \frac{dN}{dy} = \frac{dE_T}{dy}$. This energy density ε_0 is generally referred as "Bjorken energy density" [25].

Although τ_0 is not a clearly determined, the ε_0 was evaluated for the AGS, SPS and RHIC experiments using the measured value of $dE_{\rm T}/dy$ and the normally used $\tau_0 = 1.0$ fm/c. An estimation with $\tau_0 = 0.6$ (1.0) fm/c gives $\varepsilon_0 = 9$ (5.5) GeV/fm^3 for $\sqrt{s_{\rm NN}} = 200$ GeV, which is larger than the critical energy density $\varepsilon_c \sim 1$ GeV/fm^3 predicted from Lattice QCD calculations. Therefore, the energy density reached at the top RHIC energy is much higher than the threshold of QGP formation. The ε_0's are summarized in Table 1.2 and $\epsilon_{Bj} \cdot \tau$ ($=\varepsilon_0 \cdot \tau_0$) as a function of $N_{\rm part}$ with three kinds of $\sqrt{s_{\rm NN}}$ is shown in Figure 1.7.

Table 1.2: The summary of Bjorken energy density ε_0 for several collision systems and energies.

Accelerator	Colliding Nucleus	$\sqrt{s_{\rm NN}}$ (GeV)	ε_0 (GeV/fm^3)	
AGS	Au+Au	5	1.5	[27]
SPS	Pb+Pb	17	2.9	[28, 29]
RHIC	Au+Au	200	5.5	[30, 31]

1.3   Particle Production at RHIC

Extensive amount of experimental data from high-energy nucleus-nucleus collisions have been recorded at RHIC-PHENIX [6] . One of the most important discoveries is the large elliptic flow in non-central Au+Au collision.

It has been reported that the observed hadron v_2 can be well described by hydro dynamical models assuming very short thermalization times ($\leq \sim 0.5$ fm/c) in the low transverse momentum region ($p_{\rm T} \leq \sim 1$ GeV/c). In the intermediate transverse momentum region ($p_{\rm T} = \sim 1$ - 4 GeV/c), v_2 is scaled with the number of quarks in Au + Au collisions at $\sqrt{s_{\rm NN}} = 200$ GeV. It is consistent with the quark recombination/coalescence models, which indicate quark-like degrees of freedom. In this section, the fundamental findings of previous results related to the analysis of this thesis are explained.
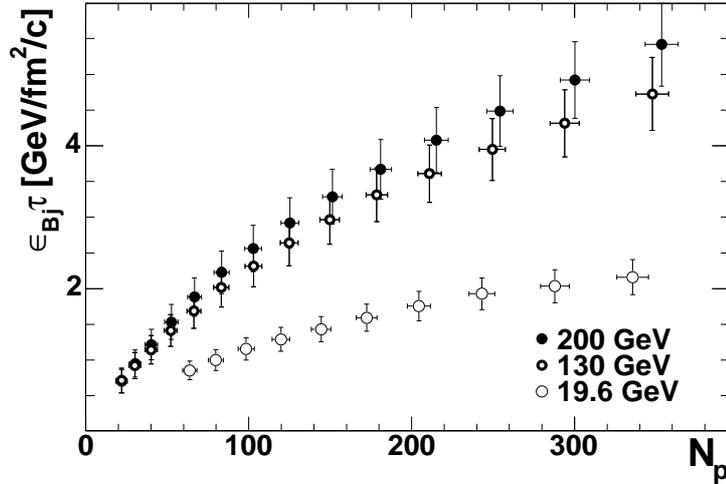
Figure 1.7: The $\epsilon_{\mathrm{Bj}} \cdot \tau$ as a function of N_{part} in different $\sqrt{s_{\mathrm{NN}}}$

1.3.1 Transverse Momentum Spectra and Radial Flow

As described in Section 1.2.3, when the mean free path becomes larger than the size of system, the momentum of hadron are fixed at freeze-out temperature. Therefore, the final momentum distributions of hadrons reflect the condition of the thermal (kinetic) freeze-out. Transverse momentum spectra have been measured for various particle species, not only in heavy ion collision but also in proton-proton (pp) or proton-nucleus (pA) collisions at various energies.

If the matter created by collisions reaches a thermal equilibrium state of hadron gas, the momentum distributions of the particles follow Boltzmann distribution. The transverse momentum distribution is simplified as

$$\frac{dN}{m_{\mathrm{T}} dm_{\mathrm{T}}} \sim \exp \frac{-m_{\mathrm{T}}}{T}, \tag{1.8}$$

with an exponential function of transverse mass m_{T} ($= \sqrt{p_{\mathrm{T}}^2 + m^2}$) .

It is known that the single-particle spectra are well described by this equation in the region $p_{\mathrm{T}} \leq \sim 2.0\,\mathrm{GeV}/c$. This is called m_{T} scaling [32]. The inverse slope parameter, T, in Equation 1.8, which is interpreted as temperature of the system at the thermal freeze-out, is identical with various particle particles such as pions, kaons and protons in high energy proton-proton/proton-nucleus collisions:

$$\mathrm{pp/pA} : T_{\pi} \sim T_{\mathrm{K}} \sim T_{\mathrm{p}} \approx 150\,\mathrm{MeV}. \tag{1.9}$$

Unlike the pp/pA collisions, it has been observed that the produced particles are strongly interacting and create common collective motion to outward (radial flow) as an explosion in high energy nucleus-nucleus collisions. The effect of this collective expansion with certain flow velocity modifies the m_{T} spectra according to the hadron masses. Figure 1.8 shows the m_{T} spectra for $\pi^{\pm}$, $K^{\pm}$, p, and $\bar{\mathrm{p}}$ for central 0 - 5 %, mid-central 40 - 50 %, and peripheral 60 - 92 % collisions [65] and the lines on each spectra curves are fitting with m_{T} exponential function. The inverse slope parameters for each particle are shown in Figure 1.9.

The slope parameters clearly depend on the particle mass and the centralities, and this indicates

the existence of the outward collective flow created by the collisions in addition to the thermal motion. With the common expanding velocity to transverse direction, the slope parameter is modified as;

$$T \simeq T_{\mathrm{f}} + \frac{1}{2}m\beta^2, \tag{1.10}$$

where T_{f} is the thermal temperature, m is particle mass, and β is the radial flow velocity. $T_{\mathrm{f}} = 177.0 \pm 1.2$ MeV and $\beta = 0.48 \pm 0.07$ are extracted in most central Au + Au collisions at $\sqrt{s_{\mathrm{NN}}} = 200$ GeV [33].
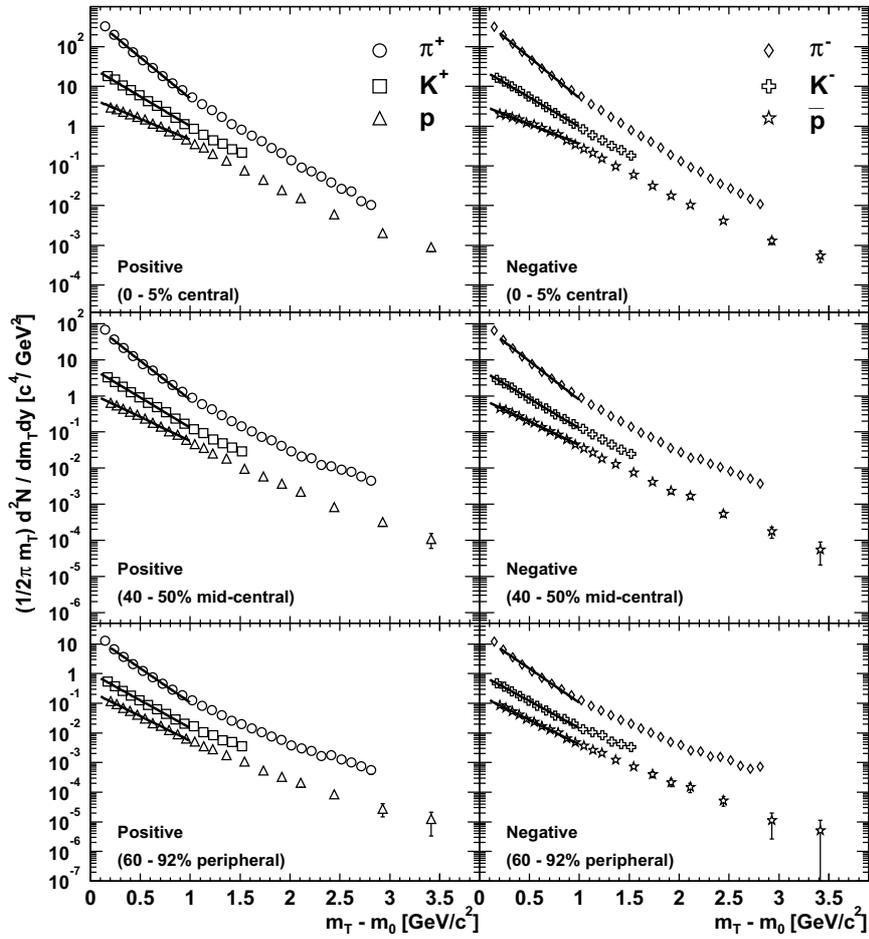
Figure 1.8: Transverse mass spectra for $\pi^{\pm}$, $K^{\pm}$, p, and $\bar{\mathrm{p}}$ for three centrality selections in Au+Au collisions at $\sqrt{s_{\mathrm{NN}}} = 200$ GeV. The lines on each spectra curves are fitting with m_{T} exponential function [65].
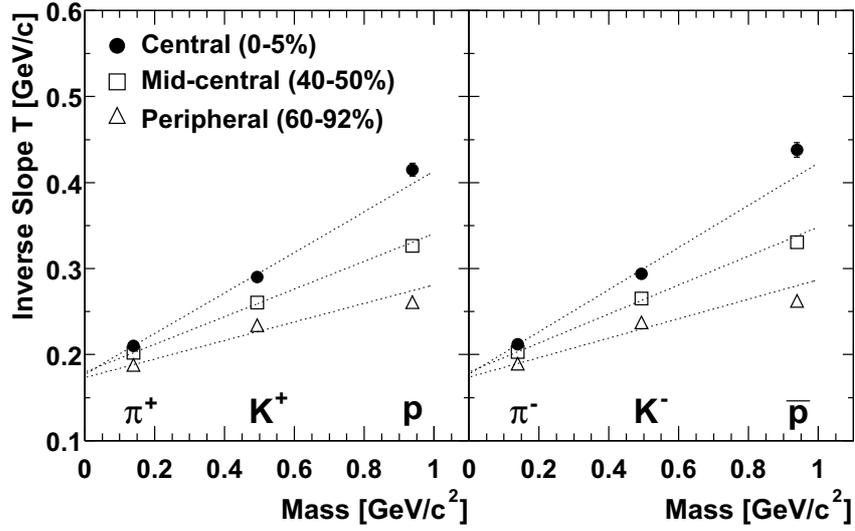
Figure 1.9: Mass and centrality dependence of inverse slope parameters T in Au + Au collisions at $\sqrt{s_{\mathrm{NN}}} = 200$ GeV.

1.3.2 Azimuthal Anisotropy
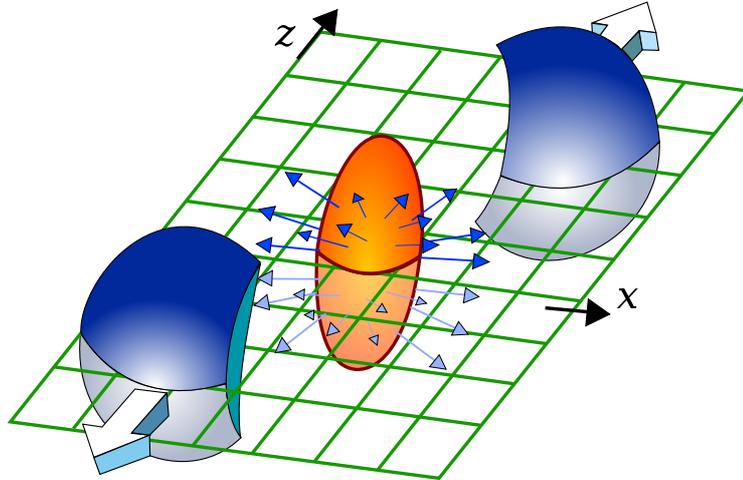
Figure 1.10: Reaction plane, (x,z) plane, and the almond shape of the participant at non-central collision.

One of the most interesting properties of the collision that can be measured through experimental techniques is the azimuthal anisotropy of particle production [79] [80] [82]. In non-central collisions, the initial geometrical overlap of two colliding nuclei in the transverse plane forms almond shape as illustrated in Figure 1.10. The reaction plane is defined as the plane which includes the directions of the beames and the impact parameter.

Frequent scatterings in the early stage of the collision convert the spatial anisotropy to a momentum anisotropy which is observable as an elliptic flow of the emitted hadrons. The emission pattern is strongly influenced by the relation of the mean free path, l, and the size of the collided system, R. When l is comparable to R, the particle production is simply a superposition of

nucleon-nucleon collisions, therefore, the particle emission is isotropic. On the other hand, when l is much shorter than R, the hydrodynamical description can be applied, and thus the emission pattern is affected by the shape of the system. In heavy ion collisions at RHIC, l is expected to be around 0.1 fm and it is smaller than the system size ($R = \sim 6$ fm).

In the hydrodynamical framework, the driving force of the flow is the pressure gradient. When the scattering of the matter is sufficient to establish local thermal equilibrium, the pressure gradient is the largest in the shortest direction of the ellipsoid almond. The larger gradient makes momenta of matter higher in its direction reducing the spatial anisotropy rapidly. The elliptical asymmetry of this gradient provides the elliptic flow in momentum space. The lack or reduction of any strong scattering in the early stage of the collision would decrease the amplitude of elliptic flow.

After the collision, it takes a finite time that the initially produced particles reach local equilibrium and the matter starts to behave the hydrodynamically.

Spatial anisotropy is the largest at the beginning of the collision and is reducing rapidly as the system expands. Thus, the anisotropy should reflect the early stage of the collisions. Indeed, it has been observed that the measured elliptic flow scales roughly with the geometrical eccentricity, ε, of the participant shape. The ε is defined by the Equation 1.11, and indicates the ellipticity of the participant nucleons.

$$\varepsilon = \frac{\langle y^2 \rangle - \langle x^2 \rangle}{\langle y^2 \rangle + \langle x^2 \rangle}. \tag{1.11}$$

The ε can be analytically calculated once the density profile of the nuclei is decided such as Woods-Saxon shape (Section 3.5). The observation of abundant elliptic flow indicates that the system reaches local thermal equilibrium before the spatial anisotropy completely vanishes when hydrodynamics is a mechanism to generate elliptic flow. It is expected that the remained eccentricity is directly corresponding to the amplitude of the observed elliptic flow. The examined hydrodynamical calculations have required quite short thermalization times, from 0.6 to 1.0 fm/c, in order to reproduce the magnitude of elliptic flow observed at RHIC [6] .

The azimuthal anisotropy can be characterized as the second Fourier coefficient, $v_2(p_{\mathrm{T}})$ as shown in Equation 1.12.

$$\frac{d^2 N}{d\phi dp_{\mathrm{T}}} = N_0[1 + 2v_2(p_{\mathrm{T}})\cos(2\phi)] \tag{1.12}$$

Both the first Fourier coefficient, v_1, and higher order coefficients have been neglected in the above expression since these are orthogonal to v_2. As discussed above, v_2 has been considered to be scaled by ε [49] . The measurement of v_2 is explained in Chapter 3 .

1.3.3   Hydrodynamics at Low p_{T}

Hydrodynamics provides a link between the fundamental properties of the hot dense matter (its equation of state (EOS) and transport coefficients) and the flow evidenced in the measured hadron spectra and azimuthal anisotropy [12] [13] [14] [15] [16] [81]. Hadron spectra reflect the integrated effects of the expansion from the beginning of the collision.

Collective Expansion Model (Blast-wave Parametrization)

It has been found that hydrodynamic models which assume thermal equilibrium reproduce p_{T} spectra for π/K/p at 130 GeV and 200 GeV in Au+Au collisions up to $p_{\mathrm{T}} \sim 1.5$ to 2.0 GeV/c [19] [35] [22] [65] [63] . One of the good approach to obtain the detailed information on the nature

of thermalization is a comparison of the collective expansion model, referred to as the "blast-wave" model, to the measured spectra for various hadrons. This is a two-parameter model describing a boosted thermal source based on relativistic hydrodynamics [23] [24] . The two parameters, the radial velocity (β_T) and the freeze-out temperature (T_{fo}), are extracted from the invariant cross section data according to the following equation:

$$\frac{dN}{m_T dm_T} \propto \int_0^R r \, dr \, m_T I_0 \left(\frac{p_T \sinh \rho}{T_{fo}}\right) K_1 \left(\frac{m_T \cosh \rho}{T_{fo}}\right), \tag{1.13}$$

where I_0 and K_1 represent modified Bessel function with ρ being the transverse boost as

$$\rho(r) = \tanh^{-1} \beta_T(r) \tag{1.14}$$

with

$$\beta_T(r) = \beta_s\left(\frac{r}{R}\right) \tag{1.15}$$

and

$$m_T = \sqrt{p_T^2 + m^2}. \tag{1.16}$$

Figure 1.11 shows the p_T spectra for $\pi/K/p$ in Au + Au collisions at $\sqrt{s_{NN}} = 200$ GeV with Blast-wave fitting result for both negative (Left) and positive (Right) charge [63].
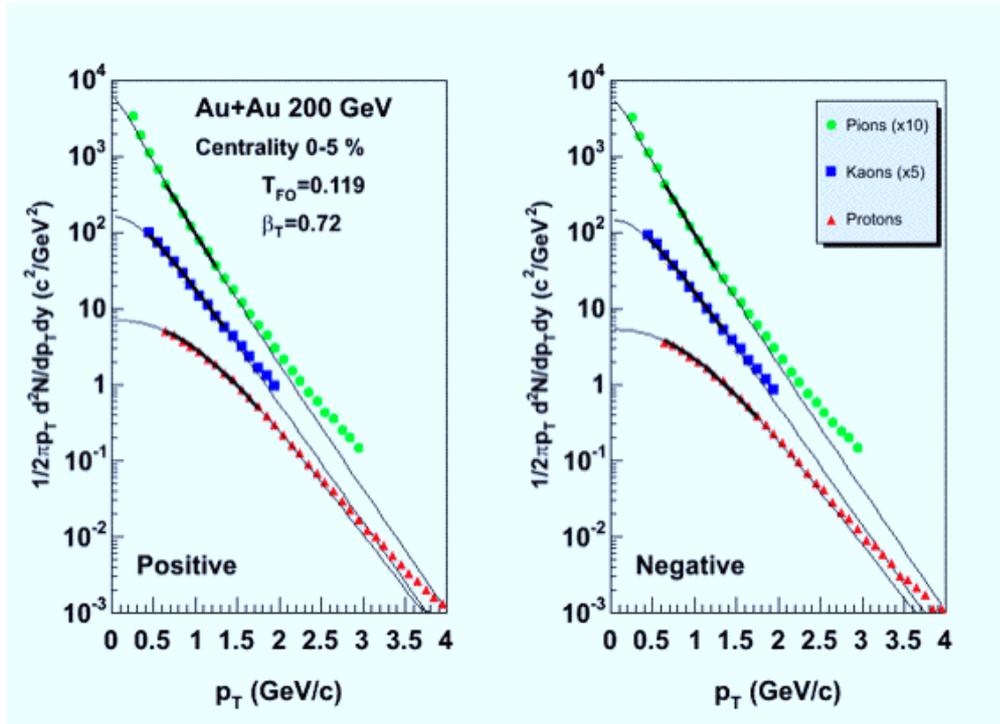
Figure 1.11: Transverse momentum spectra for $\pi/K/p$ in Au + Au collisions at $\sqrt{s_{NN}} = 200$ GeV with Blast-wave fitting result for both negative (Left) and positive (Right) charge. This figure is taken from [63].

The effect of expansion dynamics can be also seen at the mass dependence of $v_2(p_T)$ shown in Figure 1.12 which includes v_2 for $\pi/K/p$ along with a comparison with an hydrodynamic model

calculation [7] . The $v_2(p_T)$ for π is larger than that for K and p at low p_T, and this mass ordering has been understood as the result from collective flow, which produces larger p_T shift for larger hadron masses, and it makes stronger elliptic flow for smaller hadron masses. However, this calculation cannot reproduce the proton spectra, and if we attempt to fix this problem, the calculations no longer reproduce the measured v_2 for $\pi/\mathrm{K}/\mathrm{p}$. At low p_T (≤ 2.0 GeV/c) the magnitude and tendency of v_2 is found to under-predicted by a hadronic cascade model [51] . On the other hand, a broad selection of the experimental measurements at RHIC agree well with perfect fluid hydrodynamics, which means very low ratio of viscosity to entropy and very short mean free path [10] [11] [13] [16] .
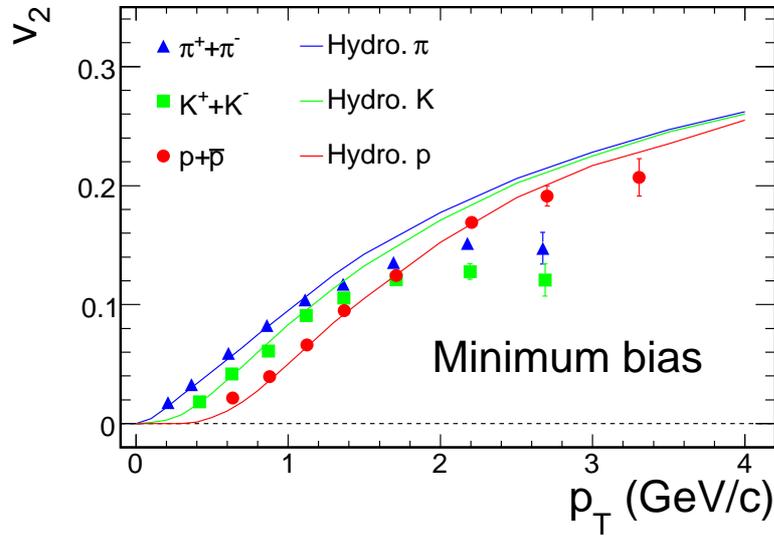
Figure 1.12: Comparison of $v_2(p_T)$ to hydrodynamical calculation for $\pi/\mathrm{K}/\mathrm{p}$ in Au+Au at 200 GeV [7] .

1.3.4   Quark Recombination at Intermediate p_T

In a contrasting situation of low p_T region, v_2 for p becomes larger than that for π and K in the intermediate p_T as also shown in Figure 1.12 , and hydro models no longer reproduce the measured hadron spectra and v_2. The quark recombination(coalescence) is a mechanism which successfully describes some aspects of hadron productions such as ratio of π to p and v_2 in heavy ion collisions in this momentum region. This mechanism is a different physics framework from hydro, in which baryons receive a larger p_T boost than mesons. In this picture, partons of thermal origin in a densely populated phase space combine to form the final state hadrons; meson is formed by coalescence of quark and anti-quark and baryon is formed of three quarks. If the observables of hadrons can be explained by recombination model, this prove the existence of a large thermalized source of quarks and anti-quarks, and thus, it is a strong evidence for a QGP formation in the early stage of the collisions [34] [35] . In a simplified version of the model, the production rates of

the mesons and baryons at mid-rapidity are evaluated as Equation 1.17 and 1.18 respectively,

$$E\frac{d^2N_\mathrm{M}}{d^2p_\mathrm{T}} \propto \int_0^1 dx\, w_a\big(R; xp_\mathrm{T}\big)\ |\phi_\mathrm{M}(x)|^2\ w_b\big(R; (1-x)p_\mathrm{T}\big), \tag{1.17}$$

$$E\frac{d^2N_\mathrm{B}}{d^2p_\mathrm{T}} \propto \int \mathcal{D}x_i\, w_a\big(R; x_1 p_\mathrm{T}\big) w_b\big(R; x_2 p_\mathrm{T}\big) w_c\big(R; x_3 p_\mathrm{T}\big)\ |\phi_\mathrm{B}(x_1, x_2, x_3)|^2, \tag{1.18}$$

$$\int \mathcal{D}x_i = \int_0^1 dx_1\, dx_2\, dx_3 \delta(x_1 + x_2 + x_3 - 1). \tag{1.19}$$

Here, E is the energy of the four vector $\mathbf{p}$. $w(\mathrm{R}; p_\mathrm{T})$ is phase space distribution of constituent quarks, x is a fraction of the momentum. a, b and c are the valence quarks and $\phi_\mathrm{B}(x_1, x_2, x_3)\big(\phi_\mathrm{M}(x)\big)$ is the effective wave function of the baryon (meson). We use the short notation, Equation 1.19, for the integration over three fractions. Assuming an equal momentum fraction such as $x = 1/2$ for mesons and $x_1 = x_2 = x_3 = 1/3$ for baryons, the approximate relations as Equation 1.20 are obtained,

$$E\frac{d^2N_\mathrm{M}}{d^2p_\mathrm{T}} \simeq C_\mathrm{M} w^2\big(p_\mathrm{T}/2\big), \quad E\frac{d^2N_\mathrm{B}}{d^2p_\mathrm{T}} \simeq C_\mathrm{B} w^3\big(p_\mathrm{T}/3\big). \tag{1.20}$$

C_M (C_B) corresponds to the coalescence probabilities for mesons (baryons). In the quark recombination picture, the azimuthal anisotropy of the produced hadrons reflects the anisotropy of the constituent quarks and anti-quarks. When quarks and anti-quarks have a pure elliptic flow, the w is written as,

$$w \propto 1 + 2v_{2,\mathrm{q}} \cos 2\phi, \tag{1.21}$$

where $v_{2,\mathrm{q}}$ is the amplitude of the elliptic flow of the quarks and anti-quarks, and ϕ is the azimuthal angle. With Equation 1.21, v_2 for meson and baryon are obtained as,

$$v_{2,\mathrm{M}} = 2v_{2,\mathrm{q}}\big(p_\mathrm{T}/2\big), \quad v_{2,\mathrm{B}} = 3v_{2,\mathrm{q}}\big(p_\mathrm{T}/3\big). \tag{1.22}$$

Therefore, this model predicts that the amplitudes of the elliptic flow for mesons and baryons are scaled by the number of constituent quarks (n_q) so called "quark number scaling".

Figure 1.13 and 1.14 indicate that the experimental results are consistent to this model [5]. The left figures of Figure 1.13 and 1.14 show v_2 vs. p_T and v_2/n_q vs. $p_\mathrm{T}/n_\mathrm{q}$ in Au+Au at 200 GeV, respectively. Comparing these two results, we can see that the scaled v_2 for identified hadrons is scaled by the number of constituent quarks. This suggests that QGP is formed in the early stage of the collision and the v_2 develops in the partonic phase. Additionally there is another scaling so called "KE_T scaling" which scales v_2 as a function of KE_T ($= m_\mathrm{T} - m_0$) instead of p_T as shown in right figure of Figure 1.13. Applying these two scaling (quark number scaling and KE_T scaling), various hadron v_2 take a same curve in the momentum region up to $KE_\mathrm{T}/n_\mathrm{q} = 1.0 \sim 1.5$ GeV/c as shown in the right of Figure 1.14. The KE_T scaling has been considered to subtract the effect of the radial flow which makes mass ordering of v_2 at low p_T as explained above. This is, however, not confirmed yet, and the some more details of the KE_T scaling will be discussed at discussion part in this thesis.
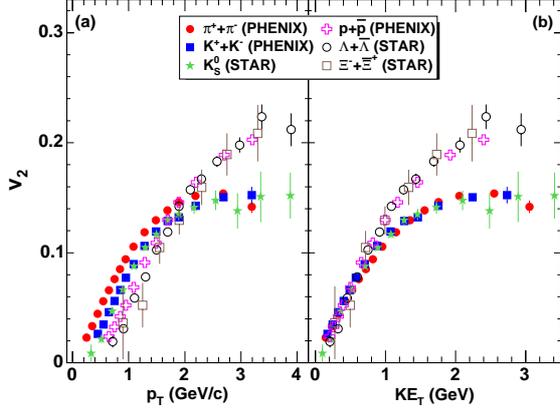
Figure 1.13: (a) v_2 vs. p_T and (b) v_2 vs. KE_T for identified hadrons for minimum bias in Au+Au collision. [5]
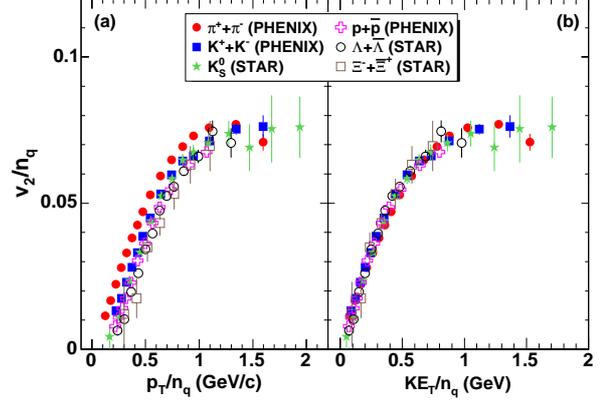
Figure 1.14: (a) v_2/n_q vs. p_T/n_q and (b) v_2/n_q vs. KE_T/n_q for identified hadrons for minimum bias in Au+Au collision. [5]

1.3.5 Suppression and Energy Loss at High p_T

At higher p_T, particles are mainly jet components which is produced from the fragmentation of high p_T parton produced at the initial stage of the collision. Jet production occurs in the overlap region and it is independent of the reaction plane. Thus, v_2 would be zero if the high p_T partons were not modified by anything related to reaction plane angle. However, we have observed that π^0 and charged hadron yields are significantly suppressed for the high p_T region ($p_T \geq \sim 4$ GeV/c) in Au+Au and Cu+Cu collision at 200 GeV compared with p+p collisions [39] [40] [41] [44] . Since there is no suppression in d+Au collisions at high p_T, it is understood that the suppression occurs due to the final state interaction at the collision such as the gluon radiation in the hot dense matter [42] . Another evidence for the suppression being a final state effect comes from the non-suppression of the direct photon yield in Au+Au collisions [43] .
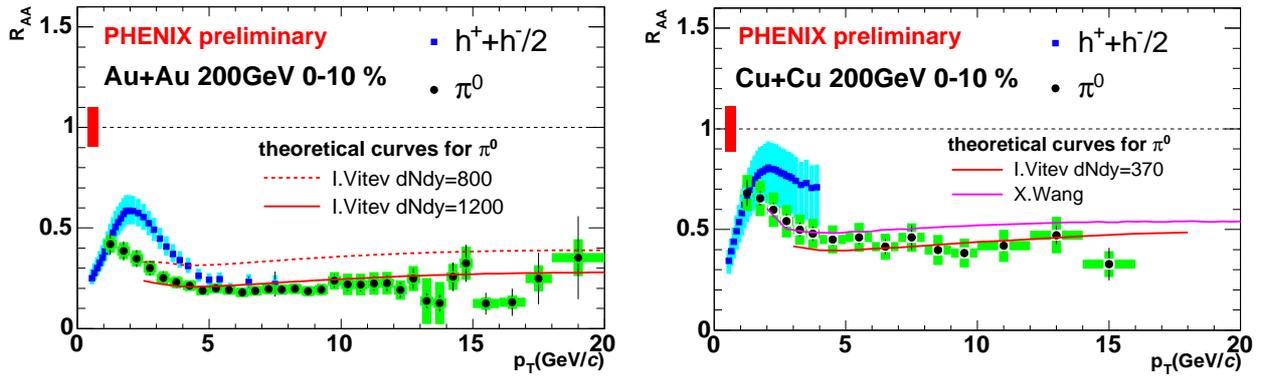
Figure 1.15: The comparison of R_{AA} for π^0 and charged hadron at 0-10 % centrality bin in Au+Au (left) and Cu+Cu (right) collisions as a function of p_T with theoretical prediction (Red [45] and purple [46] lines). The error bars are statistical error, and the boxes are systematic error.

Figure 1.15, shows the comparison of the Nuclear Modification Factor, R_{AA}, which should be unity if the nucleus-nucleus collision is just represented as superposition of p + p collision,

for π^0 and charged hadrons in 0-10 % most central Au+Au and Cu+Cu collisions as function of p_{T}. Both π^0 and charged hadron are strongly suppressed in both Au+Au and Cu+Cu collision. These results indicate the high p_{T} partons which produce jets lose its energy in the medium. Since the collision overlap region forms an almond shape (not round) in non-central collisions, high p_{T} partons traverse less medium and they could lose less energy in the in-plane direction, compared to the case of out-of-plane direction. The difference of the amount of partons absorbed in plane and out-of plane directions produces azimuthal anisotropy of jet productions, and it makes v_2 positive. Therefore, if v_2 is positive in high p_{T} region, it will also be a evidence that the collision creates a hot dense matter (QGP) and the partons are strongly interacting with this medium.

1.4 Thesis Motivation

The purpose of this thesis is to understand the thermal property of the matter created in relativistic heavy ion collisions by the systematic study of v_2 for charged hadrons. From the previous v_2 measurement at $\sqrt{s_{\mathrm{NN}}} = 200$ GeV in Au+Au non-central collisions, it has been suggested that the matter thermalized on a very rapid time scale $\tau < \sim 1$ fm/c after the collision, and the initial geometrical anisotropy transfered to the pressure gradient which produces elliptic flow. It has been considered that v_2 is determined by initial ellipticity only if the matter reaches local thermal equilibrium after collision [6] . However, since a heavy ion collision is dynamical process and the created QGP phase must evolve during a finite time, we expected that the v_2 is not only determined by initial geometrical ellipticity but also influenced by a finite evolution time which can be related to the size of collision.

For a more comprehensive understanding of the origin of v_2 in heavy ion collisions, we measured v_2 for inclusive charged hadron and identified charged hadron in Au+Au and Cu+Cu collision at $\sqrt{s_{\mathrm{NN}}} = 200$ GeV and 62.4 GeV, which were taken by PHENIX experiment in year 2004 and 2005. We study the dependence on collision energies, collision size and particle species. By comparing the v_2 in Au+Au and Cu+Cu collisions for some centrality bins, we can test that the scaling behavior of v_2 depending on geometrical eccentricity at same N_{part} and depending on N_{part} at same geometrical eccentricity.

In addition to this, a scaling of elliptic flow by number of constituent quarks, suggestive of quark-like degrees of freedom, can also be tested for a broad range of particle species produced in Cu+Cu collisions at $\sqrt{s_{\mathrm{NN}}} = 200$ GeV and in Au+Au collisions at $\sqrt{s_{\mathrm{NN}}} = 62.4$ GeV as well as we have done in Au+Au collisions at $\sqrt{s_{\mathrm{NN}}} = 200$ GeV. Moreover, by comparing the v_2 for various hadron species, we can test the performances of KE_{T} scaling which seems to work out in Au+Au at 200 GeV collisions. To understand the detail of the thermalization and the hydrodynamical behavior, a comparison of the hydrodynamical model (blast-wave model) with measured spectra and v_2 for various hadron species is also attempted simultaneously. The azimuthal dependence of the freeze-out temperature, T_{fo}, and the radial velocity, β_{T}, which are extrapolated by hydrodynamical model fitting, are also discussed.

Chapter 2

PHENIX DETECTORS

2.1 Overview
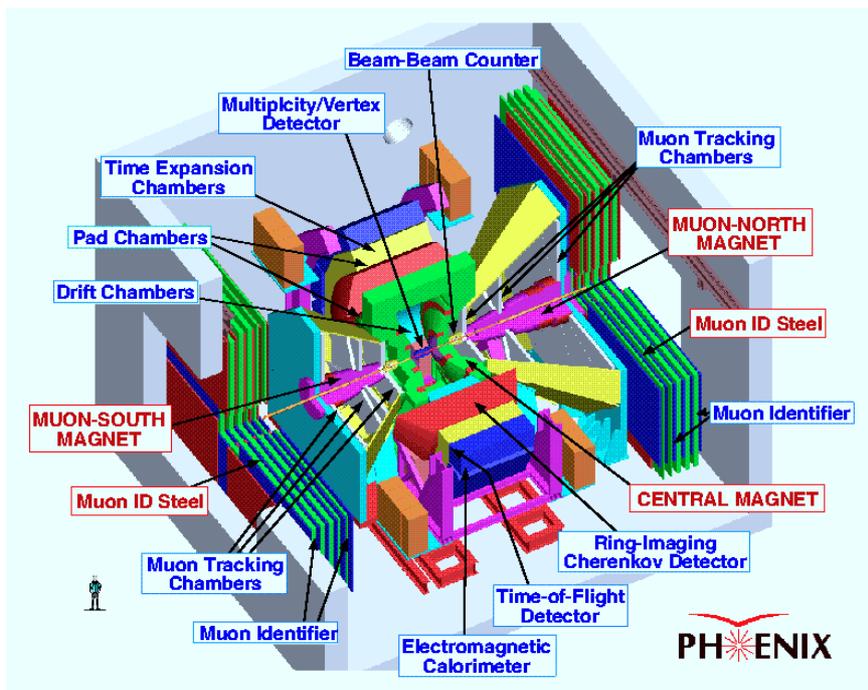
Figure 2.1: Overview of the PHENIX detector.

For the broad physics investigation, the PHENIX experiment utilizes a variety of detector technologies. Characterizing the collisions the PHENIX detector consists of four spectrometer arms - two around mid rapidity termed the central arms each subtending $90°$ in azimuth and with $|\ \eta\ | < 0.35$ to measure electrons, hadrons, and photons, and two at forward rapidity termed the muon arms covering the full azimuth for $1.1 < \eta < 2.4$ to measure muons - and a set of global detectors. Each spectrometer has a large geometrical acceptance. Counting the central magnet which is positioned around beam pipe, the spectrometers have excellent energy and momentum resolution and particle identification capability.

The central arm and south Muon arm detectors were completed in 2001 and took data during

Au + Au operation of RHIC the same year (RUN2). Since the RUN4 and Run5 data sets are analyzed in this thesis, here the detectors used at Run4 and Run5 are mainly mentioned. The overview of the PHENIX detectors are shown in Figure 2.1.
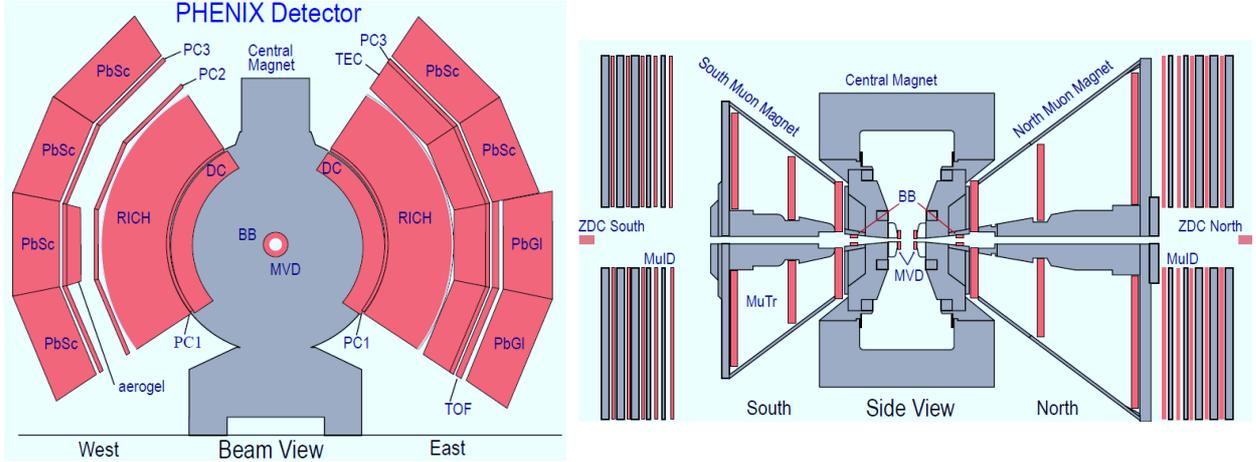
Figure 2.2: Installed and active detectors for the RUN4 configuration of the PHENIX experiment. Left figure is the two central spectrometer arms viewed in a cut through the collision vertex, and right is a side view of the PHENIX muon arm spectrometers.

2.2   Magnet

The PHENIX magnet system is composed of three spectrometer magnets with warm iron yokes and water-cooled copper coils. The Central Magnet is an axial field magnet energized by two pairs of concentric coils, which can be run separately, together, or in opposition. The Magnet has 9 meters height and almost 500 tons weight covering $-0.35 < \eta < 0.35$. Since it provides a magnetic field around the interaction vertex that is parallel to the beam, charged particles bend in a plane perpendicular to the beam axis. The bending angles are accurately measured by the DC, from which the charged particle momentum can be calculated. The field strength is about $0.48 \sim$ T at the beam line ($R = 0$), and becomes smaller with larger R. The magnetic field for the central spectrometer is axially symmetric around the beam axis as shown in Figure 2.3, and the magnitude of the field take approximately constant. However, the field is not uniform near the DC. At the region around DC, the magnitude of filed is weak but not zero. At around $z = 0$, the residual field is about $0.096 \sim$ T ($0.048 \sim$ T) at the inner (outer) radius of the DC. At large z (80 cm), the field changes direction and is much weaker ($0.04 \sim$ T ($0.02 \sim$ T) at the inner (outer) radius of the DC).

2.3   Global Detector

In order to characterize the nature of event following a heavy ion collision, three global detectors are employed. They consist of Zero-Degree Calorimeters (ZDC), Beam- Beam Counters (BBC) and the Multiplicity-Vertex Detector (MVD). The BBC and ZDC are used for definition of the centrality at PHENIX as shown at Figure 2.4.
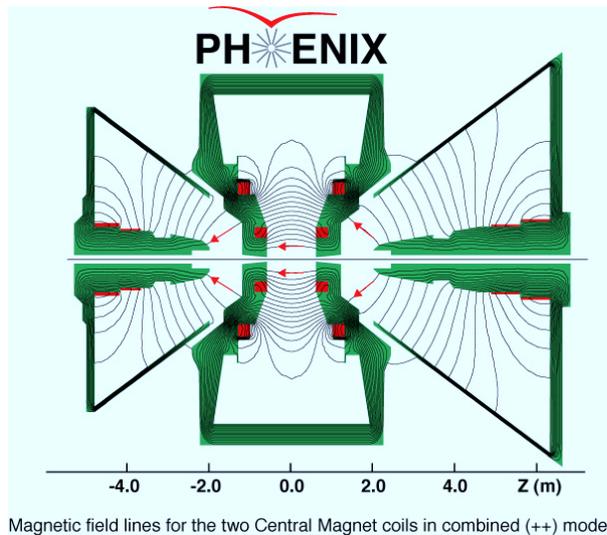
Figure 2.3: simplified cutaway of central and muon magnet field line. The beam axis is along the z and collision point is expected to be $z = 0$.

Figure 2.4: The BBC vs. ZDC analog response related to the centrality classes of the collisions at $\sqrt{s_{NN}} = 200$ GeV. The rightmost interval is the 0-5 % centrality class, the next is 5-10 % and so on.

2.3.1 ZDC

A pair of the ZDCs is used by each of all four RHIC experiments. The ZDC is a hadron calorimeter designed to detect neutrons from grazing collisions and give a trigger for the most peripheral collisions. The collisions of nuclei with high energy beam at RHIC lead to the emission of evaporation neutrons from both "beam" and "target" nuclei. The evaporated neutrons diverge by less than 2 m radians from the beam axis at 100GeV/u beam, therefore neutrons, which are neutral beam fragments, can be detected downstream from RHIC collision point while charged fragments in the same angular range are bend out of the ZDCs acceptance by the RHIC magnets which is originally designed to bend the beams. The ZDCs are placed at 18 m from the collision point at both up and down sides along the beam axis behind the RHIC magnets. They measure the energy deposited by spectator neutrons from the collisions. The produced particles by collision and the other secondary particles in this "zero degree" region deposit negligible energy compared with that of beam fragmentation neutrons.

2.3.2 BBC

A pair of PHENIX BBCs yields a trigger for the more central collisions, the collision vertex along the beam axis that helps to find correlation between tracks in various detector elements and the time that a collision occurs. The timing information is used for the measurement of the time-of-flight for particle identification combined with another detector such as TOF detector. a measurement of the time-of-flight of forward particles to determine the time that a collision occurs. The BBCs are placed upstream and downstream of the beam crossing point. Each array consists of 66 modules of counter elements surrounding the beam pipe, and covers the forward and the backward rapidity regions as shown in Figure 2.5. The average and the difference of the arrival times of fast leading particles from beam-beam collisions to the two BB counter arrays provide the time origin and the vertex position of the collisions, respectively. Each counter element is constructed
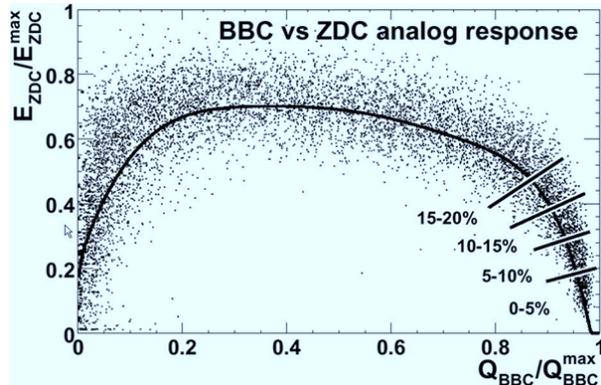
from a Cherenkov radiator of fused quartz and a 1-inch mesh-dynode photomultiplier (PMT). The fused quartz radiator is glued to the photomultiplier window. With such a combination of radiator and the photomultiplier, an intrinsic timing resolution of 44 ps was achieved for 1.6 GeV/c pions in a beam test. Because of the choice of the mesh-dynode PMT the BBCs is well operated under the PHENIX magnetic field. The electronics for BBC consist of discriminators, shaping amplifiers, time-to-voltage converters (TVC), ash ADCs (FADC) and buffer memories. The timing and pulse height information of the BB elements are digitized in each beam crossing by the TVC and FADC. The digitized data provided as a set of input of the LVL-1 trigger are stored in the buffer memory for the event building.
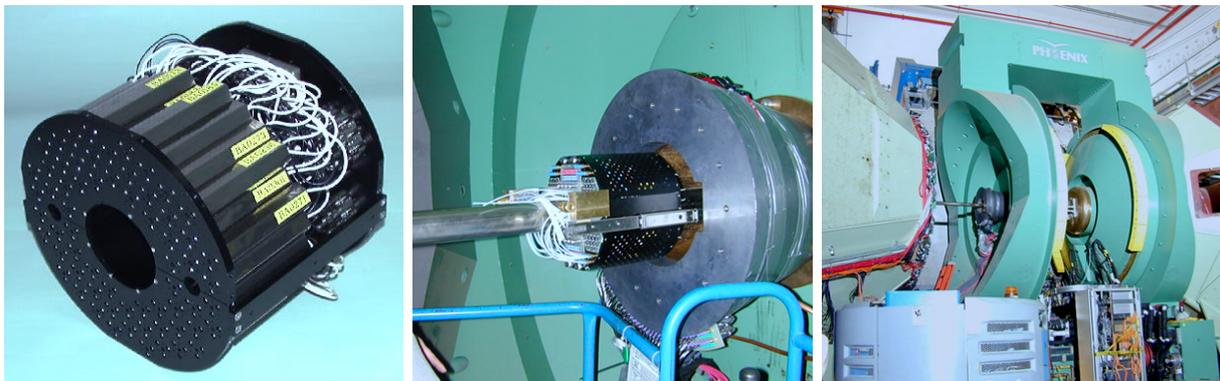
Figure 2.5: Photographs of installed BBC.

2.4 Central Arm

The central arm detectors consist of tracking systems for charged particles and electromagnetic calorimeter (EMCal). The PHENIX particle tracking system measures the momentum of charged particles from collisions, reconstructs the track from flight point and contributes to particle identification. There are three tracking subsystems designed for different functions. As the closest central detector to the beam collision point, the low-mass multi wire focusing Drift Chambers (DC) offer high resolution transverse momentum (p_T) measurements needed to determine the invariant mass of particle pairs. The DC also provides elementary position information for the reconstruction of the track through the various another PHENIX sub-systems. Positioning between the DC and EMCal, there are three Pad Chambers, termed PC1, PC2 and PC3. The PCs provide three dimensional space hit position of the charged particles and determine p_z/p_T. A Time Expansion Chamber also participates a part of particle identification using hit position and its dE/dx information. Since in this paper only the data taken from the West arm detectors is analyzed, the detail of TEC explanation is skipped here. The calorimeter is the outermost subsystem on the central arms and originally designed to measure photons and energetic electrons. Additionally, the hadrons deposit the its partial or total energy as hadronic shower with certain probability. Figure 2.2 shows a schematic drawing of the PHENIX central arms indicating the positions of DCs, PCs and EMCal.

2.4.1   Drift Chamber (DC)

The DC is a part of the both west and east arms of the PHENIX Central Detector. The east arm is a mirror image of the west arm. Each arm is a titanium framework filled with drift chamber modules. The DCs have cylindrical shape. They are placed between 2.02 and 2.46 m in radial distance from the interaction point and occupy 180 cm along the beam direction and 90° sector in ϕ. They are placed in a residual magnetic field with a maximum of 0.6 kG. The position of the DCs relative to the other detectors in the central spectrometer is show in Figure 2.2. DC framework consists of two ring frame connected with two side frames of box shape. The sketch of the DC framework and the stacking way of the sectors are shown in Figure 2.4.1. Six type modules are contained termed X1, U1, V1, X2, U2, V2. Each module contains four anode and four cathode wire nets. Cathode net consists only of cathode wires, while in addition to anode wires, anode net contains wires of other type - two channel + one guard + one field wire per each anode wire as well as four termination wires. Anode net of X-module contains 12 anode (sense) wires and anode net of U,V-module contains four anode (sense) wires. Difference in the design of X and U, V cages is conditioned by the fact that X-cage provide wire to run along z axis. The U and V planes are inclined at a small $\pm$ 5° stereo angle to allow for full three-dimensional track reconstruction. Figure 2.4.1 shows the mutual position of the X and U, V wire nets.
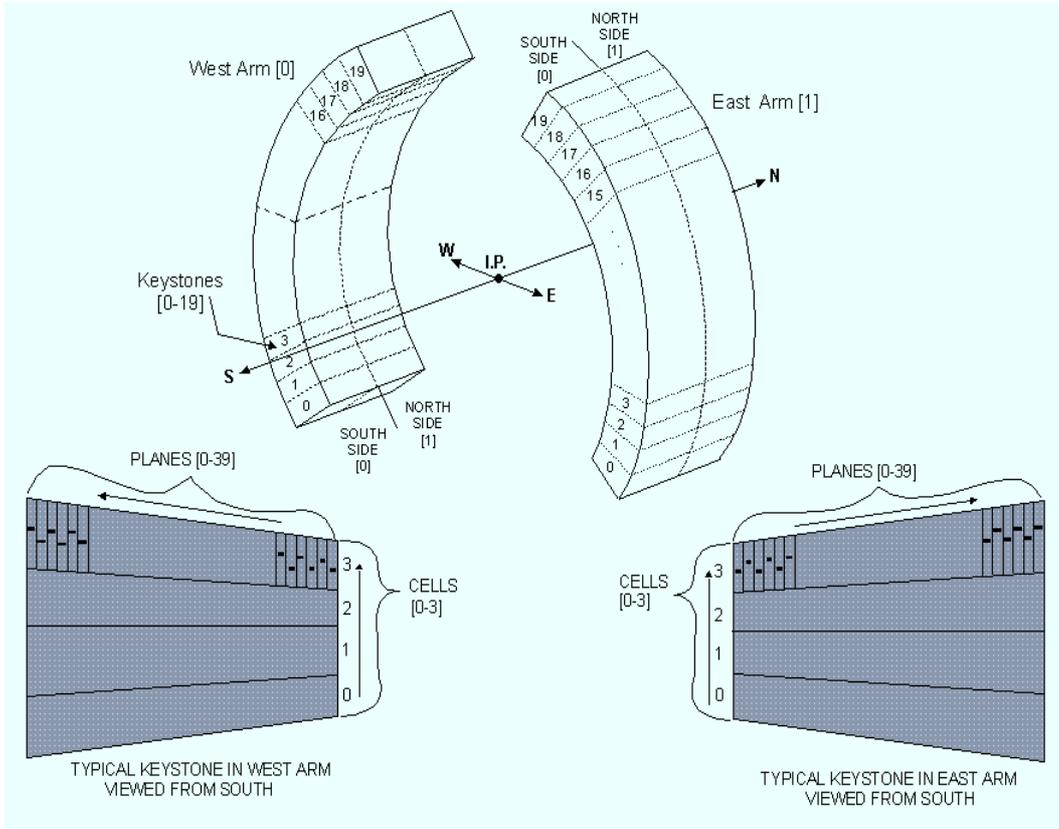
Figure 2.6: A sketch of the DC framework. Three drawings show the position and stacking way of the sectors
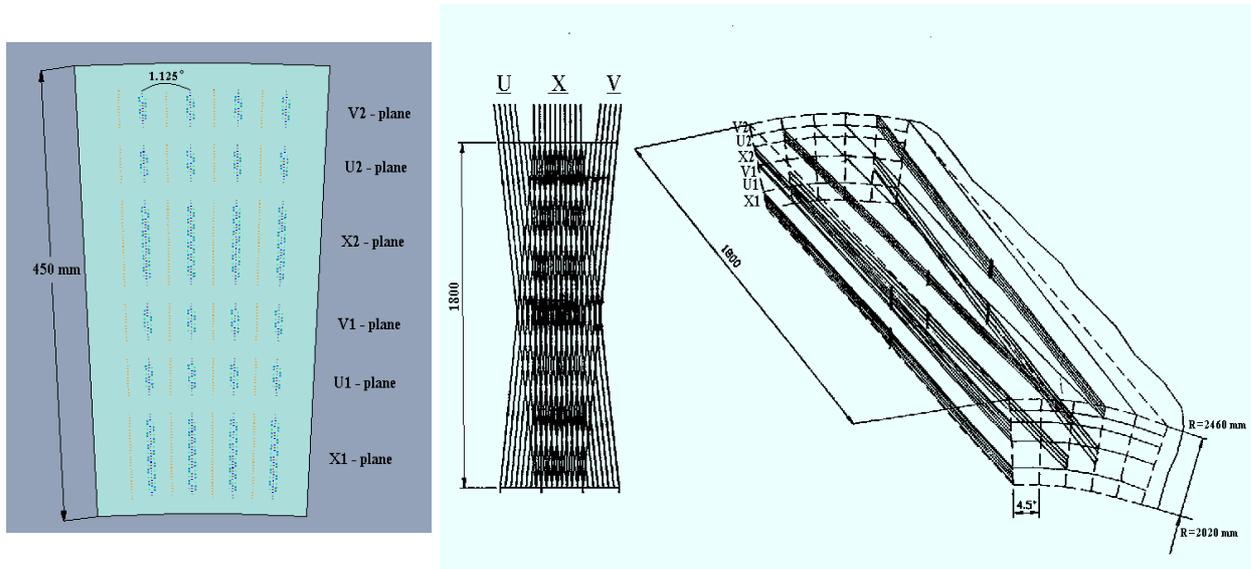
Figure 2.7: The layout of DC wire position within one sector (left). A schematic diagram of the stereo wire orientation from top of view (middle) and from diagonal view (right).

2.4.2 Pad Chamber
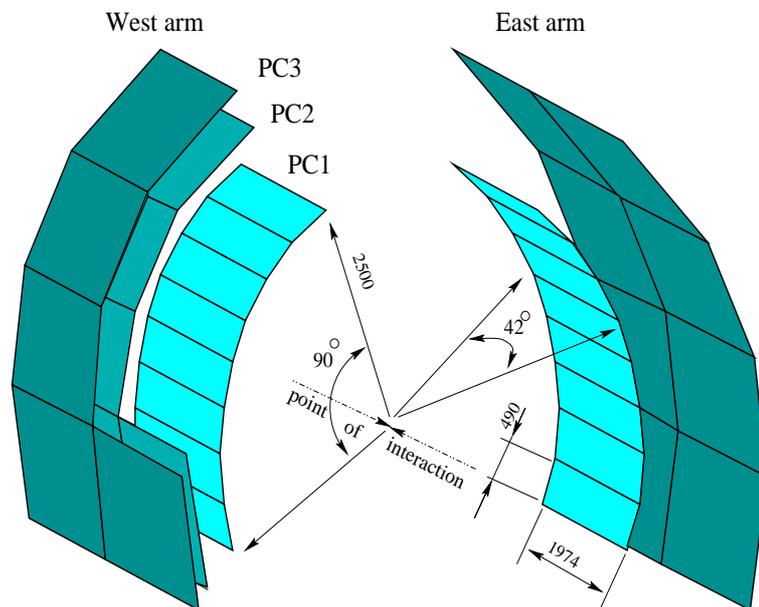
Figure 2.8: Illustration of the Pad Chamber system in PHENIX. Several sectors of PC2 and PC3 in the west arm are removed for good visibility of the drawing [54].

The PHENIX Pad Chambers (PC) are multi-wire proportional chambers that are composed of three separate layers (PC1, PC2, PC3) of pixel detectors as the part of the central tracking system. Figure 2.4.2 show the 3D sketch of the PC systems. The innermost pad chamber plane,

termed PC1 is located between the DC and Ring Imaging Cherenkov Counter (RICH) on both East and West arms. PC2 is placed in back of the RICH on the West arm from RUN2. PC3 is located in front of the Electromagnetic Calorimeters on both East and West arms. Each detector contains a single plane of wires called pad in a gas volume bounded by two cathode planes. One pad is finely segmented into nine small connected copper electrodes termed pixels. A cell is defined by the area enclosed with three contiguous pixels belonging to three different pads. More details are shown in Figure 2.4.2. The size of the cell is shown to the left (a). Assume that there are three separate layers of pad chambers (individual wire chambers) each with the pad size equal to 3×3 cells. By shifting the three layers by one cell relative to each other in both dimensions, reconstruct is possible in which cell a hit occurred, since each cell means a unique combination of pads from each of the three layers. This is illustrated in part (b). In part (c), each pad has been cut up in nine parts as previous reference, one in each cell covered by the pad. The pad is read out by a single preamplifier and discriminator. Whenever a charged track passes through the pad chamber and make an avalanche on an anode wire, there are three neighboring pads which all receive an induced signal large enough to trigger their three separate discriminators. The PC
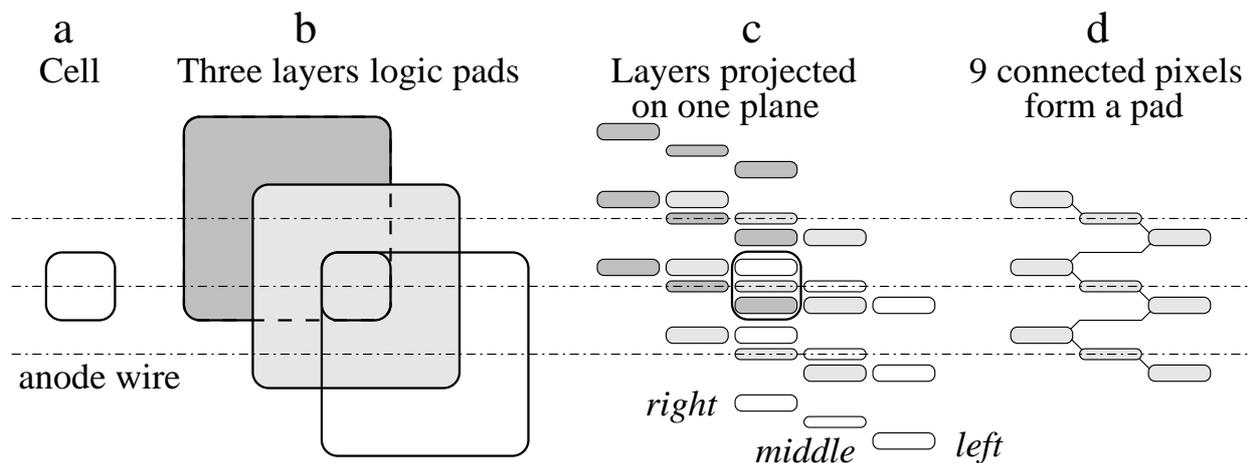
Figure 2.9: Principles of the pad geometry. (a) Cell of the size of an avalanche ($d \times d$). (b) Overlap of three larger pads defining a cell of the same size. (c) Three layers projected onto the same plane. (d) Connections between pixels on the same plane [54]

.

system determines space points along the straight line particle trajectories outside the magnetic field. The PCs are the only non-projective detectors in the central tracking system and thus are critical elements of the pattern recognition. PC1 is also essential for determining the three-dimensional momentum vector by providing the z coordinate at the exit of the DC. PC information is fundamental element for particle identification, particularly for critical electron identification. The DC and PC1 information gives direction vectors through the RICH while PC2 and PC3 are needed to resolve the background problem in the outer detectors where about 30 % of the particles striking the EMCAL are produced by either particle decays outside the aperture of the DC and PC1 or low-momentum primary tracks that curve around PC1 in the magnetic field and strike PC2 and PC3. The recognition of three points of a straight line track through the whole spectrometer

ensures that the response from the electron identifying detectors (RICH, TEC and EMCAL) and the momentum from the DC are correlated for track reconstruction and particle identification. The

Table 2.1: Performance of Pad Chambers [54]

Parameters	PC1	PC2	PC3
Pad Size $(r\text{-}\phi \times z)(cm^2)$	0.84×0.845	1.355×1.425	1.6×1.67
Single hit resolution $(r\text{-}\phi, z)$ in mm	(2.5,1.7)	(3.9,3.1)	(4.6,3.6)
Double hit resolution $(r\text{-}\phi, z)$ in cm	(2.9,2.4)	(4.6,4.0)	(5.3,5.0)
Radiation Length (% X_0)	1.2	2.4	2.4
Efficiency	> 99 %	> 99 %	> 99 %

key PC performance parameters are listed in Table 2.1. The pad size for PC1 is 0.84 cm × 0.845 cm to achieve less than 8 % occupancy in most central Au+Au collisions. This gives a position resolution of 1.7 mm along z and 2.5 mm in $r\text{-}\phi$. The pad size for PC2 and PC3 is chosen such that they have similar angular resolution compared to PC1. The use of a frame-less wire chamber held by honeycomb sandwich minimize the amount of material in the PC [54] .

2.4.3 Time of Flight (TOF)

The PHENIX time-of-flight counter (TOF) serves as a particle identification device for charged hadrons. The TOF is located 5.06 m away from the expected vertex in collisions between the PC3 and EMCAL in the east arm. The left side of Figure 2.10 shows the picture of TOF panel all together. It is designed to cover $\mid \eta \mid < 0.35$ and the azimuthal angle, $\Delta\phi = 45°$. 10 panels, which consist 960 slats of plastic scintillation counters with 1920 channels of photomultiplier tube readout, were installed and have been operated. The slat, which is oriented along the $r\text{-}\phi$, provides the time and longitudinal position of charged particles hitting the slat. Figure 2.11 shows a schematic view of one panel of the TOF detector. It consists of 96 plastic scintillation counters with PMTs at both ends, light guides and mechanical supports. Scintillator rod and light guides were wrapped with thin aluminum foil and were glued on the honeycomb board. The honeycomb boards are made of paper of a honeycomb structure sandwiched between carbon fiber sheets, which provide a "massless" rigid structure. Scintillators with two different lengths (637.7 and 433.9 mm) are assembled in an alternating fashion in order to avoid geometrical conflicts between the PMTs of neighboring slats. Each end of the scintillator slat is attached with optical glue to a 180° bent light guide. On both sides of one panel, the light guides are bent 90° so as not to conflict with the neighboring PMTs. The scintillator slats are glued on the honeycomb board which consists of carbon fiber sheet and honeycomb paper in order to reduce the amount of material but also provide the wall with sufficient mechanical strength. The total radiation length including PMTs and cables is about 6 % . Using different lengths of scintillator slats and adoption of bent light guides as described above has allowed us to achieve very small dead space between the TOF slats. Combining the information from the DC, PC1, BBC and the TOF, particle identification of charged hadrons is performed. The time resolution of the TOF system is designed to be less than 100 ps, which corresponds to π/K separation up to 2.4 GeV/c in the experiment. The right side

of Figure 2.10 illustrates the particle separation capabilities of the TOF system. The flight path length of each track from the event vertex to the TOF detector, which calculated in the momentum reconstruction algorithm, is used to correct the TOF value. The right of Figure 2.10 is a contour plot of TOF as a function of the reciprocal momentum in minimum bias Au+Au collisions after the residual cut of TOF hits association between the track projection point and TOF hit was applied.
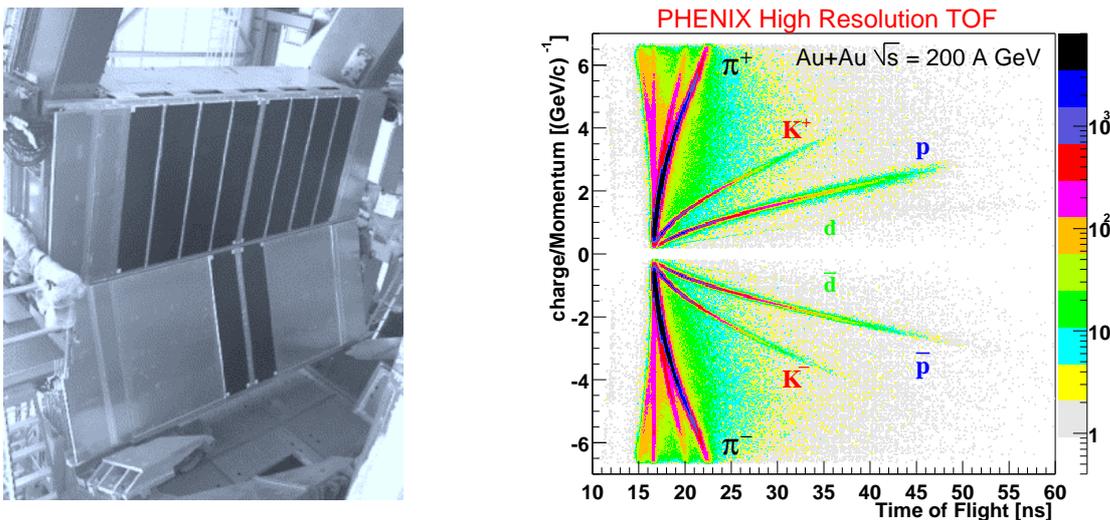
Figure 2.10: The picture of TOF detector system mounted on the PHENIX east arm showing 10 panels of the detector (left). Contour plot of the time-of-flight vs. reciprocal momentum in minimum bias Au+Au collisions at $\sqrt{s_{\mathrm{NN}}} = 200$ GeV. The figure clearly demonstrates the particle identification capability of the TOF detector. The flight path for each track is corrected (right).

2.4.4   Electro Magnetic Calorimeter(EMCal)

The PHENIX Electromagnetic Calorimeter (EMCal) is originally designed to measure the spatial position and energy of electrons and photons produced in heavy ion collisions. It also has several important roles for such as particle identification and triggering on rare events with high momentum photon and electrons. Moreover, the EMCal can provide a good measurement of the hadronic energy deposited at mid-rapidity and thus of the total transverse energy E_{T} in the reaction. Measurements of the energy deposit with the hadrons are used for this analysis which is described at following sections. The EMCal covers the full central spectrometer acceptance of $70° \leq \theta \leq 110°$ installed both two walls, each subtending $90°$ in azimuth. The PHENIX EMCal consists of six sector of the Pb-Scintillator calorimeters and two sector of the Pb-glass calorimeters. The system has 24768 individual detector modules as total. Both the Pb-Scintillator and the Pb-glass read out with photomultipliers have fine energy resolution and intrinsic timing characteristics although their design and properties are quite different. The Pb-scintillator is a sampling calorimeter which is appeared in Figure 2.4.4, while the Pb-glass is a Cherenkov detector. Due to the two detectors granularity, energy resolution is linear for hadrons. The timing properties and shower shape are also significantly different. In deed, the Pb-glass has the best energy resolution and the Pb-scintillator has the best timing resolution. According to the data analysis, for particle identification cuts and its systematic errors are also different. Since the data taken from west arm where the
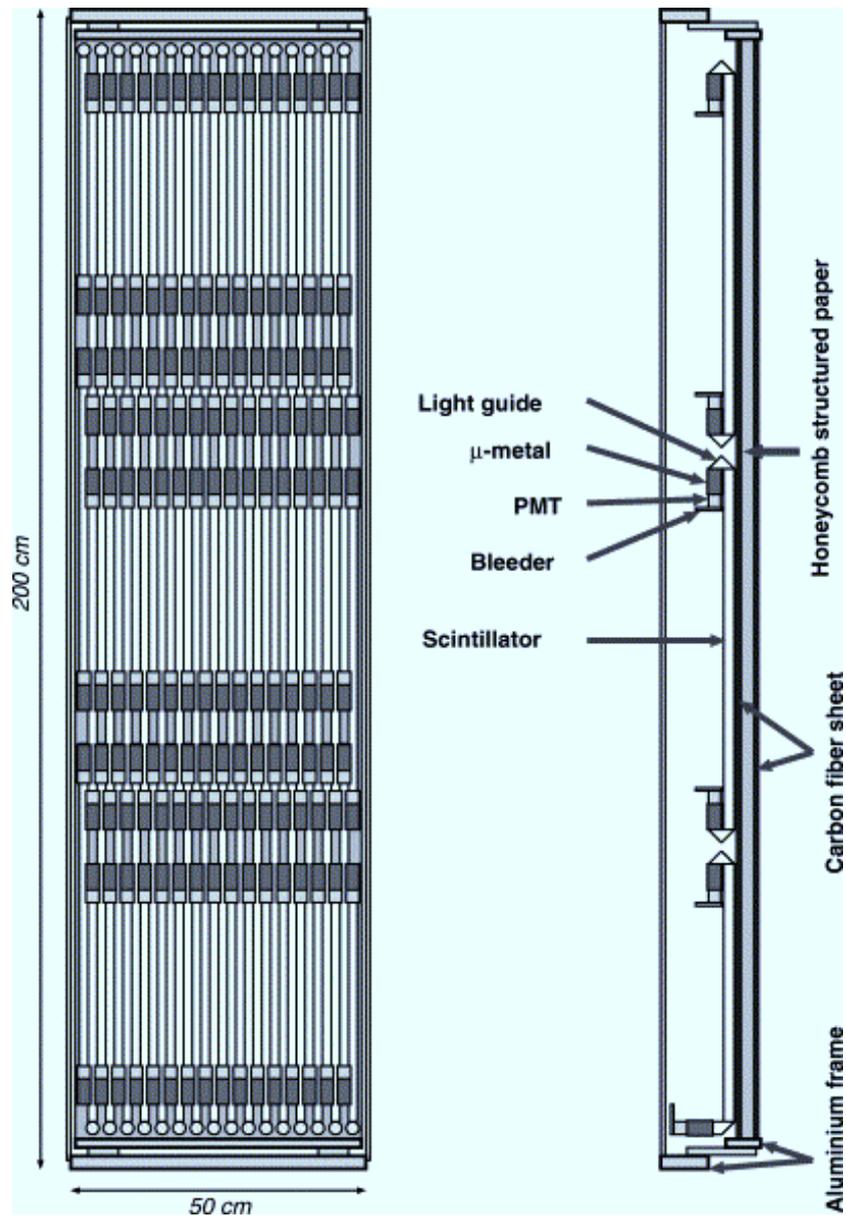
Figure 2.11: Schematic diagram of the components of a single TOF panel, which consists of 96 plastic scintillation counters with photomultiplier tubes at both ends, light guides and supports.

only Pb-scintillator is installed, are selected for the analysis in this thesis, here the Pb-scintillator is described for more detail. The Pb-scintillator electromagnetic calorimeter is a shashlik type sampling calorimeter consisting of 15552 individual towers. Each Pb-scintillator tower contains 66 sampling cells consisting of alternating tiles of Pb and scintillator. The basic building block is a module which consists of four optically isolated towers read out individually. The modules were designed to obtain large light yield in all towers. The PbSc calorimeter has a nominal energy resolution around 8.1 % / $\sqrt{E}$ (GeV) $\pm$ 2:1 % and an intrinsic timing resolution better than 200 ps for electromagnetic showers.
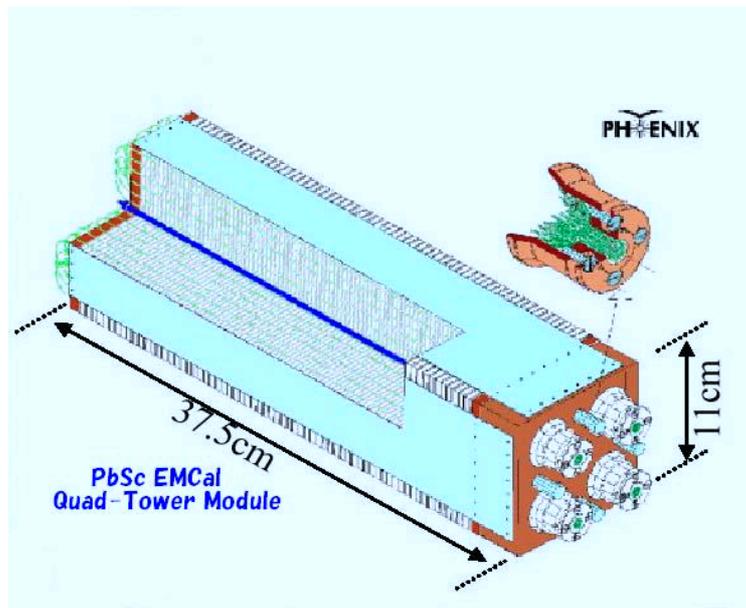
Figure 2.12: The section view of Pb-scintillator calorimeter module representing alternative stack between scintillator and lead tile layer, wavelength shifting readout fiber and leaky fiber inserted in the central hole.

Table 2.2: Summary of the PHENIX Detector Subsystems

Element	$\Delta\eta$	$\Delta\phi$	Purpose and Special Features
Magnet: central (CM)	± 0.35	$360°$	Up to 1.15 T·m.
muon (MMS)	-1.1 to -2.2	$360°$	0.72 T·m for $\eta = 2$
muon (MMN)	1.1 to 2.4	$360°$	0.72 T·m for $\eta = 2$
Beam-beam (BBC)	$\pm(3.1$ to $3.9)$	$360°$	Start timing, fast vertex.
ZDC	± 2 mrad	$360°$	Minimum bias trigger.
Drift chambers (DC)	± 0.35	$90°\times 2$	Good momentum and mass resolution, $\Delta m/m = 0.4\%$ at $m = 1$GeV.
Pad chambers (PC)	± 0.35	$90°\times 2$	Pattern recognition, tracking for non-bend direction.
RICH	± 0.35	$90°\times 2$	Electron identification.
TOF	± 0.35	$45°$	Good hadron identification, $\sigma < 100$ ps.
PbSc EMCal	± 0.35	$90°+45°$	For both calorimeters, photon and electron detection.
PbGl EMCal	± 0.35	$45°$	Good $e^\pm/\pi^\pm$ separation at $p > 1$ GeV/c by EM shower and $p < 0.35$ GeV/c by TOF. $K^\pm/\pi^\pm$ separation up to 1 GeV/c by TOF.
μ tracker: (μTS)	-1.15 to -2.25	$360°$	Tracking for muons.
(μTN)	1.15 to 2.44	$360°$	Muon tracker north
μ identifier: (μIDS)	-1.15 to -2.25	$360°$	Steel absorbers and Iarocci tubes for
(μIDN)	1.15 to 2.44	$360°$	muon/hadron separation.

Chapter 3

ANALYSIS

3.1 Data Selection

The information of the data, event and track selections is summarized in this section. All analyzed data in this thesis was taken by PHENIX experiment at RHIC from Run4 (year 2004) to Run5 (year 2005).

3.1.1 Data Sets and Event Selection

Four independent data sets are used for this systematic analysis. The trigger is minimum bias (MB) trigger. The minimum bias trigger requires at least two PMTs firing at north and south Beam-Beam Counter (BBC) and at least one forward neutron detected in north and south Zero Degree Calorimeters (ZDC) at $\sqrt{s_{\mathrm{NN}}} = 200$ GeV in Au+Au and at least one fired PMT at north and south BBC for other three data sets. The absolute value of BBC vertex position, $|\,\mathrm{bbcz}\,| \leq$ 30 cm is also required. Based on the detailed simulation with BBC response and input $\mathrm{d}N/\mathrm{d}y$ distributions, the efficiencies of minimum bias trigger are estimated. The data sets, the number of analyzed events and the trigger efficiency for minimum bias are summarized in Table 3.1 [78] [20].

Table 3.1: Table of the four analyzed data sets and the trigger efficiency [78] [20].

Run	Collision System	Energy $\sqrt{s_{NN}}$	Number of events	MB Trigger efficiency
Run4	Au+Au	200 GeV	860 Millions	92 ± 3 %
Run4	Au+Au	62.4 GeV	37.6 Millions	83 ± 3 %
Run5	Cu+Cu	200 GeV	713 Millions	94 ± 4 %
Run5	Cu+Cu	62.4 GeV	315 Millions	88 ± 4 %

3.1.2 Track Selection

The data taken by each PHENIX detector are combined and reconstructed before stored into data base. The elemental procedure for tracking reconstruction is explained as follows referring Figure 3.3. Track reconstruction with the drift chamber is handled with a combinatorial Hough transform (CHT) technique. In this technique, the 3D position hits detected at DC (on X1, X2, U, V wires) and PC1 are mapped with a pair of the polar angles (ϕ and θ) at the intersection

of the track with a reference radius near the mid-point of the drift chamber and the inclination angle (α) of the track at that point. The reconstructed tracks are labeled by quality bits which are defined by the hit information of these wires. Since the α variable is proportional to the inverse
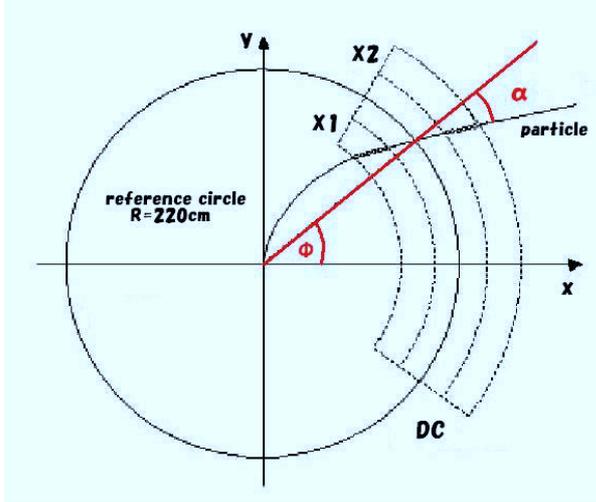
Figure 3.1: Illustration of the Hough transform parameters for drift chamber track reconstruction. The outline shows the drift chamber active volume. The small circles represent drift chamber hits along the particle trajectory.
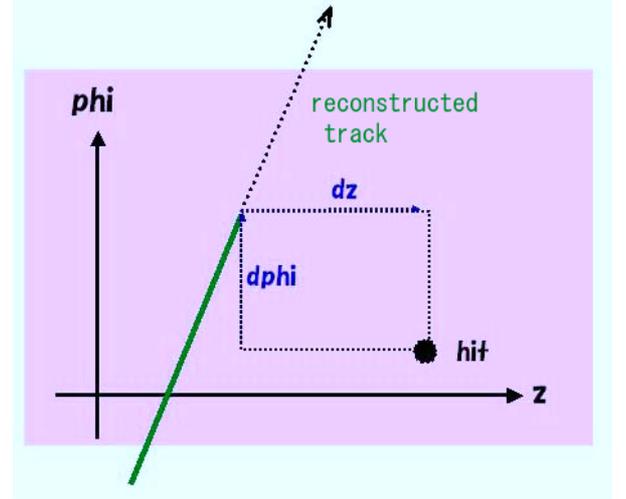
Figure 3.2: Definition of $d\phi$ and dz as ϕ and z components of the vector from reconstructed truck to nearest hit point.

of the transverse momentum at certain magnetic field, it provide the fundamental value to the momentum reconstruction procedure. The transverse momentum is obtained as

$$p_{\mathrm{T}} \simeq \frac{K_1}{\alpha} \tag{3.1}$$

where K_1 is the field integral along the track trajectory,

$$K_1 = \frac{0.3}{r_{\mathrm{DC}}} \int lBdl = 101 \text{ mrad GeV}/c. \tag{3.2}$$

Using this method, the DC tracking efficiency indicates that the probability of the spurious track is less than 1 % at $p_{\mathrm{T}} \leq 1.5$ GeV.

Second, assuming that all tracks are coming from vertex position, which is measured by BBC at each event, the track is drawn from DC to collision point. Next, considering the magnetic field effect behind DC at that calculated momentum, the track is extended through PCs, TOF, and EMCal. Every reconstructed truck is associated to the nearest hit point on each detector, and the reconstructed track which has the no proper hit point on PCs is discarded.

On the PHENIX data taking and reconstructed system, z axis is defined as beam direction from South to North, y axis is vertical direction from ground to sky, x axis is from East to West, and the ϕ axis is azimuthal direction from x axis to y axis rotating around PHENIX detectors. ϕ and z direction shown in the left figure of Figure 3.3 are mainly used on this analysis. As indicated on Figure 3.2, $d\phi$ and dz are defined as z and ϕ components of the vector from the point on
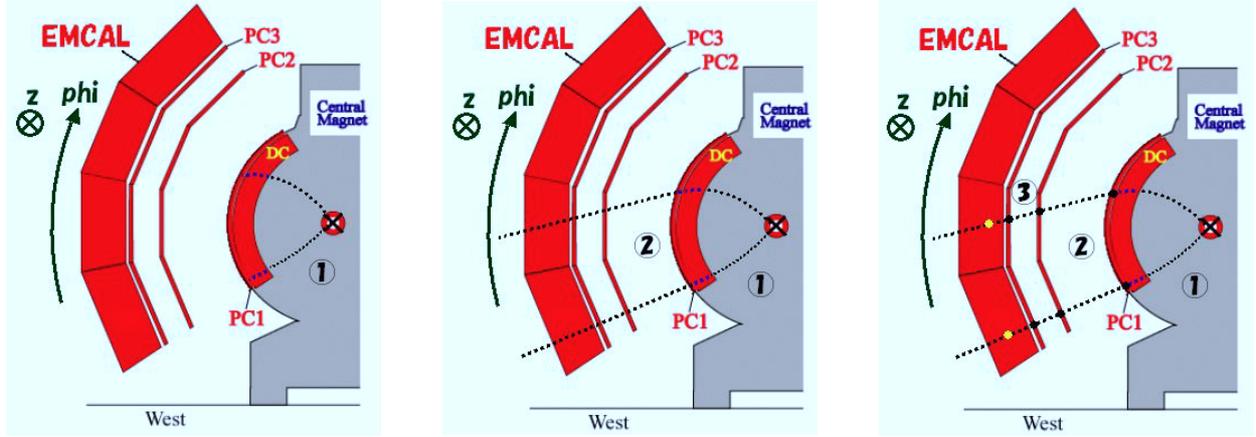
Figure 3.3: Procedure of the track reconstruction. 1) According to 4 point hits on DC, draw the track from vertex to DC. 2) Considering the magnetic field effect, extend the track through PCs and EMCAL. 3) Associate the reconstructed track to nearest hit point on each detector.

which the reconstructed track hit the PC to nearest hit point which is associated with this track respectively.

If there are only genuine tracks composed of charged hadron particles emitted from vertex, the $d\phi$ and dz distributions are Gaussian where the width ($\sigma_{\mathrm{matching}}$) is derived as

$$\sigma_{\mathrm{matching}} = \sqrt{\sigma_{\mathrm{detector}}^2 + \left(\frac{\sigma_{\mathrm{multi\cdot scat}}}{p\beta}\right)^2} \tag{3.3}$$

where $\sigma_{\mathrm{detector}}$ is the resolution of the detector and $\sigma_{\mathrm{multi\cdot scat}}$ is the multiple scattering contribution. The width is mostly depend on only resolution of the detector at p_T more than around 1 GeV since the multiple scattering effect becomes small and negligible compared with the detector resolution.

The requirement for track selection is listed below.

- Position matching hits ($|\,d\phi\,| < 3.0\ \sigma$ and $|\,dz\,| < 3.0\ \sigma$) on Electromagnetic Calorimeter (EMCal) and Pad Chamber 3 (PC3), or on time of flight detector (TOF).

- Require a hit on Lead Scintillator when using EMCal.

- p_T cut off for EMCal.

    - π : $0.2 < p_T < 1.5$ GeV/c.
    - K : $0.3 < p_T < 1.2$ GeV/c.
    - p : $0.5 < p_T < 2.0$ GeV/c.

- p_T cut off for TOF.

    - π : $0.2 < p_T < 4.0$ GeV/c.
    - K : $0.3 < p_T < 3.0$ GeV/c.
    - p : $0.5 < p_T < 4.0$ GeV/c.

- Drift Chamber (DC) hit position cut : $|\,zed\,| \leq 80$ cm.

- EMCal energy cut for a cluster : ecent > 0.1 GeV.

The difference between 1.0 σ and 2.5 σ matching cut with enough statistics is included into the systematic errors of the v_2 results.

3.2 Evaluation of Backgrounds

Since the DC, which is located around two meters from collision vertex, is the closest tracking detector to the vertex, there is no information about the track reconstruction between the vertex and DC. Thus, it is impossible to distinguish the particles flying from the collision vertex or the particles which decay or convert before DC on a track by track. The decayed hadron or electron-positron produced by photon conversion can pretend to be a high momentum track at momentum measurement by DC because the particles usually receive kinematical momentum transformation from decay or conversion and change the flight direction. The primary contents of background have following conditions;

- Low momentum charged particles.

- The particle receives large kick from decay.

- The particle decays closely before DC.

The secondary contents are;

- Low momentum neutral particles.

- The particle receives small kick from decay or conversion.

- The particle decays closely before DC.

- The decay or conversion produces charged particle.

The reasons are described here. The collision produces much more low p_T particles than medium or high p_T particles since the spectra curve is approximately exponential as the function of p_T. Therefore, the number of low p_T tracks, which decay or convert and are miss-reconstructed as high p_T tracks, is much larger than the number of the real high p_T tracks. For instance, approximately the 25 % of K^+ at 2 GeV/c decay within 1 m - 2.1 m (where DC is located), and this amount is about fifty times larger than the amount of produced charged particles at 8 GeV/c.

In order to be miss-reconstructed as high p_T, the low momentum charged particles have to change the flight direction considerably as shown in Figure 3.4, since high p_T charged particles do not bend in the magnetic field very much. In addition, the low momentum particles which decay much before DC bend a lot due to the magnetic field, and fly away, and those kind of particles are not detected. Therefore, the fake tracks are the particles which decay or convert close to DC.

Because the low momentum neutral particles do not receive magnetic filed effect and fly straight to DC, the particles have to have small change at decay or conversion in order to be miss-reconstructed as high p_T particles as also shown in Figure 3.4. Since neutral particles do not fire DC, they have to decay into charged particles before DC to be the background. (Due to the same reason as the charged particles, the decay should be occurred close to DC.)
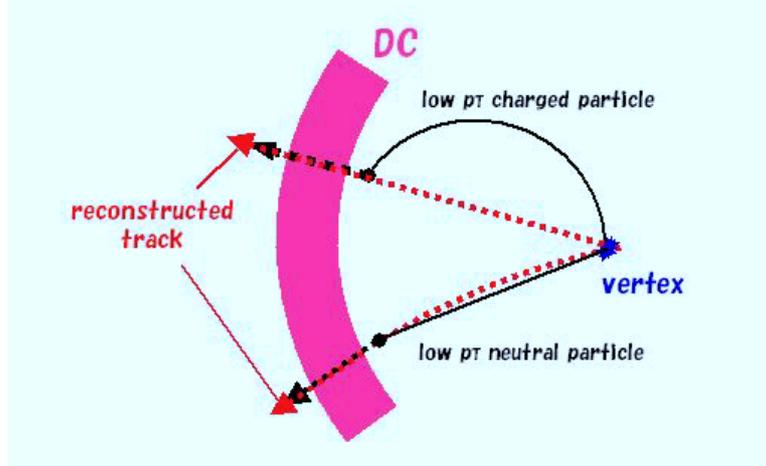
Figure 3.4: Illustrations of typical background.   Above particle is the example of miss-reconstruction from low p_T charged decayed particle. Below is the example of miss-reconstruction from the particle produced by low p_T neutral particle decay.

3.2.1   Energy Cut Method

To obtain high p_T charged hadron v_2 without the background, "Energy Cut method" is applied. The method uses the phenomenon that the hadron deposits its energy on electromagnetic calorimeters (EMCal) exponentially.

Applying $E/p >$ certain value cut, where E is the energy deposited on EMCal and p is the momentum calculated by Drift Chamber (DC), can reject the fake high momentum track. Since the fake track is estimated too high momentum, the E/p value is always small. This cut rejects a part of the real tracks with certain probability, and therefore the efficiency correction is needed to obtain the spectra, but not necessary to obtain the v_2.
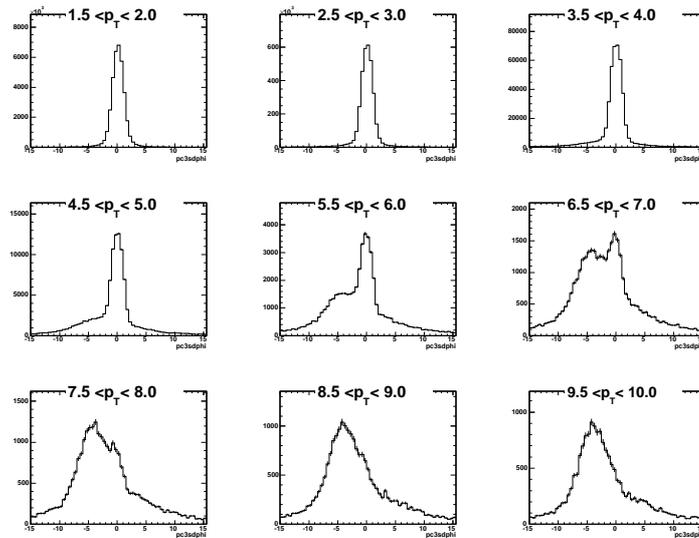
Figure 3.5: The distribution of $sd\phi$ on PC3 without E/p cut for every 0.5 GeV/c p_T bin.
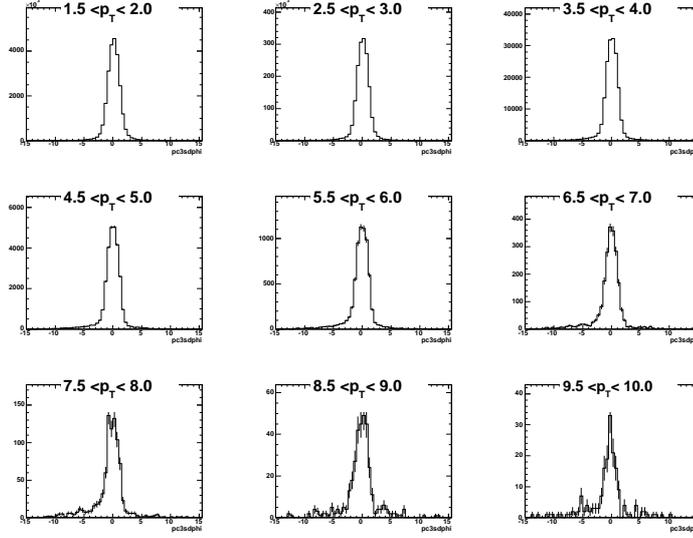
Figure 3.6: The distribution of $sd\phi$ on PC3 with $E/p > 0.2$ cut for every 0.5 GeV/c p_T bin.

Figure 3.5 and 3.6 are the $sd\phi$ distributions on PC3 (where the particles are detected as $\alpha > 0$ at $++$ magnetic field) with and without E/p cut respectively. The vertex cut and the matching cut are applied. Comparison of Figure 3.5 to 3.6 shows that $E/p > 0.2$ cut can remove the backgrounds for high p_T region.

For the systematic study, $E/p > 0.3$ cut is also attempted. The difference between $E/p > 0.2$ and 0.3 cut is included in systematic error where the statistics of signal with $E/p > 0.3$ cut is enough ($p_T \leq \sim 5$ GeV/c).

3.3 Particle Identification

We measured v_2 for identified charged hadron in Au+Au collision at $\sqrt{s_{NN}}=$ 62.4 GeV and in Cu+Cu collision at $\sqrt{s_{NN}}=$ 200 GeV for the following centrality selections.

- $\pi^+ + \pi^- / K^+ + K^- / p + \bar{p}$ in Au+Au at $\sqrt{s_{NN}}=$ 62.4 GeV

    − 0-10 % , 10-20 % , 20-30 % , 30-40 % , 40-50 %

- $\pi^+ / \pi^- / K^+ / K^- / p / \bar{p}$ in Au+Au at $\sqrt{s_{NN}}=$ 62.4 GeV

    − 10-40 %

- $\pi^+ + \pi^- / K^+ + K^- / p + \bar{p}$ in Cu+Cu at $\sqrt{s_{NN}}=$ 200 GeV

    − 0-10 % , 10-20 % , 20-30 % , 30-40 % , 40-50 % .

Particle identification for pi/K/p is based on the separation of the mass square distributions. The mass square for each particle is calculated with flight time, momentum and path length along the trajectory. The flight time is measured by Electromagnetic Calorimeter (EMCal) or Time of Flight counter (TOF). The momentum is measured by Drift Chamber (DC). The performance of

these detectors is described in Section 2 . EMCal can provide more statistics than TOF due to
the large acceptance while TOF detector has better timing resolution which can provide $\pi/K/p$
separation up to higher p_T. We use EMCal for low p_T and TOF for high p_T. The overall timing
resolution including BBC timing resolution is ~ 130 ps for TOF and ~ 350 ps for EMCal in
Au+Au/Cu+Cu.

The mass square of each charged particle is calculated by the following formula,

$$m^2 = \frac{p^2}{c^2}[(\frac{t}{L/c})^2 - 1] \tag{3.4}$$

where p is the particle momentum (GeV/c), L is a flight path-length, and c is the speed of
light (29.98 cm/ns). Figure 3.7 shows the typical two dimentional scatter plot of mass square
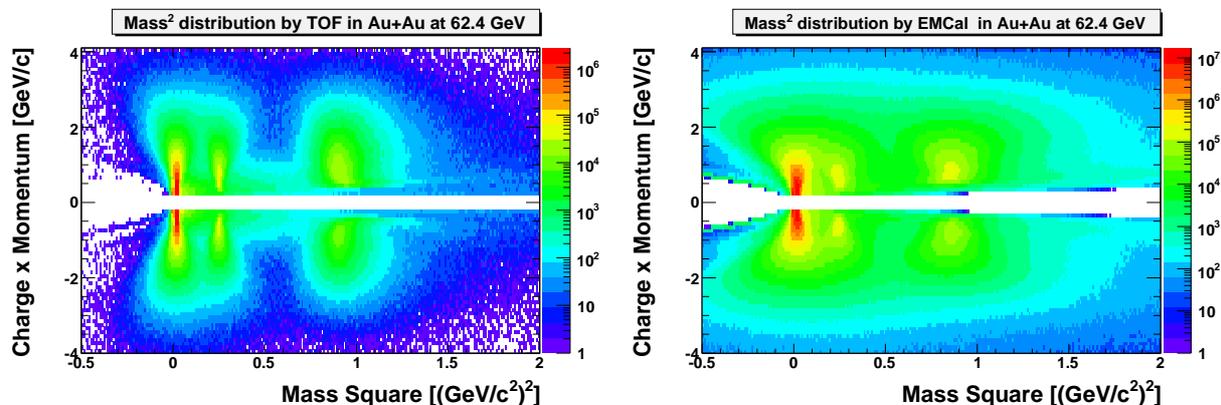
Figure 3.7: Mass square distribution calculated with flight time measured by TOF (left panel) and
EMCal (right panel) in Au+Au at $\sqrt{s_{NN}} = 62.4$ GeV

distribution for TOF. The x axis indicates the mass square and the y axis indicates charge $\times$
momentum. Charged particles are identified by the 2.5 σ width cut in the mass^2 and momentum
space for each particle species.

The width of the mass squre can be parameterized as

$$\sigma_{m^2}^2 = \frac{\sigma_\alpha^2}{K_1^2} + \frac{\sigma_{\text{multi-scat}}^2}{K_1^2}[4m^4(1 + \frac{m^2}{p^2})] + \frac{\sigma_{\text{TOF}}^2 c^2}{L^2}[4p^2(m^2 + p^2)] \tag{3.5}$$

where σ_α is the angular resolution, $\sigma_{\text{multi-scat}}$ is the multiple scattering term, σ_{TOF} is overall
TOF resolution, K_1 is the field integral value, and m is the centroid of mass square distribution
with given momentum p. Fitting the mass square distributions by Gaussian formula for certain
momentum bins, the σ_{m^2} and m are obtained as a function of p_T as shown in Figure 3.8 and 3.9
. The parameterization by Equation 3.5 is applied to this σ_{m^2} vs. p_T for $\pi/K/p$ simulataneously,
which is appeared as lines in Figure 3.9 . The mean of $mass^2$ is fitted by constant value which is
appeared as lines in Figure 3.8 . For this v_2 analysis, we selects the tracks within $m \pm 2.5\ \sigma_{m^2}$ of
the objective specie and with the veto of $m \pm 3.0\ \sigma_{m^2}$ of other species.

3.4   Azimuthal anisotropy analysis

Analysis of the azimuthal anisotropy is expected to be an informative direction in studying
the early stage of high energy nuclear collisions [80] . The possible formation of QGP affects
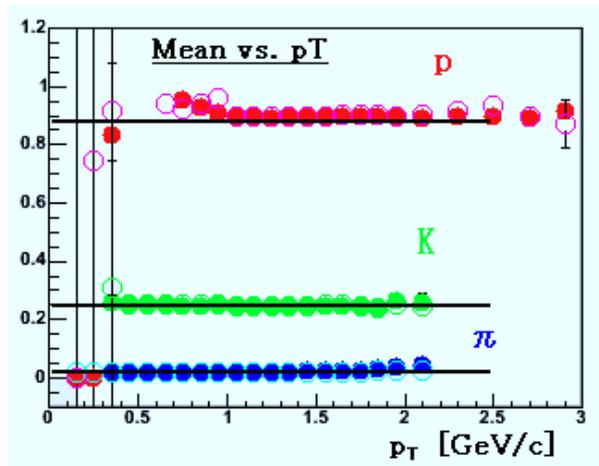
Figure 3.8: Mean of mass^2 as a function of p_T for π/K/p calculating with flight time measured by TOF in Au+Au at $\sqrt{s_{NN}} = 62.4$ GeV
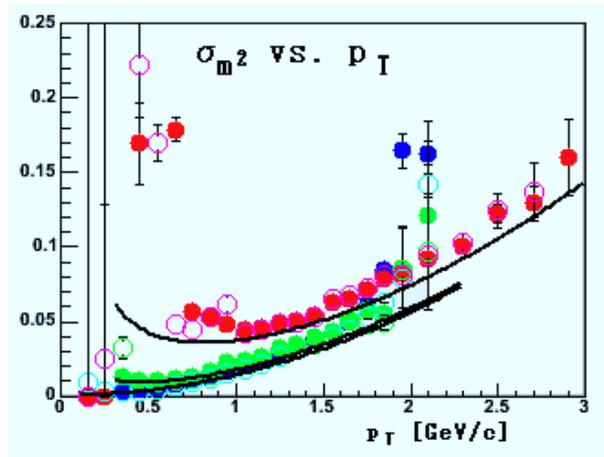
Figure 3.9: The width (σ_{m^2}) of mass^2 as a function of p_T for π/K/p calculating with flight time measured by TOF in Au+Au at $\sqrt{s_{NN}} = 62.4$ GeV

how the initial geometrical anisotropy is transferred into momentum anisotropy in the final state. We, therefore, investigate the strength of the anisotropy to approach the shapes of azimuthal distribution, especially its ellipticity. In this section, the measurement of the strength of the azimuthal anisotropy will be explained.

3.4.1 Fourier Expansion of Azimuthal Distribution

The azimuthal distribution function $r(\phi)$, which is obtained event by event, is written in the form of Fourier expansion since $r(\phi)$ is a 2π periodical function:

$$r(\phi) = \frac{x_0}{2\pi} + \frac{1}{\pi} \sum_{n=1}^{\infty} [x_n \cos(n\phi) + y_n \sin(n\phi)], \tag{3.6}$$

where n is the event number. The coefficients, x_n and y_n, in the Fourier expansion of $r(\phi)$ are integrals of the $r(\phi)$ for x and y directions with the weights proportional to $\cos(n\phi)$ and $\sin(n\phi)$ respectively. In experiment a finite number of particles are emitted from matter and construct the distribution function, therefore, the integrals become simple sums over particles found in the certain rapidity window in which we analyze the data :

$$x_n = \int_0^{2\pi} r(\phi) \cos(n\phi) d\phi = \sum_i r_i \cos(n\phi_i), \tag{3.7}$$

$$y_n = \int_0^{2\pi} r(\phi) \sin(n\phi) d\phi = \sum_i r_i \sin(n\phi_i), \tag{3.8}$$

where i runs over all detected particles, and ϕ_i is the azimuthal angle of the ith particle. If there is no flow and neglecting the fluctuations, the function $r(\phi)$ is constant and all Fourier coefficients except the first one are zero. The transverse anisotropic flow is expected to appear at non-central collision, namely non-zero value of an impact parameter. We define the beam direction as z axis,

and the transverse plane as x-y plane. The reaction plane is defined as a plane spanned by the vector of the impact parameter and the beam direction as described in Section 1.3.2. The reaction plane angle Ψ ($0 \leq \Psi \leq 2\pi$) is the angle between x-axis and reaction plane. A value of the n-th harmonic parameter (v_n) is defined as:

$$v_n \;\; = \;\; \frac{\sqrt{x_n^2 + y_n^2}}{x_0}, \tag{3.9}$$

$$\Psi_n = \frac{1}{n} \tan^{-1}\left(\frac{y_n}{x_n}\right), \qquad 0 \leq \Psi_n \leq \frac{2\pi}{n} \tag{3.10}$$

When one defines the azimuthal angle ϕ in Equation 3.6 as relative to the reaction plane, namely $\phi = \phi_{\text{lab}} - \Psi$ where ϕ_{lab} is the azimuthal angle in the laboratory frame, the sine terms are cancelled out since the distribution is symmetry with respect to the reaction plane, and the $r(\phi)$ becomes an even function:

$$
\begin{aligned}
r(\phi) \;\; &= \;\; \frac{x_0}{2\pi}\left\{1 + 2\sum_{n=1}^{\infty}\left(\frac{x_n}{x_0}\cos(n[\phi_{\text{lab}} - \Psi_n])\right)\right\} \\
&= \;\; \frac{x_0}{2\pi}\left\{1 + 2\sum_{n=1}^{\infty}\left(v_n\cos\left(n\phi_{\text{lab}}\right)\cos(n\Psi_n)\right)\right\} \\
&= \;\; \frac{x_0}{2\pi}\left\{1 + 2\sum_{n=1}^{\infty}\left(v_n\cos\left[n(\phi_{\text{lab}} - \Psi_n)\right]\right)\right\}.
\end{aligned}
\tag{3.11}
$$

The v_n coefficients are used as a quantitative characterization of the nth anisotropy, and are calculated by

$$v_n = \langle\cos(n(\phi - \Psi_n))\rangle \tag{3.12}$$

where the angle brackets mean an average over all particles in all events. In the Fourier decomposition, v_1 and v_2 are called the directed and elliptic flows, respectively since v_1 is the strength of the directed flow and v_2 is the strength of the elliptic flow.

3.4.2   Reaction Plane Determination

Azimuthal anisotropy in particle momentum distributions is measured with respect to the reaction plane. Its azimuthal angle is given by Ψ_{RP}. The particle azimuthal distribution is experimentally to expand it in a Fourier series as follows:

$$\frac{dN}{d\phi} = N_0\left(1 + \sum_1 2v_n\cos\left[n(\phi - \Psi_{\text{RP}})\right]\right) \tag{3.13}$$

where ϕ is the azimuthal angle of the particle. Because the vector of the impact parameter cannot be measured directly in the experiment, the azimuthal angle of the reaction plane is estimated from the observed event plane angle determined from the anisotropic flow itself. This is basically done for each harmonic, n, of the Fourier expansion. The event flow vector Q_n in the reaction plane angle, Ψ_n, for the nth harmonic are defined as

$$Q_{n,x} = \mathbf{Q}_n\cos\left(n\Psi_n\right) = \sum_i w_i\cos\left(n\phi_i\right), \tag{3.14}$$

$$Q_{n,y} = \mathbf{Q}_n \sin(n\Psi_n) = \sum_i w_i \sin(n\phi_i). \qquad (3.15)$$

Therefore, the Ψ_n is determined by

$$\Psi_n = \frac{1}{n}\Big(\tan^{-1}\frac{\sum_i w_i \sin(n\phi_i)}{\sum_i w_i \cos(n\phi_i)}\Big), \qquad (3.16)$$

where ϕ_i is the lab azimuthal angle of the emitted particle i used for the reaction plane determination, and w_i is the corresponding weight, for which the transverse momentum is often used. Since finite multiplicity reconstructs the reaction plane, the Fourier coefficients v_n^{obs} with respect to the "observed" reaction plane are smaller than the coefficients v_n^{real} with respect to the "real" reaction plane. The relation between v_n^{obs} and v_n^{real} is given by the following equation:

$$
\begin{aligned}
v_n^{\mathrm{obs}} &= \langle\cos(n[\phi_{\mathrm{lab}} - \Psi_{\mathrm{obs}}])\rangle \\
&= \langle\cos(n[\phi_{\mathrm{lab}} - \Psi_{\mathrm{obs}} + \Psi_{\mathrm{real}} - \Psi_{\mathrm{real}}])\rangle \\
&= \langle\cos(n[\phi_{\mathrm{lab}} - \Psi_{\mathrm{real}}])\cos(n[\Psi_{\mathrm{obs}} - \Psi_{\mathrm{real}}])\rangle \\
&+ \langle\sin(n[\phi_{\mathrm{lab}} - \Psi_{\mathrm{real}}])\sin(n[\Psi_{\mathrm{obs}} - \Psi_{\mathrm{real}}])\rangle \\
&= v_n^{\mathrm{real}}\langle\cos(n[\Psi_{\mathrm{obs}} - \Psi_{\mathrm{real}}])\rangle,
\end{aligned}
\qquad (3.17)
$$

where average over the sine term vanishes due to the reflectional symmetry of $\phi_{\mathrm{lab}} - \Psi_{\mathrm{real}}$ and $\Psi_{\mathrm{obs}} - \Psi_{\mathrm{real}}$ with large multiplicity. Thus, v_n^{real} is given by

$$v_n^{\mathrm{real}} = \frac{v_n^{\mathrm{obs}}}{\langle\cos(n[\Psi_{\mathrm{obs}} - \Psi_{\mathrm{real}}])\rangle}, \qquad (3.18)$$

and $\langle\cos(n[\Psi_{\mathrm{obs}} - \Psi_{\mathrm{real}}])\rangle$ is so called the reaction plane resolution.

At PHENIX experiment the reaction plane is calculated event by event using the data taken by Beam Beam Counter (BBC) which has 64 PMTs on each. It is possible to measure a reaction plane by central arm detectors. BBC has advantage to avoid the non-flow effects such as jets, resonance decays and HBT since BBC has roughly three units of pseudo rapidity gap from the central arms by which the azimuthal distribution of emitted particles is measured. Since a better accuracy of v_n is obtained by using the same harmonic reaction plane [79], the reaction plane angle for this v_2 analysis is calculated for both south and north BBCs by the following equation:

$$\Psi_{\mathrm{obs}} = \frac{1}{2}\Big(\tan^{-1}\frac{Q_y}{Q_x}\Big), \qquad (3.19)$$

$$Q_x = \sum_{i=1}^{64} q_i \cos(2\phi_i), \qquad (3.20)$$

$$Q_y = \sum_{i=1}^{64} q_i \sin(2\phi_i), \qquad (3.21)$$

where ϕ_i is the azimuthal angle of each PMT in BBC and q_i is the charge of each PMT as a weight.

3.4.3 Reaction Plane Calibration

Since the impact parameter vector takes random direction to the lab frame, the azimuthal distribution of the reaction planes should be flat, however, the measured reaction plane is often not

flat due to several reason such as the imperfection of the detector acceptance, dead PMT channels in BBC, beam condition and so on. To remove these effect the two calibration steps so called $re-centering$ and $flattening$ have been applied. The calibration of the reaction plane at BBC is done for each 5 % centrality step [68] [67]. First, in order to re-center the averages of Q_x and Q_y, one subtracts the $\langle Q_x \rangle$ and $\langle Q_y \rangle$ over many event from the Q_x and Q_y of each event and obtains corrected reaction plane Ψ^{corr} as

$$Q_x^{\mathrm{corr}} = \frac{Q_x - \langle Q_x \rangle}{\sigma_x}, \tag{3.22}$$

$$Q_y^{\mathrm{corr}} = \frac{Q_y - \langle Q_y \rangle}{\sigma_y}, \tag{3.23}$$

$$2\Psi^{\mathrm{corr}} = \tan^{-1}\frac{Q_y^{\mathrm{corr}}}{Q_x^{\mathrm{corr}}}, \tag{3.24}$$

where $\langle Q_x \rangle$ and $\langle Q_x \rangle$ are the mean of Q_x and Q_y distributions, and σ_x and σ_y are the width of these. The mean and width are extracted by fitting the Q_x and Q_y distributions by Gaussian function. The re-centering does not affect higher harmonic components. To remove these effect, one fits the non-flat distribution of Ψ averaged over many events with a Fourier expansion and calculates the shifts for each event Ψ necessary to force a flat distribution on average:

$$\Delta\Psi = \sum_{f=1} \left(A_f \cos\left(fn\Psi^{\mathrm{corr}}\right) + B_f \sin\left(fn\Psi^{\mathrm{corr}}\right)\right), \tag{3.25}$$

$$n\Psi^{\mathrm{flat}} = n\Psi^{\mathrm{obs}} + n\Delta\Psi, \tag{3.26}$$

where the shift $\Delta\Psi$ is the correction factor, and the coefficients A_f and B_f are obtained by requiring that the fth Fourier moment of the Ψ distribution is zero. Assuming small $\Delta\Psi$,

$$\begin{aligned}
\langle \cos\left(fn\Psi\right)\rangle &= 0 \\
&= \langle \cos\left(fn\Psi^{\mathrm{corr}} + fn\Delta\Psi\right)\rangle \\
&= \langle \cos\left(fn\Psi^{\mathrm{corr}}\right)\cos\left(fn\Delta\Psi\right)\rangle - \langle \sin\left(fn\Psi^{\mathrm{corr}}\right)\sin\left(fn\Delta\Psi\right)\rangle \\
&\simeq \langle \cos\left(fn\Psi^{\mathrm{corr}}\right)\rangle - \langle \sin\left(fn\Psi^{corr}\right)(fn\Delta\Psi)\rangle \\
&= \langle \cos\left(fn\Psi^{\mathrm{corr}}\right)\rangle - \langle \sin^2\left(fn\Psi^{corr}\right)\rangle \\
&= \langle \cos\left(fn\Psi^{\mathrm{corr}}\right)\rangle - \frac{fB_f}{2}.
\end{aligned} \tag{3.27}$$

The sine term can be expanded as same way, and we obtain

$$\Psi = \Psi^{\mathrm{corr}} + \Delta\Psi, \tag{3.28}$$

$$\Delta\Psi = \sum_f \left(A_f \cos\left(2f\Psi^{\mathrm{corr}}\right) + B_f \sin\left(2f\Psi^{\mathrm{corr}}\right)\right), \tag{3.29}$$

$$A_f = -\frac{2}{f}\langle \sin\left(2f\Psi^{\mathrm{corr}}\right)\rangle, \tag{3.30}$$

$$B_f = \frac{2}{f}\langle \cos\left(2f\Psi^{\mathrm{corr}}\right)\rangle, \tag{3.31}$$

where f is the degree of Fourier expansion. We check the dependence of v_2 value on f changing from 0 to 19 and confirm that no significant difference appear on v_2 with $f \geq 2$ as shown in Figure 3.10 . We use 19 for f in PHENIX calibration as conservative way. We perform these calibration run by run and for each 5 % centrality step. Figure 3.11 shows the example plots of the reaction plane distributions before and after re-centering/flattening calibration.
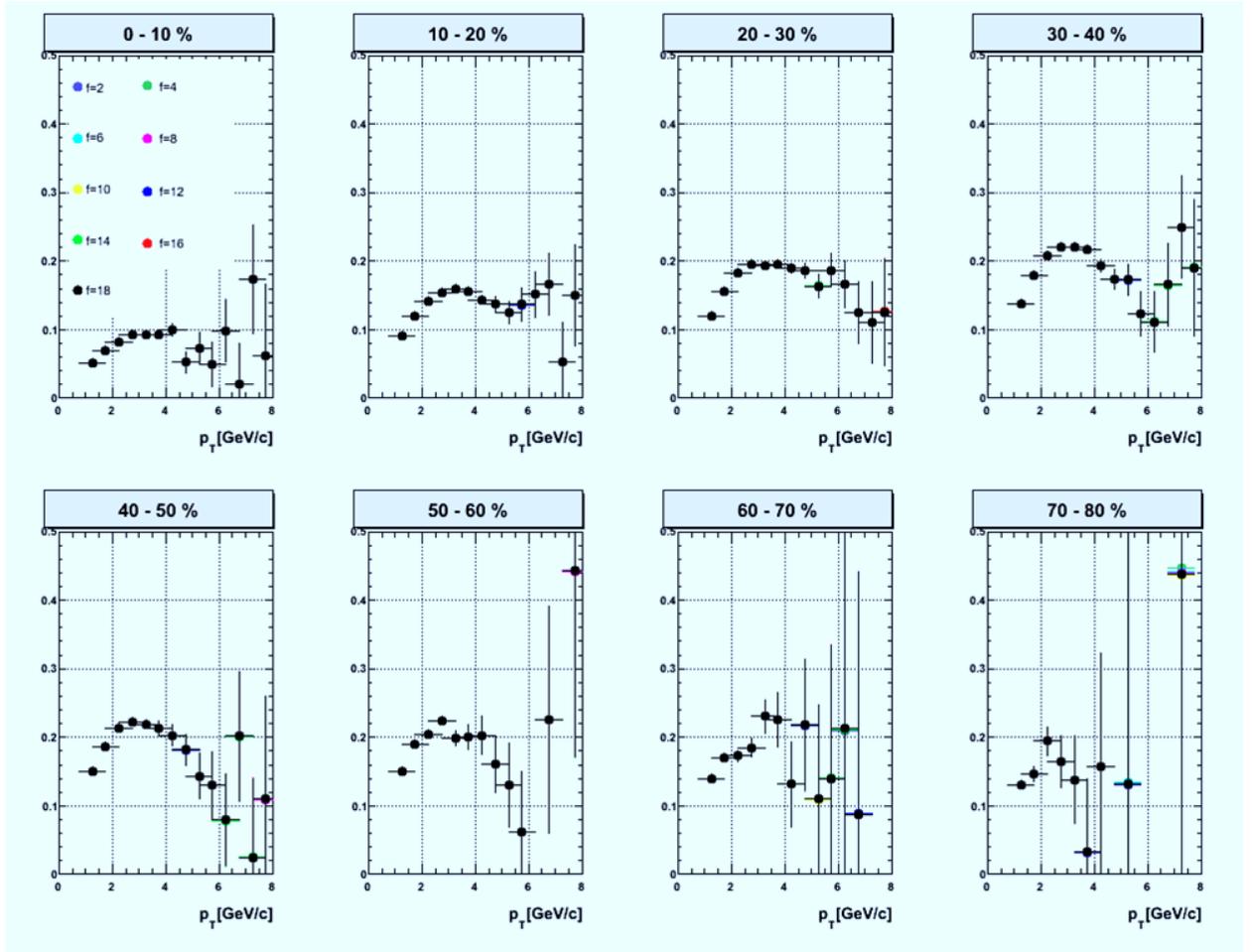
Figure 3.10: The value of v_2 as a function of p_T with the different degree f of Fourier expansion from 2 to 19 for indicated centrality bins. Different color shows v_2 obtained with the reaction plane calibrated by different f. There is no significant difference with $f \geq 2$.
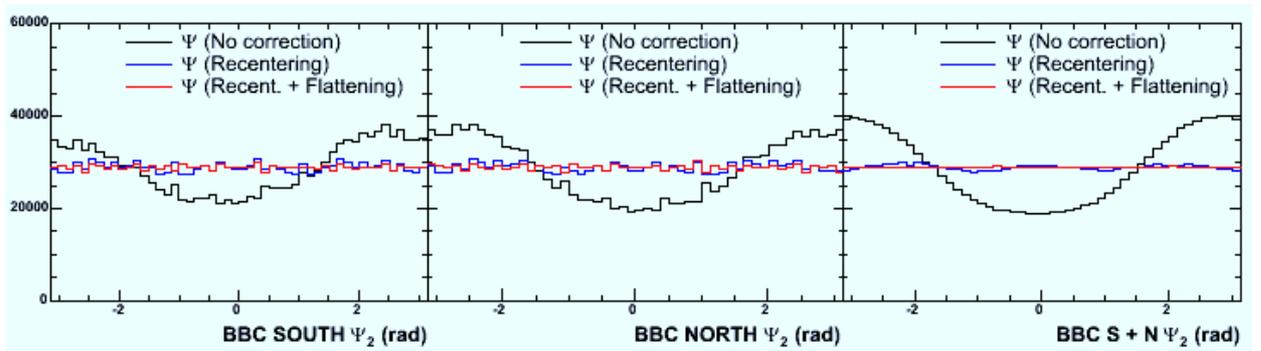
Figure 3.11: The reaction plane distributions before and after re-centering/flattening calibration.

3.4.4   Reaction Plane Resolution

As described previous section, the v_2 measured with respect to the observed reaction plane is corrected with its resolution since the true reaction can not be measured event by event experimentally. The resolution is expressed as [79]

$$\langle \cos \left[2(\Psi^{\mathrm{true}} - \Psi^{\mathrm{obs}})\right] \rangle = \frac{\sqrt{\pi}}{2\sqrt{2}} \chi_m \exp \left(-\chi_m^2/4\right) [I_0(\chi_m^2/4) + I_1(\chi_m^2/4)], \tag{3.32}$$

where $\chi_m = v_m \sqrt{2N}$ and I_n is the modified Bessel function of nth order. Since we utilize two BBC at north and south side, two independent reaction planes are obtained and can be used to estimate the event plane resolution as

$$
\begin{aligned}
\sigma_{\mathrm{A}} &= \langle \cos \left[2(\Psi^{\mathrm{true}} - \Psi_{\mathrm{A}})\right] \rangle \\
\sigma_{\mathrm{B}} &= \langle \cos \left[2(\Psi^{\mathrm{true}} - \Psi_{\mathrm{B}})\right] \rangle \\
\sigma_{\mathrm{AB}} &\equiv \langle \cos \left[2(\Psi_{\mathrm{A}} - \Psi_{\mathrm{B}})\right] \rangle \\
&= \langle \cos \left[2(\Psi^{\mathrm{true}} - \Psi^{A})\right] \rangle \langle \cos \left[2(\Psi^{\mathrm{true}} - \Psi^{B})\right] \rangle \\
&= \sigma_A \sigma_B.
\end{aligned}
\tag{3.33}
$$

We assume that the resolutions of BBC-north (BBCN) and BBC-south (BBCS) are same because of the same acceptance

$$\sigma_{\mathrm{BBCN}} = \sigma_{\mathrm{BBCS}} = \sqrt{\sigma_{\mathrm{BBCNS}}} = \sqrt{\langle \cos \left[2(\Psi_{\mathrm{BBCN}} - \Psi_{\mathrm{BBCS}})\right] \rangle} \tag{3.34}$$

$$\sigma_{\mathrm{BBCNS}} = \sqrt{\sigma_{\mathrm{BBCN}}^2 + \sigma_{\mathrm{BBCS}}^2} = \sqrt{2\langle \cos \left[2(\Psi_{BBCN} - \Psi_{BBCS})\right] \rangle} \tag{3.35}$$

We combined the south and north BBC information (BBCSN) to obtain better resolution of the reaction plane in this analysis.

3.4.5   Measurement of v_2

$v_2{}^{\mathrm{obs}}$ is obtained by the following

$$\frac{dN}{d\phi} = N \frac{1}{\pi} [1 + 2v_2^{\mathrm{obs}} \cos 2(\phi - \Psi_{\mathrm{RP}})] \tag{3.36}$$

where ϕ is the azimuthal angle of detected particles and Ψ_{RP} is azimuthal angle of re-calibrated reaction plane. If the particle yield along the reaction plane is larger than the yield which is perpendicular to the reaction plane, the value of v_2 is positive. The resolution correction is done by

$$v_2^{\mathrm{true}} = \frac{v_2^{\mathrm{obs}}}{\sqrt{2\langle \cos \left[2(\Psi_{BBCN} - \Psi_{BBCS})\right] \rangle}}. \tag{3.37}$$

Figure 3.12 shows the BBC north-south-combined resolution of the reaction plane as a function of the centrality in Au+Au and Cu+Cu at $\sqrt{s_{\mathrm{NN}}} = 200$ and 62.4 GeV. The reaction plane resolution and its errors in Au+Au at 62.4 GeV and in Cu+Cu at 200 GeV are summarized in Table 3.2 and 3.3 respectively.

Table 3.2: Reaction plane resolution for each centrality in Au+Au at $\sqrt{s_{NN}} = 62.4$ GeV.

Centrality [%]	Resolution	1.0/resolution	Stat Error for v_2[%]	Number of tracks
0-10	0.128	7.783	2.028	4461049
10-20	0.189	5.289	0.935	4477890
20-30	0.186	5.374	0.965	4478761
30-40	0.163	6.154	1.265	4479879
40-50	0.118	8.482	2.404	4477819
50-60	0.079	12.709	5.397	4479177
60-70	0.044	22.913	17.539	4478177
70-80	0.026	37.959	48.159	4477666
10-40	0.180	5.568	0.598	13436530

Table 3.3: Reaction plane resolution for each centrality in Cu+Cu at $\sqrt{s_{NN}} = 200$ GeV

Centrality [%]	Resolution	1.0/resolution	Stat Error for v_2[%]	Number of tracks
0-10	0.147	6.786	0.363	80222477
10-20	0.168	5.946	0.279	80149916
20-30	0.165	6.043	0.288	80130596
30-40	0.145	6.879	0.374	80130450
40-50	0.118	8.470	0.567	80175316
50-60	0.089	11.258	1.001	80161249
60-70	0.063	15.837	1.981	80157109
70-80	0.041	24.419	4.709	80174196
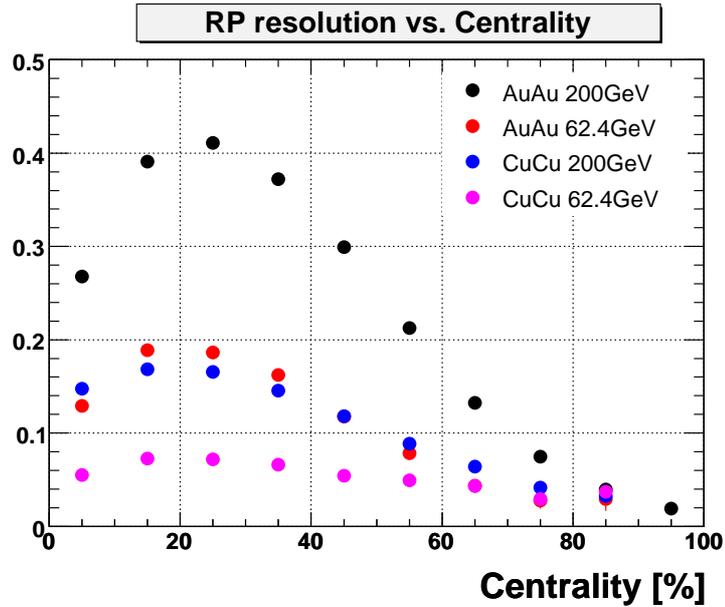
Figure 3.12: Reaction plane resolution vs. centrality in Au+Au and Cu+Cu at $\sqrt{s_{NN}} = 200$ and 62.4 GeV. The reaction plane is calculated by combining the south and north BBC information.

3.5   Initial Geometrical Eccentricity

For the PHENIX experiment, the essential parameters to describe collision, such as the number of nucleon participating the collision (N_{part}) , the number of binary collision of nucleons (N_{coll}) , nuclear overlap function (T_{AB}) and impact parameter (b), are obtained by Glauber Monte-Carlo Calculation. Eccentricity ($\varepsilon_{\text{stand}}$) calculation in which x axis is along the impact parameter vector is also calculated and is used to understand the data [75] [77] .

Proceeding the systematic study of v_2 for inclusive and identified charged hadrons in Au+Au and Cu+Cu collisions at $\sqrt{s_{\text{NN}}} = 62.4$ and 200 GeV, it is important to study the dependence of initial geometrical eccentricity ($\varepsilon_{\text{part}}$). For this study, we calculated $\varepsilon_{\text{part}}$, for which x and y axes are defined by the participant distribution, corresponding to centrality in a Glauber Monte-Carlo model.

3.5.1   Glauber Model

A Glauber model is a simple model to describe a high-energy collision of two nuclei as the superposition of the nucleon-nucleon collisions. In this model, the nucleons are assumed to travel on straight line trajectories in parallel with the beam axis. Also, it's assumed that the basic nucleon-nucleon cross sections is same as that in the vacuum and don't change during the collisions. Both of these assumptions are reasonable for high-energy nucleus-nucleus collisions. Using the nucleon-nucleon inelastic cross section ($\sigma_{\text{nn}}^{\text{inel}}$) and integrating over the full distribution of nucleons in each nucleus, the model can calculates number of nucleon-nucleon collisions, number of participant nucleons, and initial eccentricity. To approach the realistic density profile for the nuclei, we use a Woods-Saxon density profile with proper parameters

$$\rho(r) = \frac{1}{1 + \exp\frac{r-r_{\text{n}}}{d}}. \tag{3.38}$$

To approach the realistic experimental condition, we use the Monte-Carlo technique for this calculation, since the Monte-Carlo can include the effect from positioning fluctuation of participant nucleons. In the Monte-Carlo framework the nucleons of the two nuclei are distributed in space according to the nucleon density profile, and impact parameter b of the two nuclei is chosen randomly. It is considered as a collision of two nucleons when the distance d of the two nucleons satisfies

$$d < \sqrt{\frac{\sigma_{nn}}{\pi}}. \tag{3.39}$$

Details of the PHENIX Glauber Monte-Carlo calculation is explained in [74] [76] [77] and the essential variables such as N_{part},N_{coll}, T_{AB}, b and $\varepsilon_{\text{stand}}$ have been calculated. Compared with PHENIX Glauber Monte-Carlo calculation, the calculation we use does not include the detector efficiency. We use the distribution of N_{part} to divide event classes as centrality classes (0 - 100 % as 10 % step). In Figure 3.13 the left panel shows the event distribution of N_{part} and the right panel shows the $\varepsilon_{\text{stand}}$ vs. N_{part} distribution by Glauber Monte-Carlo simulation in Au+Au at $\sqrt{s_{\text{NN}}} = 200$ GeV. The $\varepsilon_{\text{stand}}$ on each centrality is obtained by taking the average of $\varepsilon_{\text{stand}}$ in each centrality bin which is divided by N_{part} separation.

The parameters are listed in Table 3.4. To obtain the systematic error the calculation is done with several parameters, some of which are also used for systematic errors determination of
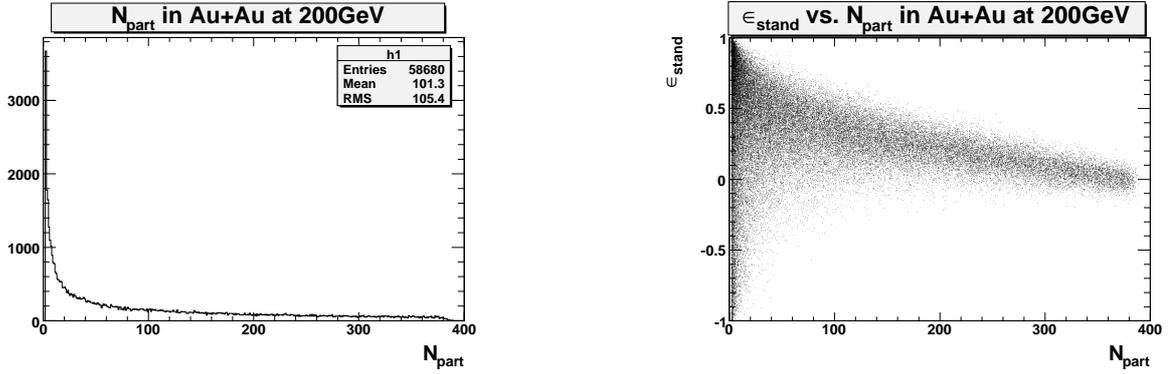
Figure 3.13: Distribution of N_{part} (left) and $\varepsilon_{\mathrm{stand}}$ vs. N_{part} (right) by Glauber Monte-Carlo simulation in Au+Au at $\sqrt{s_{\mathrm{NN}}} = 200$ GeV.

PHENIX calculation. Note that for "sys4" the distribution of b (impact parameter) is used to divide the centrality, and $\langle N_{\mathrm{part}} \rangle$ (centrality) is the average of that divided events.

Table 3.4: Parameters in Glauber Monte-Carlo calculation

		Au+Au 200 GeV	Au+Au 62.4 GeV	Cu+Cu 200 GeV	Cu+Cu 62.4 GeV
Default	σ_{nn} mb	42.0	37.0	42.0	35.6
	r fm	6.38	6.38	4.2064	4.2064
	d fm	0.54	0.54	0.5977	0.5977
sys0	σ_{nn} mb	39.0	35.0	39.0	33.6
	r fm	6.386	6.386	4.215	4.215
	d fm	0.54	0.54	0.5977	0.5977
sys1	σ_{nn} mb	45.0	39.0	45.0	37.6
	r fm	6.386	6.386	4.215	4.215
	d fm	0.54	0.54	0.5977	0.5977
sys2	σ_{nn} mb	42.0	37.0	42.0	35.6
	r fm	6.619	6.619	4.3744	4.3744
	d fm	0.55	0.55	0.6277	0.6277
sys3	σ_{nn} mb	42.0	37.0	42.0	35.6
	r fm	6.1533	6.1533	4.0561	4.0561
	d fm	0.53	0.53	0.5677	0.5677
sys4	σ_{nn} mb	42.0	37.0	42.0	35.6
	r fm	6.386	6.386	4.215	4.215
	d fm	0.54	0.54	0.5977	0.5977
sys5	σ_{nn} mb	42.0	37.0	42.0	35.6
	r fm	6.386	6.386	4.215	4.215
	d fm	0.54	0.54	0.5977	0.5977

The values such as N_{part}, N_{coll} and $\varepsilon_{\mathrm{stand}}$ of PHENIX calculation are compared to these of our calculation. Participant eccentricity, $\varepsilon_{\mathrm{part}}$ is newly obtained by our calculation.

3.5.2   Calculation for Participant Eccentricity, $\varepsilon_{\mathrm{part}}$

Eccentricity(ϵ) defined by the Equation 3.40 indicates the ellipticity of the participant nucleons at the start of the collision.

$$\varepsilon = \frac{\langle y^2 \rangle - \langle x^2 \rangle}{\langle y^2 \rangle + \langle x^2 \rangle} \tag{3.40}$$

where x and y are spatial positions of participant nucleons. ϵ for given impact parameter is also calculated in the Glauber Monte-Carlo simulations. We define two kinds of eccentricity so called standard eccentricity ($\varepsilon_{\mathrm{stand}}$) and participant eccentricity ($\varepsilon_{\mathrm{part}}$). The difference of these two eccentricities is how to take the axes for x and y. For the $\varepsilon_{\mathrm{stand}}$, the x axis is defined to be along the impact parameter vector and the y axis perpendicular to that in the transverse plane. The definition of $\varepsilon_{\mathrm{stand}}$ is same as that of the eccentricity in PHENIX calculation [75].

For the $\varepsilon_{\mathrm{part}}$, the principal axes are rotated to make $\langle x^2 \rangle$ minimized, so that the $\varepsilon_{\mathrm{part}}$ is related to only the distribution of the participant. The fact that using the BBC to determine the reaction plane by experimental data means that we measured v_2 using the axes related to participant distribution, therefore the participant eccentricity is more relevant one than standard eccentricity. The effect of the difference between $\varepsilon_{\mathrm{stand}}$ and $\varepsilon_{\mathrm{part}}$ is larger at smaller collision system in which the fluctuations in the nucleon position become larger. Figure 3.14 shows $\varepsilon_{\mathrm{stand}}$ and $\varepsilon_{\mathrm{part}}$ vs. N_{part} and Figure 3.15 shows $\varepsilon_{\mathrm{stand}}$ and $\varepsilon_{\mathrm{part}}$ vs. centrality by this simulation.
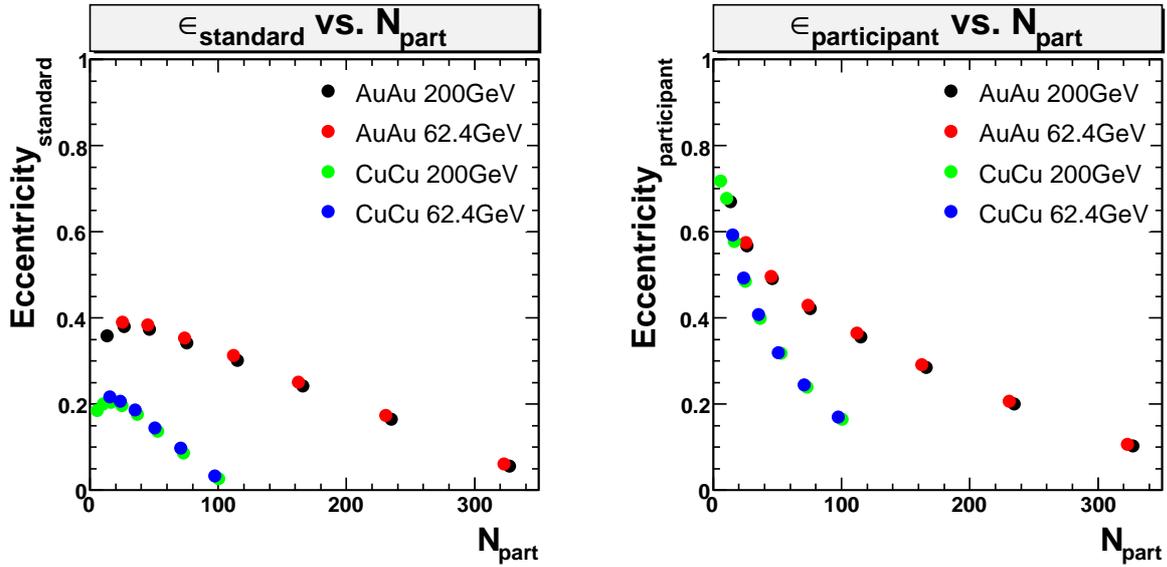
Figure 3.14: Comparison between $\varepsilon_{\mathrm{stand}}$ and $\varepsilon_{\mathrm{part}}$ in Au+Au and Cu+Cu at 62.4 and 200 GeV. The left panel is $\varepsilon_{\mathrm{stand}}$ vs. N_{part}, and the right panel is $\varepsilon_{\mathrm{part}}$ vs. N_{part}.

Figure 3.16 - 3.19 are comparison of N_{part} by our calculation to PHENIX value. Figure 3.24 - 3.27 are comparison of $\varepsilon_{\mathrm{stand}}$ by our calculation to PHENIX value. Error bars are with PHENIX values. The results of by our calculations are consistent to the PHENIX values.
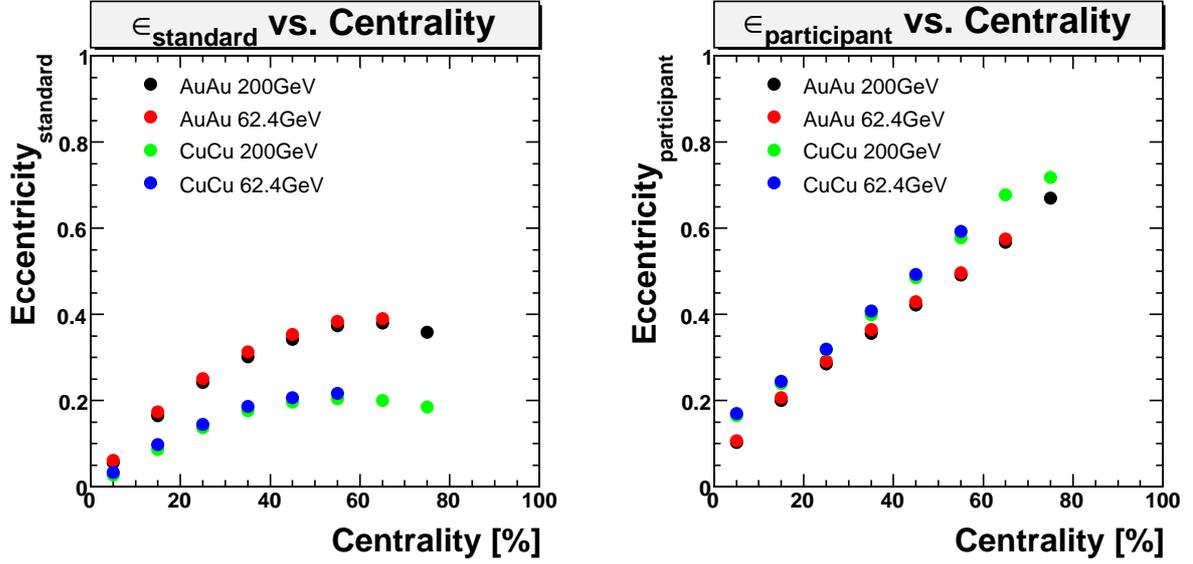
Figure 3.15: Comparison between $\varepsilon_{\text{stand}}$ $\varepsilon_{\text{part}}$ in Au+Au and Cu+Cu at 62.4 and 200 GeV. The left panel shows $\varepsilon_{\text{stand}}$ vs. centrality , and the right panel shows $\varepsilon_{\text{part}}$ vs. centrality .
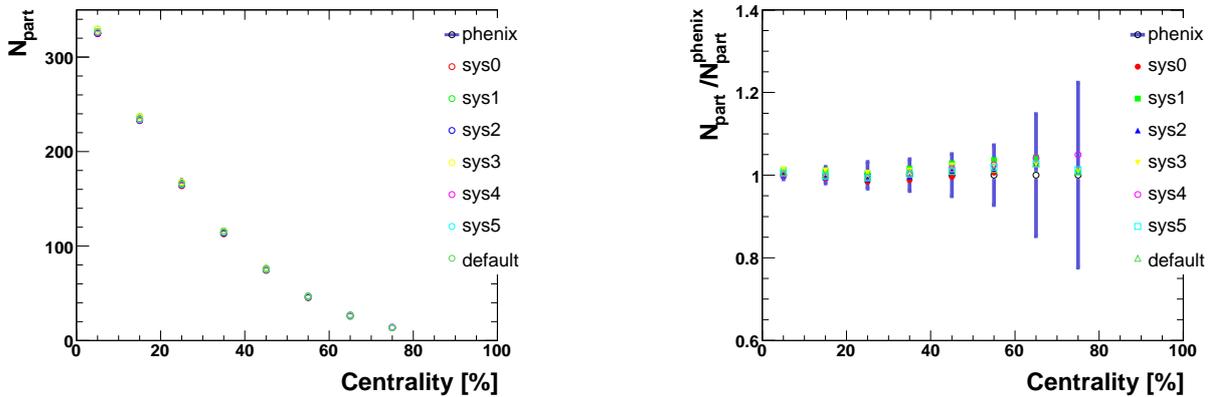
Figure 3.16: N_{part} (left) and the ratio of N_{part} to PHENIX N_{part} (right) as a function of the centrality in Glauber Monte-Carlo simulation in Au+Au at $\sqrt{s_{\text{NN}}} = 200$ GeV
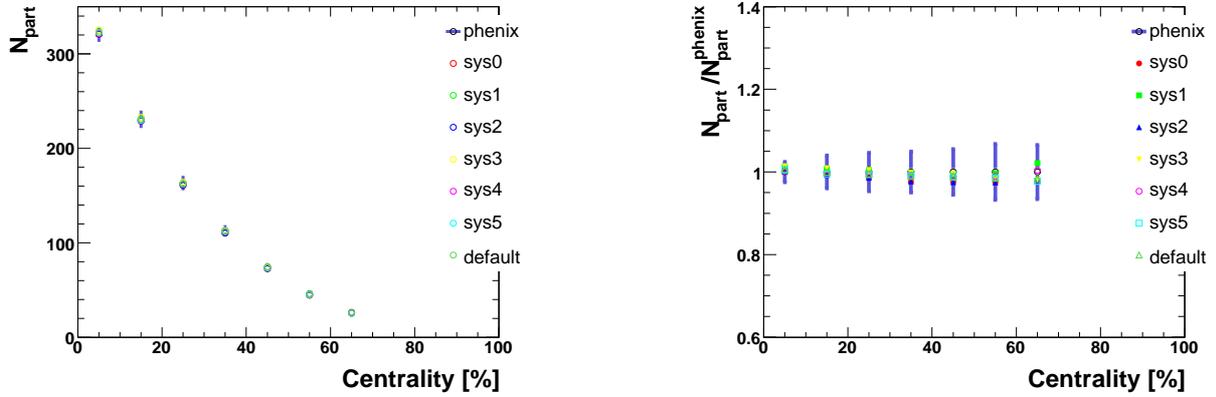
Figure 3.17: N_{part} (left) and the ratio of N_{part} to PHENIX N_{part} (right) as a function of the centrality in Glauber Monte-Carlo simulation in Au+Au at $\sqrt{s_{\mathrm{NN}}} = 62.4$ GeV
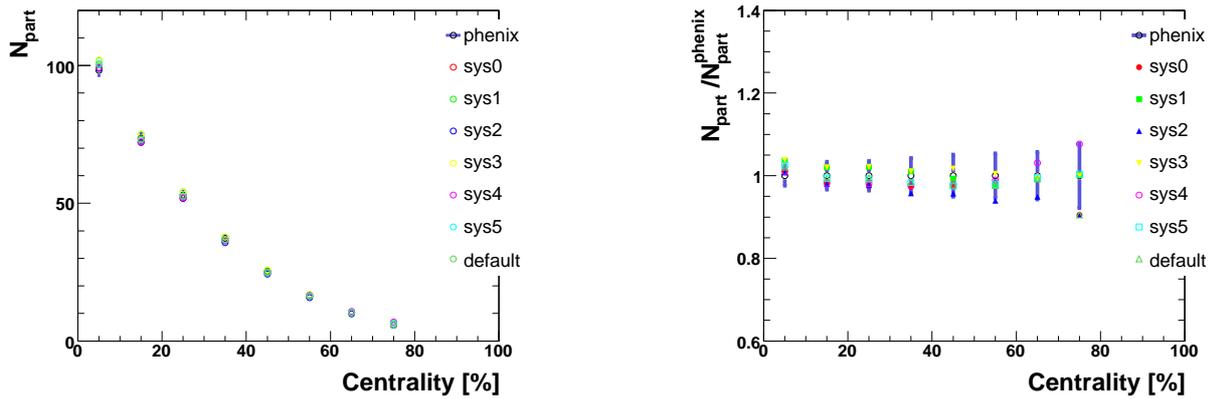
Figure 3.18: N_{part} (left) and the ratio of N_{part} to PHENIX N_{part} (right) as a function of the centrality in Glauber Monte-Carlo simulation in Cu+Cu at $\sqrt{s_{\mathrm{NN}}} = 200$ GeV
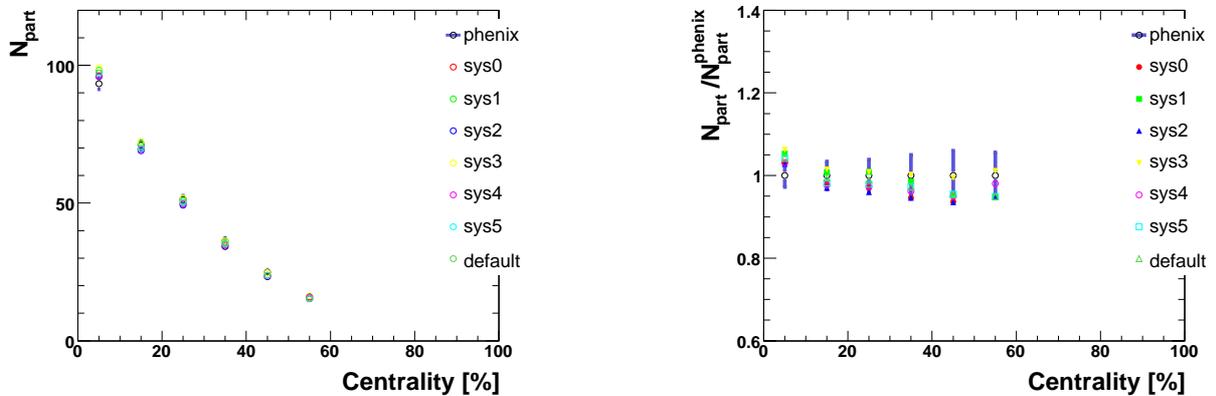
Figure 3.19: N_{part} (left) and the ratio of N_{part} (right) to PHENIX N_{part} as a function of the centrality in Glauber Monte-Carlo simulation in Cu+Cu at $\sqrt{s_{\mathrm{NN}}} = 62.4$ GeV
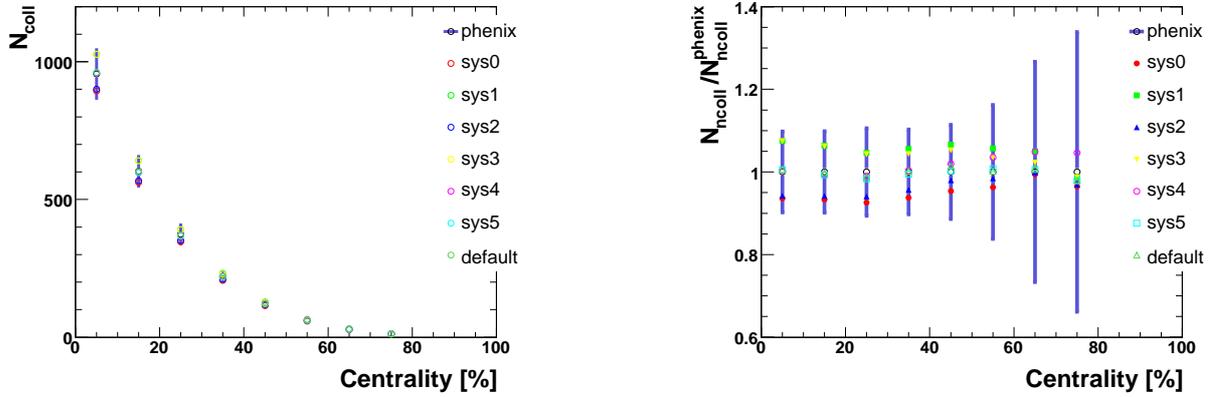
Figure 3.20: N_{coll} (left) and the ratio of N_{coll} to PHENIX N_{coll} (right) as a function of the centrality in Glauber Monte-Carlo simulation in Au+Au at $\sqrt{s_{\mathrm{NN}}} = 200$ GeV
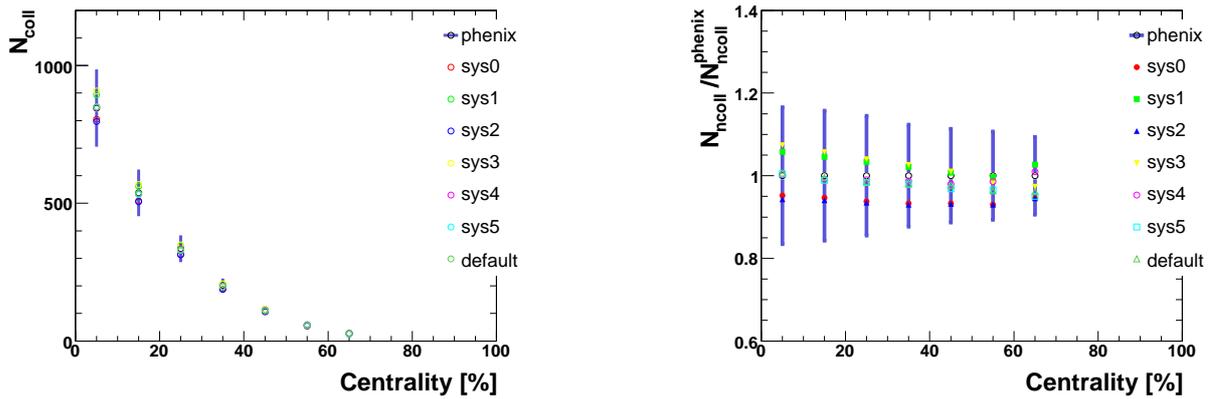
Figure 3.21: N_{coll} (left) and the ratio of N_{coll} to PHENIX N_{coll} (right) as a function of the centrality in Glauber Monte-Carlo simulation in Au+Au at $\sqrt{s_{\mathrm{NN}}} = 62.4$ GeV
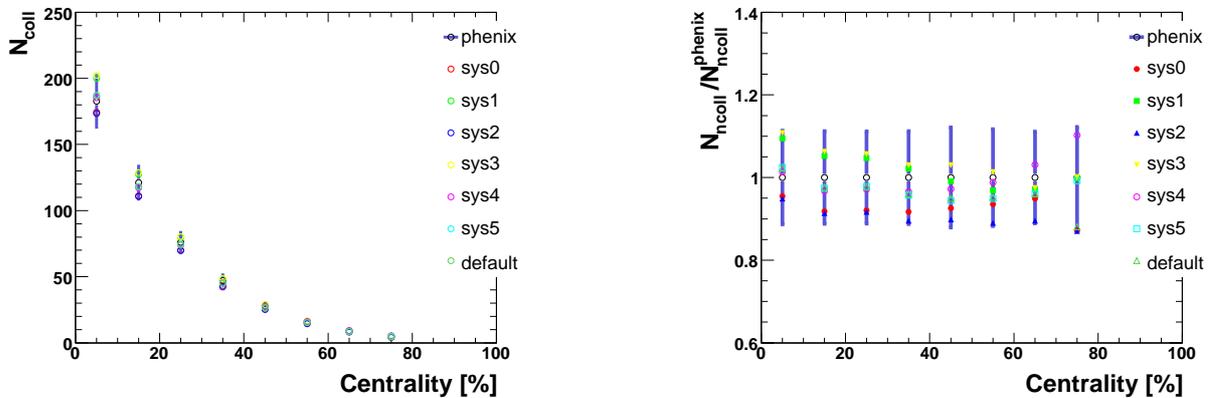
Figure 3.22: N_{coll} (left) and the ratio of N_{coll} to PHENIX N_{coll} (right) as a function of the centrality in Glauber Monte-Carlo simulation in Cu+Cu at $\sqrt{s_{\mathrm{NN}}} = 200$ GeV
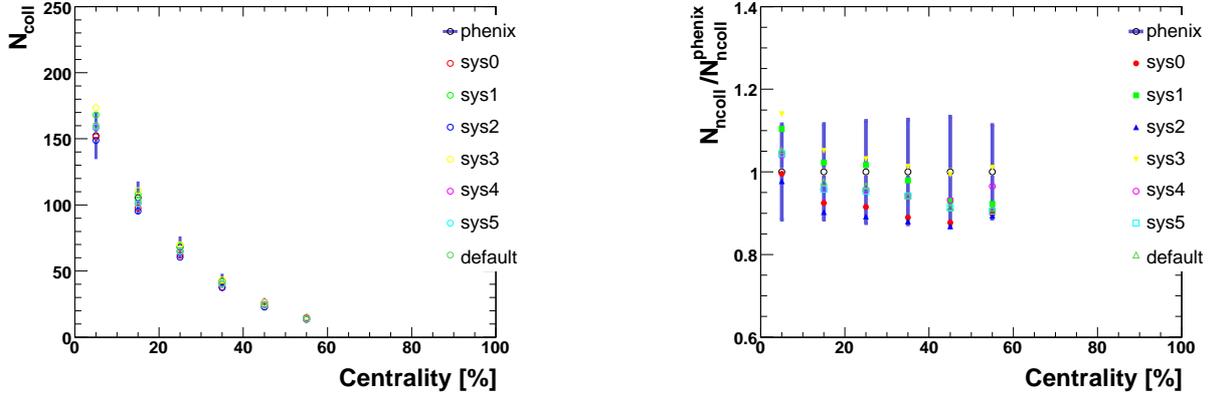
Figure 3.23: N_{coll} (left) and the ratio of N_{coll} to PHENIX N_{coll} (right) as a function of the centrality in Glauber Monte-Carlo simulation in Cu+Cu at $\sqrt{s_{\mathrm{NN}}} = 62.4$ GeV
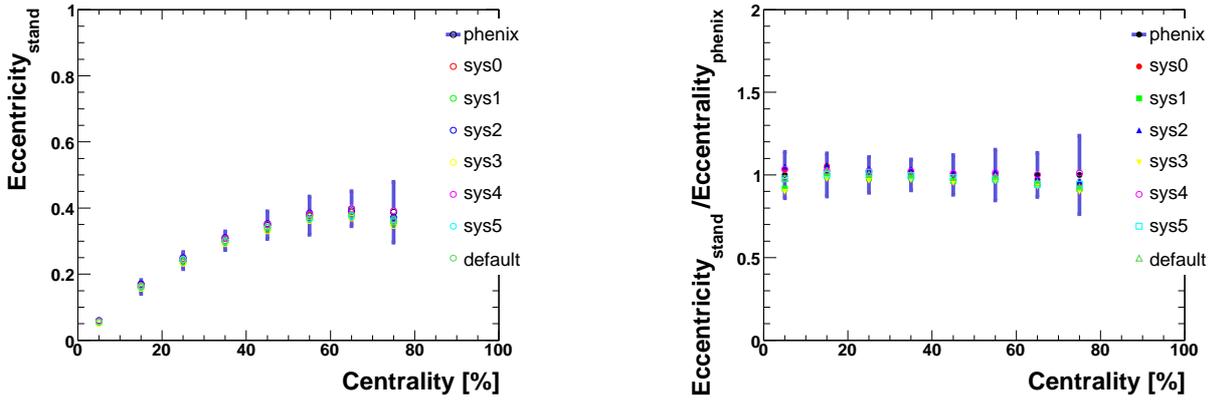
Figure 3.24: $\varepsilon_{\mathrm{stand}}$ (left) and the ratio of $\varepsilon_{\mathrm{stand}}$ to PHENIX ε (right) as a function of the centrality in Glauber Monte-Carlo simulation in Au+Au at $\sqrt{s_{\mathrm{NN}}} = 200$ GeV

Figure 3.28 - 3.31 are comparison of $\varepsilon_{\mathrm{part}}$ with above conditions. In these ratio figures, the ratios of $\varepsilon_{\mathrm{part}}$ with some parameters which are different from default setting (see above list) to that by default setting are shown. Table 3.5 - 3.8 are the table of $\varepsilon_{\mathrm{part}}$ and these systematic errors calculated by same condition and parameters as above calculations.
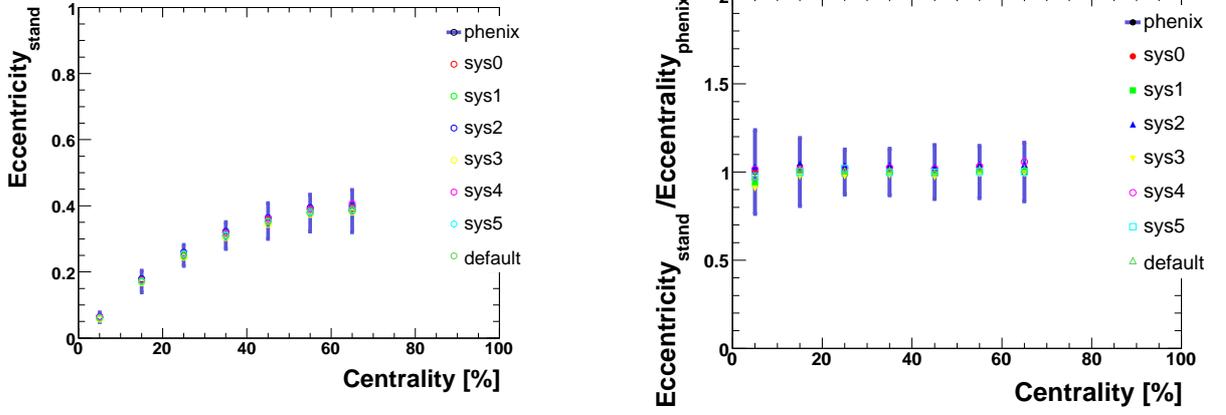
Figure 3.25: $\varepsilon_{\text{stand}}$ (left) and the ratio of $\varepsilon_{\text{stand}}$ to PHENIX ε (right) as a function of the centrality in Glauber Monte-Carlo simulation in Au+Au at $\sqrt{s_{\text{NN}}} = 62.4$ GeV
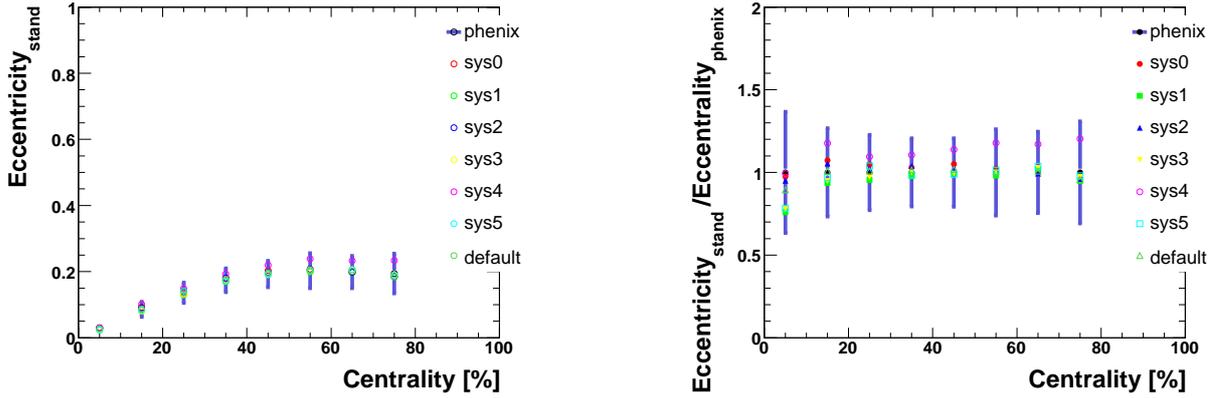
Figure 3.26: $\varepsilon_{\text{stand}}$ (left) and the ratio of $\varepsilon_{\text{stand}}$ to PHENIX ε (right) as a function of the centrality in Glauber Monte-Carlo simulation in Cu+Cu at $\sqrt{s_{\text{NN}}} = 200$ GeV
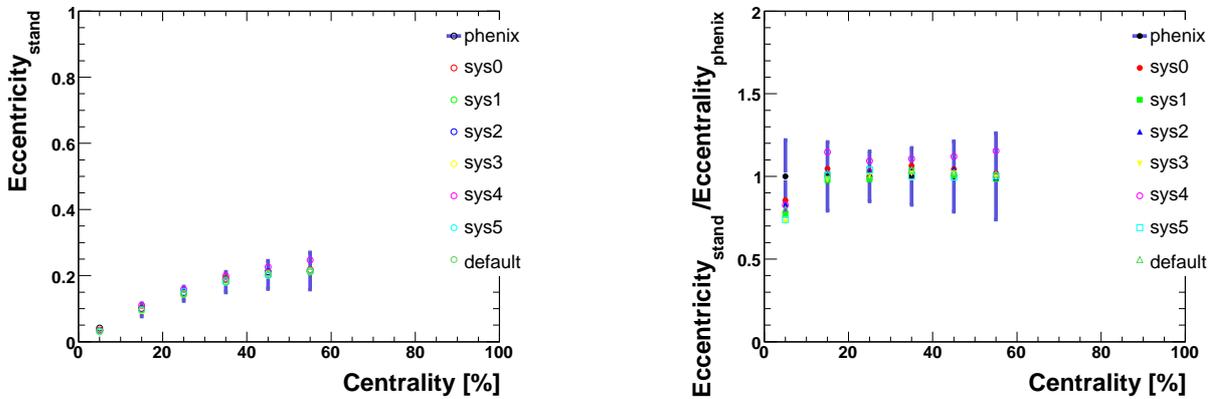
Figure 3.27: $\varepsilon_{\text{stand}}$ (left) and the ratio of $\varepsilon_{\text{stand}}$ to PHENIX ε(right) as a function of the centrality in Glauber Monte-Carlo simulation in Cu+Cu at $\sqrt{s_{\text{NN}}} = 62.4$ GeV.
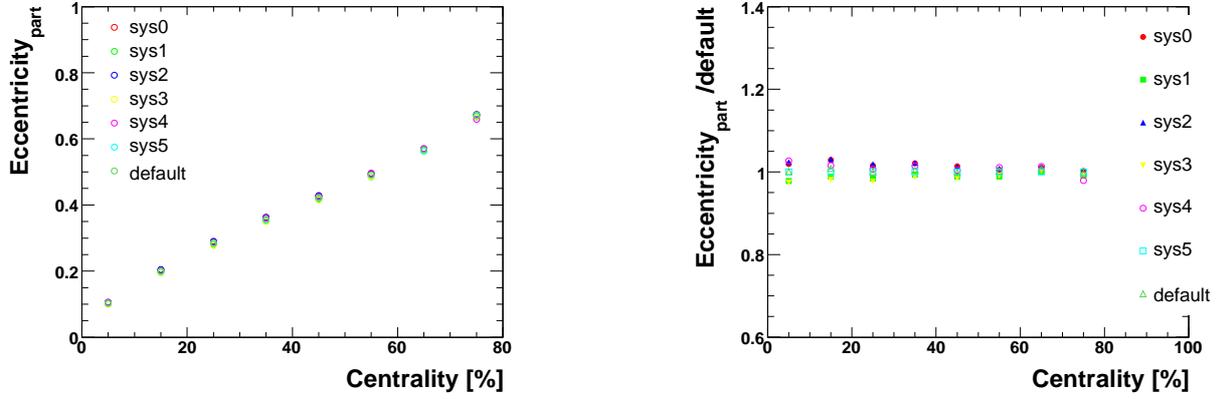
Figure 3.28: The $\varepsilon_{\mathrm{part}}$ (left) and the ratio of $\varepsilon_{\mathrm{part}}$ to default (right) as a function of centrality in Glauber Monte-Carlo simulation in Au+Au at $\sqrt{s_{\mathrm{NN}}} = 200$ GeV.
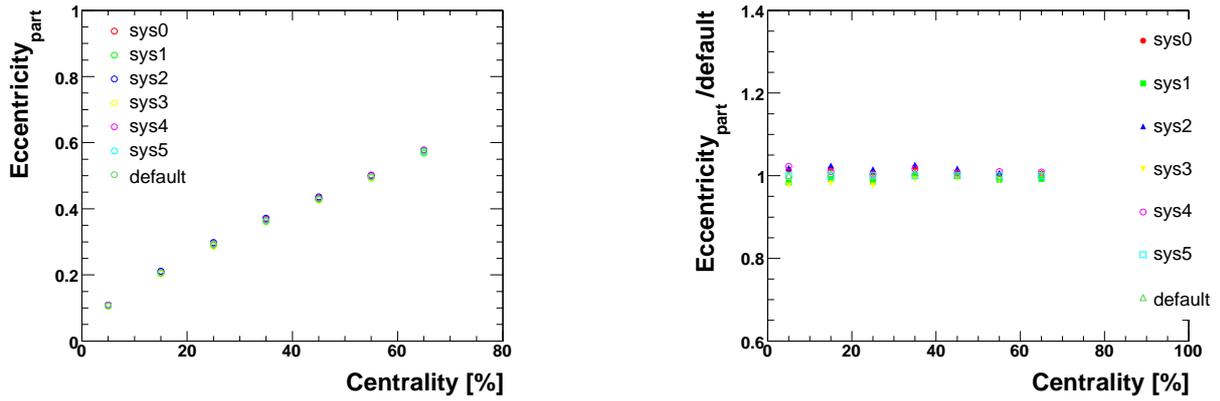
Figure 3.29: The $\varepsilon_{\mathrm{part}}$ (left) and the ratio of $\varepsilon_{\mathrm{part}}$ to default (right) as a function of centrality in Glauber Monte-Carlo simulation in Au+Au at $\sqrt{s_{\mathrm{NN}}} = 62.4$ GeV.
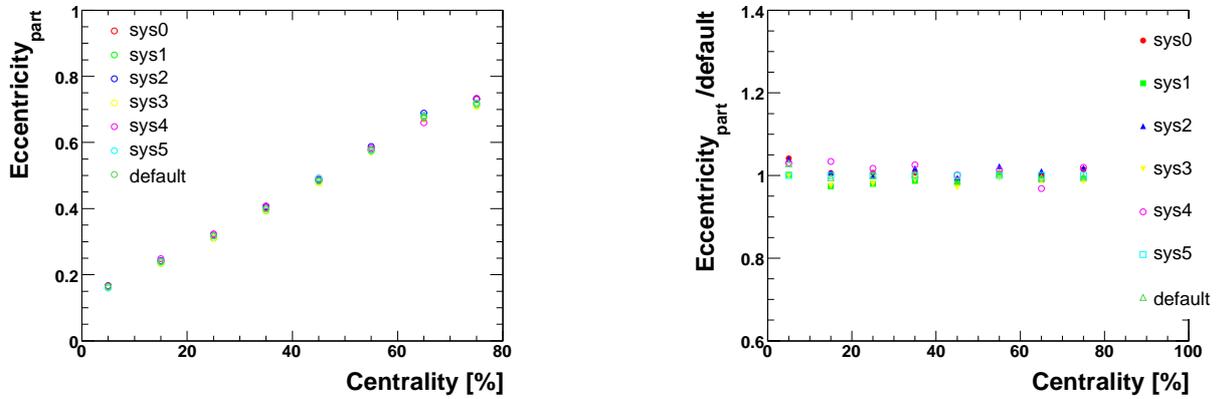
Figure 3.30: The $\varepsilon_{\mathrm{part}}$ (left) and the ratio of $\varepsilon_{\mathrm{part}}$ to default (right) as a function of centrality in Glauber Monte-Carlo simulation in Cu+Cu at $\sqrt{s_{\mathrm{NN}}} = 200$ GeV
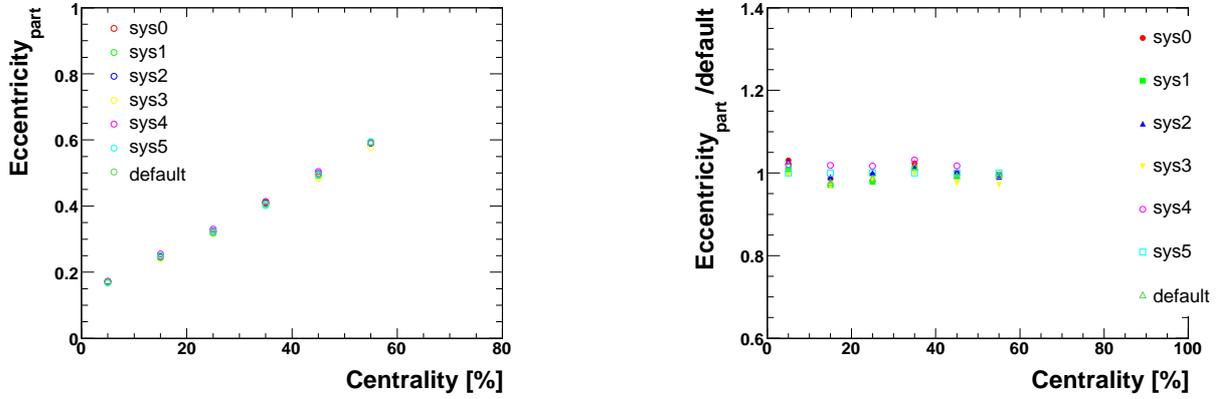
Figure 3.31: The $\varepsilon_{\text{part}}$ (left) and the ratio of $\varepsilon_{\text{part}}$ to default (right) as a function of centrality in Glauber Monte-Carlo simulation in Cu+Cu at $\sqrt{s_{\text{NN}}} = 62.4$ GeV

Table 3.5: Results of Glauber Monte Carlo simulations for participant eccentricity ($\varepsilon_{\text{part}}$) for Au+Au collisions at $\sqrt{s_{\text{NN}}} = 200$ GeV

Centrality [%]	participant Eccentricity	Systematic Error [%]
0-10	0.103	0.026
10-20	0.200	0.025
20-30	0.284	0.021
30-40	0.356	0.017
40-50	0.422	0.015
50-60	0.491	0.011
60-70	0.567	0.007
70-80	0.666	0.012
80-90	0.726	0.028

Table 3.6: Results of Glauber Monte Carlo simulations for participant eccentricity ($\varepsilon_{\text{part}}$) for Au+Au collisions at $\sqrt{s_{\text{NN}}} = 62.4$ GeV

Centrality [%]	Participant Eccentricity	Systematic Error [%]
0-10	0.107	0.023
10-20	0.207	0.022
20-30	0.292	0.020
30-40	0.365	0.018
40-50	0.431	0.013
50-60	0.498	0.010
60-70	0.573	0.008
70-80	0.678	0.011
80-90	0.740	0.022

Table 3.7: Results of Glauber Monte Carlo simulations for participant eccentricity ($\varepsilon_{\mathrm{part}}$) for Cu+Cu collisions at $\sqrt{s_{\mathrm{NN}}} = 200$ GeV

Centrality [%]	Participant Eccentricity	Systematic Error [%]
0-10	0.163	0.020
10-20	0.241	0.030
20-30	0.317	0.019
30-40	0.401	0.019
40-50	0.484	0.016
50-60	0.579	0.014
60-70	0.674	0.021
70-80	0.721	0.017
80-90	0.856	0.072

Table 3.8: Results of Glauber Monte Carlo simulations for participant eccentricity ($\varepsilon_{\mathrm{part}}$) for Cu+Cu collisions at $\sqrt{s_{\mathrm{NN}}} = 62.4$ GeV

Centrality [%]	Participant Eccentricity	Systematic Error [%]
0-10	0.169	0.017
10-20	0.248	0.026
20-30	0.324	0.019
30-40	0.408	0.016
40-50	0.494	0.021
50-60	0.587	0.015
60-70	0.696	0.023
70-80	0.742	0.016
80-90	0.867	0.062

3.6 Systematic Uncertainty

In this section, we describe the systematic uncertainty of the v_2 measurement. The actual values of the systematic uncertainty are included into the tables and figures in Chapter 4 . Since the analysis methods are slightly different between inclusive charged hadrons and identified charged hadrons, the concerned sources of systematic errors are also different. The systematic uncertainty of v_2 for inclusive charged hadrons is estimated concerning the following sources.

- The uncertainty of Reaction Plane determination

- The differential between different E/p cut ($E/p \geq 0.2 \sim 0.3$)

- The differential between different matching cut ($\mid \sigma \mid \leq 1.0 \sim 2.5$)

The systematic uncertainty of v_2 for identified charged hadrons is estimated concerning the following sources.

- The uncertainty from Reaction Plane determination

- The difference between different track quality cut

- The difference between different position matching cut for each detector.

- The difference between different timing matching cut for each detector.

- The difference between EMC detector and TOF detector.

- The difference among the different run periods.

3.6.1 Uncertainty from Reaction Plane Determination

The uncertainty of measured v_2 from Reaction Plane determination is obtained by taking the difference of v_2 with three different reaction planes, BBC north, BBC south, and BBC north+south. The uncertainty has centrality dependence. We used inclusive charged hadrons to get the reaction plane uncertainties since inclusive hadron has the largest statistics. The uncertainties in Au+Au at $\sqrt{s_{\mathrm{NN}}} = 62.4$ GeV collisions are summarized in Table 3.9 . The left panel of Figure 3.32 shows v_2 with respect to the different reaction planes as a function of the centrality for inclusive hadrons in Au+Au at $\sqrt{s_{\mathrm{NN}}} = 62.4$ GeV at $p_{\mathrm{T}} = 0.2$ - 4.0 GeV/c. The ratio of v_2 with respect to the different reaction planes, which indicates the uncertainty of the v_2 value from reaction plane determination, is shown in the right panel of Figure 3.32.

In Cu+Cu collisions at $\sqrt{s_{\mathrm{NN}}} = 200$ GeV the percentages of the uncertainties are summarized in Table 3.10 . The left panel of Figure 3.33 shows v_2 with respect to the different reaction planes as a function of the centrality for inclusive hadrons in Cu+Cu at $\sqrt{s_{\mathrm{NN}}} = 200$ GeV at $p_{\mathrm{T}} \geq 0.2$ GeV/c. The ratio of v_2 with respect to the different reaction planes, which indicates the uncertainty of the v_2 value from reaction plane determination, is shown in the right panel of Figure 3.33.

3.6.2 Uncertainty from Track Quality Cut

The uncertainty of measured v_2 from the track quality cut is obtained by taking the difference of v_2 with different track quality cuts as listed bellow.
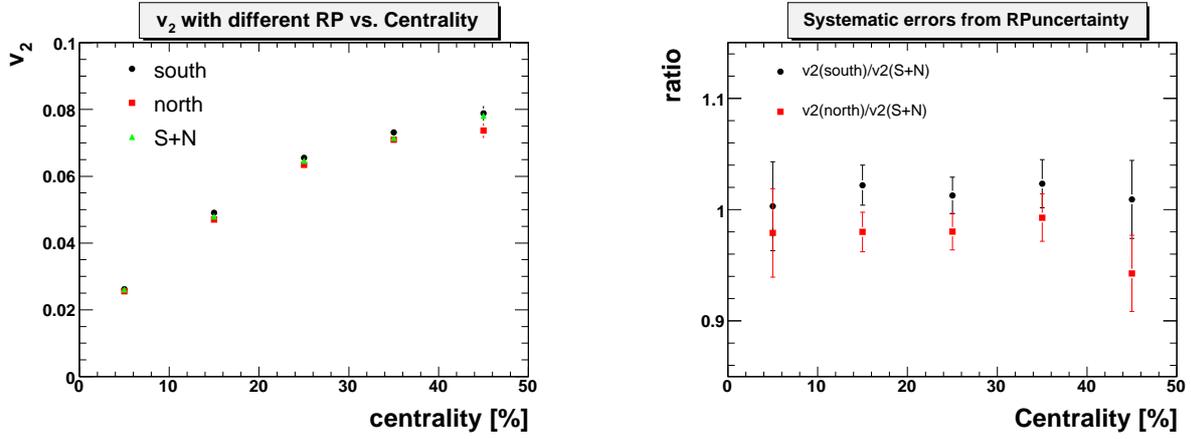
Figure 3.32: v_2 (left) and the ratio of v_2 (right) with respect to the different reaction planes as a function of the centrality for inclusive hadrons in Au+Au at $\sqrt{s_{NN}} = 62.4$ GeV at $p_T = 0.2$ - 4.0 GeV/c
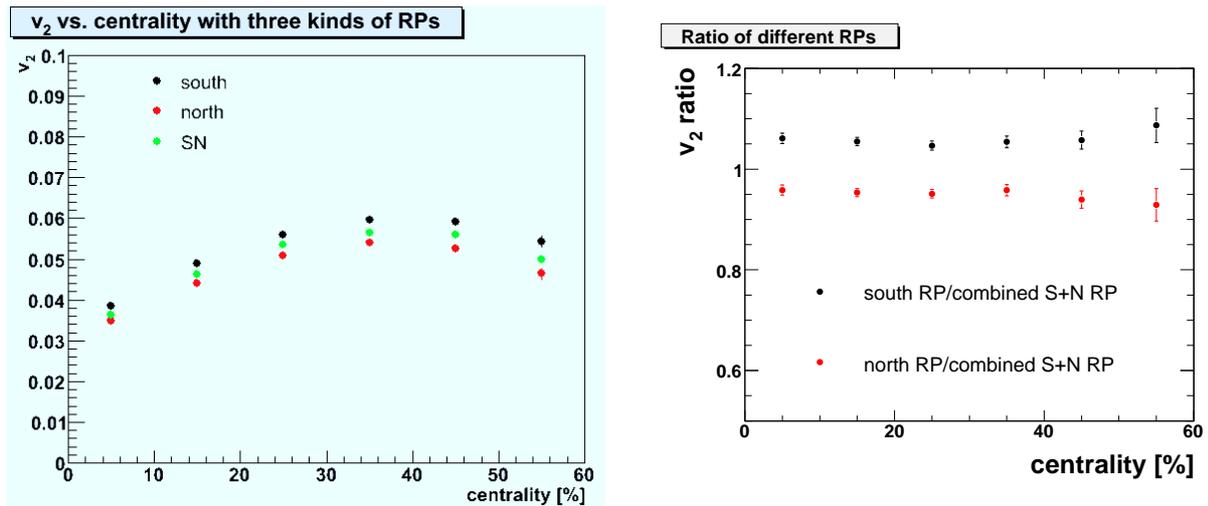
Figure 3.33: v_2 (left) and the ratio of v_2 (right) with respect to the different reaction planes as a function of the centrality for inclusive hadrons in Cu+Cu at $\sqrt{s_{NN}} = 200$ GeV at $p_T \geq 0.2$ GeV/c

Table 3.9: Systematic uncertainties of v_2 from the reaction plane determination in Au+Au at $\sqrt{s_{\mathrm{NN}}} = 62.4$ GeV at $p_{\mathrm{T}} = 0.2$ - 4.0 GeV/c

Centrality [%]	Integrated v_2	Systematic Errors [%]
0 -10	0.026	2.10
10 -20	0.048	2.20
20 -30	0.065	1.97
30 -40	0.071	2.33
40 -50	0.078	5.73
50 -60	0.069	5.462
60 -70	0.065	25.553
70 -80	0.050	64.989
10 -40	0.058	1.90
0 -84	0.048	3.236

Table 3.10: Systematic uncertainties of v_2 from the reaction plane determination in Cu+Cu at $\sqrt{s_{\mathrm{NN}}} = 200$GeV at $p_{\mathrm{T}} \geq 0.2$ GeV/c.

Centrality [%]	Integrated v_2	Systematic Errors [%]
0 -10	0.036	6.10
10 -20	0.046	5.49
20 -30	0.054	4.90
30 -40	0.056	5.42
40 -50	0.056	6.04
50 -60	0.050	8.699
60 -70	0.042	6.684
70 -80	0.045	11.814
80 -90	0.037	45.057

- Track quality > 4

- Track quality $= 63$ or 31

We used inclusive charged hadrons in minimum bias events to get the uncertainties from track quality cut since inclusive hadron has the largest statistics. The left panel of Figure 3.34 shows v_2 for charged hadrons with different track quality cuts in Au+Au at $\sqrt{s_{\mathrm{NN}}} = 62.4$ GeV. The ratio of v_2 with these cuts is shown in the right panel of Figure 3.34 . The black line is the fitting line which fits the ratio as constant. The uncertainty which is obtained by the fitting is ~ 1 % in Au+Au at $\sqrt{s_{\mathrm{NN}}} = 62.4$ GeV.

3.6.3 Uncertainty from Position Matching and Particle Identification Cuts

We estimate the uncertainty of measured v_2 from position matching and particle identification (PID) with mass^2 by taking different σ cuts. The cuts are listed here. 3σ veto cut is always applied for particle identification. Other cuts and conditions are same as the final results.
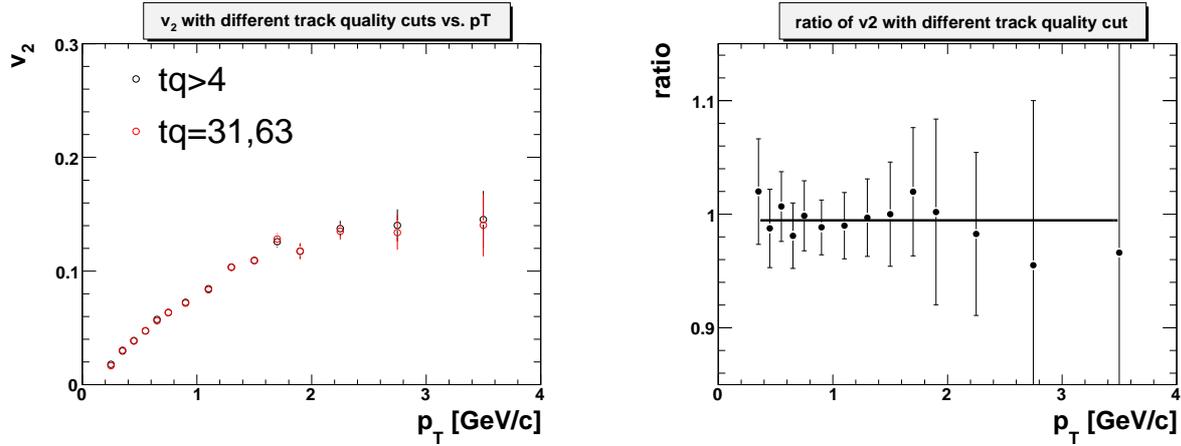
Figure 3.34: v_2 with different track quality cuts (left) and the uncertainty from the track quality cut (right) as a function of p_T for inclusive charged hadrons in Au+Au at $\sqrt{s_{NN}} = 62.4$ GeV. The black line is the fitting line which fits the ratio as constant.

- $\sqrt{\Delta\phi^2 + \Delta z^2} < 3.0\sigma$ && PID $< 2.0\sigma$

- $\sqrt{\Delta\phi^2 + \Delta z^2} < 3.0\sigma$ && PID $< 2.5\sigma$ (Default cut)

- $\sqrt{\Delta\phi^2 + \Delta z^2} < 3.0\sigma$ && PID $< 3.0\sigma$

- $\sqrt{\Delta\phi^2 + \Delta z^2} < 2.0\sigma$ && PID $< 2.5\sigma$

- $\sqrt{\Delta\phi^2 + \Delta z^2} < 2.5\sigma$ && PID $< 2.5\sigma$

Figure 3.35 - 3.40 show the difference of v_2 with these cuts depending on p_T and centrality (10 % step for 0-50 %) in Au+Au at $\sqrt{s_{NN}} = 62.4$ GeV. The ratios of v_2 with these different cuts to v_2 with default cut are shown in Figure 3.41 - 3.46.

It seems that there is no p_T dependence. Since statistical errors are big, we cannot see the p_T dependence. Therefore, we used fitting values as systematic errors. The uncertainties from position matching and PID are ~ 1 % and all these errors are within statistical errors.

3.6.4   Uncertainty from the Difference between TOF and EMCal

Figure. 3.47 and 3.49 show the comparisons of identified v_2 measured by EMC and TOF in Au+Au at $\sqrt{s_{NN}} = 62.4$ GeV. Figure. 3.48 and 3.50 show the ratios of these comparisons. We include this difference as systematic errors and combined TOF results to EMCal results for final results.

3.6.5   Run Dependence

We estimate the uncertainty from run dependence by taking the difference of v_2 for charged hadrons dividing whole data to seven different run periods. The dependence is shown in Figure 3.51 in Au+Au at $\sqrt{s_{NN}} = 62.4$ GeV. The uncertainty from the dependence is 4.4 % in Au+Au at $\sqrt{s_{NN}} = 62.4$ GeV.
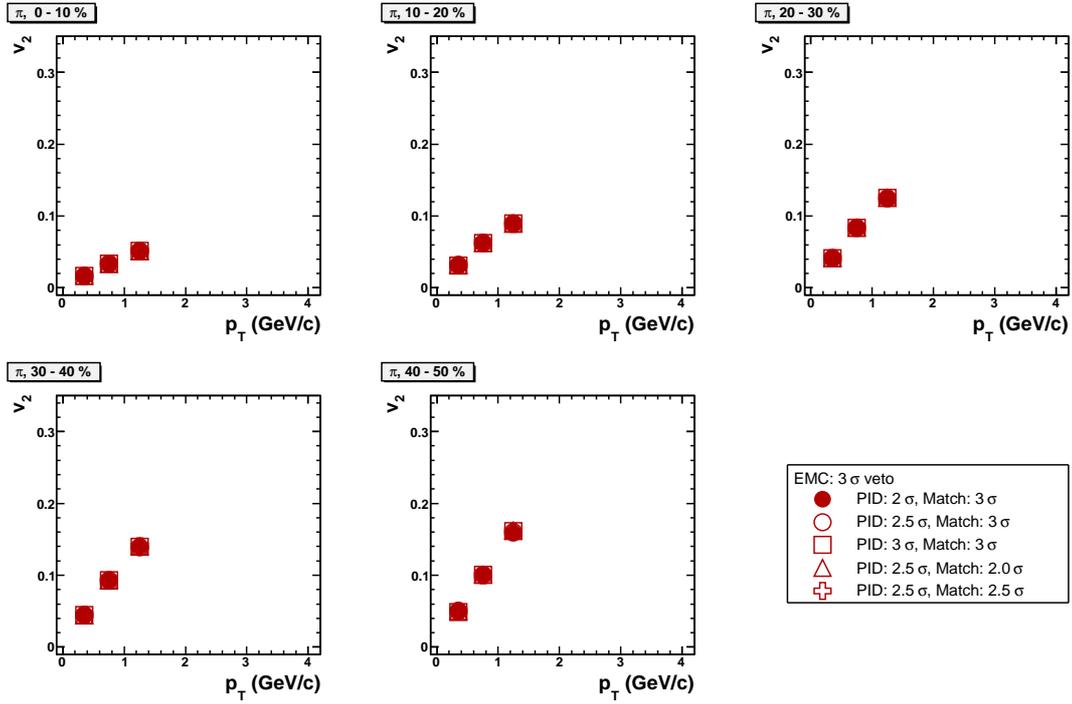
Figure 3.35: v_2 for π by EMC with five different position matching and PID cuts in Au+Au at $\sqrt{s_{\mathrm{NN}}} = 62.4$ GeV
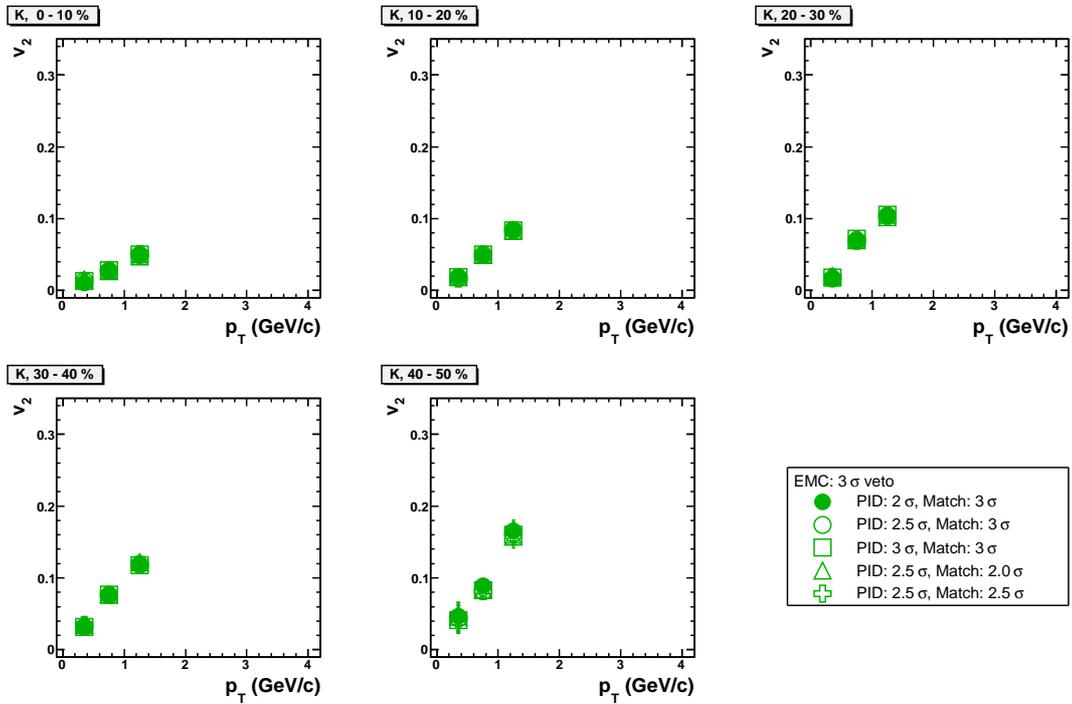
Figure 3.36: v_2 for K by EMC with five different position matching and PID cuts in Au+Au at $\sqrt{s_{\mathrm{NN}}} = 62.4$ GeV
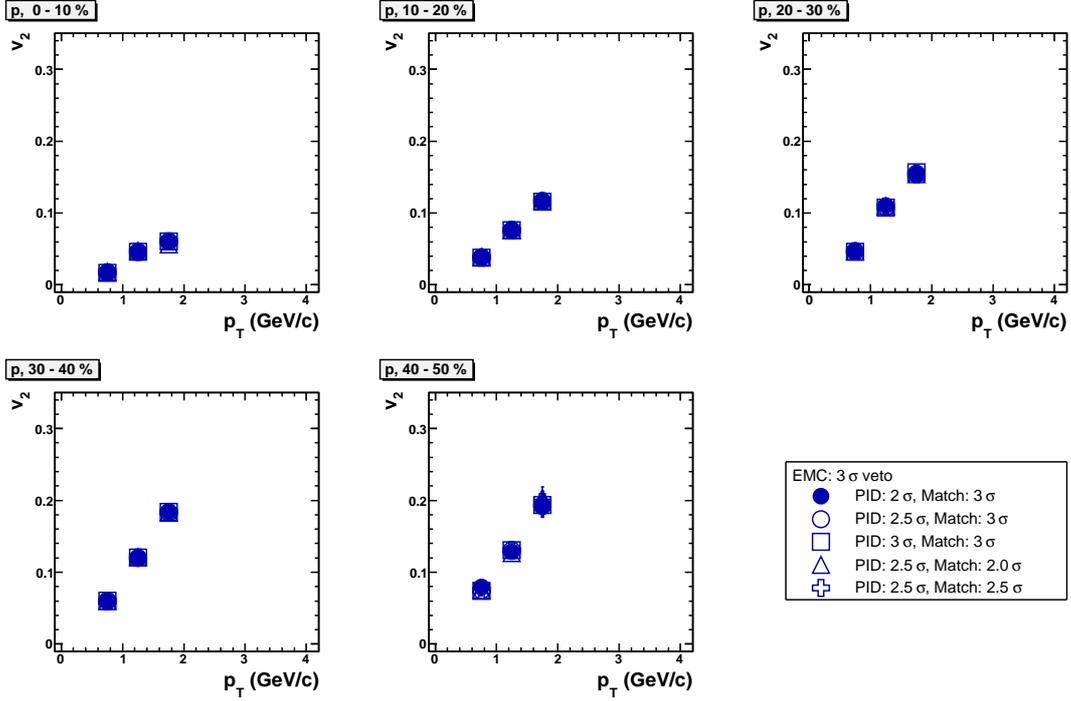
Figure 3.37: v_2 for p by EMC with five different position matching and PID cuts in Au+Au at $\sqrt{s_{\mathrm{NN}}} = 62.4$ GeV
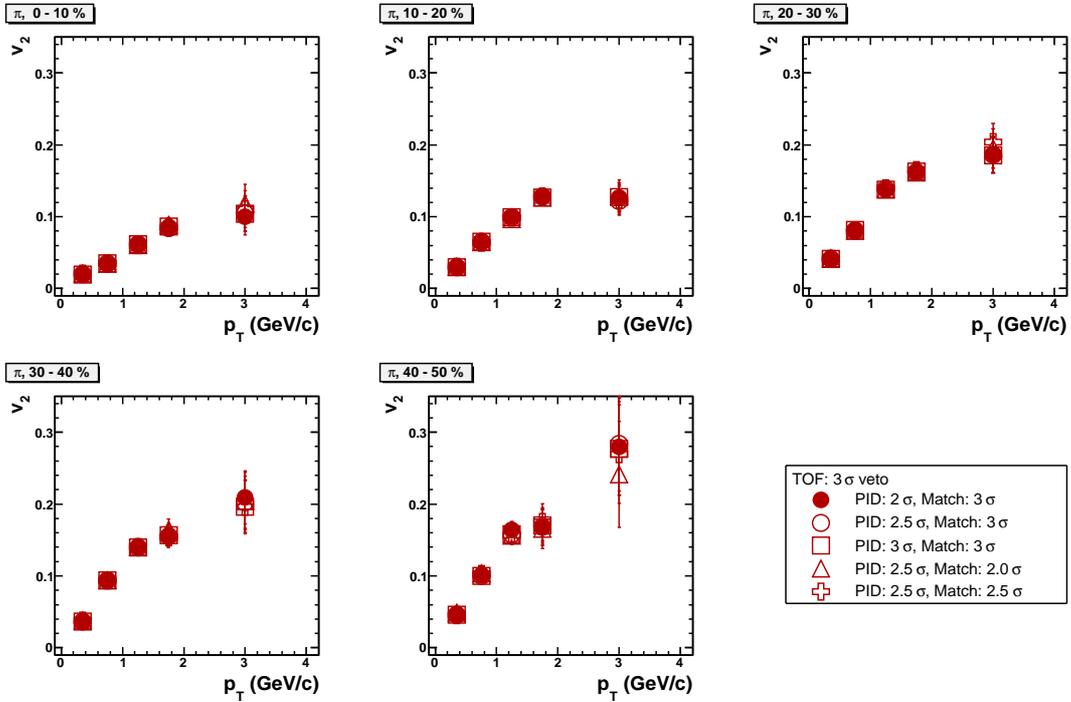
Figure 3.38: v_2 for π by TOF with five different position matching and PID cuts in Au+Au at $\sqrt{s_{\mathrm{NN}}} = 62.4$ GeV
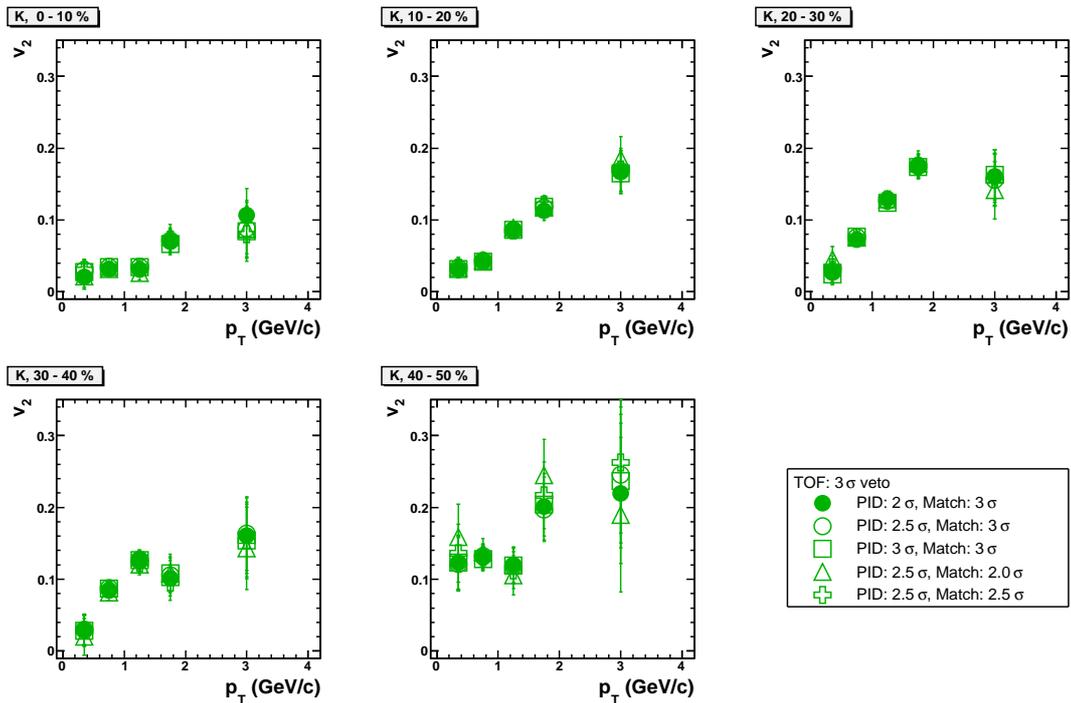
Figure 3.39: v_2 for K by TOF with five different position matching and PID cuts in Au+Au at $\sqrt{s_{\mathrm{NN}}} = 62.4$ GeV
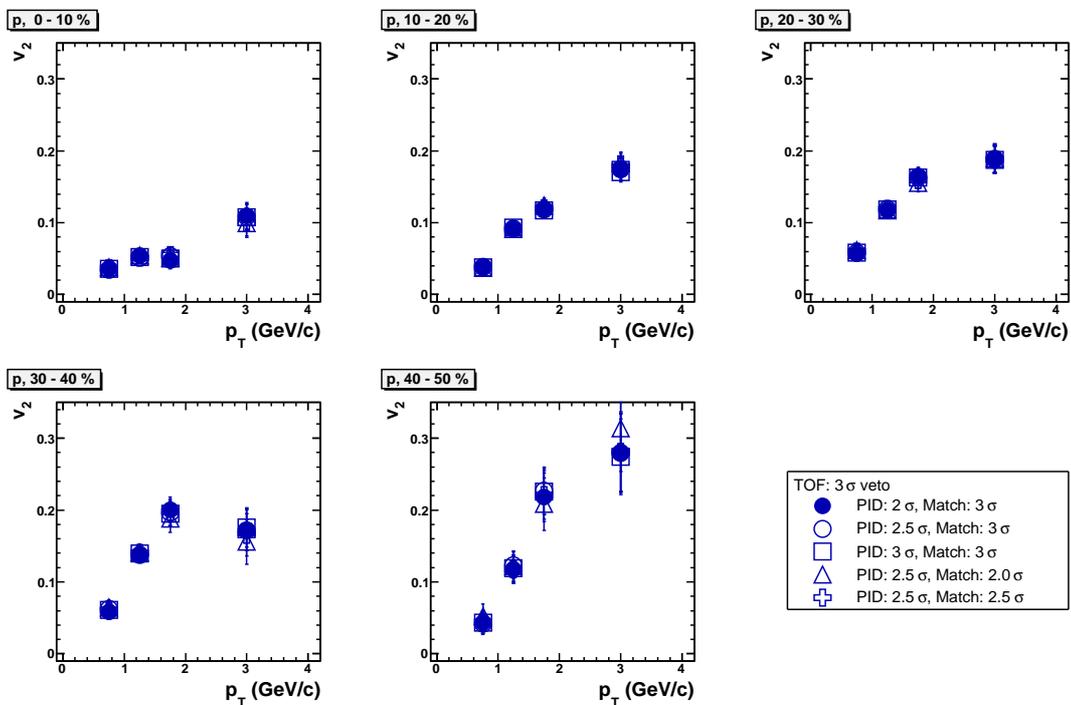
Figure 3.40: v_2 for p by TOF with five different position matching and PID cuts in Au+Au at $\sqrt{s_{\mathrm{NN}}} = 62.4$ GeV
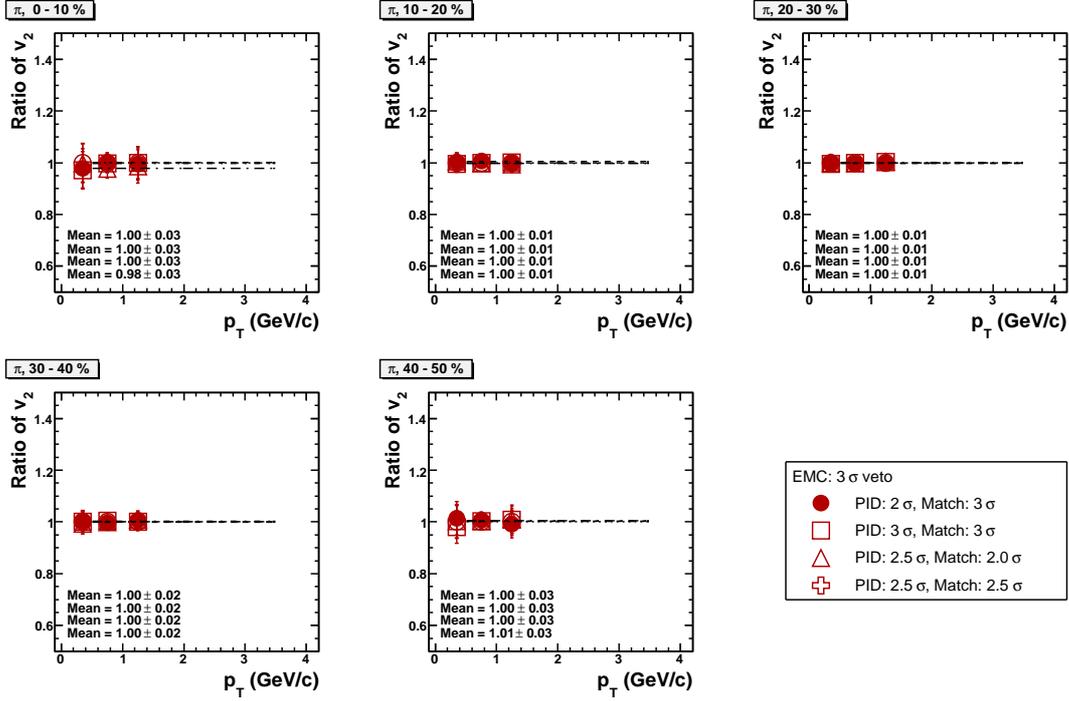
Figure 3.41: Ratios of v_2 for π by EMC with five different position matching and PID cuts to default cut in Au+Au at $\sqrt{s_{\mathrm{NN}}} = 62.4$ GeV
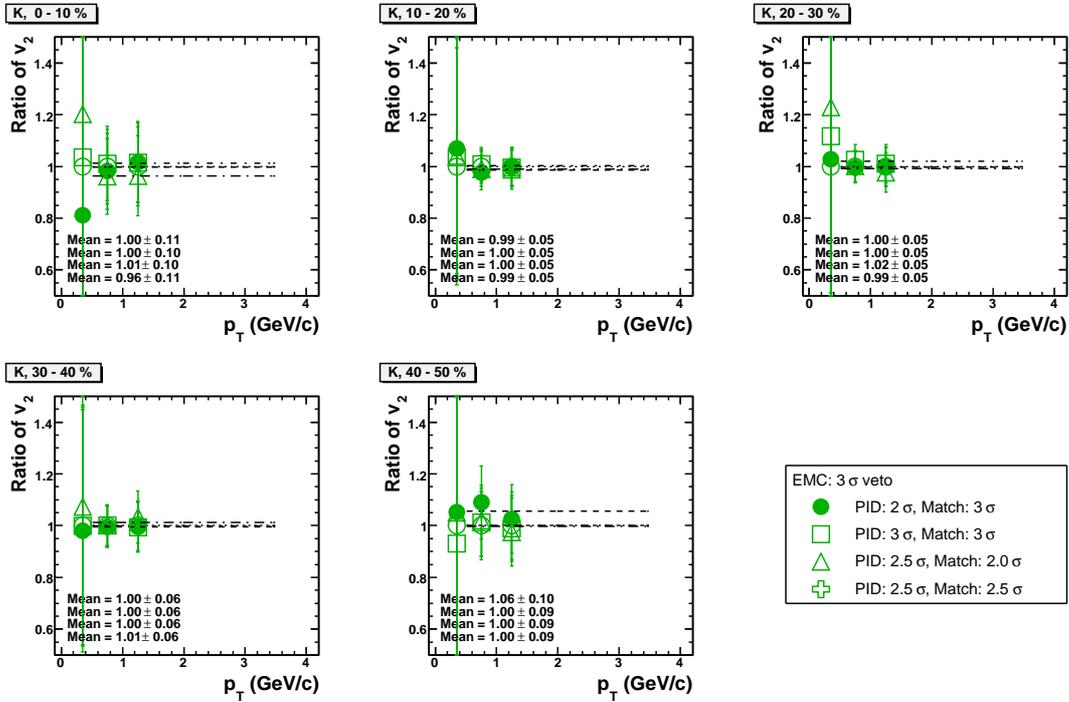
Figure 3.42: Ratios of v_2 for K by EMC with five different position matching and PID cuts to default cut in Au+Au at $\sqrt{s_{\mathrm{NN}}} = 62.4$ GeV
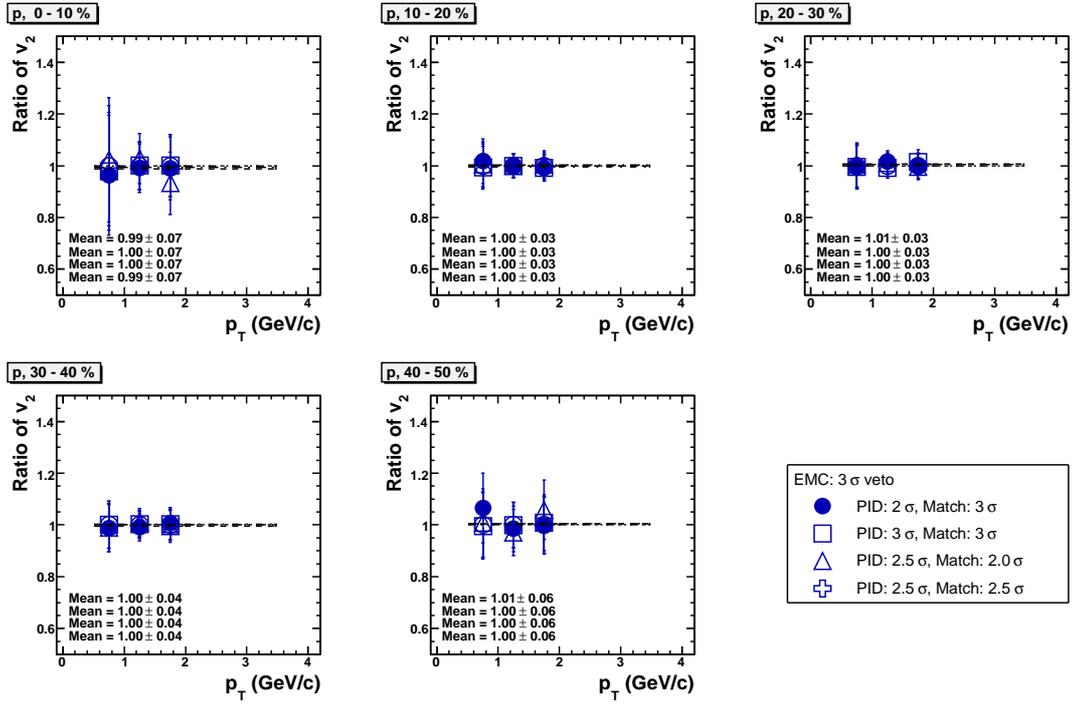
Figure 3.43: Ratios of v_2 for p by EMC with five different position matching and PID cuts to default cut in Au+Au at $\sqrt{s_{\mathrm{NN}}} = 62.4$ GeV
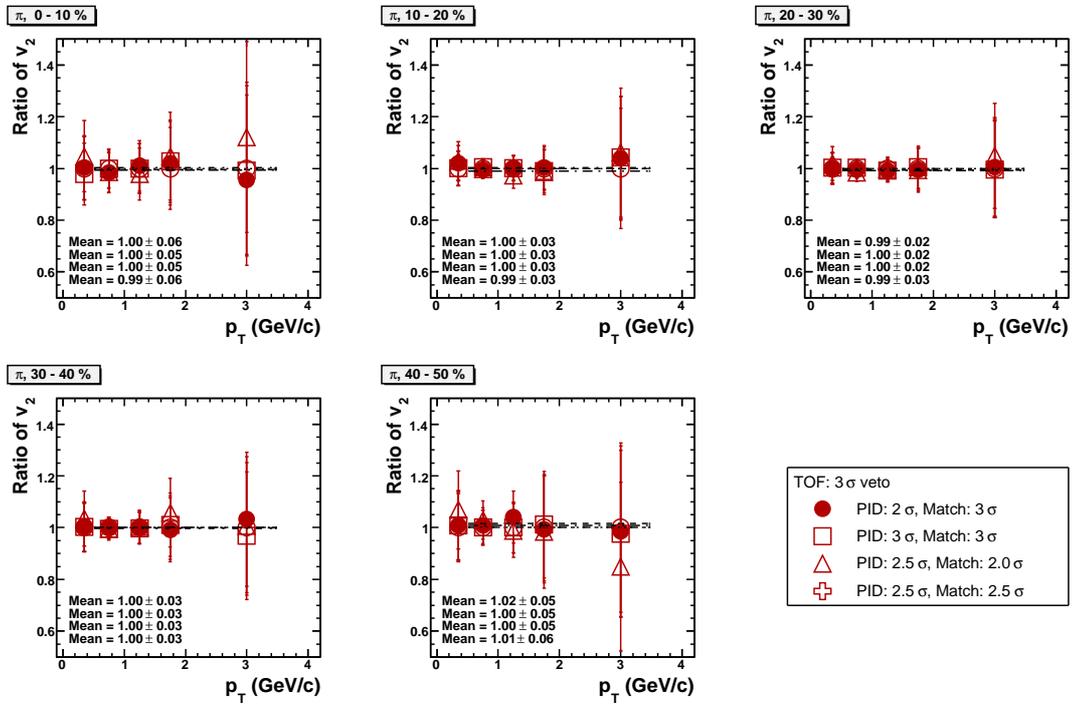
Figure 3.44: Ratios of v_2 for π by TOF with five different position matching and PID cuts to default cut in Au+Au at $\sqrt{s_{\mathrm{NN}}} = 62.4$ GeV
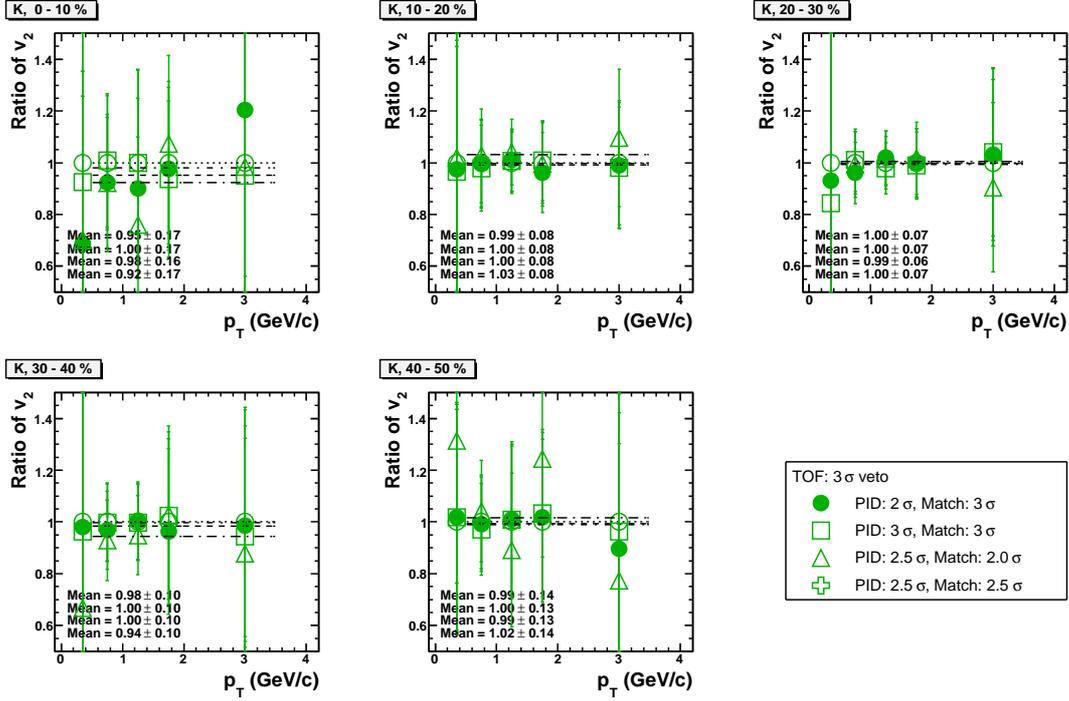
Figure 3.45: Ratios of v_2 for K by TOF with five different position matching and PID cuts to default cut in Au+Au at $\sqrt{s_{\mathrm{NN}}} = 62.4$ GeV
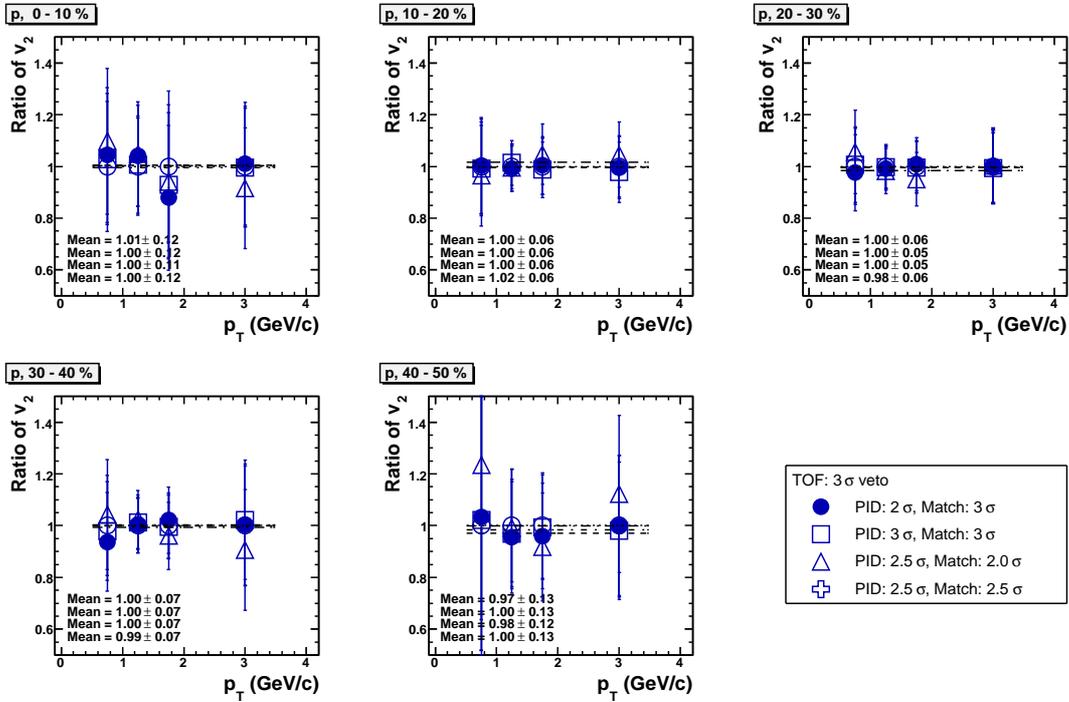
Figure 3.46: Ratios of v_2 for p by TOF with five different position matching and PID cuts to default cut in Au+Au at $\sqrt{s_{\mathrm{NN}}} = 62.4$ GeV
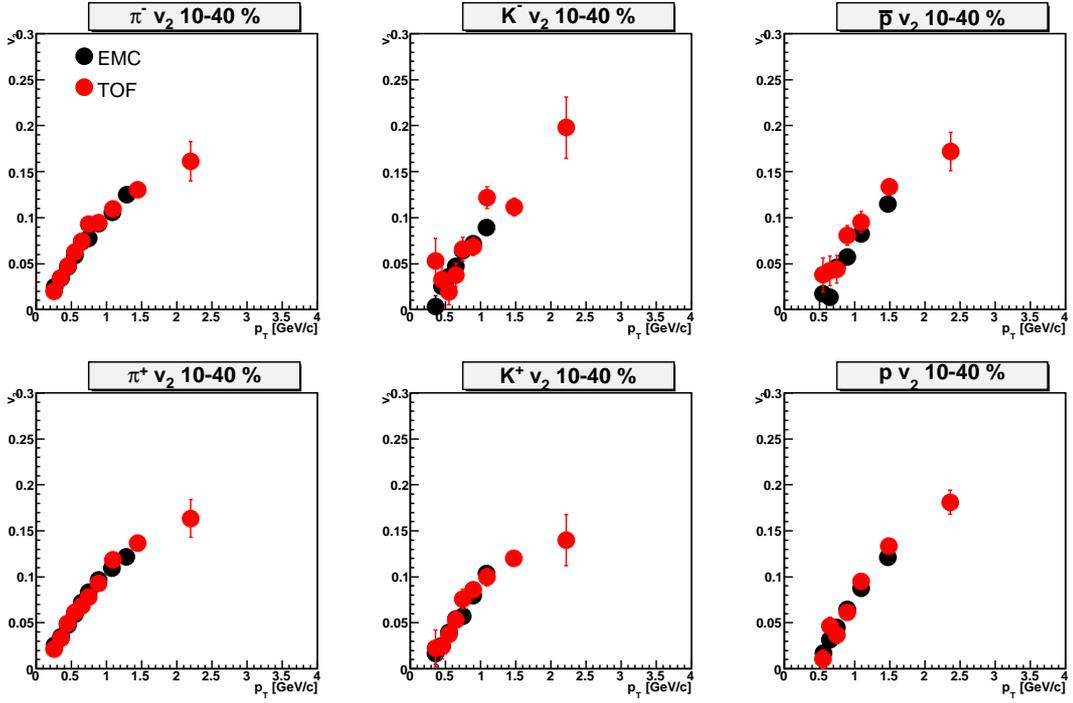
Figure 3.47: Comparison of TOF results to EMC from 10 to 40 % centrality in Au+Au at $\sqrt{s_{NN}} = 62.4$ GeV.
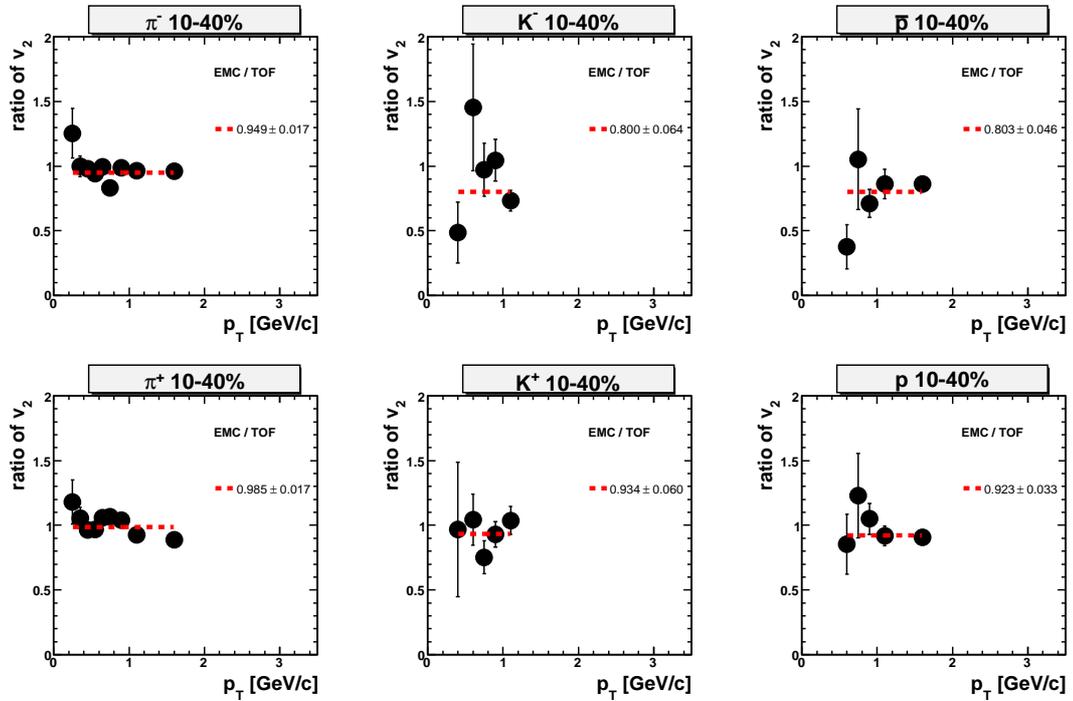
Figure 3.48: The ratio of the comparison of v_2 identified by TOF and EMC from 10 to 40 % centrality in Au+Au at $\sqrt{s_{NN}} = 62.4$ GeV.
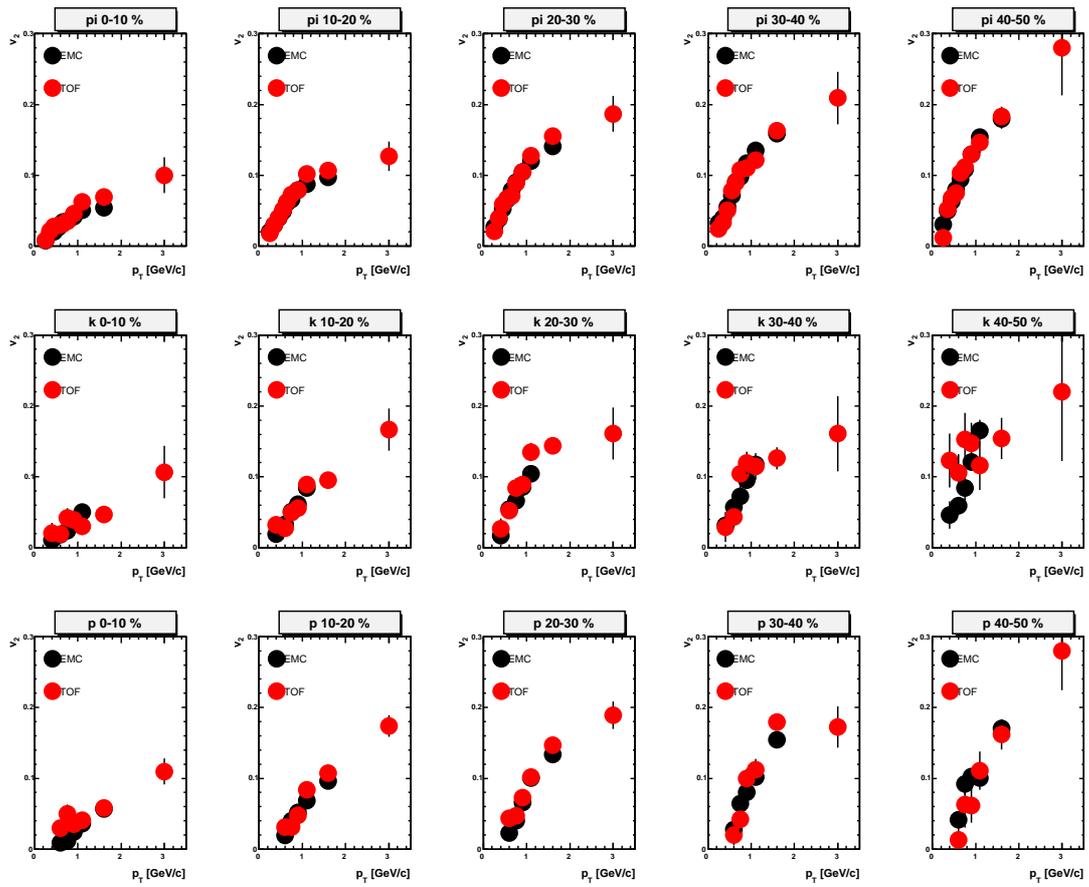
Figure 3.49: The ratio of the comparison of v_2 identified by TOF and EMC for 10 % step centrality from 0 to 50 % in Au+Au at $\sqrt{s_{\mathrm{NN}}} = 62.4$ GeV.
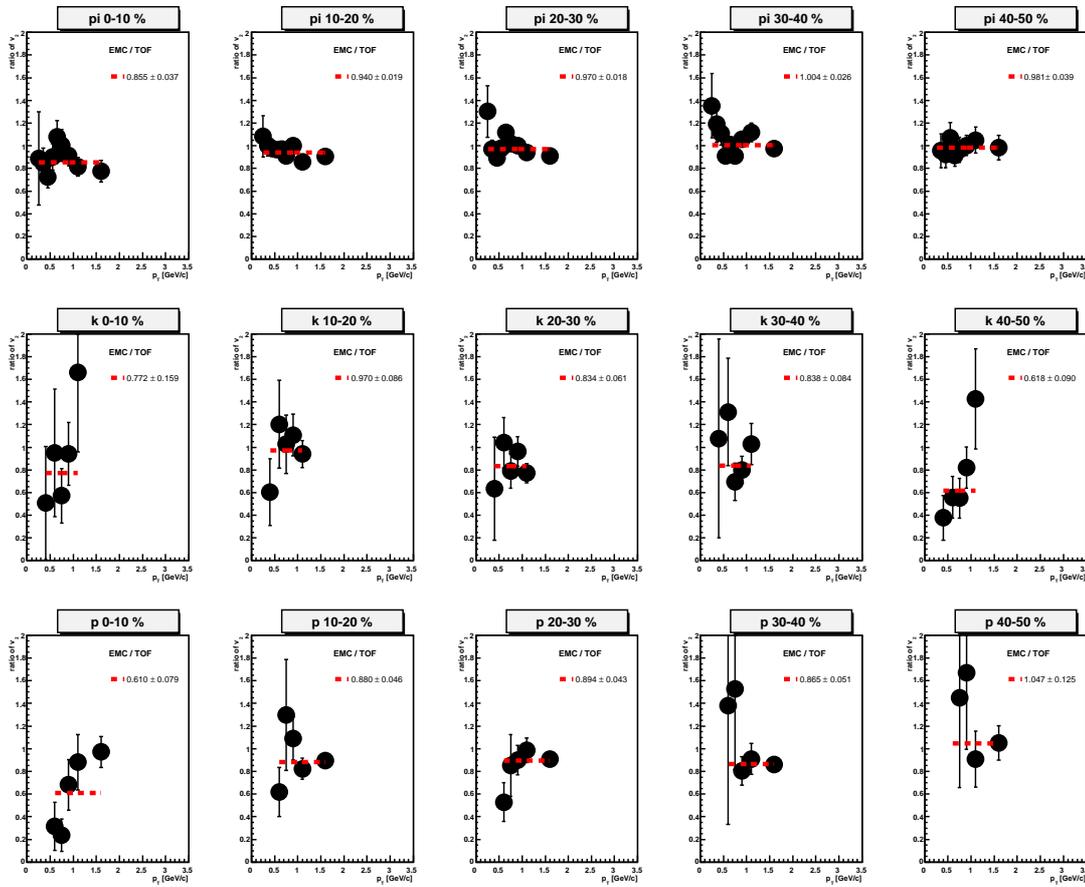
Figure 3.50: The ratio of the comparison of v_2 identified by TOF and EMC for 10 % step centrality from 0 to 50 % in Au+Au at $\sqrt{s_{\mathrm{NN}}} = 62.4$ GeV.
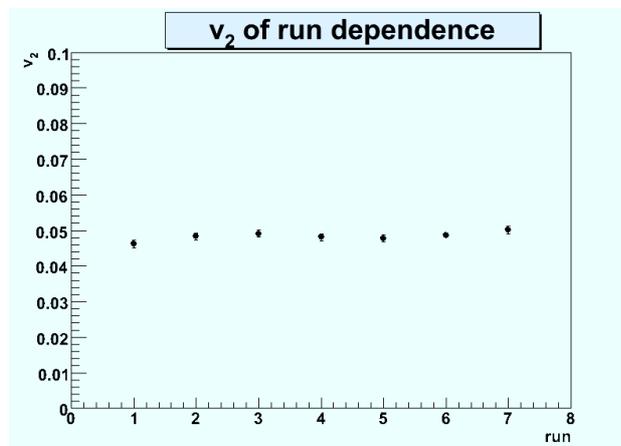
Figure 3.51: Run dependence of v_2 for inclusive charged hadrons in Au+Au at $\sqrt{s_{\mathrm{NN}}} = 62.4$ GeV.

Chapter 4

Results

In this chapter, we present the experimental results of v_2 measurements as a function of transverse momentum (p_T) and collision centrality for the following colliding systems and particle species:

1. In Au+Au at $\sqrt{s_{NN}} = 200$ GeV for inclusive charged hadrons

2. In Cu+Cu at $\sqrt{s_{NN}} = 200$ GeV for π, K, p+$\bar{p}$

3. In Au+Au at $\sqrt{s_{NN}} = 62.4$ GeV for $\pi^{\pm}$, K$^{\pm}$, p,$\bar{p}$, inclusive charged hadrons

4. In Cu+Cu at $\sqrt{s_{NN}} = 62.4$ GeV for inclusive charged hadrons

4.1   Inclusive Charged Hadron v_2

In this section, we present the results of v_2 as a function of transverse momentum p_T, for inclusive charged hadrons for the following bins in collision centrality;

1. Au+Au collisions at $\sqrt{s_{NN}} = 200$ GeV

   - Minimum Bias ; 0-92 %
   - 10 % step from 0 to 50 % ; 0-10, 10-20, 20-30, 30-40, 40-50, 50-60 %
   - 20 % step from 0 to 60 % ; 0-20, 20-40, 40-60 %
   - Most peripheral wide centrality bin; 60-92 %

2. Au+Au collisions at $\sqrt{s_{NN}} = 62.4$ GeV

   - Minimum Bias ; 0-83 %
   - 10 % step from 0 to 50 % ; 0-10, 10-20, 20-30, 30-40, 40-50 %

3. Cu+Cu collisions at $\sqrt{s_{NN}} = 62.4$ GeV

   - Minimum Bias ; 0-88 %
   - 10 % step from 0 to 80 % ; 0-10, 10-20, 20-30, 30-40, 40-50, 50-60, 60-70, 70-80 %
   - 20 % step from 0 to 60 % ; 0-20, 20-40, 40-60, 60-80 %

To study the dependences of v_2 on the energy and size of collisional nucleus, we have compared the measured v_2 for four data sets; Au+Au collisions at $\sqrt{s_{NN}} = 200$ GeV, Au+Au collisions at $\sqrt{s_{NN}} = 62.4$ GeV, Cu+Cu collisions at $\sqrt{s_{NN}} = 200$ GeV and Cu+Cu collisions at $\sqrt{s_{NN}} = 62.4$ GeV. The results of measured v_2 as a function of p_T and centrality for inclusive charged hadron in Cu+Cu at $\sqrt{s_{NN}} = 200$ GeV are taken from [5] .

4.1.1 Measured v_2 in Au+Au Collisions at the Energy of $\sqrt{s_{NN}} = 200$ GeV

Since the statistics of the analyzed data in Run4 is around 860 Millions which is more than 20 times larger compared with Run2 (30 Millions), the detailed v_2 measurement of centrality dependence and p_T dependence can be done in Au+Au at $\sqrt{s_{NN}} = 200$ GeV. Moreover, the energy cut method described in Section 3.2.1 with the large statistics enables us to measure v_2 up to much higher p_T (up to 13 GeV/c for minimum bias) compared with previous measurement. The presented results are in good agreements with previous measurement. This measurement is used as a base line for comparison with other colliding system such as Au+Au collisions at $\sqrt{s_{NN}} = 62.4$ GeV or Cu+Cu collisions at $\sqrt{s_{NN}} = 200/62.4$ GeV. Figure. 4.1 - 4.2 show v_2 as the function of p_T for each centrality bin. The tables of the data are written in Appendix C . The systematic errors for v_2 are not symmetric, so that we give the lower and upper values for systematic errors in each table.

Non zero v_2 has been observed at $p_T \simeq 5$ GeV/c for 0-70 % central collisions, and up to $p_T \sim 15$ GeV/c for minimumbias events. As explained in Section 1.3.5, this result is consistent with the scenario that the jet lose its energy in the medium. More detail is discussed in Appendix B .

4.1.2 Measured v_2 in Au+Au Collisions at the Energy of $\sqrt{s_{NN}} = 62.4$ GeV

To study the dependence of collisional energy, we have also measured v_2 at $\sqrt{s_{NN}} = 62.4$ GeV. Figure 4.3 shows the p_T dependence of v_2 for inclusive charged hadrons emitted from Au+Au collisions at $\sqrt{s_{NN}} = 62.4$ GeV. The results are presented for several bins in collision centrality: 0-10 %, 10-20 %, 20-30 %, 30-40 %, 40-50 % as well as minimum bias collisions. The tables of the results are written in Appendix C .

4.1.3 Measured v_2 in Cu+Cu Collisions at the Energy of $\sqrt{s_{NN}} = 62.4$ GeV

To study the dependence of collisional energy and system, we have also measured v_2 in Cu+Cu collisions at $\sqrt{s_{NN}} = 62.4$ GeV. Figure 4.4 and 4.5 show the results of v_2 as a function of p_T for inclusive charged hadrons emitted from Cu+Cu collisions at $\sqrt{s_{NN}} = 62.4$ GeV. The results are presented for several bins in collision centrality; 0-10 %, 10-20 %, 20-30 %, 30-40 %, 40-50 %, 50-60 %, 60-70 %, 70-80 %, 0-20 %, 20-40 %, 40-60 %, 60-80 % as well as minimum bias collisions.The tables of the results are written in Appendix C .
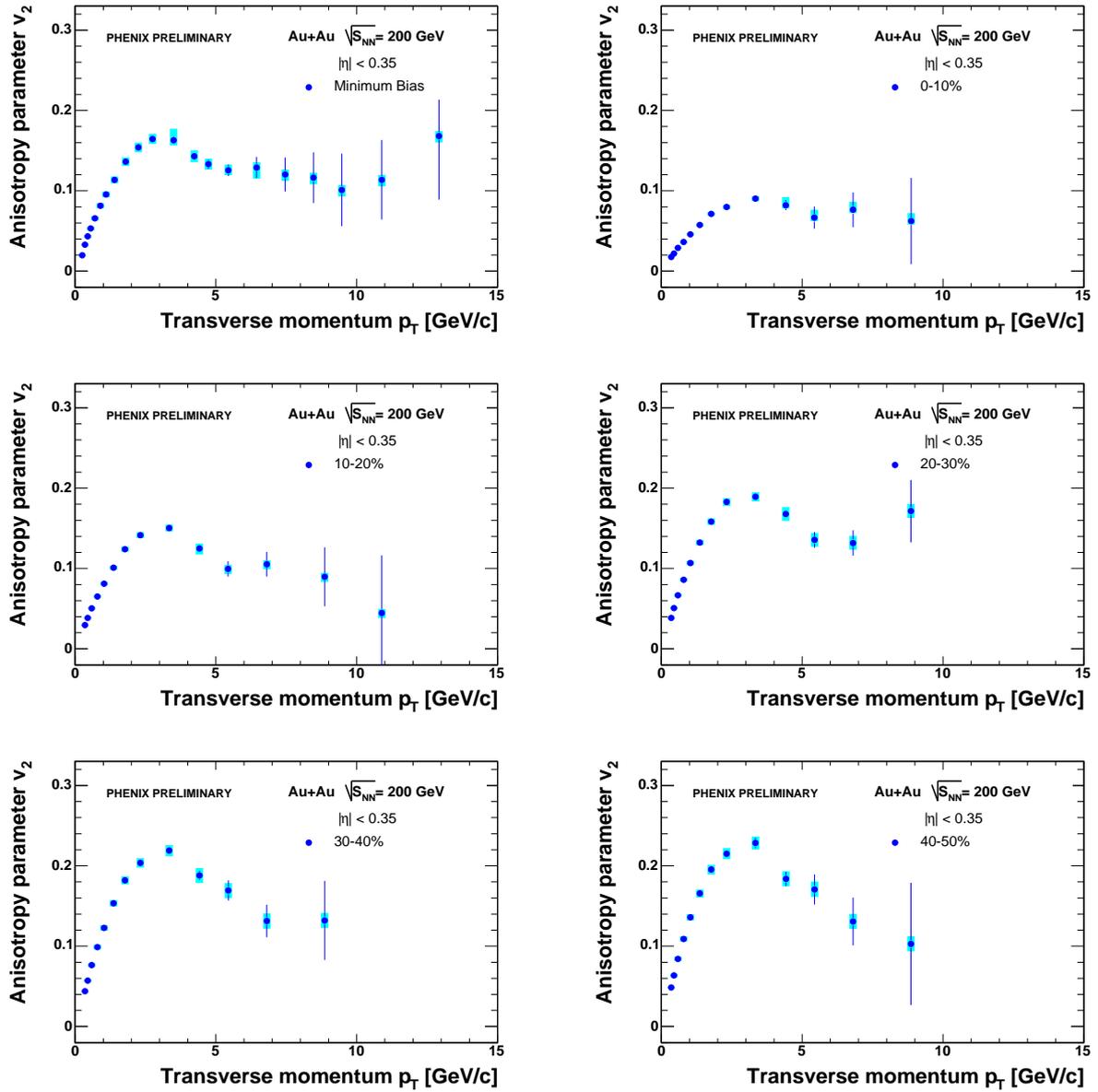
Figure 4.1: v_2 for inclusive charged hadron in Au+Au at $\sqrt{s_{\mathrm{NN}}} = 200$ GeV for the centralities indicated.
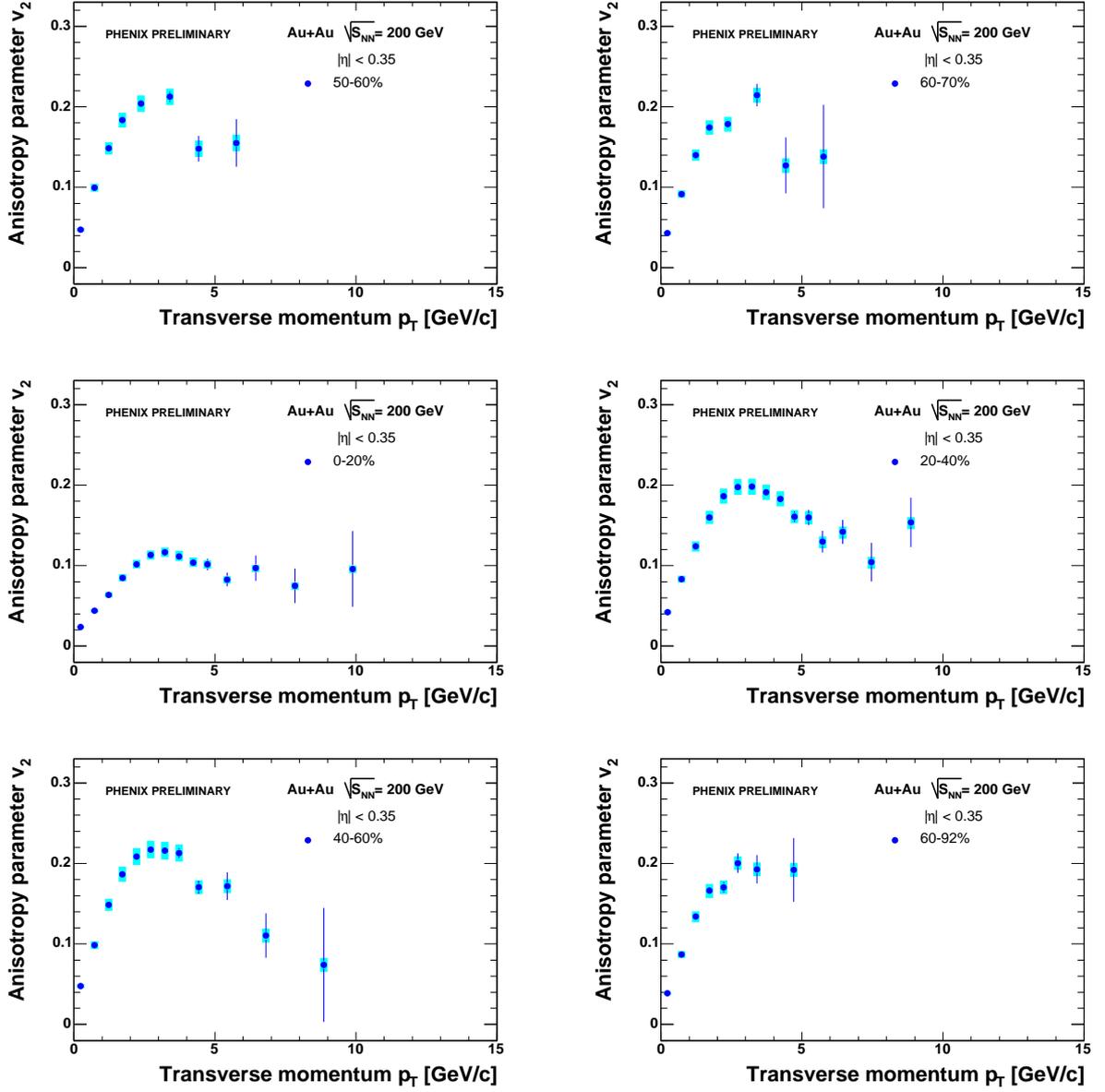
Figure 4.2: v_2 for inclusive charged hadrons in Au+Au at $\sqrt{s_{NN}} = 200$ GeV for the centralities indicated.
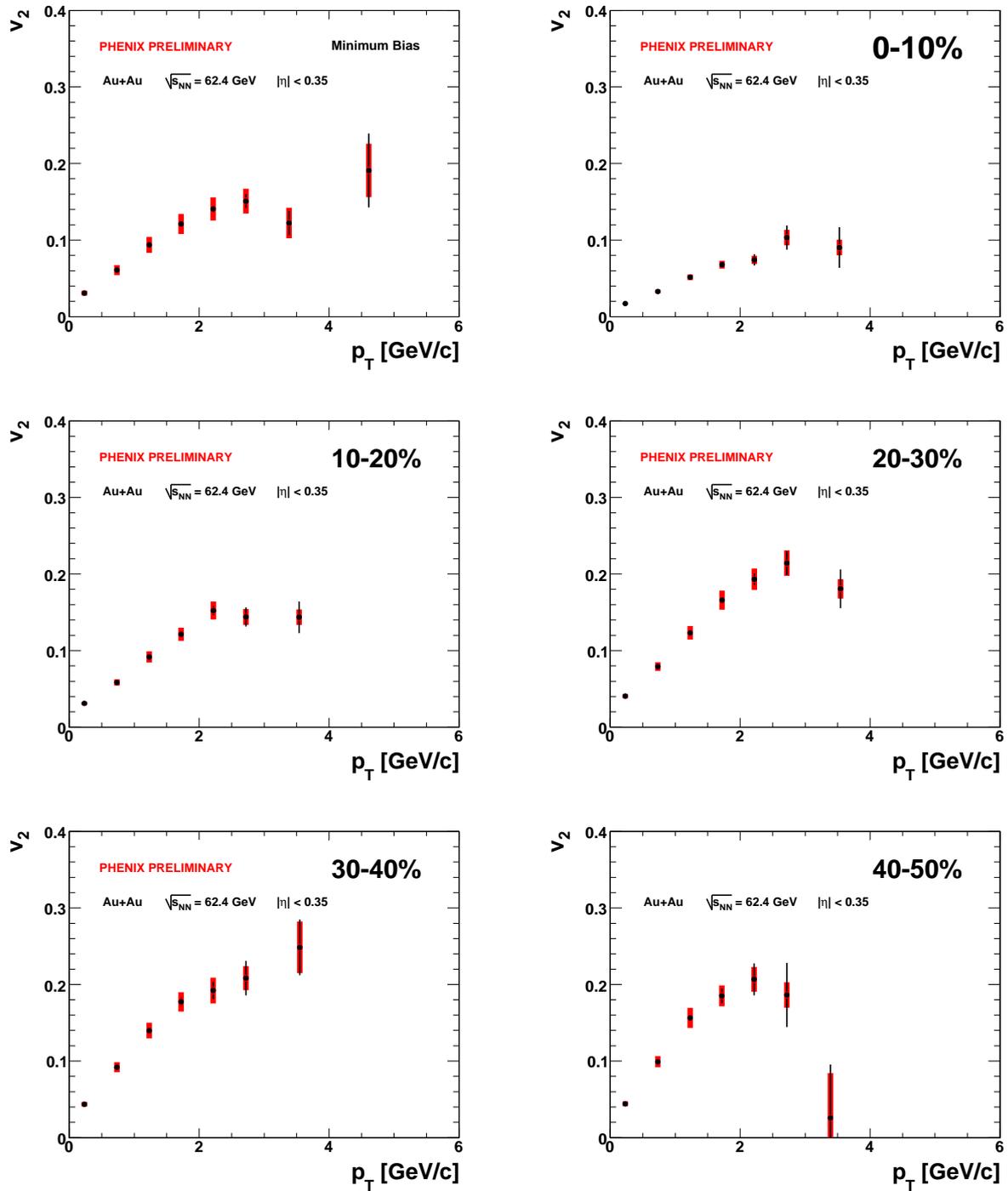
Figure 4.3: v_2 for inclusive charged hadrons in Au+Au at $\sqrt{s_{\mathrm{NN}}} = 62.4$ GeV for the centralities indicated.
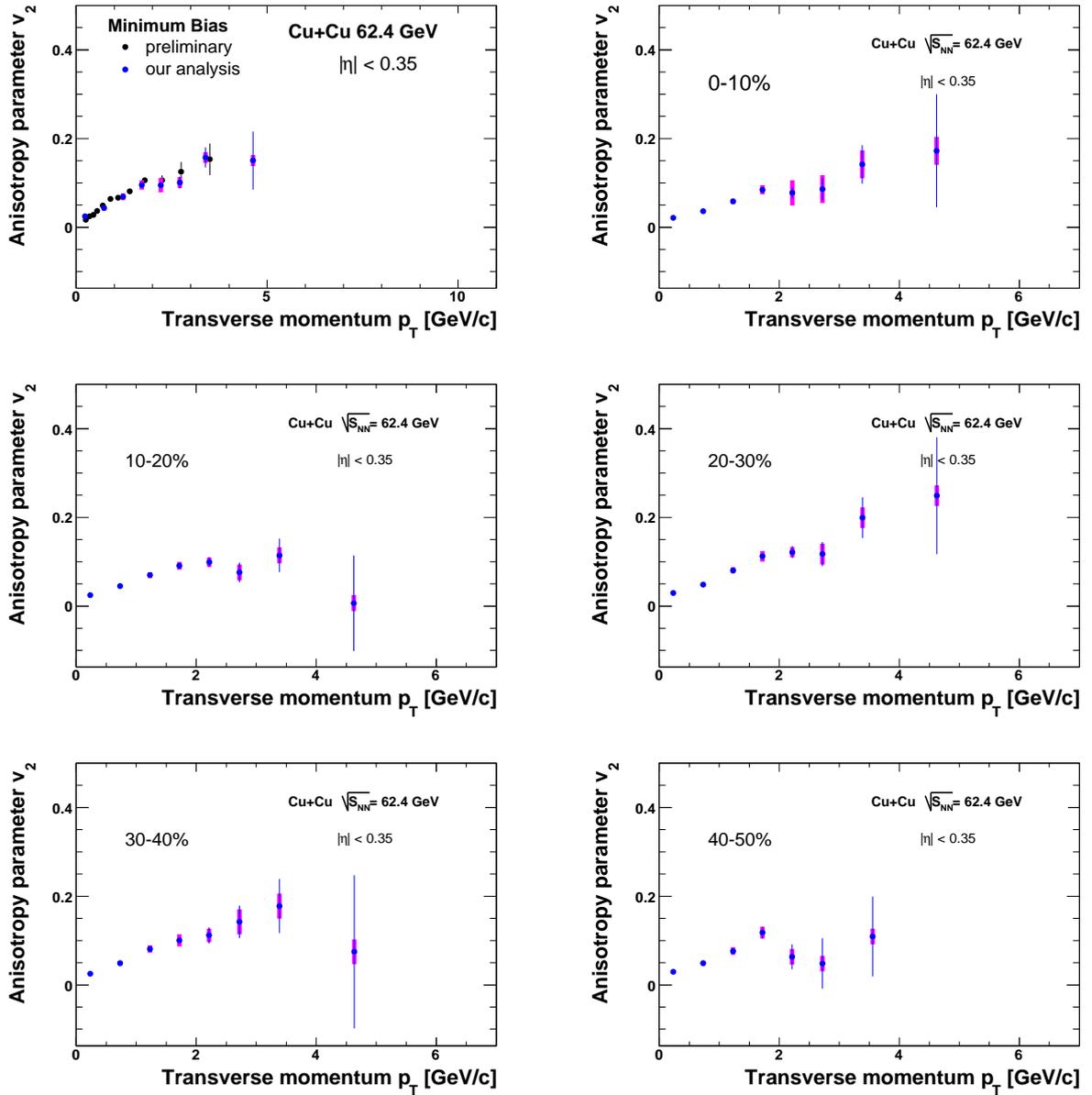
Figure 4.4: v_2 for inclusive charged hadrons in Cu+Cu at $\sqrt{s_{\mathrm{NN}}} = 62.4$ GeV for the centralities indicated.
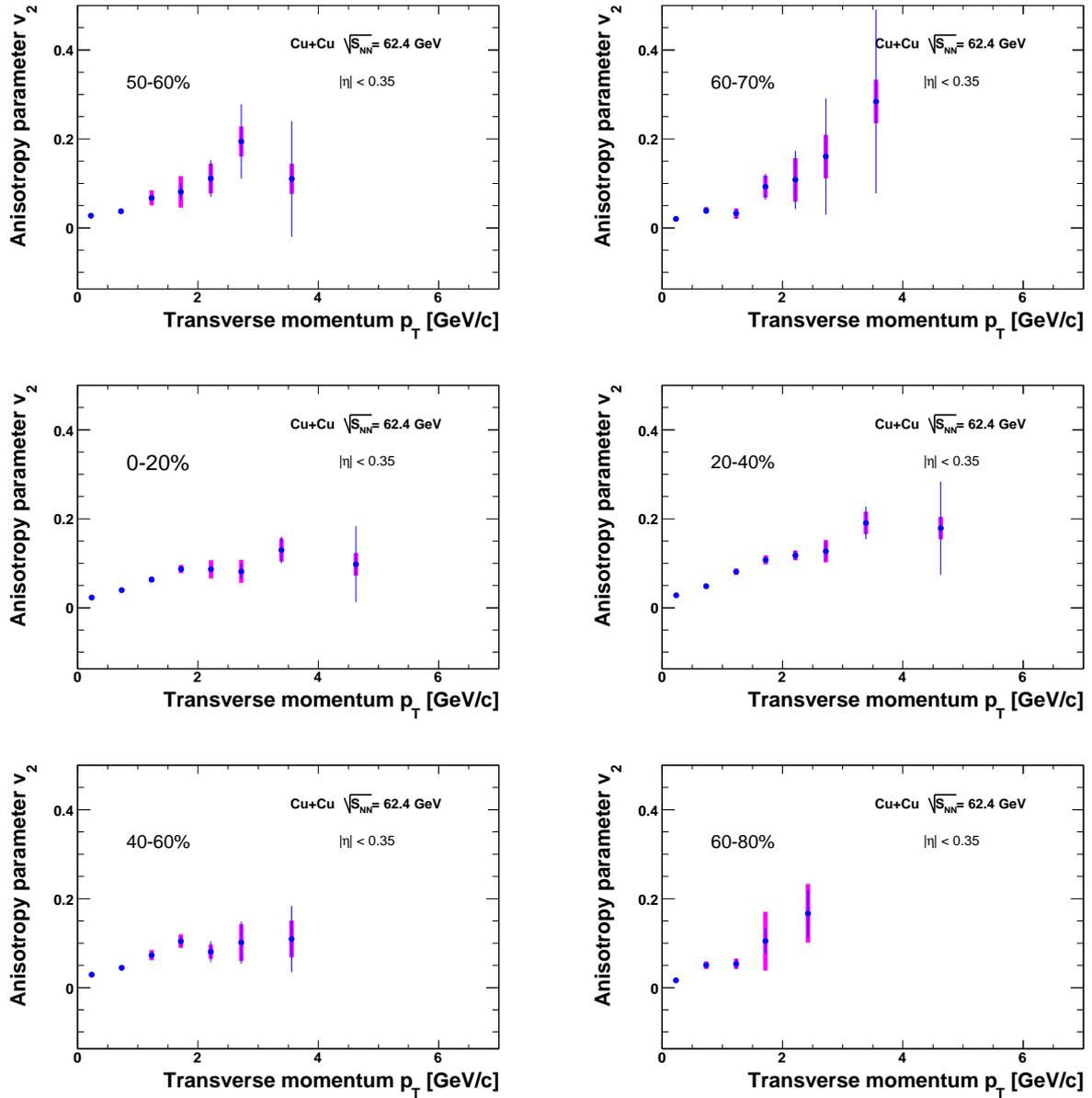
Figure 4.5: v_2 for inclusive charged hadrons in Cu+Cu at $\sqrt{s_{\mathrm{NN}}} = 62.4$ GeV for the centralities indicated.

4.2 Identified Charged Hadron v_2

In this section, we present the results of v_2 as a function of transverse momentum p_T, for charged pions, kaons and (anti-) protons ($\pi/K/p$) for the following bins in collision centrality;

1. Au+Au collisions at $\sqrt{s_{NN}} = 62.4$ GeV

   - 10-40 % (Particles and anti-particles are measured separately.)
   - 10 % step from 0 to 50 % ; 0-10, 10-20, 20-30, 30-40, 40-50 %

2. Cu+Cu collisions at $\sqrt{s_{NN}} = 200$ GeV

   - 10 % step from 0 to 50 % ; 0-10, 10-20, 20-30, 30-40, 40-50 %

The charged particles are identified by TOF and EMCal.

4.2.1 Measured v_2 in Au+Au Collisions at the Energy of $\sqrt{s_{NN}} = 62.4$ GeV

Figure 4.6 shows p_T dependence of v_2 for $\pi^\pm$, $K^\pm$, $p+\bar{p}$ emitted from Au+Au collisions at $\sqrt{s_{NN}} = 62.4$ GeV. The particle identification was performed using TOF detector and EMCal. The results are presented for several bins in collision centrality: 0-10 %, 10-20 %, 20-30 %, 30-40 % and 40-50 % . The data points include both statistical and systematic errors. The lines for each point indicate the statistical errors, and the boxes are systematic errors. The tables of the results are written in Appendix C .
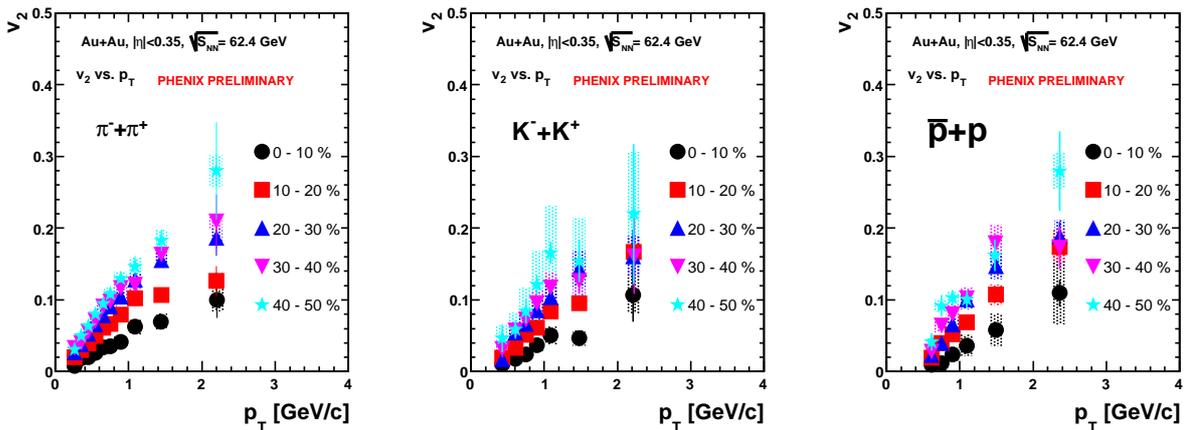
Figure 4.6: v_2 vs. p_T for charged pions, kaons and (anti-)protons emitted from Au+Au at $\sqrt{s_{NN}} = 62.4$ GeV collisions for the centralities indicated. The lines for each point indicate the statistical errors, and the boxes are systematic errors.

Comparison of Particle and Anti-Particle

Also, we measured particle and anti-particle separately in Au+Au collisions at $\sqrt{s_{NN}} = 62.4$ GeV. v_2 as a function of p_T for $\pi^\pm$, $K^\pm$, p and $\bar{p}$ emitted from 10 - 40 % is obtained as a function of p_T as shown in Figure 4.7. In the figure, the thiner lines for each point show the statistical errors and the wider lines are systematic errors. The ratio of anti-particles to particles is shown in Figure 4.8 . There is no significant difference between π^- and π^+ while one can see a few percent difference between particle and anti-particle of Kaon and proton. We cannot examine the difference minutely due to the large errors as well as the results in Au+Au at $\sqrt{s_{NN}} = 200$ GeV [64]. To see whether there is difference or not, it is expected that we can use the data from later experiment which provides much higher statistics such as Run 7 data. From present results we can only say the v_2 of particle and anti-particle agree within error. The red horizontal lines in each figure are the fitting to the ratio as constant. The tables of the results are written in Appendix C .
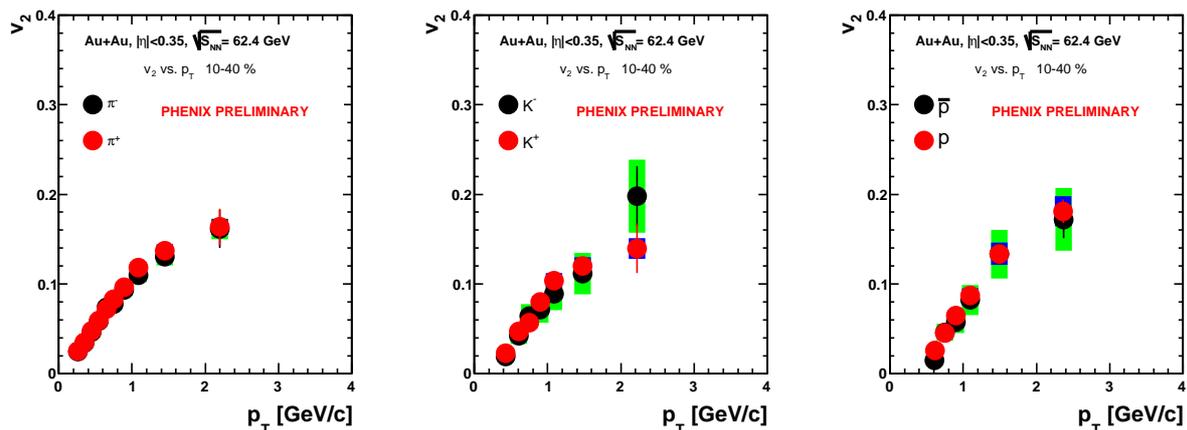
Figure 4.7: Comparison of v_2 of particle to anti-particle emitted from 10-40 % central Au+Au collisions at $\sqrt{s_{NN}} = 62.4$ GeV. The lines for each point indicate the statistical errors, and the boxes are systematic errors.

Comparison of the v_2 results with STAR data

Figure 4.9 shows the present v_2 results together with STAR results. STAR results are taken from [38]. One can see pion has a good agreement between present results and STAR results as well as kaon and proton. Λ at STAR data is also compared with proton. It seems that the v_2 of proton, anti-proton and Λ agree at mid-p_T , and this fact is consistent to the quark recombination scenario.
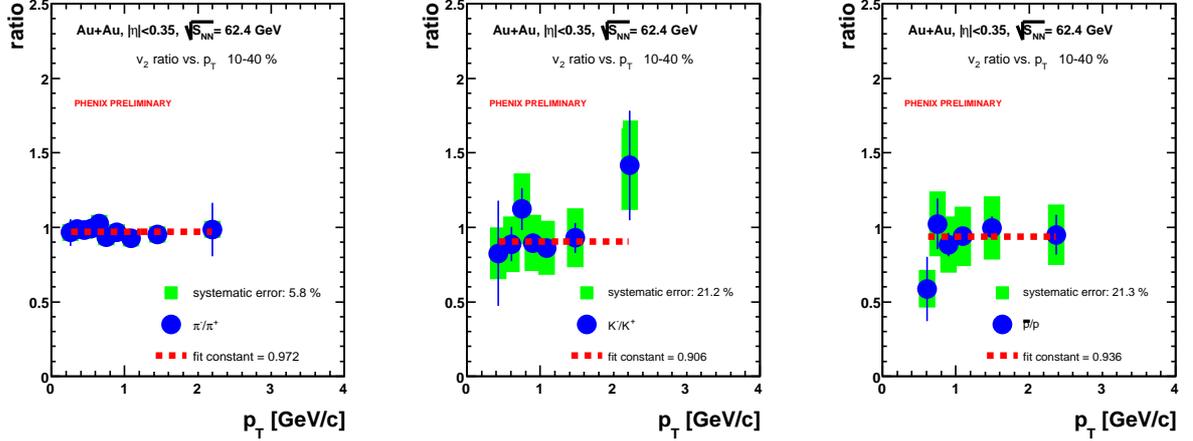
Figure 4.8: Ratio of v_2 for particle to anti-particle emitted from 10-40 % central Au+Au collisions at $\sqrt{s_{\mathrm{NN}}}$ = 62.4 GeV. The lines for each point indicate the statistical errors, and the boxes are systematic errors. The red horizontal lines in each figure are the fitting to the ratio as constant.
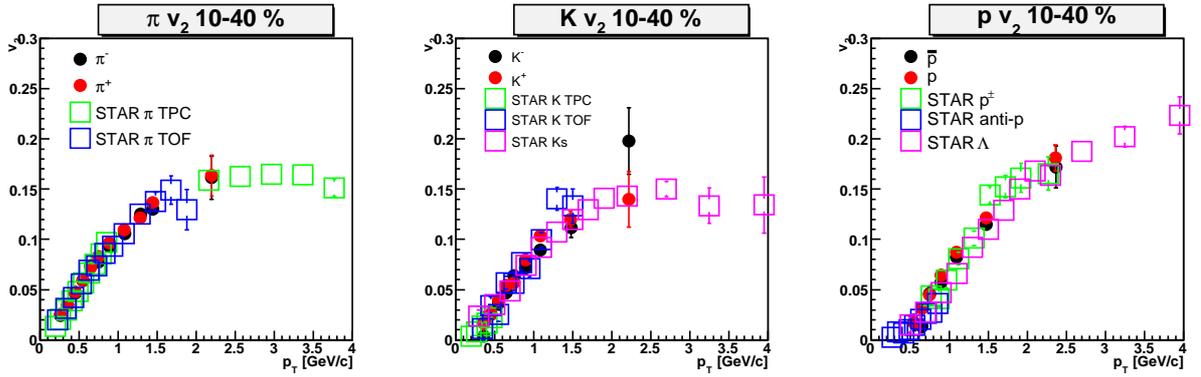
Figure 4.9: Comparison between PHENIX and STAR v_2 for 10 to 40 % in Au+Au at 62.4 GeV. Both agree well. Only statistical errors are shown in the figure. STAR results are taken from [38].

4.2.2   Measured v_2 in Cu+Cu Collisions at the Energy of $\sqrt{s_{\mathrm{NN}}} = 200$ GeV

Centrality dependence of v_2 as a function of transverse momentum p_{T} for charged pions, kaons and (anti-)protons ($\pi/K/p$) emitted from Cu+Cu collisions at $\sqrt{s_{\mathrm{NN}}} = 200$ GeV is presented in Figure 4.10. The particle identification was performed using TOF detector and EMCal. The results are presented for several bins in collision centrality: 0-10 %, 10-20 %, 20-30 %, 30-40 % and 40-50 % . The data points include both statistical and systematic errors. The lines for each point indicate the statistical errors, and the boxes are systematic errors. The tables of the results are written in Appendix C .
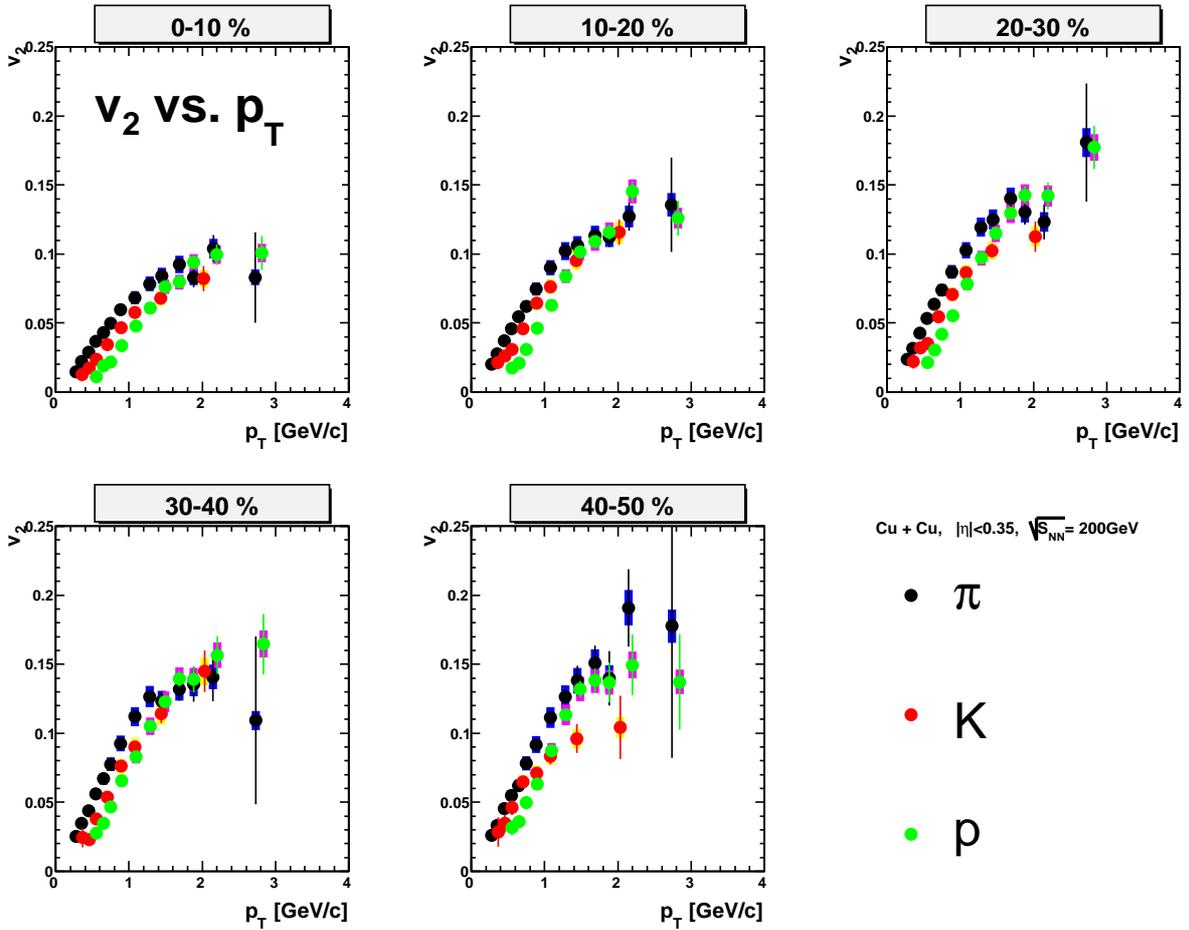
Figure 4.10: v_2 vs. p_{T} for charged pions, kaons and (anti-)protons emitted from Cu+Cu at $\sqrt{s_{\mathrm{NN}}} = 200$ GeV collisions for the centralities indicated. The lines indicate statistical errors, and the boxes indicate systematic errors.

Chapter 5

Discussion

5.1   Collision Energy Dependence

In this chapter we discuss the collision energy dependence of differential v_2 as a function of transverse momentum p_T and collision centrality for charged hadrons emitted from Cu+Cu/Au+Au collisions at $\sqrt{s_{NN}} = 62.4$ - 200 GeV. Figure 5.1 compares the centrality and p_T dependence of the v_2 for charged hadrons in Au+Au at $\sqrt{s_{NN}} = 62.4$ - 200 GeV. The triangles, boxes and circles in Figure 5.1 show v_2 as a function of the number of participants N_{part} for three p_T bins: 0.2 - 1.0, 1.0 - 2.0 and 2.0 - 4.0 GeV/c. The red and black symbols show the measurement at $\sqrt{s_{NN}} = 62.4$ and 200 GeV respectively. The results indicate a rather striking agreement in magnitudes of the v_2 values at $\sqrt{s_{NN}} = 62.4$ and 200 GeV for all measured centralities, 0 - 60 %. Figure 5.2 shows the comparison of v_2 for π/K/p as a function of p_T at $\sqrt{s_{NN}} = 62.4$ and 200 GeV. The v_2 values of 200 GeV are taken from [71]. The lines indicate the statistical errors and the boxes indicate the systematic errors at each point for both $\sqrt{s_{NN}} = 62.4$ and 200 GeV. Figure 5.3 shows the comparison of mean p_T ($\langle p_T \rangle$) between $\sqrt{s_{NN}} = 62.4$ and 200 GeV for π/K/p [63]. Both results at all measured centralities agree within the errors. Since the mean p_T of the particle spectra are the same at $\sqrt{s_{NN}} = 62.4$ and 200 GeV, v_2 values at $\sqrt{s_{NN}} = 62.4$ and 200 GeV should be the same. From the comparison of v_2 measured at SPS to RHIC ($\sqrt{s_{NN}} = 17.2$, 62.4, 130 and 200 GeV) for the centrality cut of 13 - 26 % and p_T selections of 1.75 and 0.65 GeV/c, the magnitude of v_2 significantly increases by 50 % from SPS to RHIC energies up to $\sqrt{s_{NN}} = 62.4$ GeV while it seems to be saturated above $\sqrt{s_{NN}} = 62.4$ GeV as shown in Figure 5.4 [8] . Since the energy density estimated with Bjorken formula increases (by 30 %) over $\sqrt{s_{NN}} = 62.4$ to 200 GeV, this saturation of v_2 may imply that the matter reaches local thermal equilibrium beyond the phase transition.   Figure 5.5 compares the centrality and p_T dependence of v_2 for charged hadrons emitted from lighter colliding system: Cu+Cu collisions at $\sqrt{s_{NN}} = 62.4$ - 200 GeV. The error bars are much larger due to poor statistics for the Cu+Cu at $\sqrt{s_{NN}} = 62.4$ GeV data sample. This allows us to provide the comparison only for inclusive charged hadrons and less number of p_T bins : 0.2 - 1.0 and 1.0 - 2.0 GeV/c. There seems to be some deviation especially toward peripheral collisions.

Taking a closer look, v_2 and $\langle p_T \rangle$ for π/K/p in Au+Au seem to show small difference between $\sqrt{s_{NN}} = 62.4$ and 200 GeV especially for proton although they agree within the errors. The v_2 at $\sqrt{s_{NN}} = 62.4$ GeV is higher than that at $\sqrt{s_{NN}} = 200$ GeV at low p_T and $\langle p_T \rangle$ at $\sqrt{s_{NN}} = 62.4$ GeV is lower than that at $\sqrt{s_{NN}} = 200$ GeV. This tendency is consistent to the effect of radial
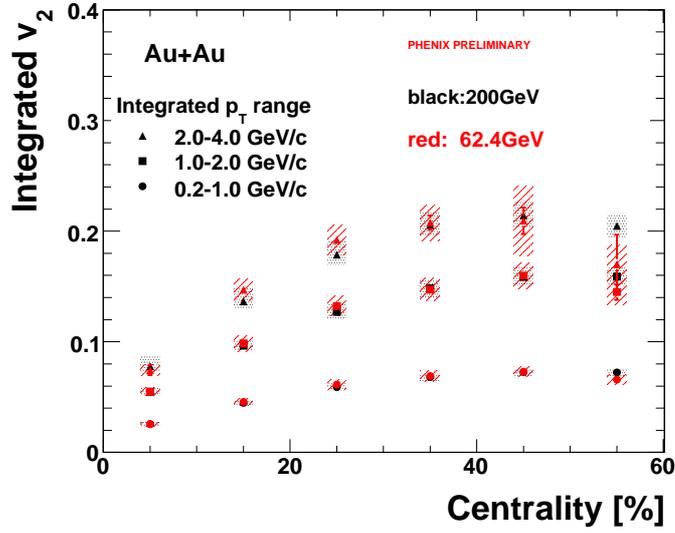
Figure 5.1: Comparison of integrated v_2 at $\sqrt{s_{NN}} = 62.4$ and 200 GeV in Au+Au. Red symbols indicate $\sqrt{s_{NN}} = 62.4$ GeV and black symbols indicate $\sqrt{s_{NN}} = 200$ GeV. Ranges of p_T integrated are 0.2 - 1.0, 1.0 - 2.0, and 2.0 - 4.0 GeV/c as shaped by circle, square and triangle, respectively. The results have a good agreement in all centralities. The bars indicate the statistical errors and the boxes indicate the systematic errors.
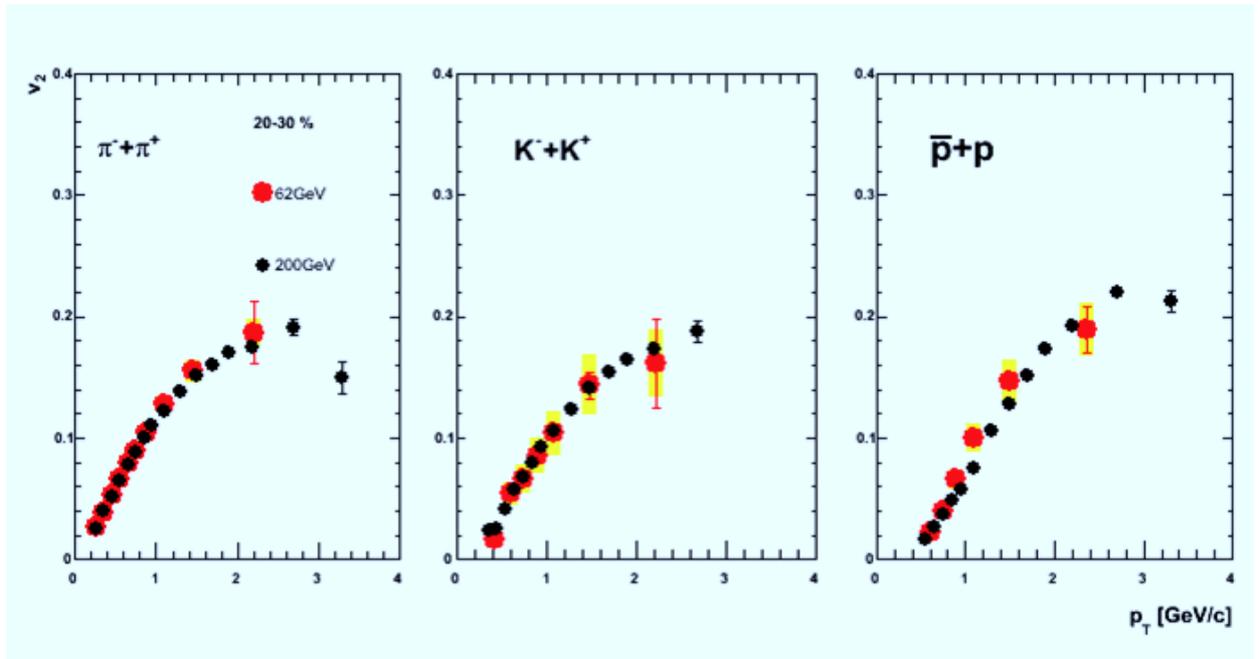
Figure 5.2: Comparison of v_2 between $\sqrt{s_{NN}} = 62$ and 200 GeV for π/K/p emitted from 20 - 30 % central Au+Au collisions. Both results for all species agree within the errors. The lines indicate the statistical errors at each point of both $\sqrt{s_{NN}} = 62.4$ and 200 GeV. The yellow boxes indicate the systematic errors at each point of $\sqrt{s_{NN}} = 62.4$ GeV.
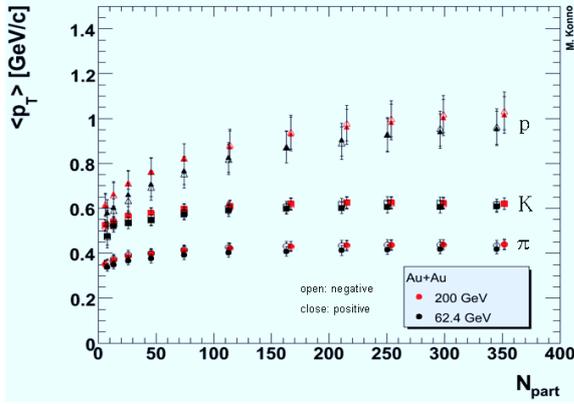
Figure 5.3: Comparison of mean p_T ($\langle p_T \rangle$) between $\sqrt{s_{NN}} = 62.4$ and 200 GeV for π/K/p. Both results at all centralities agree within the errors. The figure is taken from Reference [63] .
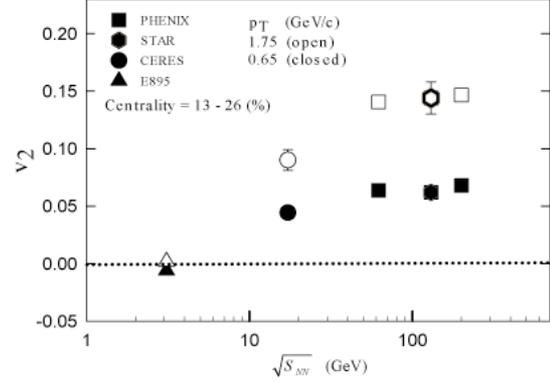
Figure 5.4: v_2 vs. $\sqrt{s_{NN}}$ measured at collision energy of $\sqrt{s_{NN}} = 17.2$ - 200 GeV for charged hadrons. Results are shown for the centrality cut of 13 - 26 % and p_T selections of 1.75 GeV/c (open symbols) and 0.65 GeV/c (closed symbols). The figure is taken from Reference [8] .

flow which is expected to become larger at higher $\sqrt{s_{NN}}$. On the other hand, the difference of v_2 for charged hadrons in Cu+Cu between $\sqrt{s_{NN}} = 62.4$ and 200 GeV has the opposite tendency, namely v_2 at $\sqrt{s_{NN}} = 62.4$ GeV is lower than that at $\sqrt{s_{NN}} = 200$ GeV. Therefore, the reason of the difference in Cu+Cu may not be the effect of flow, but it may be due to the insufficient thermalization at $\sqrt{s_{NN}} = 62.4$ GeV in Cu+Cu. This will be discussed later in Section. 5.4 after taking all scalings.

5.2 Particle Species Dependence

Comparing the present v_2 for pions, kaons and (anti-)protons (π/K/p) in Au+Au at $\sqrt{s_{NN}} = 62.4$ GeV and in Cu+Cu at $\sqrt{s_{NN}} = 200$ GeV, the scaling property such as quark number and KE_T scalings are examined in this section.

5.2.1 Quark Number Scaling

The left panel in Figure 5.6 shows v_2 vs.p_T, the middle panel is v_2/n_q (= number of quarks) vs. p_T/n_q for various hadron species emitted from 10 - 40 % central Au+Au collisions at $\sqrt{s_{NN}} = 62.4$ GeV including the results measured by STAR experiments. As we expect from the fact that the values of v_2 at $\sqrt{s_{NN}} = 62.4$ GeV and 200 GeV agree within errors in Au+Au, the v_2 for these hadrons at $\sqrt{s_{NN}} = 62.4$ GeV is consistent with the quark number scaling in Au+Au as observed at $\sqrt{s_{NN}} = 200$ GeV. Meson and baryon are scaled by the number of quarks particularly seen at mid p_T ($1.0 \leq p_T \leq 4.0$).

How about in Cu+Cu collisions at $\sqrt{s_{NN}} = 200$ GeV ? Figure 5.7 shows the v_2/n_q vs. p_T/n_q for π/K/p emitted from Cu+Cu collisions at $\sqrt{s_{NN}} = 200$ GeV for the five centrality bins: 0 - 10 %, 10 - 20 %, 20 - 30 %, 30 - 40 % and 40 - 50 %. It is found that the v_2 in Cu+Cu at $\sqrt{s_{NN}} = 200$ GeV is also consistent with the quark number scaling for most of the measured centrality bins
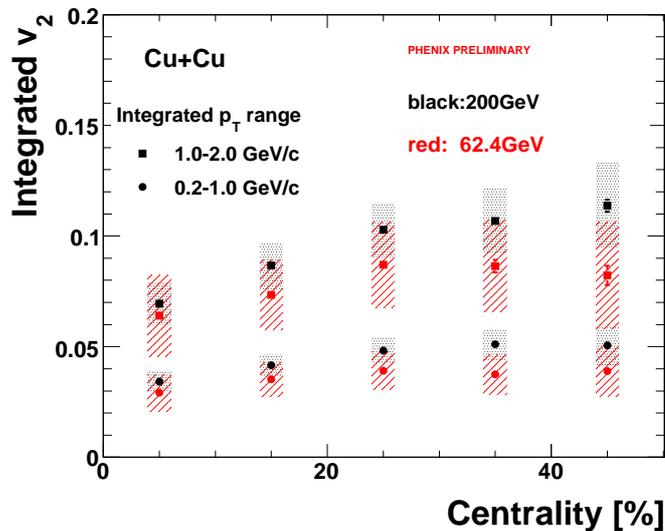
Figure 5.5: Comparison of integrated v_2 at $\sqrt{s_{\mathrm{NN}}} = 62.4$ and 200 GeV in Cu+Cu. Red symbols indicate $\sqrt{s_{\mathrm{NN}}} = 62.4$ GeV and black symbols indicate $\sqrt{s_{\mathrm{NN}}} = 200$ GeV. Ranges of p_{T} integrated are 0.2 - 1.0 and 1.0 - 2.0 GeV/c as shaped by circle and square respectively. The bars indicate the statistical errors and the boxes indicate the systematic errors.

as seen in Au+Au. Looking at the peripheral result closely, however, there are small deviation from n_{q} scaling at 40 - 50 % , especially between pion and proton. Since the statistical errors are large at the peripheral, it is difficult to conclude, but this deviation may suggest that there may be critical volume for the formation of hydrodynamical QGP phase.

5.2.2 KE_{T} Scaling

Applying both quark number scaling and KE_{T} ($= m_{\mathrm{T}}$ - m_0) scaling, various mesons and baryons of v_2/n_{q} vs. $KE_{\mathrm{T}}/n_{\mathrm{q}}$ show a universal curve in Au+Au at $\sqrt{s_{\mathrm{NN}}} = 200$ GeV at each centrality bin as shown in Figure 5.9. The right panel in Figure 5.6 shows v_2/n_{q} vs. $KE_{\mathrm{T}}/n_{\mathrm{q}}$ for π/K/p at $\sqrt{s_{\mathrm{NN}}} = 62.4$ GeV in Au+Au. The result supports the KE_{T} scaling at low p_{T} region as well as the results at $\sqrt{s_{\mathrm{NN}}} = 200$ GeV. Also, the results in Cu+Cu at $\sqrt{s_{\mathrm{NN}}} = 200$ GeV indicate that quark number and KE_{T} scalings hold at most of the centrality bins between 0 - 50 %. Deviation at peripheral collisions are also visible when plotted against KE_{T}. Figure 5.10 and 5.11 show the ratios of the v_2/n_{q} to the fitting function of these results as a function of $KE_{\mathrm{T}}/n_{\mathrm{q}}$ for π/K/p in Au+Au and Cu+Cu respectively. One can tell the deviation is seen even in Au+Au collisions. It is found that the deviation becomes larger at smaller N_{part}. The nature of this scaling will be discussed in the Section 5.5.1.

These scaling properties indicate that collective motions are created at quark level both at $\sqrt{s_{\mathrm{NN}}} = 62.4$ GeV in Au+Au and at $\sqrt{s_{\mathrm{NN}}} = 200$ GeV in Cu+Cu. Thus, these scaling properties
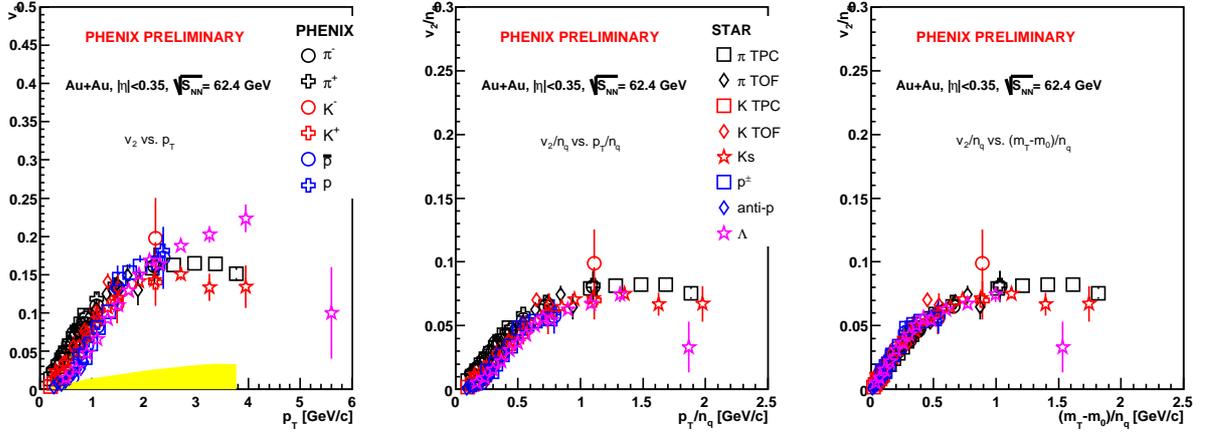
Figure 5.6: The left panel shows v_2 vs. p_T, the midle panel is v_2/n_q vs. p_T/n_q, and the right panel is v_2/n_q vs. KE_T/n_q for the indicated hadrons emitted from 10 - 40 % central Au+Au collisions in Au+Au at $\sqrt{s_{NN}} = 62.4$ GeV measured by PHENIX and STAR. The error bars of PHENIX results include both systematic and statistical errors. The error bars of STAR results show statistical errors. The yellow band around zero shows systematic error for STAR results.

of v_2 are one of the evidences for the formation of QGP.

At SPS, the result of v_2 measurement at $\sqrt{s_{NN}} = 17.2$ GeV by NA49 experiment doesn't seem to show quark number and KE_T scalings where the collision energy might be too low to create the QGP as shown in Figure 5.12 [36] [37] . Left panel in Figure 5.12 shows v_2 vs. KE_T and right panel shows v_2/n_q vs. KE_T/n_q for π^+, π^-, K_s^0, p and Λ at $\sqrt{s_{NN}} = 17.2$ GeV. This fact also support the saturation feature seen in Figure 5.4.

5.3 System Size Dependence

There are two ways to test the system size dependence for v_2. One is to change the collision centrality. The other is to change the colliding nuclei. One can control the number of participant nucleons, N_{part}, and the eccentricity, ε, of collision in both ways. In this section, we study the dependence of v_2 on collision size.

5.3.1 Au+Au Collisions vs. Cu+Cu Collisions

Comparing the measured v_2 in Au+Au and Cu+Cu collisions, v_2 of Cu+Cu collisions does not agree with that of Au+Au at the same N_{part} as shown in Figure 5.13.

Since the eccentricity, initial geometrical anisotropy, is different between Au+Au and Cu+Cu collisions at the same N_{part}, the eccentricity scaling is applied first to cancel out the effect of initial geometrical anisotropy for the four data sets, namely Au+Au at $\sqrt{s_{NN}} = 200$ GeV, Au+Au at $\sqrt{s_{NN}} = 62.4$ GeV, Cu+Cu at $\sqrt{s_{NN}} = 200$ GeV and Cu+Cu at $\sqrt{s_{NN}} = 62.4$ GeV. Eccentricity, ε, defined by the Equation 1.11, indicates the initial anisotropy of the participant nucleons. The values of ε have been calculated via a Glauber Monte Carlo using Woods-Saxon density distributions. The detail of this calculation is given in Section 3.5. Here, we use participant eccentricity, ε_{part},
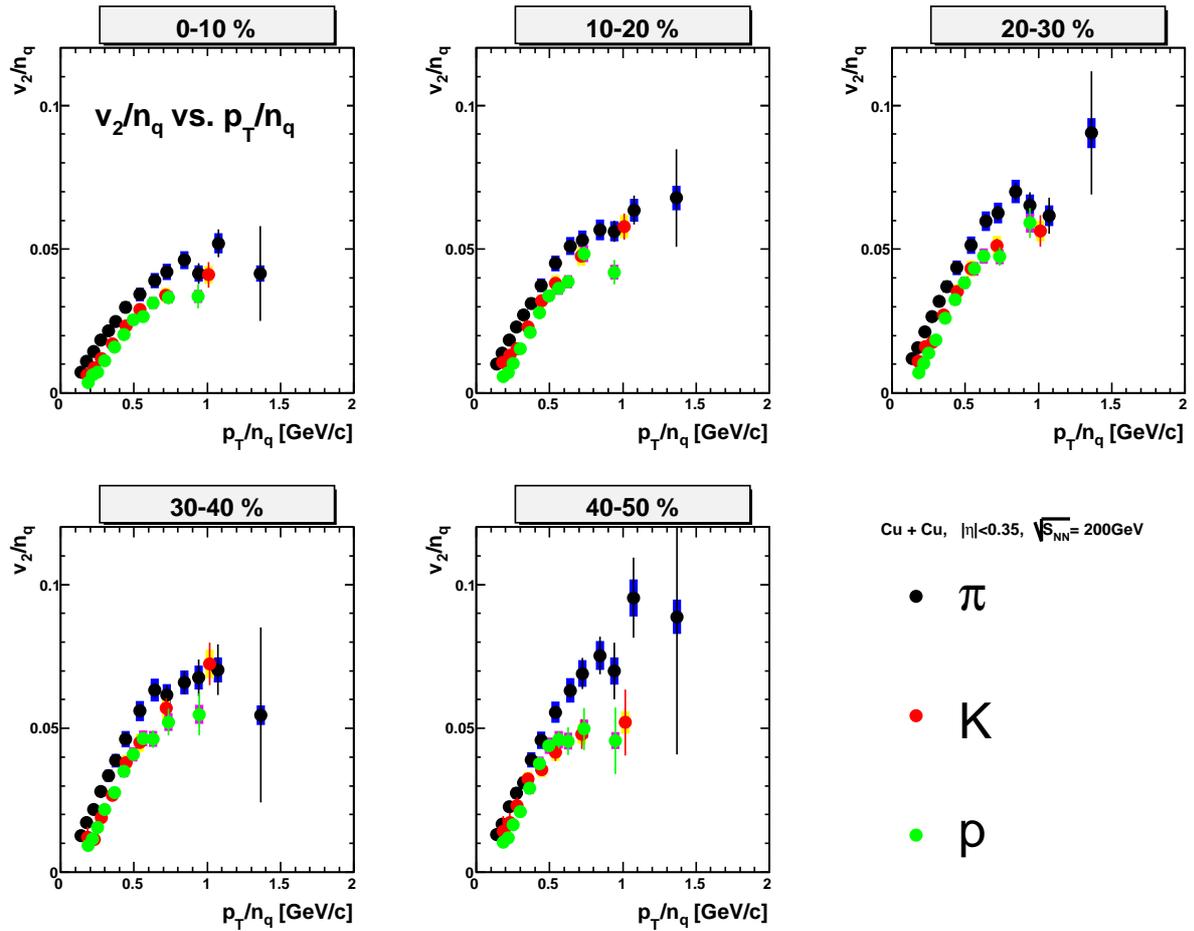
Figure 5.7: v_2/n_q vs. p_T/n_q for π/K/p in Cu+Cu at $\sqrt{s_{NN}} = 200$GeV for the centralities indicated. The lines indicate statistical errors, and the boxes indicate systematic errors.
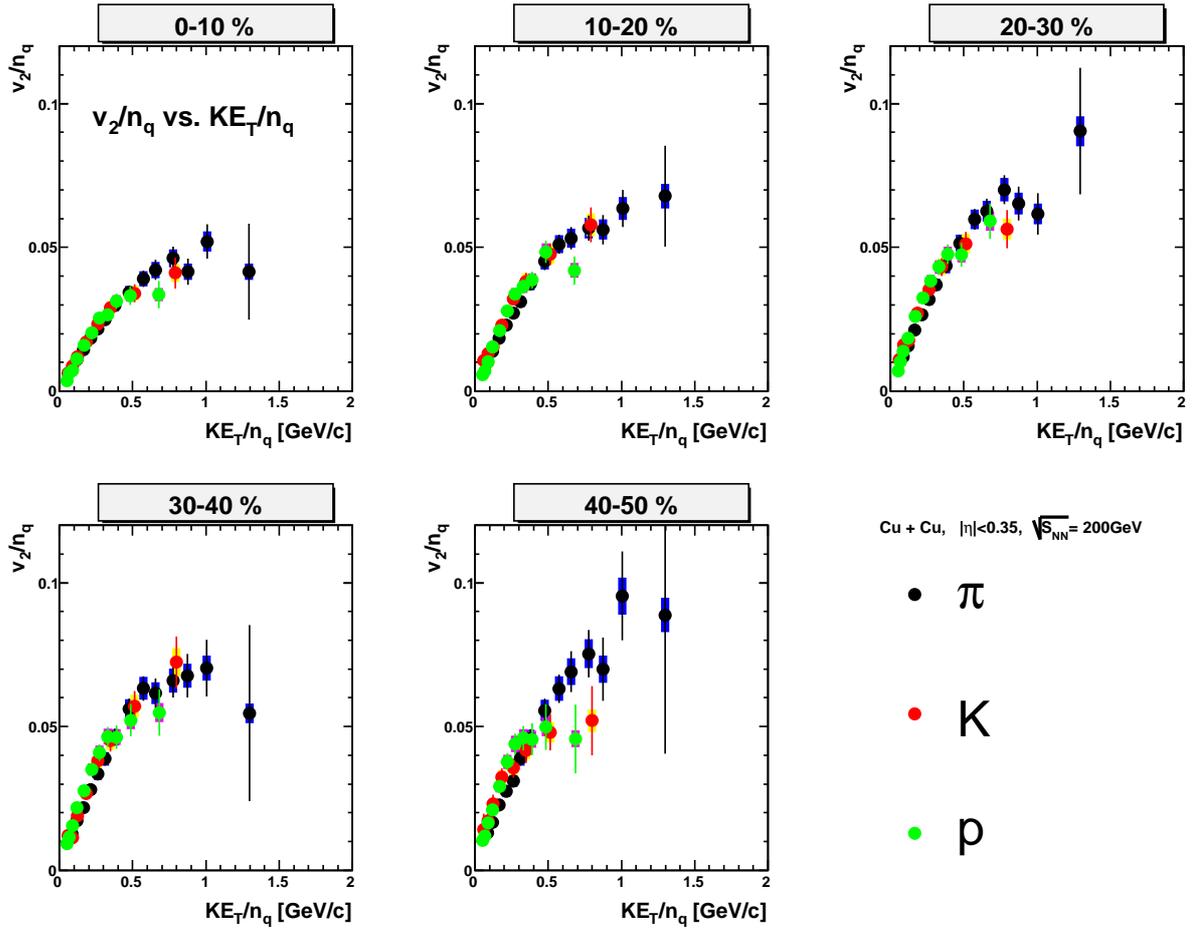
Figure 5.8: v_2/n_q vs. KE_T/n_q for $\pi/K/p$ at $\sqrt{s_{NN}} = 200$ GeV in Cu+Cu for the centralities indicated. The lines indicate the statistical errors, and the boxes indicate the systematic errors on each point.
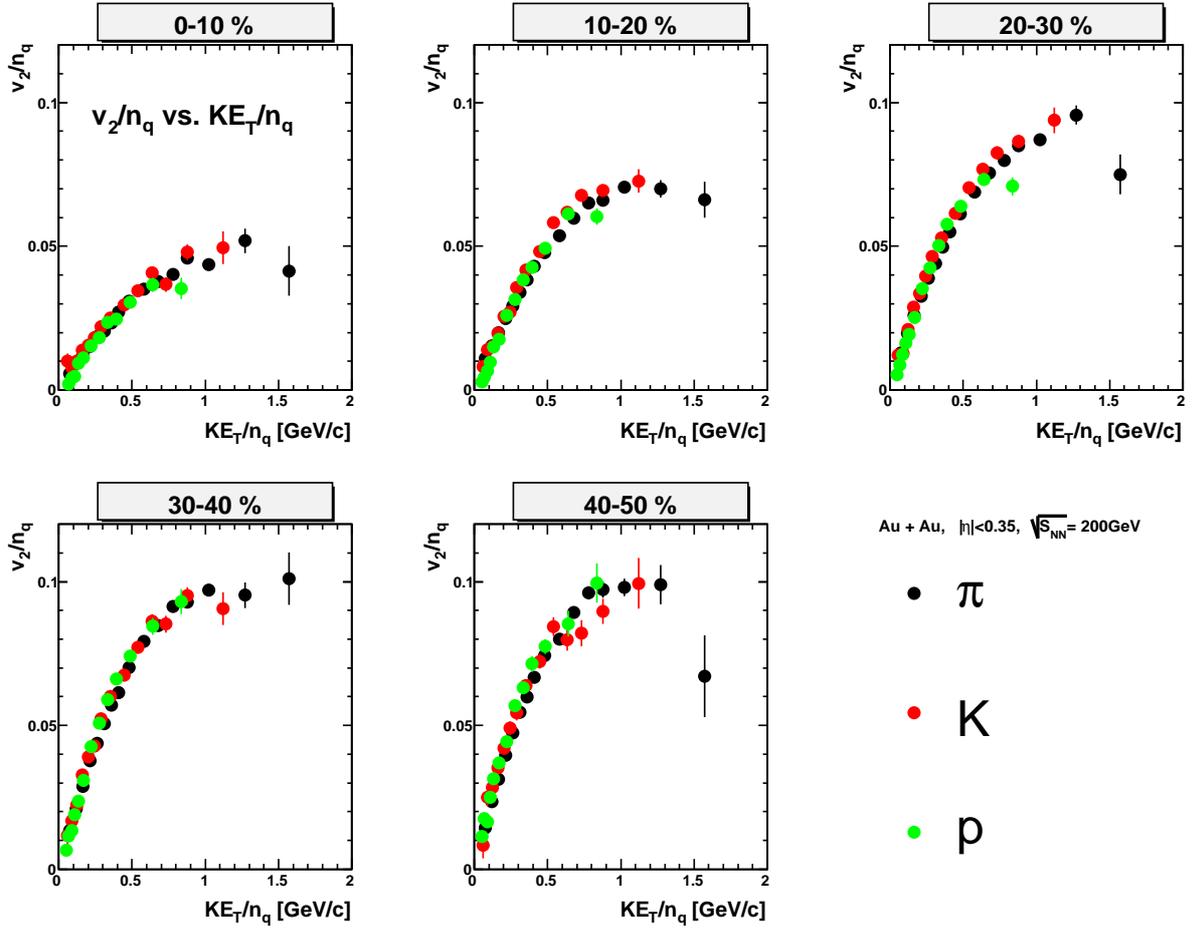
Figure 5.9: v_2/n_q vs. KE_T/n_q for π/K/p at $\sqrt{s_{NN}} = 200$ GeV in Au+Au for the centralities indicated. The lines indicate the statistical errors, and the boxes indicate the systematic errors on each point.
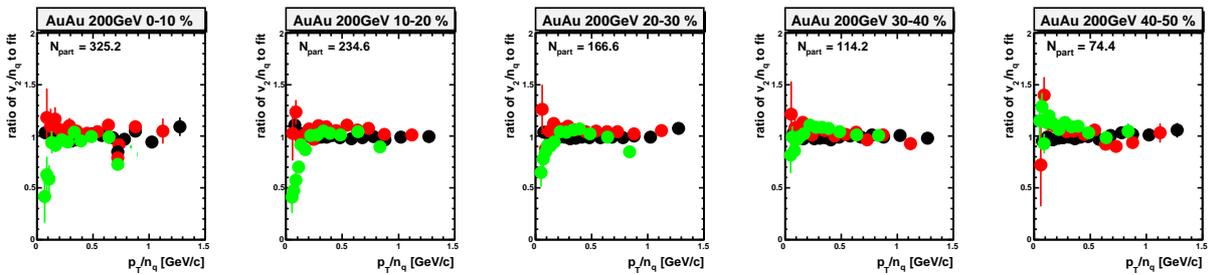
Figure 5.10: Ratio of v_2/n_q to the fitting function as a function of KE_T/n_q for π/K/p at $\sqrt{s_{NN}} = 200$ GeV in Au+Au for the centralities (N_{part}) indicated.

Figure 5.11: Ratio of v_2/n_q to the fitting function as a function of KE_T/n_q for π/K/p at $\sqrt{s_{NN}} = 200$GeV in Cu+Cu for the centralities (N_{part}) indicated.

Figure 5.12: Left panel shows v_2 vs. KE_T and right panel shows v_2/n_q vs. KE_T/n_q for π^+, π^-, K_s^0, p and Λ at $\sqrt{s_{NN}} = 17.2$ GeV in SPS-NA49 experiment [36] [37].
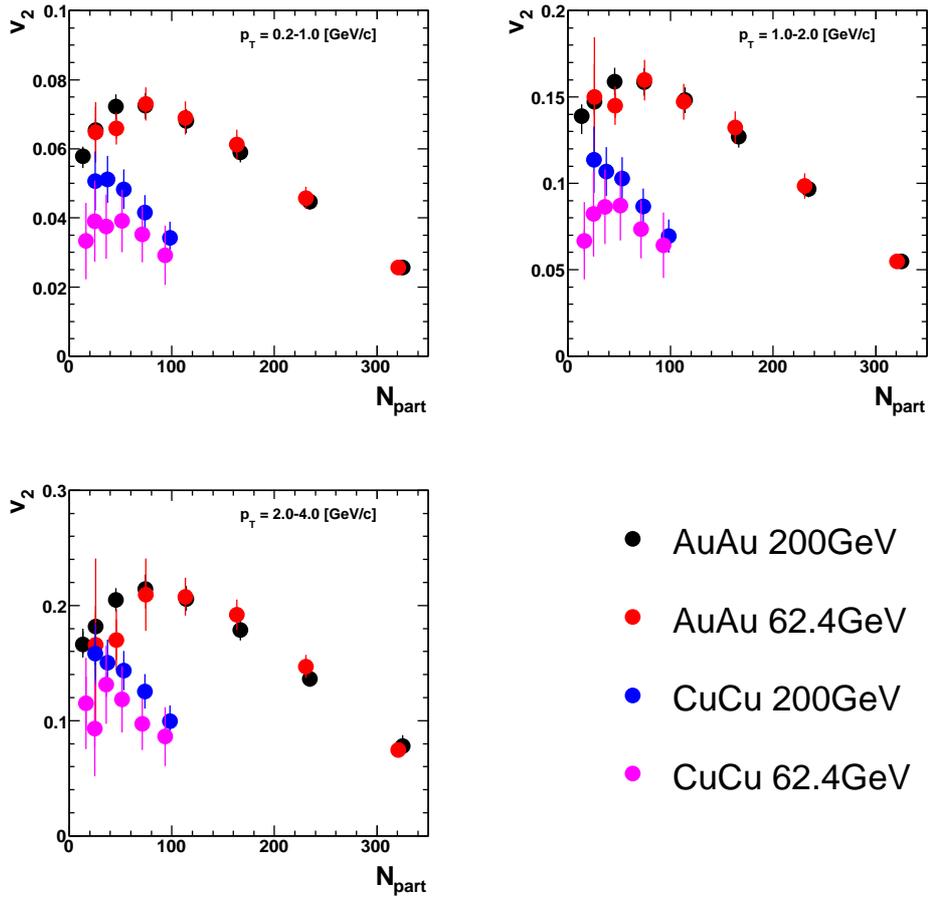
Figure 5.13: Comparison of integrated v_2 as a function of N_{part} for two collision energy and two collision systems (in Au+Au at $\sqrt{s_{\text{NN}}} = 200$ GeV, in Au+Au at $\sqrt{s_{\text{NN}}} = 62.4$ GeV, in Cu+Cu at $\sqrt{s_{\text{NN}}} = 200$ GeV and in Cu+Cu at $\sqrt{s_{\text{NN}}} = 62.4$ GeV). Ranges of p_{T} integrated are 0.2 - 1.0, 1.0 - 2.0 and 2.0 - 4.0 GeV/c from left to right and top to bottom figures respectively. Both statistical and systematic errors are included in the bars.

which takes into account the fluctuation of geometrical axes of ellipsoid. This correction becomes important in Cu+Cu due to smaller number of N_{part}. As shown in Figure 5.14 v_2 normalized by $\varepsilon_{\text{part}}$ has good agreement between Cu+Cu and Au+Au collisions at any N_{part}. The results for all three p_{T} bins (0.2 - 1.0, 1.0 - 2.0 and 2.0 - 4.0 GeV/c) show good agreements.
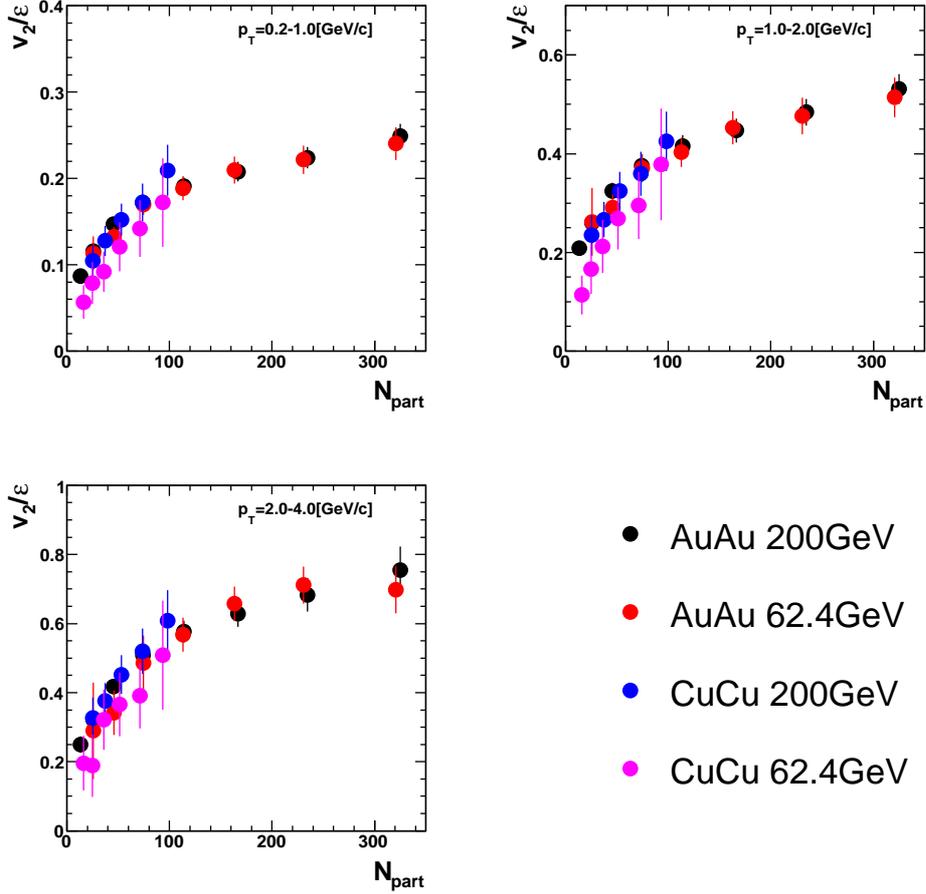
Figure 5.14: Comparison of integrated $v_2/\varepsilon_{\text{part}}$ vs. N_{part} for two collision energy and two collision systems, namely Au+Au at $\sqrt{s_{\text{NN}}} = 200$ GeV, Au+Au at $\sqrt{s_{\text{NN}}} = 62.4$ GeV, Cu+Cu at $\sqrt{s_{\text{NN}}} = 200$ GeV and Cu+Cu at $\sqrt{s_{\text{NN}}} = 62.4$ GeV). Ranges of p_{T} integrated are 0.2 - 1.0, 1.0 - 2.0 and 2.0 - 4.0 GeV/c from left to right and top to bottom figures respectively. The statistical and systematic errors from measured v_2 and the systematic errors from $\varepsilon_{\text{part}}$ are included in the bars.

5.4 Universal Scaling

5.4.1 Proposed Scaling Parameter, $N_{\text{part}}^{1/3}$

As shown in the previous section, v_2 normalized by $\varepsilon_{\text{part}}$ has good agreement between Cu+Cu and Au+Au collisions at any N_{part}, but, the ratio of $v_2/\varepsilon_{\text{part}}$ is not a constant. Figure 5.15 is the comparison of v_2 as a function of p_{T} between Au+Au and Cu+Cu at the same $\varepsilon_{\text{part}}$ bin. It is clear that v_2 is different with different N_{part} even where the $\varepsilon_{\text{part}}$ is the same.
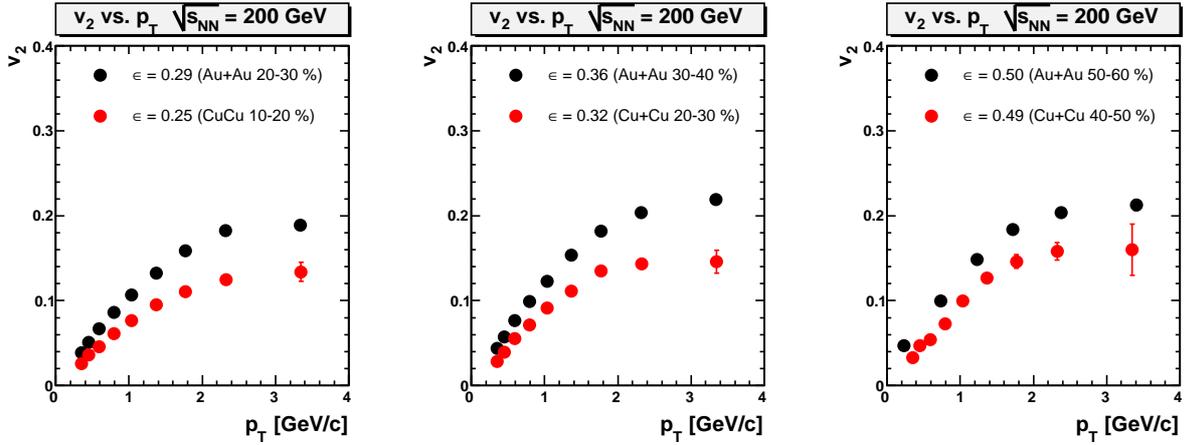
Figure 5.15: Comparison of $v_2(p_T)$ at similar ε_{part} with different collision size (Au+Au or Cu+Cu) at $\sqrt{s_{NN}} = 200$ GeV. Black symbols indicate Au+Au and red symbols indicate Cu+Cu.

We have newly found that v_2/ε_{part} is proportional to $N_{part}^{1/3}$, thus, $v_2/(\varepsilon_{part}\cdot N_{part}^{1/3})$ is independent of the collision systems. This indicates that the v_2 is determined by the initial geometrical anisotropy and the number of participants. Figure 5.16 shows the comparison with these normalization for $p_T = 0.2$ - 1.0 GeV/c. The result for $p_T = 1.0$ - 2.0 and 2.0 - 4.0 GeV/c show the same tendency as well. The results in Cu+Cu at $\sqrt{s_{NN}} = 62.4$ GeV show deviation from the universal scaling particularly at $N_{part} \leq 40$. This may indicate that the produced matter does not reach the local thermal equilibrium with the small collision system ($N_{part} \leq 40$) at $\sqrt{s_{NN}} = 62.4$ GeV, and the v_2 of Cu+Cu does not reach the value expected in fully equilibrated system although they have large error to discuss the difference precisely.

5.4.2   Universal Scaling of v_2

We have finally obtained a universal v_2 curve which can scale for all v_2 measured at RHIC. As same as the results in Au+Au at 200 GeV, v_2 in Au+Au at 62.4 GeV and in Cu+Cu at 200 GeV are mostly consistent with quark number(n_q) scaling and KE_T ($= m_T$ - m_0) scaling for all measured centrality bins (0-50 %). In addition to the fact that v_2 does not depend on collision energy at RHIC energies, applying the four scalings (quark number scaling, KE_T scaling, eccentricity scaling and $N_{part}^{1/3}$ scaling), normalized v_2 as the function of p_T show a universal curve as shown in Figure 5.17. This figure includes the data in Au+Au at $\sqrt{s_{NN}} = 200$ GeV, in Au+Au at $\sqrt{s_{NN}} = 62.4$ GeV and in Cu+Cu at $\sqrt{s_{NN}} = 200$ GeV at five centrality bins for 0 - 50 % as 10 % step at each system. There are 45 curves. Applying polinorminal fit, we obtaines χ^2/NDF = 2.1 with errors. If we apply $N_{coll}^{1/3}$ scaling to same data sets instead of $N_{part}^{1/3}$ scaling, we obtain $\chi^2/NDF = 5.3$, therefore, the $N_{part}^{1/3}$ is better scale factor than $N_{coll}^{1/3}$.
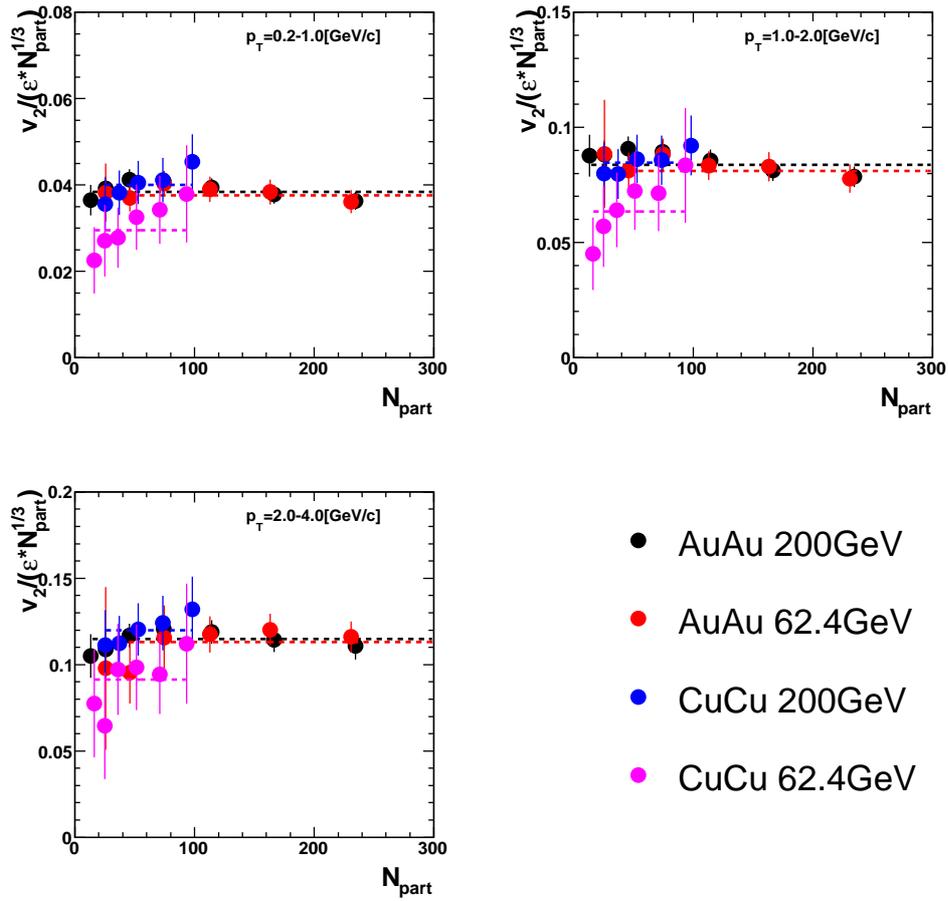
Figure 5.16: Comparison of integrated $v_2/(\varepsilon_{\mathrm{part}} \cdot N_{\mathrm{part}}^{1/3})$ as a function of N_{part} for two collision energies and two collision systems, namely Au+Au at $\sqrt{s_{\mathrm{NN}}} = 200$ GeV, Au+Au at $\sqrt{s_{\mathrm{NN}}} = 62.4$ GeV, Cu+Cu at $\sqrt{s_{\mathrm{NN}}} = 200$ GeV and Cu+Cu at $\sqrt{s_{\mathrm{NN}}} = 62.4$ GeV. Ranges of p_{T} integrated are 0.2 - 1.0, 1.0 - 2.0 and 2.0 - 4.0 GeV/c from left to right and top to bottom figures respectively. The all errors from measured v_2, $\varepsilon_{\mathrm{part}}$ and N_{part} are included in the bars.
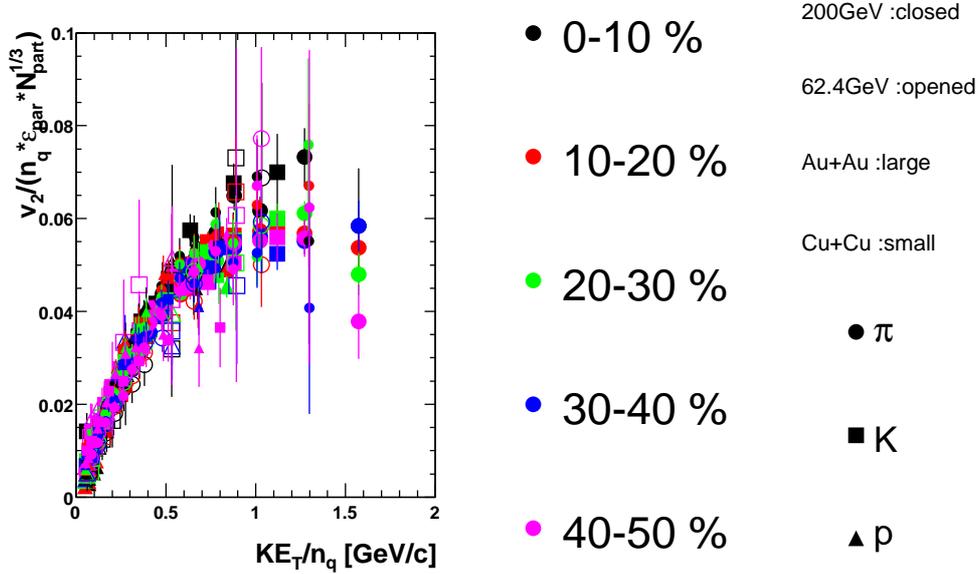
Figure 5.17: $v_2/(\varepsilon_{\mathrm{part}}\cdot N_{\mathrm{part}}^{1/3}\cdot n_{\mathrm{q}})$ vs. $KE_{\mathrm{T}}/n_{\mathrm{q}}$ for $\pi/\mathrm{K/p}$ in Au+Au at $\sqrt{s_{\mathrm{NN}}}$ = 200 GeV, in Au+Au at $\sqrt{s_{\mathrm{NN}}}$ = 62.4 GeV and in Cu+Cu at $\sqrt{s_{\mathrm{NN}}}$ = 200 GeV at five centrality bins for 0 - 50 % as 10 % step at each system. There are 45 curves. Applying polinorminal fit, χ^2/NDF is 2.1.

5.5   Interpretation with Models

5.5.1   Blast-wave Model

To understand the universal scaling behavior, in particular $N_{\mathrm{part}}^{1/3}$ dependence of v_2, we examine hydrodynamical model, namely Blast-wave model. With this model one can extract dynamical properties of the matter especially at the freeze-out (Section 1.3.3). This model is similar to the freeze-out configuration obtained from hydrodynamical model but the physical parameters of the configuration are treated as free parameters. The model has two free parameters, which are the radial flow velocity (β_{T}) and the freeze-out temperature (T_{fo}). We use both the p_{T} spectra and the v_2 data together to fit both results at the same time by this model.

The procedure for the fitting is following.

1) Re-plotting the measured p_{T} spectra , which is taken from [63], weighted by the measured $v_2(p_{\mathrm{T}})$, we obtain the azimuthal dependence of the p_{T} distribution.

2) From this distribution, we obtain p_{T} spectra in plane and out-of plane separately. Figure 5.19 shows inclusive spectra and in plane and out-of plane spectra which are weighted by v_2 for $\pi/\mathrm{K/p}$. Thus, p_{T} spectra with respect to the reaction plane can be obtained with proper resolution correction of the azimuthal angle, ϕ. Figure 5.18 shows v_2 as a function of p_{T} for $\pi/\mathrm{K/p}$ with polynomial fitting by which inclusive spectra is weighted.

3) We apply the Blast-wave fitting function, Equation 1.13, to the spectra at azimuthal angle, ϕ, with respect to the reaction plane. The p_{T} spectra of $\pi/\mathrm{K/p}$ are fitted, and β_{T} and T_{fo} are obtained for each data set at ϕ . The past study teaches us that we need to use the proper p_{T} region (π: 0.6 - 1.2 GeV/c, K: 0.4 - 1.4 GeV/c, p: 0.6 - 1.7 GeV/c) in the fitting to minimize the

contribution from resonance decays for low p_T cut off and to reject hard component of spectra for high p_T cut off ($m_T - m_0 \leq 1.0$ GeV/c) [65] [63] .   Figure 5.20 shows the $\langle \beta_T \rangle$ and the T_{fo} as a
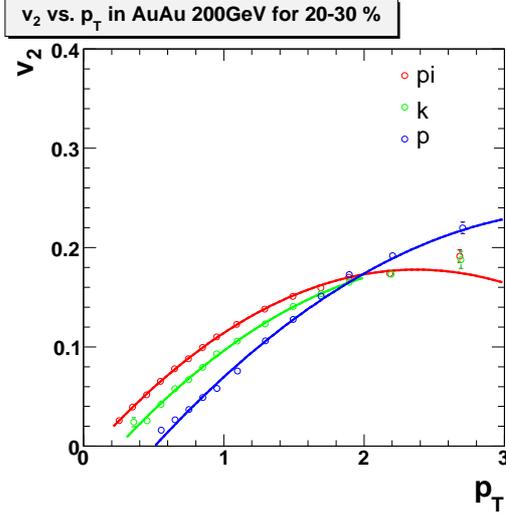
Figure 5.18: Measured v_2 vs. p_T for $\pi/K/p$ with polynomial fitting
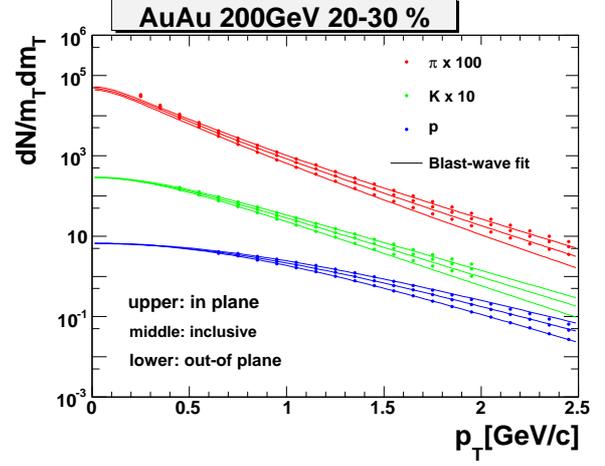
Figure 5.19: The p_T spectra of inclusive, in plane and out-of plane re-plotting the measured inclusive p_T spectra weighted by measured $v_2(p_T)$ with Blast-wave fit.
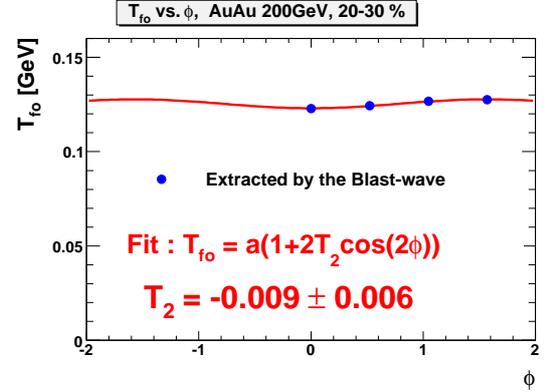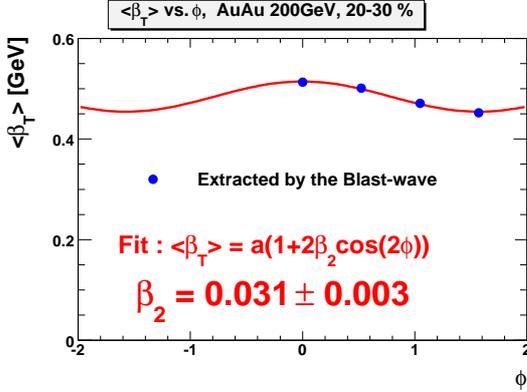
Figure 5.20: Azimuthal dependence of $\langle \beta_T \rangle$ (left) and T_{fo} (right) obtained by Blast-wave fit for 20 - 30 % centrality in Au+Au at $\sqrt{s_{NN}} = 200$ GeV.

function of the azimuthal angle, ϕ , for 20 - 30 % in Au+Au at $\sqrt{s_{NN}} = 200$ GeV. The $\langle \beta_T \rangle$ shows clear modulation while T_{fo} has much less azimuthal dependence. To study the N_{part} dependence of these modulation extracting the $\langle \beta_T \rangle$ and T_{fo} in plane and out-of plane separately, β_{T2} and T_{fo2} are calculated by following equations ;

$$\beta_{T2} = (\langle \beta_{Tin} \rangle - \langle \beta_{Tout} \rangle)/(2(\langle \beta_{Tin} \rangle + \langle \beta_{Tout} \rangle)), \tag{5.1}$$

$$T_{fo2} = (T_{foin} - T_{foout})/(2(T_{foin} + T_{foout})). \tag{5.2}$$

The $\beta_{T2}(T_{fo2})$ indicates the amplitude of second harmonic of the $\langle \beta_T \rangle(T_{fo})$ azimuthal distribution, which are the same as β_2 (T_2) in Figure 5.20 where the azimuthal distributions can be written by $a(1 + 2b_2 \cos \phi)$.

The β_{T} and T_{fo} for inclusive, in plane and out-of plane are extracted separately in Cu+Cu and Au+Au at $\sqrt{s_{\mathrm{NN}}} = 200$ GeV. Figure 5.21 shows the $\langle\beta_{\mathrm{T}}\rangle$ vs. N_{part} (left) and T_{fo} vs. N_{part} (right) in Cu+Cu and Au+Au. The $\langle\beta_{\mathrm{T}}\rangle$ and T_{fo} depend on the system size of collision and do not depend on the collision nuclei (Au or Cu). The χ^2 of the fitting shows that the $\langle\beta_{\mathrm{T}}\rangle$ and T_{fo} in plane have better agreement between Au+Au and Cu+Cu than that of inclusive and out of plane, and we have not figure out the reason for this behavior. This might be understood as the effect of less-interacting-participants, so called "Corona effect" in core-corona model explained in [9]. In this model the "effective" N_{part} to produce the flow velocity in Au+Au is smaller than that in Cu+Cu at the same N_{part} due to the difference of ellipticity. Therefore, re-plotting the $\langle\beta_{\mathrm{T}}\rangle$ and T_{fo} as a function of "effective" N_{part} , the values in Au+Au and Cu+Cu may be able to agree in case of inclusive spectra other than in case of in plane, but one needs the further detailed study to understand this behavior.
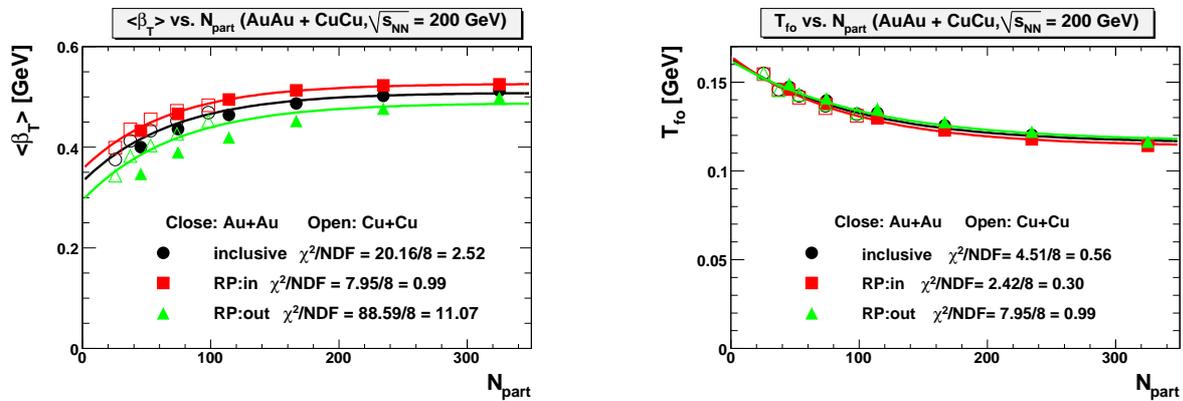
Figure 5.21: The $\langle\beta_{\mathrm{T}}\rangle$ (left) and T_{fo} (right) as a function of N_{part} for in and out-of plane at Cu+Cu and Au+Au in $\sqrt{s_{\mathrm{NN}}} = 200$ GeV. The lines indicate the fitting by the exponential function to the Au+Au and Cu+Cu points together in these figures. The χ^2 of the fitting shows that the $\langle\beta_{\mathrm{T}}\rangle$ and T_{fo} in plane have better agreement between Au+Au and Cu+Cu than that of inclusive and out of plane.
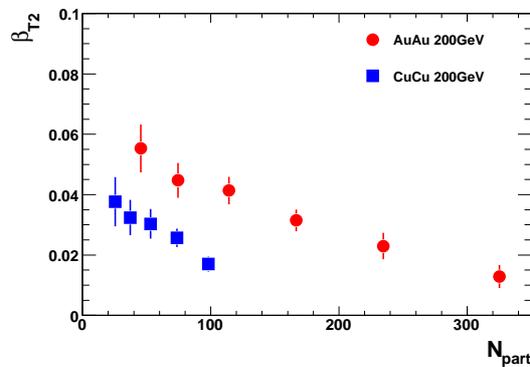
Figure 5.22: β_{T2} vs. N_{part} at Cu+Cu and Au+Au in $\sqrt{s_{\mathrm{NN}}} = 200$ GeV
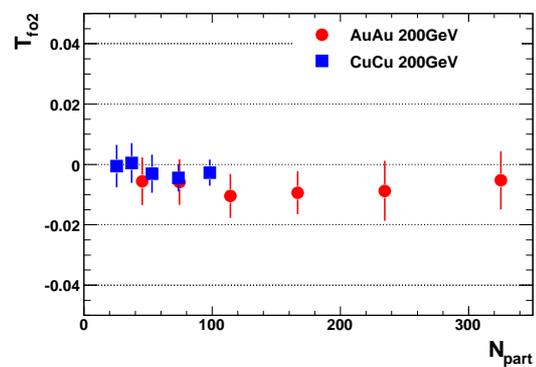
Figure 5.23: T_{fo2} vs. N_{part} at Cu+Cu and Au+Au in $\sqrt{s_{\mathrm{NN}}} = 200$ GeV

Figure 5.22 shows the β_{T2} vs. N_{part} and Figure 5.23 shows the T_{fo2} vs. N_{part}. As explained above, β_{T2} has a finite value while T_{fo2} is mostly consistent to be zero within error. This indicates that the difference of the β_{T}, namely β_{T2}, produces the v_2. This β_{T2} is, of course, not same between Cu+Cu and Au+Au at same N_{part} since the initial geometrical eccentricity which produces the pressure gradient, therefore, produces the β_{T2}, is different between Cu+Cu and Au+Au at same N_{part}. With scaled by $\varepsilon_{\mathrm{part}}$, $\beta_{\mathrm{T2}}/\varepsilon_{\mathrm{part}}$ becomes constant for Cu+Cu and Au+Au as shown in Figure 5.24. Also, we have newly found that $\beta_{\mathrm{T2}}/\varepsilon_{\mathrm{part}}$ as a function of N_{part} becomes a constant at $N_{\mathrm{part}} \geq 40$. Therefore, β_{T} is determined only by $\varepsilon_{\mathrm{part}}$. Since v_2 is proportional to β_{T2} in this Blast-wave model when the other possible parameters are all fixed, v_2 should be scaled by participant eccentricity. However, as shown in Figure 5.14, it is not happened to the measured v_2 results. This implies that v_2 is not determined by only β_{T2} but also by other effect. This can be due to the other parameter, T_{fo}, which is the thermal freeze-out temperature of the particle production. The higher T_{fo} makes p_{T} spectra flatter and it makes v_2 smaller with fixed β_{T2}.
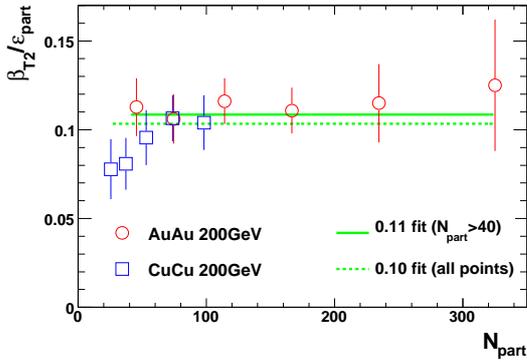
Figure 5.24: $\beta_{\mathrm{T2}}/\varepsilon_{\mathrm{part}}$ vs. N_{part} at Cu+Cu and Au+Au in $\sqrt{s_{\mathrm{NN}}} = 200$ GeV
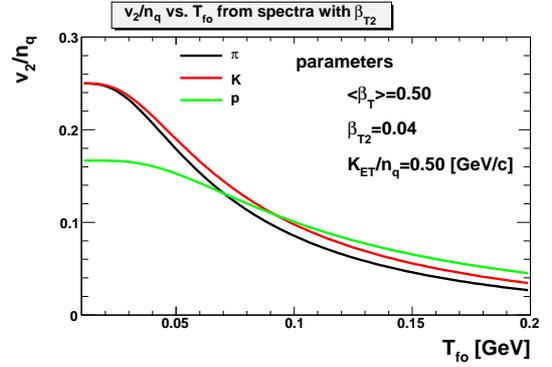
Figure 5.25: The v_2/n_{q} vs. T_{fo} by the Blast-wave calculation with fixed parameters ($\langle\beta_{\mathrm{T}}\rangle$ =0.5, β_{T2} =0.12, $KE_{\mathrm{T}}/n_{\mathrm{q}} = 0.5$ GeV/c).

5.5.2 Radial Flow Effect Relative to KE_{T} Scaling

Figure 5.26 and 5.27 are the comparison of the measured v_2 to the v_2 calculated by the spectra functions obtained by the Blast-wave fitting. The figures show v_2 vs. p_{T} for π/K/p in $\sqrt{s_{\mathrm{NN}}} = 200$ GeV at Au+Au and Cu+Cu. One can see that the fitting works well at low p_{T} region for all measured centralities, and this tells us that the radial flow in the Blast-wave model is able to reproduce the mass dependence of v_2 at low p_{T}. Therefore, the KE_{T} scaling can be understood as the radial flow effect. Also, in this Blast-wave framework, v_2/n_{q} is calculated as a function of T_{fo} as shown in Figure 5.25 with fixing the parameters to reasonable values ($\langle\beta_{\mathrm{T}}\rangle$ =0.5, β_{T2} =0.12, $KE_{\mathrm{T}}/n_{\mathrm{q}} = 0.5$ GeV/c) and changing only T_{fo}. In the temperature region (T_{fo} =0.10 - 0.15 GeV) of the measured spectra, it can be seen that KE_{T} scaling approximately hold. In this figure, going to peripheral from central, finite deviation are expected, and v_2 for proton becomes larger than that for pion. This deviation has same tendency as what can be seen in Figure 5.10 and Figure 5.11 . This may indicate that KE_{T} scaling is accidentally hold for this N_{part} region. For detailed study to conclude it, the same measurement will be useful in LHC energy ($\sqrt{s_{\mathrm{NN}}} = 5.5$ TeV) .
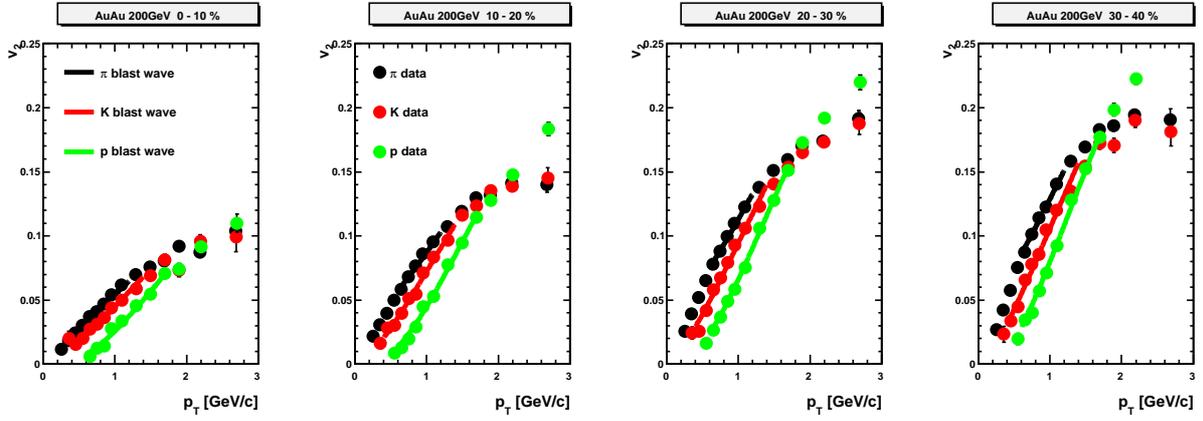
Figure 5.26: v_2 vs. p_{T} for $\pi/\mathrm{K}/\mathrm{p}$ with Blast-wave fitting at Au+Au in $\sqrt{s_{\mathrm{NN}}} = 200$ GeV. The circles indicate the measured v_2, and the lines are the v_2 calculated by the fitting.
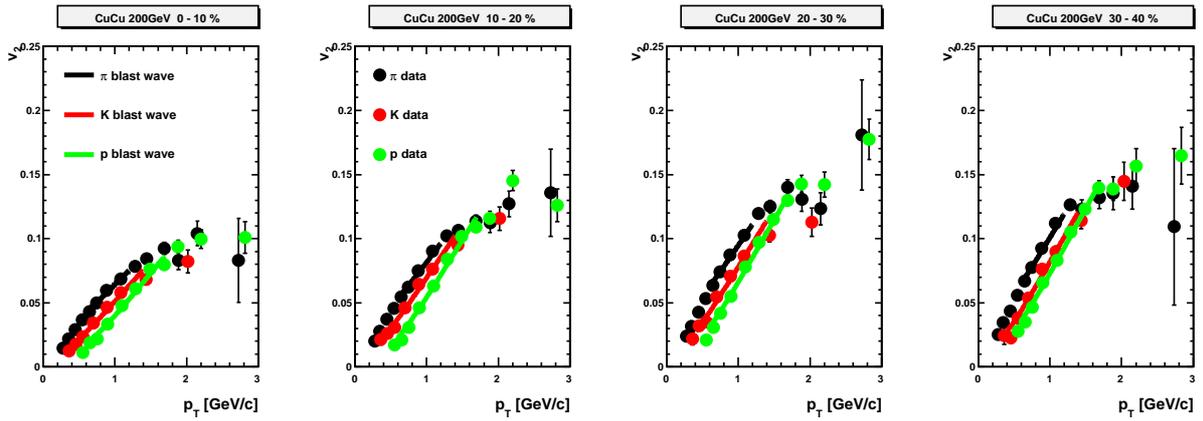
Figure 5.27: v_2 vs. p_{T} for $\pi/\mathrm{K}/\mathrm{p}$ with Blast-wave fitting at Cu+Cu in $\sqrt{s_{\mathrm{NN}}} = 200$ GeV. The circles are measured v_2, and the lines are the v_2 calculated by the fitting.

5.5.3 Adiabatic Expansion

At the most central collision in Au+Au, $\langle \beta_{\mathrm{T}} \rangle$ is $\sim 0.5c$, and T_{fo} is ~ 120 MeV with inclusive spectra as shown in Figure 5.21 . When the collision system is larger, namely N_{part} is larger, the thermal freeze-out temperature, T_{fo}, is lower and the radial flow velocity, β_{T}, is larger. Figure 5.29 taken from [63] shows the comparison of the chemical freeze-out temperature to the thermal freeze-out temperature as a function of N_{part}. The chemical freeze-out temperature, which is calculated by the statistical model [63] [66], is ~ 160 MeV and is mostly independent of the system size while the thermal freeze-out temperature is relatively lower and depending on the system size. This indicates that the matter expands for some time from chemical freeze-out to thermal freeze-out and this further expansion makes temperature lower. There is a calculation result which show the time (t_{fo}) to freeze-out increases proportionally to $N_{\mathrm{part}}^{1/3}$ as shown in Figure 5.28 . The data are given by [63] . The calculation is based on a simple adiabatic expansion model assuming ideal gas ($\mathrm{P} = \frac{1}{3}\epsilon$, P: pressure, ϵ: energy density) with thermodynamic relations. This model includes longitudinal expansion with the velocity of light and radial expansion with flow velocity extracted by Blast-wave fitting. The model defines that the matter freezes out thermally when the mean free path is equal to the radial size of the expanding matter. The calculation fixes that the freeze-out time at the most central collision is 10 fm/c . The time and the freeze-out temperature for the other centrality bins are compared with the model prediction as shown in Figure 5.28 and 5.29 respectively. As a result of this model calculation, the centrality dependence of freeze-out temperature is explained only by the dependence of system size (N_{part}). The central collision takes a longer time to freeze out than peripheral collision due to larger N_{part}. Since T_{fo} is lower with larger N_{part} due to the longer freeze-out time, v_2 at the freeze-out is expected to become larger with larger N_{part}. Therefore, N_{part} dependence of v_2 can be explained as the change of T_{fo} which related to N_{part}. In summary, p_{T} spectra and v_2 as a function of N_{part} can be understood as thermal nature.
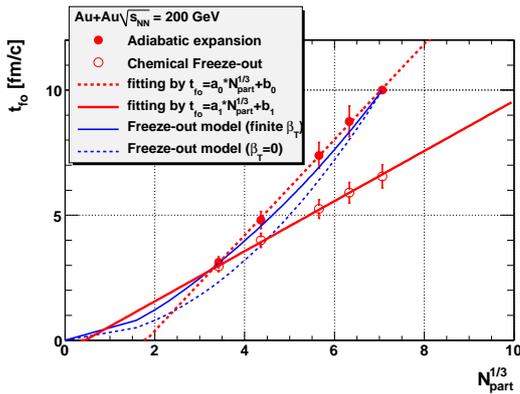
Figure 5.28: Freeze out time vs. $N_{\mathrm{part}}^{1/3}$ calculated with an adiabatic expansion model taken from [63] .
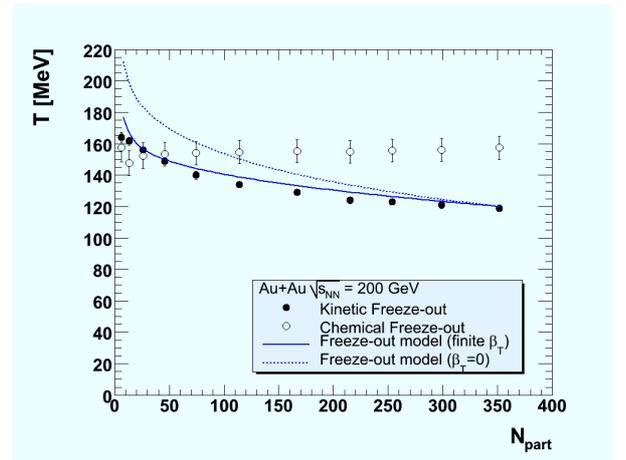
Figure 5.29: Freeze out temperature as a function of N_{part} by spectra measurement taken from [63].

Chapter 6

Conclusion

Systematic study of elliptic anisotropy has been done for charged hadrons in ultra-relativistic heavy ion collisions. Since the elliptic anisotropy in the momentum phase space is transferred from the geometrical anisotropy of the initial collisional region by the pressure gradient, the v_2 has been expected to be sensitive to the early stage of the collisions. Therefore, it is important to measure the v_2 in order to understand the underlying collision dynamics in heavy ion collisions.

We have measured the strength of the elliptic anisotropy, v_2, for inclusive charged hadron and identified charged hadrons (mainly $\pi/\mathrm{K/p}$) in Au+Au and Cu+Cu collisions at $\sqrt{s_{\mathrm{NN}}} = $ 200 and 62.4 GeV and studied the dependence on collision energy, species and centrality. The data sets were taken in Run-4 and Run-5 periods by PHENIX at RHIC. The great capability of particle identification by Electro-Magnetic Calorimeter and Time of Flight Counter provides the measurement of v_2 for various hadron species.

This systematic study gives the following features. Comparing between $\sqrt{s_{\mathrm{NN}}} = 200$ and 62.4 GeV, we found that v_2 as a function of the transverse momentum, p_{T}, has a good agreement at all measured centralities in Au+Au. The fact that there is no significant collision energy dependence of the anisotropy over this range in Au + Au collision indicates that the matter reaches local thermal equilibrium at RHIC energy.

As same as the results at $\sqrt{s_{\mathrm{NN}}} = 200$ GeV in Au+Au collisions, v_2 as a function of p_{T} for various hadron species are scaled by quark number particularly at $\sqrt{s_{\mathrm{NN}}} = 62.4$ GeV in Au+Au collision and at $\sqrt{s_{\mathrm{NN}}} = 200$ GeV in Cu+Cu particularly in the intermediate transverse momentum region ($p_{\mathrm{T}} = 1$ - 4 GeV/c). This scaling property indicates that the matter flows with quark-like degrees of freedom, and therefore, it can be one of the strong evidences for the formation of the QGP matter.

Also, the results of these two data sets are consistent to KE_{T} scaling. The small deviation from KE_{T} scaling can be seen for both Au+Au and Cu+Cu collisions, and the tendency of this deviation is independent of the collision nuclei, and only dependents on the number of participants, N_{part}. This tendency can be represented by Blast-wave calculation which is based on hydrodynamical model, and it indicates that KE_{T} scaling is the result of the radial flow effect and is accidentally hold for this N_{part} region. For detailed study to conclude it, the same measurement will be useful at LHC energy ($\sqrt{s_{\mathrm{NN}}} = 5.5$ TeV) .

Comparing Au+Au to Cu+Cu collision, v_2 scaled by participant eccentricity ($\varepsilon_{\mathrm{part}}$) at same N_{part} shows a good agreement. This indicates that the effect on the v_2 by initial geometrical anisotropy of the participant almond shape can be subtracted by eccentricity scaling. This fact

suggests the produced matter reaches the local thermal equilibrium, and is consistent with the interpretation from result of the energy comparison. On the other hand, since v_2 scaled by $\varepsilon_{\mathrm{part}}$ is not a constant at different N_{part}, v_2 is not determined only by $\varepsilon_{\mathrm{part}}$ in spite of the previous expectation.

Through this systematic study, we have newly found that $v_2/\varepsilon_{\mathrm{part}}$ is proportional to $N_{\mathrm{part}}^{1/3}$. Taking account for these all scalings, "$v_2/n_{\mathrm{q}}/\varepsilon_{\mathrm{part}}/N_{\mathrm{part}}^{1/3}$ vs. $KE_{\mathrm{T}}/n_{\mathrm{q}}$" has a universal curve. This indicates that v_2 is determined by not only the initial geometrical anisotropy but also the initial participant size, N_{part}.

To understand how this N_{part} effects on the v_2 value, we compare the Blast-wave model, which is based on hydrodynamical model containing essential freeze-out features, to the v_2 and p_{T} spectra data at the same time. The thermal freeze-out temperature (T_{fo}) and radial flow velocity (β_{T}) are extracted in plane and out-of plane separately using the Blast-wave model fitting procedure. While T_{fo} is the same between in plane and out-of plane within the errors, the β_{T} is clearly different between in plane and out-of plane. Since v_2 comes from the difference between in and out-of plane, the β_{T} is the parameter which makes v_2.

It is also found that β_{T2}, which is the amplitude of β_{T} in azimuthal distribution, is proportional to $\varepsilon_{\mathrm{part}}$ at $N_{\mathrm{part}} \geq 40$. Therefore, the $\varepsilon_{\mathrm{part}}$ determines the β_{T2}. In the Blast-wave frame work, the β_{T2} is proportional to v_2 when the other parameters are all fixed. Since v_2 is not proportional to the $\varepsilon_{\mathrm{part}}$ on the experimental results, v_2 is not determined only by β_{T2}, but also other parameter, T_{fo}. As a result of the comparison, the thermal freeze-out temperature, T_{fo}, is lower at more central collisions. The lower T_{fo} makes the slope of p_{T} spectra steeper, and it makes v_2 larger. Assuming the simple adiabatic expansion with β_{T} and T_{fo} which is extracted by the Blast-wave calculation, it is found that a time to take for the thermal freeze-out increases with the larger system size of collision (larger N_{part}) due to the thermal nature based on hydro-dynamical behavior.

As a results of this systematic study of v_2, we conclude that the matter reaches thermal equilibrium and the QGP is created at RHIC energy. The initial geometrical eccentricity determines the β_{T2} which makes v_2. The larger collision system takes longer to freeze out thermally and becomes lower temperature at freeze out, which makes v_2 larger. The $N_{\mathrm{part}}^{1/3}$ scaling indicates that the v_2 is evolving within a finite time before freeze-out which is related to the collision size.

Appendix A

Comparison with Hydrodynamical Model

Figure A.1 and A.2 show the comparison of the measured v_2 for pion (π) to that of hydrodynamical calculation in Au+Au collisions at $\sqrt{s_{NN}} = 200$ and 62.4 GeV respectively for two centrality bins, 20 - 30 % and 40 - 50 %. The black points indicate v_2 obtained by the calculation, and the red points are measured v_2. Figure A.3 is the comparison of measured v_2 for π with that of the hydrodynamical calculation at $\sqrt{s_{NN}} = 200$ GeV in Cu+Cu for two centrality bins, 0 - 10 % and 20 - 30 %. The black points indicate v_2 obtained by the calculation. The red and green points are measured v_2. The centrality of the calculation in the right panel of Figure A.3 is between 0-10 % and 10-20 %, therefore, the black symbols should be between red and green symbols when the measurement and the simulation agree. The results of this hydrodynamical calculation are done by Dr. Hirano assuming the formation of QGP fluid and hadron gas with Glauber initial condition. The detail of the calculation is explained in [17] [18] . At $\sqrt{s_{NN}} = 200$ and 62.4 GeV in Au+Au collisions these figures show that the experimental measurement and the model calculation have a good agreement while v_2 in Cu+Cu at $\sqrt{s_{NN}} = 200$ GeV does not agree between the measurement and the calculation.

This difference between the measurement and the calculation in Cu+Cu may be because the initial geometrical eccentricity (ε) used in this calculation is different from that at the experiment. In the real collision, the eccentricity is so-called "participant eccentricity" ($\varepsilon_{\mathrm{part}}$) which includes the participant fluctuation while this simulation uses so-called "standard eccentricity" ($\varepsilon_{\mathrm{stand}}$) which does not include the effect of the participant fluctuation. This effect becomes larger at smaller system such as Cu+Cu compared with Au+Au. Figure A.4, A.5 and A.6 show the comparison of measured $v_2/\varepsilon_{\mathrm{part}}$ with calculated $v_2/\varepsilon_{\mathrm{stand}}$ for π at these three data sets. Normalizing by corresponding eccentricities, v_2 of data and hydrodynamical calculation agree beautifully not only in Au+Au but also in Cu+Cu. For proton, however, measured $v_2/\varepsilon_{\mathrm{part}}$ and calculated $v_2/\varepsilon_{\mathrm{stand}}$ do not agree as well as these for π as shown in Figure A.7.
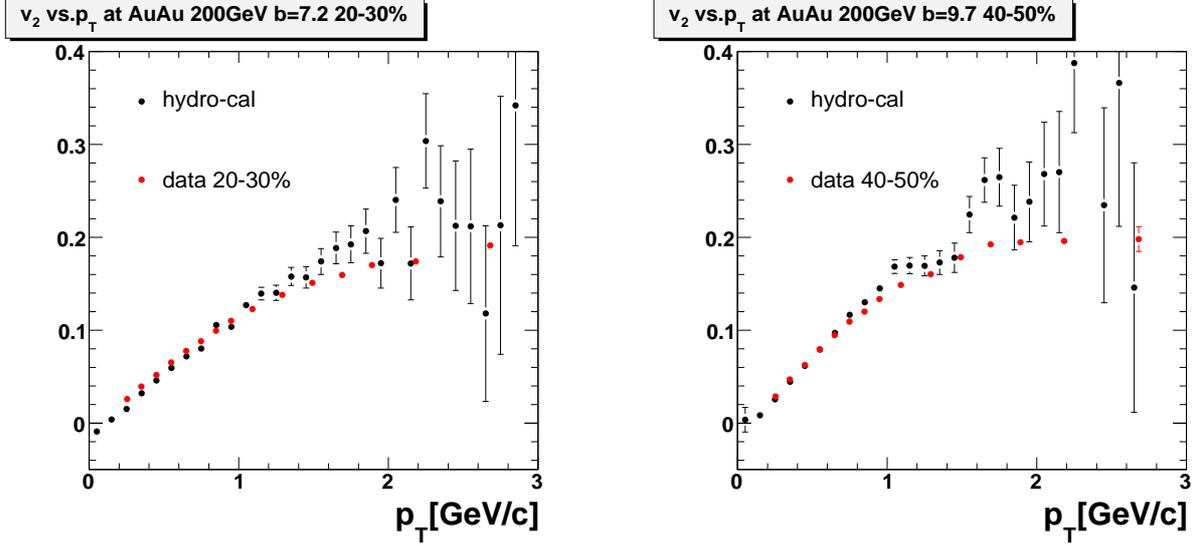
Figure A.1: Comparison of measured v_2 for π with that of the hydrodynamical calculation at $\sqrt{s_{\mathrm{NN}}} = 200$ GeV in Au+Au for the centralities indicated. The black points indicate v_2 obtained by the calculation. The red points are measured v_2.
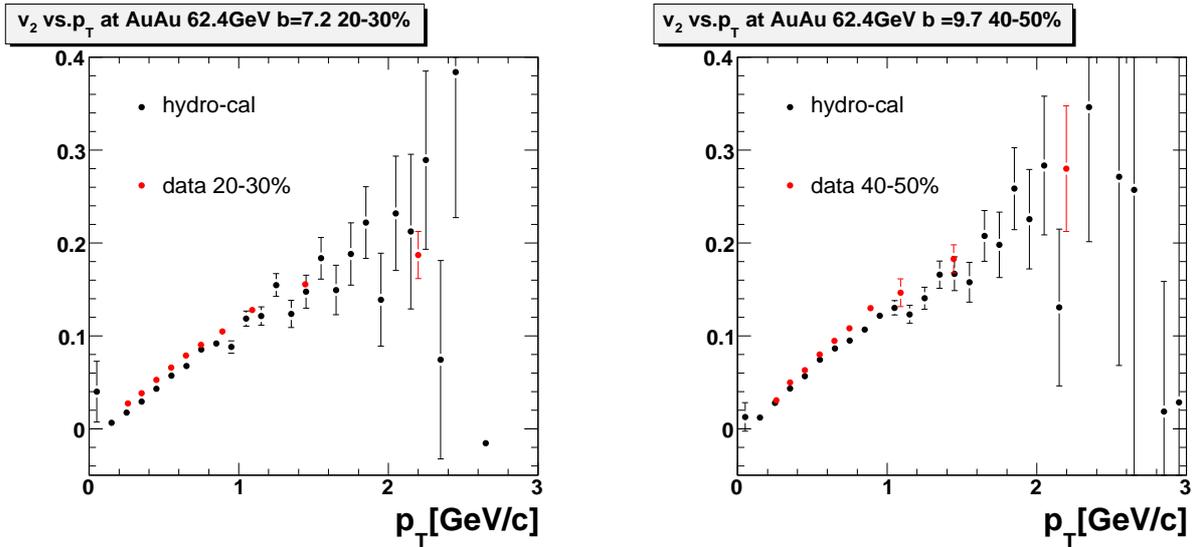
Figure A.2: Comparison of measured v_2 for π with that of the hydrodynamical calculation at $\sqrt{s_{\mathrm{NN}}} = 62.4$ GeV in Au+Au for the centralities indicated. The black points indicate v_2 obtained by the calculation. The red points are measured v_2.
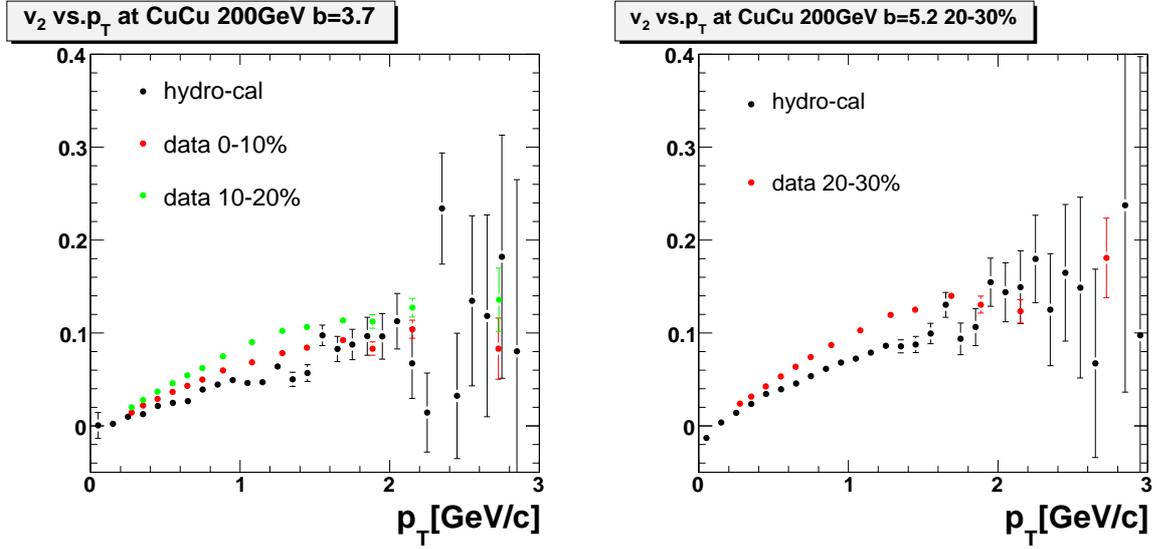
Figure A.3: Comparison of measured v_2 for π with that of the hydrodynamical calculation at $\sqrt{s_{\mathrm{NN}}} = 200$ GeV in Cu+Cu for the centralities indicated. The black points indicate v_2 obtained by the calculation. The red and green points are measured v_2. In the right panel, the calculation is between 0-10 % and 10-20 % centrality, therefore if the measurement and the simulation agree, the black symbols should be between red and green symbols.
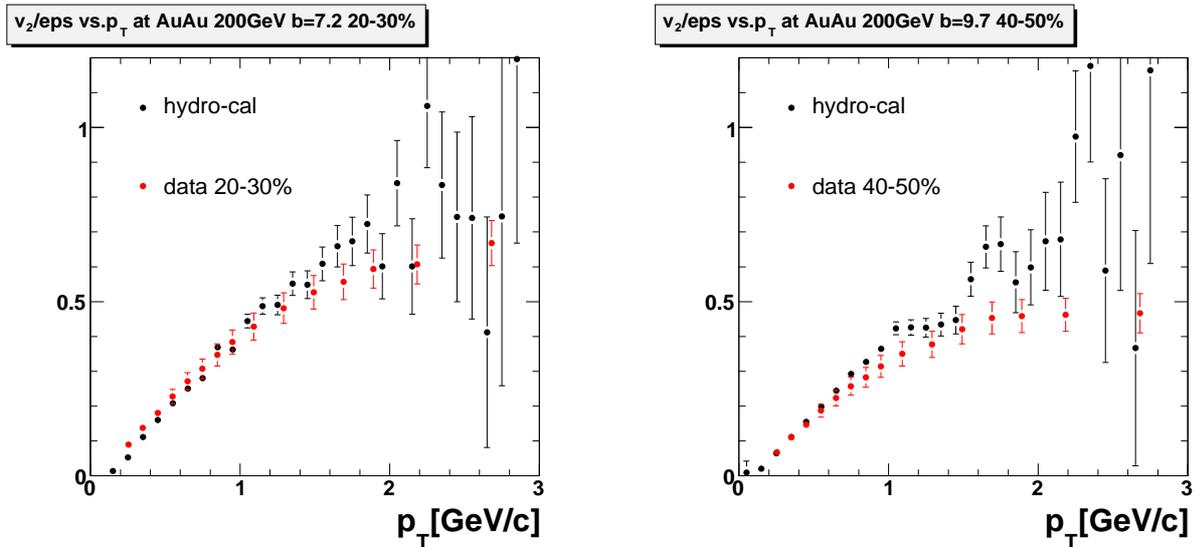
Figure A.4: Comparison of measured $v_2/\varepsilon_{\mathrm{part}}$ with calculated $v_2/\varepsilon_{\mathrm{stand}}$ for π at $\sqrt{s_{\mathrm{NN}}} = 200$ GeV in Au+Au for the centralities indicated. The black points are the hydrodynamical calculation. The red points are the measurement.
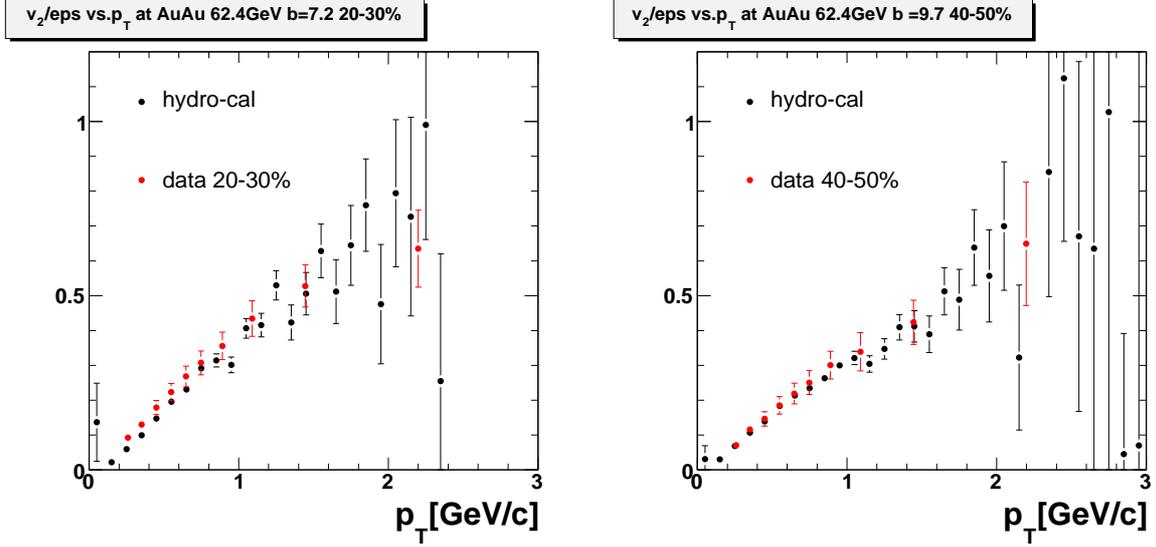
Figure A.5: Comparison of measured $v_2/\varepsilon_{\mathrm{part}}$ with calculated $v_2/\varepsilon_{\mathrm{stand}}$ for π at $\sqrt{s_{\mathrm{NN}}} = 62.4$ GeV in Au+Au for the centralities indicated. The black points are the hydrodynamical calculation. The red points are the measurement.
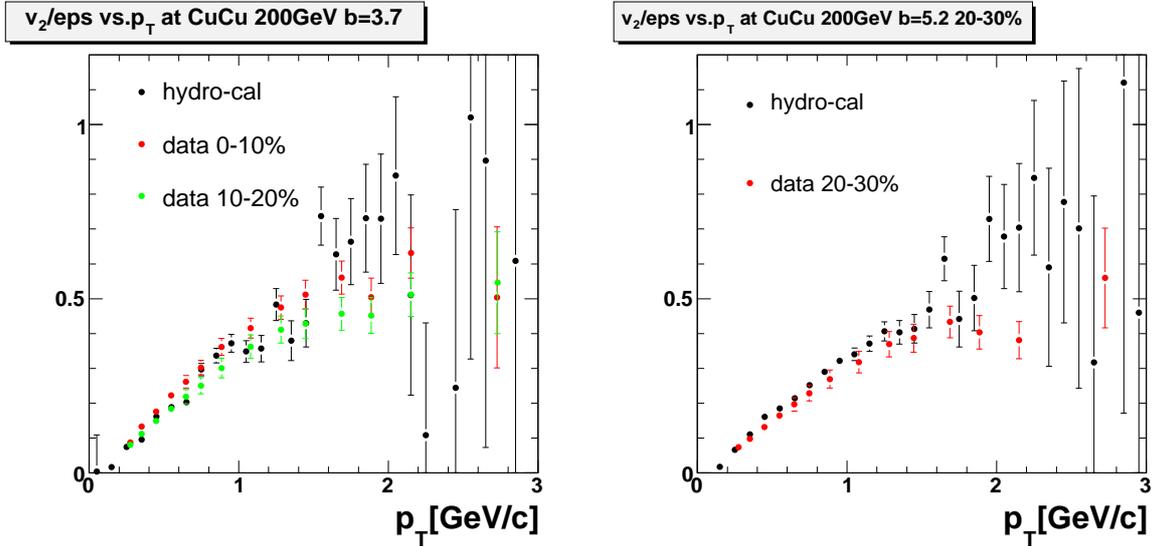
Figure A.6: Comparison of measured $v_2/\varepsilon_{\mathrm{part}}$ with calculated $v_2/\varepsilon_{\mathrm{stand}}$ for π at $\sqrt{s_{\mathrm{NN}}} = 200$ GeV in Cu+Cu for the centralities indicated. The black points are the hydrodynamical calculation. The red and green points are the measurement. In the right panel, the calculation is between 0-10 % and 10-20 % centrality, therefore if the measurement and the simulation agree, the black symbols should be between red and green symbols.
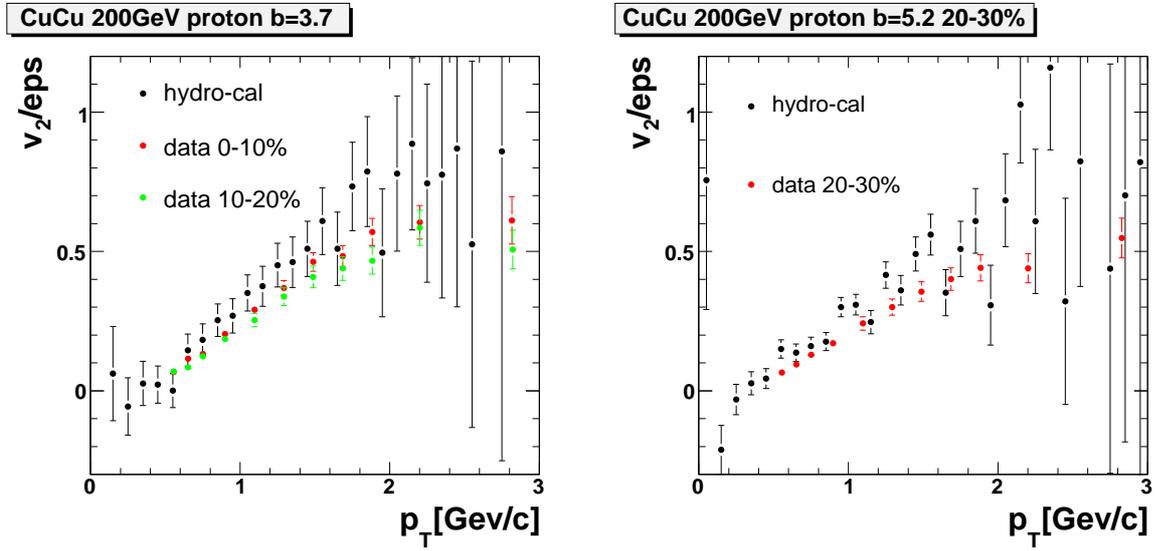
Figure A.7: Comparison of measured $v_2/\varepsilon_{\mathrm{part}}$ with calculated $v_2/\varepsilon_{\mathrm{stand}}$ for proton at $\sqrt{s_{\mathrm{NN}}} = 200$ GeV in Cu+Cu for the centralities indicated. The black points are the hydrodynamical calculation. The red and green points are the measurement. In the right panel, the calculation is between 0-10 % and 10-20 % centrality, therefore if the measurement and the simulation agree, the black symbols should be between red and green symbols.

Appendix B

High-p_T v_2 with Energy Loss

We have learned that the behavior of anisotropy can be explained by a hydro-dynamical model and initial pressure gradient at transverse momentum, $p_\mathrm{T} < 2$ GeV/c, but not at higher p_T. As explained in Section 1.3.5, most part of the high p_T particles comes from the (parton) jets which are produced by the at the initial stage. The jet production occurs in the overlap region and is independent of the reaction plane. In the high p_T region, a non zero v_2 is still observed as shown in Figure B.1 . One possible explanation is that jets lose its energy in the medium. Since the collision overlap region forms an almond shape (not round) in non-central collisions, high p_T partons which goes to jets traverse less medium and thus lose less energy in the in-plane direction, compared to the case of out-of plane direction. The difference of the amount of jets absorbed in the in-plane and out-of-plane directions can produce the positive v_2. In Figure B.1, the lines at left figure are calculations of energy loss models done by Dr. Vitev [83] . Therefore, the fact that the measured v_2 in high p_T region is positive is the another strong evidence for the formation of QGP in which matter strongly interact.
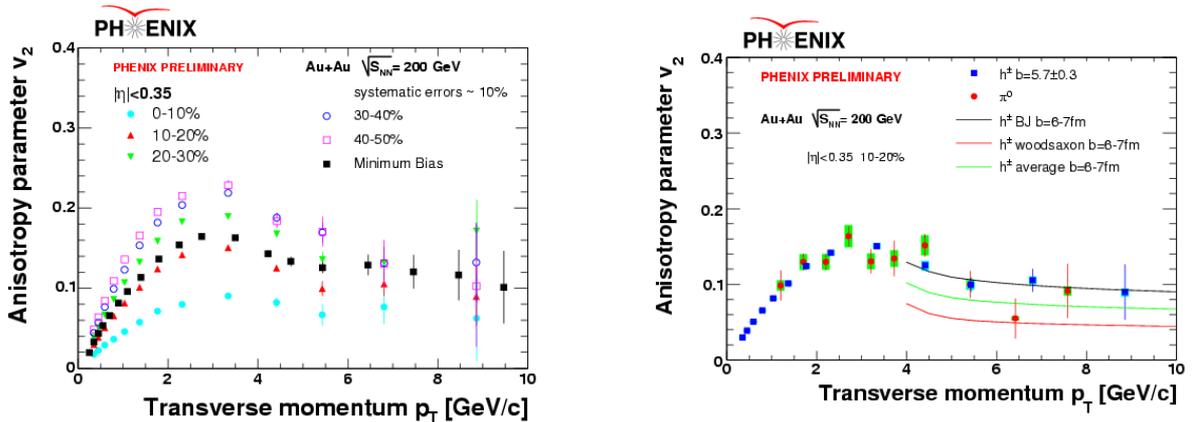
Figure B.1: The v_2 for inclusive charged hadrons and π^0 as a function of p_T at $\sqrt{s_\mathrm{NN}} = 200$ GeV in Au+Au. The left panel shows the v_2 vs. p_T for several centrality bins. The right panel shows the comparison of π^0 to inclusive charged hadrons for 0 - 10 % centrality. The lines at left panel are the calculations of energy loss models described in [83] . **BJ** is assuming uniform Bjorken expanding fireball. **WoodSaxon** assumes the matter is produced with a binary collision density, and the density stays as it is. The bars show the statistical errors and the boxes indicate the systematic errors.

Appendix C

Data Tables

C.1 The Tables of v_2 for Inclusive Charged Hadrons

C.1.1 Charged Hadron v_2 in Au+Au Collisions at $\sqrt{s_{\mathrm{NN}}} = 200$ GeV

Table C.1: v_2 as a function of p_{T} for charged hadrons emitted from minimum bias Au+Au collisions at $\sqrt{s_{\mathrm{NN}}} = 200$ GeV

p_{T} [GeV/c]	v_2	Stat Error [%]	Lower Sys Error [%]	Upper Sys Error [%]
0.250	0.020	0.3	3.8	3.8
0.350	0.033	0.2	3.8	3.8
0.450	0.043	0.2	3.8	3.8
0.550	0.053	0.1	3.8	3.8
0.700	0.066	0.1	3.8	3.8
0.900	0.082	0.1	3.8	3.8
1.100	0.096	0.1	3.8	3.8
1.400	0.113	0.1	3.8	3.8
1.800	0.136	0.1	3.8	3.8
2.250	0.154	0.1	3.8	3.8
2.750	0.165	0.2	3.8	3.9
3.500	0.163	0.4	3.8	8.9
4.229	0.143	2.7	5.0	5.3
4.732	0.133	4.4	5.1	5.0
5.436	0.126	5.6	5.0	5.7
6.450	0.129	10.1	10.8	5.0
7.459	0.120	17.5	6.6	5.0
8.464	0.116	27.2	6.9	5.2
9.470	0.101	44.7	7.9	6.0
10.891	0.114	43.6	7.0	5.3
12.916	0.168	47.1	4.8	3.6

Table C.2: v_2 as a function of p_T for charged hadrons emitted from 0-10% central Au+Au collisions at $\sqrt{s_{NN}} = 200$ GeV

p_T [GeV/c]	v_2	Stat Error [%]	Lower Sys Error [%]	Upper Sys Error [%]
0.350	0.018	2.1	2.5	2.5
0.449	0.022	1.7	3.5	3.5
0.594	0.029	1.1	3.4	3.4
0.792	0.036	1.0	3.4	3.4
1.033	0.046	0.9	3.2	3.2
1.368	0.057	0.9	3.2	3.2
1.768	0.071	1.2	3.0	3.0
2.318	0.080	1.5	3.2	3.2
3.341	0.090	4.1	3.4	3.4
4.415	0.082	7.6	5.0	12.0
5.435	0.067	20.7	6.2	14.8
6.806	0.076	28.3	5.4	12.9
8.867	0.062	86.0	6.6	15.9

Table C.3: v_2 as a function of p_T for charged hadrons emitted from 10-20% central Au+Au collisions at $\sqrt{s_{NN}} = 200$ GeV

p_T [GeV/c]	v_2	Stat Error [%]	Lower Sys Error [%]	Upper Sys Error [%]
0.350	0.030	1.0	2.1	2.1
0.449	0.038	0.8	2.7	2.7
0.594	0.050	0.5	2.7	2.7
0.792	0.065	0.5	2.5	2.5
1.033	0.081	0.4	2.5	2.5
1.368	0.101	0.4	2.5	2.5
1.768	0.124	0.5	2.4	2.4
2.318	0.141	0.6	2.5	2.5
3.341	0.150	1.9	2.9	2.9
4.417	0.125	3.5	5.9	5.0
5.435	0.099	9.6	6.2	5.0
6.807	0.105	14.5	5.8	4.7
8.862	0.090	41.1	6.9	5.5
10.892	0.045	160.2	13.8	11.1

Table C.4: v_2 as a function of p_T for charged hadrons emitted from 20-30% central Au+Au collisions at $\sqrt{s_\mathrm{NN}} = 200$ GeV

p_T [GeV/c]	v_2	Stat Error [%]	Lower Sys Error [%]	Upper Sys Error [%]
0.350	0.038	0.9	2.2	2.2
0.449	0.051	0.7	2.7	2.7
0.594	0.067	0.4	2.7	2.7
0.792	0.086	0.4	2.6	2.6
1.033	0.107	0.3	2.6	2.6
1.368	0.132	0.4	2.6	2.6
1.768	0.158	0.5	2.5	2.5
2.318	0.183	0.5	2.6	2.6
3.341	0.189	1.6	3.0	3.0
4.419	0.168	2.7	5.0	5.2
5.436	0.136	7.3	6.2	6.5
6.807	0.132	12.0	6.4	6.7
8.863	0.171	22.6	4.9	5.1

Table C.5: v_2 as a function of p_T for charged hadrons emitted from 30-40% central Au+Au collisions at $\sqrt{s_\mathrm{NN}} = 200$ GeV

p_T [GeV/c]	v_2	Stat Error [%]	Lower Sys Error [%]	Upper Sys Error [%]
0.350	0.044	1.0	2.3	2.3
0.449	0.057	0.8	2.9	2.9
0.594	0.077	0.5	2.8	2.8
0.792	0.099	0.5	2.7	2.7
1.033	0.123	0.4	2.7	2.7
1.368	0.153	0.4	2.7	2.7
1.768	0.182	0.6	2.7	2.7
2.318	0.204	0.7	2.8	2.8
3.341	0.219	1.8	3.1	3.1
4.421	0.188	3.1	5.0	5.0
5.437	0.169	7.4	5.6	5.6
6.806	0.131	15.5	7.2	7.2
8.859	0.132	37.3	7.1	7.1

Table C.6: v_2 as a function of p_T for charged hadrons emitted from 40-50% central Au+Au collisions at $\sqrt{s_{NN}} = 200$ GeV

p_T [GeV/c]	v_2	Stat Error [%]	Lower Sys Error [%]	Upper Sys Error [%]
0.350	0.048	1.5	2.5	2.5
0.449	0.064	1.1	3.1	3.1
0.594	0.084	0.7	3.1	3.1
0.792	0.109	0.6	3.0	3.0
1.033	0.136	0.6	3.0	3.0
1.368	0.166	0.6	3.0	3.0
1.768	0.195	0.8	3.0	3.0
2.318	0.215	1.0	3.2	3.2
3.341	0.229	2.8	3.5	3.5
4.423	0.184	4.8	5.0	5.2
5.438	0.171	10.9	5.4	5.7
6.807	0.131	22.8	7.0	7.4
8.860	0.103	74.0	8.9	9.4

Table C.7: v_2 as a function of p_T for charged hadrons emitted from 50-60% central Au+Au collisions at $\sqrt{s_{NN}} = 200$ GeV

p_T [GeV/c]	v_2	Stat Error [%]	Lower Sys Error [%]	Upper Sys Error [%]
0.233	0.047	0.828	5.0	5.0
0.733	0.100	0.411	5.1	5.0
1.231	0.148	0.359	5.0	5.0
1.721	0.184	0.626	5.0	5.0
2.376	0.204	0.995	5.0	5.0
3.405	0.213	2.970	4.8	4.8
4.424	0.148	10.758	6.9	7.0
5.762	0.155	19.113	6.6	6.6

Table C.8: v_2 as a function of p_T for charged hadrons emitted from 0-20% central Au+Au collisions at $\sqrt{s_{NN}} = 200$ GeV

p_T [GeV/c]	v_2	Stat Error [%]	Lower Sys Error [%]	Upper Sys Error [%]
0.235	0.024	0.340	5.0	5.0
0.735	0.044	0.180	5.0	5.0
1.233	0.064	0.171	5.0	5.0
1.723	0.085	0.265	5.0	5.4
2.220	0.102	0.449	5.0	5.2
2.721	0.113	0.778	5.0	5.0
3.224	0.117	1.386	5.0	5.1
3.726	0.112	2.511	5.0	6.1
4.229	0.104	4.398	5.0	6.2
4.731	0.101	6.971	5.0	5.0
5.435	0.083	10.203	6.0	5.0
6.450	0.097	16.209	5.1	4.3
7.843	0.075	28.756	6.6	5.5
9.886	0.096	49.151	5.2	4.3

Table C.9: v_2 as a function of p_T for charged hadrons emitted from 20-40% central Au+Au collisions at $\sqrt{s_{NN}} = 200$ GeV

p_T [GeV/c]	v_2	Stat Error [%]	Lower Sys Error [%]	Upper Sys Error [%]
0.235	0.042	0.201	5.0	5.0
0.735	0.083	0.101	5.0	5.0
1.233	0.124	0.090	5.0	5.0
1.723	0.160	0.145	5.0	5.1
2.220	0.186	0.250	5.0	5.0
2.722	0.198	0.445	5.0	5.0
3.225	0.198	0.794	5.0	5.1
3.727	0.191	1.390	5.1	5.0
4.230	0.183	2.349	5.0	5.2
4.732	0.161	4.088	5.1	5.0
5.234	0.160	5.967	5.4	5.0
5.735	0.130	10.428	6.4	5.0
6.450	0.142	10.380	5.9	4.6
7.460	0.104	22.957	8.0	6.2
8.862	0.154	19.941	5.4	4.2

Table C.10: v_2 as a function of p_T for charged hadrons emitted from 40-60% central Au+Au collisions at $\sqrt{s_{NN}}$ = 200 GeV

p_T [GeV/c]	v_2	Stat Error [%]	Lower Sys Error [%]	Upper Sys Error [%]
0.234	0.048	0.417	5.0	5.0
0.734	0.099	0.207	5.0	5.0
1.232	0.149	0.179	5.0	5.0
1.722	0.187	0.304	5.0	5.0
2.219	0.209	0.546	5.0	5.0
2.723	0.217	0.973	5.0	5.1
3.226	0.216	1.709	5.1	5.0
3.728	0.213	2.870	5.0	5.0
4.423	0.170	4.739	5.0	5.0
5.438	0.172	9.995	5.0	5.0
6.807	0.110	24.874	7.7	7.8
8.863	0.074	95.512	11.5	11.6

Table C.11: v_2 as a function of p_T for charged hadrons emitted from 60-92% central Au+Au collisions at $\sqrt{s_{NN}}$ = 200 GeV

p_T [GeV/c]	v_2	Stat Error [%]	Lower Sys Error [%]	Upper Sys Error [%]
0.232	0.039	2.997	5.3	5.0
0.732	0.087	1.400	5.0	5.0
1.230	0.134	1.125	5.2	5.0
1.720	0.166	1.976	5.4	5.0
2.218	0.170	3.851	5.0	5.0
2.723	0.200	6.028	4.3	4.3
3.406	0.193	9.148	4.4	4.4
4.707	0.192	20.552	4.4	4.4

Table C.12: v_2 as a function of centrality (N_{part}) at p_T = 0.2-1.0 GeV/c in Au+Au at $\sqrt{s_{NN}}$ = 200 GeV

Centrality [%]	N_{part}	v_2	Statistical Error [%]	Systematic Error [%]
0-10	325.2	0.026	0.3	5.0
10-20	234.6	0.045	0.1	5.0
20-30	166.6	0.059	0.1	5.0
30-40	114.2	0.068	0.1	5.1
40-50	74.4	0.072	0.2	5.1
50-60	45.5	0.072	0.4	5.1
60-70	25.7	0.065	1.0	5.1
70-80	13.4	0.058	2.8	5.4

Table C.13: v_2 as a function of centrality (N_{part}) at $p_{\mathrm{T}} = 1.0$-2.0 GeV/c in Au+Au at $\sqrt{s_{\mathrm{NN}}} = 200$ GeV

Centrality [%]	N_{part}	v_2	Statistical Error [%]	Systematic Error [%]
0-10	325.2	0.055	0.4	5.0
10-20	234.6	0.097	0.2	5.0
20-30	166.6	0.127	0.1	5.0
30-40	114.2	0.148	0.2	5.0
40-50	74.4	0.159	0.2	5.0
50-60	45.5	0.159	0.4	5.0
60-70	25.7	0.147	1.1	5.0
70-80	13.4	0.139	3.2	6.2

Table C.14: v_2 as a function of centrality (N_{part}) at $p_{\mathrm{T}} = 2.0$-4.0 GeV/c in Au+Au at $\sqrt{s_{\mathrm{NN}}} = 200$ GeV

Centrality [%]	N_{part}	v_2	Statistical Error [%]	Systematic Error [%]
0-10	325.2	0.078	0.8	8.6
10-20	234.6	0.136	0.3	6.6
20-30	166.6	0.179	0.3	5.7
30-40	114.2	0.206	0.3	5.3
40-50	74.4	0.214	0.5	5.4
50-60	45.5	0.205	0.9	5.0
60-70	25.7	0.182	2.4	7.4
70-80	13.4	0.166	6.8	6.5

C.1.2 Charged Hadron v_2 in Cu+Cu Collisions at $\sqrt{s_{\mathrm{NN}}} = 200$ GeV

Table C.15: v_2 as a function of centrality (N_{part}) at $p_{\mathrm{T}} = 0.2$-1.0 GeV/c in Cu+Cu at $\sqrt{s_{\mathrm{NN}}} = 200$ GeV

Centrality [%]	N_{part}	v_2	Statistical Error [%]	Systematic Error [%]
0-10	98.2	0.034	1.6	13.9
10-20	73.6	0.042	1.3	12.0
20-30	53	0.048	1.4	12.0
30-40	37.3	0.051	1.8	13.3
40-50	25.4	0.051	2.9	16.8

Table C.16: v_2 as a function of centrality (N_{part}) at $p_{\mathrm{T}} = 1.0$-2.0 GeV/c in Cu+Cu at $\sqrt{s_{\mathrm{NN}}} = 200$ GeV

Centrality [%]	N_{part}	v_2	Statistical Error [%]	Systematic Error [%]
0-10	98.2	0.069	1.4	13.9
10-20	73.6	0.087	1.2	12.0
20-30	53	0.103	1.2	12.0
30-40	37.3	0.107	1.6	13.3
40-50	25.4	0.114	2.4	16.8

Table C.17: v_2 as a function of centrality (N_{part}) at $p_{\mathrm{T}} = 2.0$-4.0 GeV/c in Cu+Cu at $\sqrt{s_{\mathrm{NN}}} = 200$ GeV

Centrality [%]	N_{part}	v_2	Statistical Error [%]	Systematic Error [%]
0-10	98.2	0.099	3.6	13.9
10-20	73.6	0.125	2.9	12.0
20-30	53	0.143	3.1	12.0
30-40	37.3	0.150	4.1	13.3
40-50	25.4	0.158	6.3	16.8

C.1.3   Charged Hadron v_2 in Au+Au Collisions at $\sqrt{s_{\mathrm{NN}}} = 62.4$ GeV

Table C.18: v_2 as a function of p_{T} for charged hadrons emitted from minimum bias Au+Au collisions at $\sqrt{s_{\mathrm{NN}}} = 62.4$ GeV

p_{T} [GeV/c]	v_2	Statistical Error [%]	Systematic Error [%]
0.234	0.031	1.7	10.9
0.734	0.061	0.8	11.0
1.231	0.094	1.0	11.3
1.720	0.121	1.7	11.0
2.217	0.140	3.1	10.9
2.718	0.151	6.0	10.9
3.384	0.124	12.7	16.7
4.609	0.194	24.8	19.3

Table C.19: v_2 as a function of p_{T} for charged hadrons emitted from 0-10 % central Au+Au collisions at $\sqrt{s_{\mathrm{NN}}} = 62.4$ GeV

p_{T} [GeV/c]	v_2	Statistical Error [%]	Systematic Error [%]
0.234	0.017	5.0	7.1
0.734	0.033	2.4	7.3
1.232	0.052	2.9	7.1
1.720	0.067	5.0	7.2
2.217	0.074	10.1	7.2
2.718	0.104	15.1	10.2
3.526	0.088	30.1	12.1

Table C.20: v_2 as a function of p_{T} for charged hadrons emitted from 10-20 % central Au+Au collisions at $\sqrt{s_{\mathrm{NN}}} = 62.4$ GeV

p_{T} [GeV/c]	v_2	Statistical Error [%]	Systematic Error [%]
0.234	0.031	2.2	7.0
0.734	0.058	1.1	7.0
1.232	0.092	1.3	7.8
1.720	0.121	2.3	7.1
2.217	0.153	4.0	7.8
2.718	0.144	8.6	7.1
3.538	0.145	14.3	7.0

Table C.21: v_2 as a function of p_T for charged hadrons emitted from 20-30 % central Au+Au collisions at $\sqrt{s_{NN}} = 62.4$ GeV

p_T [GeV/c]	v_2	Statistical Error [%]	Systematic Error [%]
0.234	0.041	2.1	7.1
0.734	0.079	1.0	7.2
1.231	0.123	1.2	7.1
1.720	0.166	2.1	7.5
2.217	0.192	3.9	7.3
2.719	0.215	7.2	7.8
3.545	0.180	14.0	7.0

Table C.22: v_2 as a function of p_T for charged hadrons emitted from 30-40 % central Au+Au collisions at $\sqrt{s_{NN}} = 62.4$ GeV

p_T [GeV/c]	v_2	Statistical Error [%]	Systematic Error [%]
0.233	0.044	2.7	7.1
0.733	0.092	1.2	7.1
1.231	0.140	1.6	7.4
1.719	0.177	2.9	7.1
2.216	0.192	5.8	8.5
2.719	0.208	10.8	7.5
3.550	0.252	14.4	13.5

Table C.23: v_2 as a function of p_T for charged hadrons emitted from 40-50 % central Au+Au collisions at $\sqrt{s_{NN}} = 62.4$ GeV

p_T [GeV/c]	v_2	Statistical Error [%]	Systematic Error [%]
0.233	0.044	4.7	7.4
0.733	0.099	2.1	7.4
1.231	0.156	2.6	8.4
1.719	0.185	5.1	7.4
2.216	0.206	10.1	7.7
2.719	0.189	22.1	9.6
3.388	0.022	320.7	280.6

Table C.24: v_2 as a function of centrality (N_{part}) at $p_{\mathrm{T}} = 0.2\text{-}1.0$ GeV/c in Au+Au at $\sqrt{s_{\mathrm{NN}}} = 62.4$ GeV

Centrality [%]	N_{part}	v_2	Statistical Error [%]	Systematic Error [%]
0-10	320.7	0.026	2.2	7.2
10-20	230.7	0.046	1.0	7.0
20-30	163.2	0.061	0.9	7.0
30-40	113	0.069	1.1	7.0
40-50	74.5	0.073	1.9	6.6
50-60	45.9	0.066	4.3	6.9
60-70	25.9	0.065	11.2	13.4

Table C.25: v_2 as a function of centrality (N_{part}) at $p_{\mathrm{T}} = 1.0\text{-}2.0$ GeV/c in Au+Au at $\sqrt{s_{\mathrm{NN}}} = 62.4$ GeV

Centrality [%]	N_{part}	v_2	Statistical Error [%]	Systematic Error [%]
0-10	320.7	0.055	2.2	7.1
10-20	230.7	0.098	1.0	7.4
20-30	163.2	0.132	0.9	7.1
30-40	113	0.147	1.2	7.1
40-50	74.5	0.160	2.1	7.3
50-60	45.9	0.145	4.9	7.7
60-70	25.9	0.150	12.9	23.1

Table C.26: v_2 as a function of centrality (N_{part}) at $p_{\mathrm{T}} = 2.0\text{-}4.0$ GeV/c in Au+Au at $\sqrt{s_{\mathrm{NN}}} = 62.4$ GeV

Centrality [%]	N_{part}	v_2	Statistical Error [%]	Systematic Error [%]
0-10	320.7	0.074	6.1	7.3
10-20	230.7	0.147	2.4	6.9
20-30	163.2	0.192	2.3	6.9
30-40	113	0.208	3.1	7.9
40-50	74.5	0.209	5.7	15.0
50-60	45.9	0.170	15.6	10.3
60-70	25.9	0.166	45.1	16.7

C.1.4 Charged Hadron v_2 in Cu+Cu Collisions at $\sqrt{s_{\mathrm{NN}}} = 62.4$ GeV

Table C.27: v_2 as a function of p_{T} for charged hadrons emitted from minimum bias Cu+Cu collisions at $\sqrt{s_{\mathrm{NN}}} = 62.4$ GeV

p_{T} [GeV/c]	v_2	Statistical Error [%]	Systematic Error [%]
0.733	0.043	1.5	33.4
1.231	0.069	1.9	33.1
1.719	0.095	3.1	33.2
2.216	0.095	7.0	35.5
2.718	0.101	13.4	33.6
3.387	0.157	14.5	21.5
4.627	0.150	43.4	22.5

Table C.28: v_2 as a function of p_{T} for charged hadrons emitted from 0-10 % central Cu+Cu collisions at $\sqrt{s_{\mathrm{NN}}} = 62.4$ GeV

p_{T} [GeV/c]	v_2	Statistical Error [%]	Systematic Error [%]
0.733	0.036	3.4	29.8
1.231	0.059	4.1	29.6
1.719	0.084	6.6	30.4
2.216	0.077	15.8	46.3
2.718	0.086	29.5	46.0
3.384	0.142	30.6	27.9
4.621	0.172	73.9	23.0

Table C.29: v_2 as a function of p_{T} for charged hadrons emitted from 10-20 % central Cu+Cu collisions at $\sqrt{s_{\mathrm{NN}}} = 62.4$ GeV

p_{T} [GeV/c]	v_2	Statistical Error [%]	Systematic Error [%]
0.733	0.045	2.4	23.0
1.231	0.070	3.1	23.0
1.719	0.091	5.5	23.2
2.216	0.099	11.0	23.8
2.718	0.076	29.4	31.6
3.387	0.114	33.1	21.0
4.627	0.006	1660.3	370.4

Table C.30: v_2 as a function of p_T for charged hadrons emitted from 20-30 % central Cu+Cu collisions at $\sqrt{s_{NN}} = 62.4$ GeV

p_T [GeV/c]	v_2	Statistical Error [%]	Systematic Error [%]
0.733	0.048	2.7	23.4
1.231	0.081	3.3	23.1
1.719	0.112	5.5	23.9
2.216	0.122	11.1	23.4
2.719	0.117	23.3	29.2
3.388	0.199	23.0	17.2
4.627	0.249	52.9	13.8

Table C.31: v_2 as a function of p_T for charged hadrons emitted from 30-40 % central Cu+Cu collisions at $\sqrt{s_{NN}} = 62.4$ GeV

p_T [GeV/c]	v_2	Statistical Error [%]	Systematic Error [%]
0.733	0.049	3.6	25.7
1.231	0.081	4.3	25.4
1.718	0.100	8.2	27.0
2.215	0.112	16.2	26.9
2.719	0.142	25.7	30.4
3.389	0.178	34.4	24.4
4.636	0.075	231.2	58.0

Table C.32: v_2 as a function of p_T for charged hadrons emitted from 40-50 % central Cu+Cu collisions at $\sqrt{s_{NN}} = 62.4$ GeV

p_T [GeV/c]	v_2	Statistical Error [%]	Systematic Error [%]
0.732	0.049	5.4	30.7
1.230	0.076	7.1	30.6
1.718	0.118	11.0	30.6
2.215	0.063	44.8	39.6
2.719	0.048	118.3	51.9
3.557	0.109	82.5	23.0

Table C.33: v_2 as a function of p_T for charged hadrons emitted from 50-60 % central Cu+Cu collisions at $\sqrt{s_{NN}} = 62.4$ GeV

p_T [GeV/c]	v_2	Statistical Error [%]	Systematic Error [%]
0.722	0.037	9.9	33.2
1.230	0.067	11.5	40.1
1.717	0.081	23.1	53.5
2.215	0.111	37.0	43.5
2.719	0.194	42.9	24.9
3.557	0.110	118.0	43.8

Table C.34: v_2 as a function of p_T for charged hadrons emitted from 60-70 % central Cu+Cu collisions at $\sqrt{s_{NN}} = 62.4$ GeV

p_T [GeV/c]	v_2	Statistical Error [%]	Systematic Error [%]
0.731	0.039	14.1	40.7
1.229	0.032	37.1	50.8
1.716	0.093	31.5	44.6
2.214	0.108	60.1	57.8
2.718	0.160	81.4	38.9
3.557	0.284	72.7	22.0

Table C.35: v_2 as a function of p_T for charged hadrons emitted from 70-80 % central Cu+Cu collisions at $\sqrt{s_{NN}} = 62.4$ GeV

p_T [GeV/c]	v_2	Statistical Error [%]	Systematic Error [%]
0.730	0.071	15.5	56.9
1.228	0.096	25.6	61.1
1.715	0.129	47.3	45.3
2.414	0.245	48.2	23.8

Table C.36: v_2 as a function of p_T for charged hadrons emitted from 0-20 % central Cu+Cu collisions at $\sqrt{s_{NN}} = 62.4$ GeV

p_T [GeV/c]	v_2	Statistical Error [%]	Systematic Error [%]
0.733	0.040	2.1	26.4
1.231	0.063	2.6	26.2
1.719	0.087	4.4	26.8
2.216	0.087	9.8	34.0
2.718	0.082	21.3	39.8
3.385	0.130	22.8	25.0
4.624	0.098	87.4	33.3

Table C.37: v_2 as a function of p_T for charged hadrons emitted from 20-40 % central Cu+Cu collisions at $\sqrt{s_{NN}} = 62.4$ GeV

p_T [GeV/c]	v_2	Statistical Error [%]	Systematic Error [%]
0.733	0.049	2.2	24.5
1.231	0.081	2.6	24.0
1.719	0.108	4.6	24.2
2.216	0.118	9.2	24.1
2.719	0.127	17.3	29.8
3.388	0.191	19.3	19.9
4.631	0.179	58.7	21.2

Table C.38: v_2 as a function of p_T for charged hadrons emitted from 40-60 % central Cu+Cu collisions at $\sqrt{s_{NN}} = 62.4$ GeV

p_T [GeV/c]	v_2	Statistical Error [%]	Systematic Error [%]
0.732	0.045	4.9	32.0
1.230	0.073	6.1	33.6
1.718	0.104	10.2	33.3
2.215	0.081	29.0	35.6
2.719	0.101	46.8	50.5
3.557	0.109	68.1	46.8

Table C.39: v_2 as a function of p_T for charged hadrons emitted from 60-80 % central Cu+Cu collisions at $\sqrt{s_{NN}} = 62.4$ GeV

p_T [GeV/c]	v_2	Statistical Error [%]	Systematic Error [%]
0.731	0.050	10.5	47.5
1.229	0.054	21.3	49.1
1.716	0.105	26.8	77.1
2.422	0.167	32.3	48.3

Table C.40: v_2 as a function of centrality (N_{part}) at $p_T = 0.2$-1.0 GeV/c in Cu+Cu at $\sqrt{s_{NN}} = 62.4$ GeV

Centrality [%]	N_{part}	v_2	Statistical Error [%]	Systematic Error [%]
0-10	93.3	0.029	2.9	28.7
10-20	71.1	0.035	2.1	21.7
20-30	51.3	0.039	2.3	22.0
30-40	36.2	0.037	3.2	23.9
40-50	24.9	0.039	4.6	29.3
50-60	16.1	0.033	7.5	32.4

Table C.41: v_2 as a function of centrality (N_{part}) at $p_{\text{T}} = 1.0$-2.0 GeV/c in Cu+Cu at $\sqrt{s_{\text{NN}}} = 62.4$ GeV

Centrality [%]	N_{part}	v_2	Statistical Error [%]	Systematic Error [%]
0-10	93.3	0.064	3.0	28.8
10-20	71.1	0.073	2.3	21.7
20-30	51.3	0.087	2.4	22.1
30-40	36.2	0.086	3.2	24.0
40-50	24.9	0.082	5.3	29.3
50-60	16.1	0.067	9.3	32.7

Table C.42: v_2 as a function of centrality (N_{part}) at $p_{\text{T}} = 2.0$-4.0 GeV/c in Cu+Cu at $\sqrt{s_{\text{NN}}} = 62.4$ GeV

Centrality [%]	N_{part}	v_2	Statistical Error [%]	Systematic Error [%]
0-10	93.3	0.086	8.3	29.0
10-20	71.1	0.097	6.5	22.2
20-30	51.3	0.118	6.5	23.2
30-40	36.2	0.131	7.9	24.9
40-50	24.9	0.093	17.3	43.9
50-60	16.1	0.115	20.4	33.9

C.2   The Tables of v_2 for Identified Charged Hadrons

C.2.1   Pion, Kaon and Proton v_2 in Cu+Cu Collisions at $\sqrt{s_{\mathrm{NN}}} = 200$ GeV

Table C.43: v_2 as a function of p_{T} for π emitted from 0-10 % central Cu+Cu collisions at $\sqrt{s_{\mathrm{NN}}} = 200$ GeV

p_{T} [GeV/c]	v_2	Statistical Error [%]	Systematic Error [%]
0.276	0.014	4.2	6.8
0.350	0.022	1.9	6.8
0.449	0.029	1.5	6.8
0.548	0.037	1.3	6.8
0.648	0.043	1.3	6.8
0.748	0.050	1.3	6.8
0.885	0.060	1.0	6.8
1.080	0.068	1.5	6.8
1.282	0.078	2.3	6.8
1.446	0.084	4.6	6.8
1.688	0.092	5.3	6.8
1.885	0.083	8.6	6.8
2.151	0.104	9.3	6.8
2.726	0.083	39.6	6.8

Table C.44: v_2 as a function of p_{T} for π emitted from 10-20 % central Cu+Cu collisions at $\sqrt{s_{\mathrm{NN}}} = 200$ GeV

p_{T} [GeV/c]	v_2	Statistical Error [%]	Systematic Error [%]
0.276	0.020	3.1	6.3
0.350	0.028	1.6	6.3
0.449	0.037	1.2	6.3
0.548	0.046	1.1	6.3
0.648	0.054	1.1	6.3
0.748	0.062	1.1	6.3
0.885	0.075	0.8	6.3
1.080	0.090	1.2	6.3
1.282	0.102	1.9	6.3
1.446	0.106	3.8	6.3
1.688	0.113	4.4	6.3
1.885	0.112	6.6	6.3
2.151	0.127	7.9	6.3
2.730	0.136	25.1	6.3

Table C.45: v_2 as a function of p_T for π emitted from 20-30 % central Cu+Cu collisions at $\sqrt{s_{NN}} = 200$ GeV

p_T [GeV/c]	v_2	Statistical Error [%]	Systematic Error [%]
0.276	0.024	3.2	5.8
0.350	0.032	1.7	5.8
0.449	0.043	1.3	5.8
0.548	0.053	1.2	5.8
0.648	0.064	1.1	5.8
0.748	0.074	1.1	5.8
0.884	0.087	0.9	5.8
1.080	0.103	1.3	5.8
1.282	0.119	2.0	5.8
1.446	0.125	4.0	5.8
1.688	0.140	4.3	5.8
1.885	0.131	7.0	5.8
2.149	0.123	10.2	5.8
2.724	0.181	23.7	5.8

Table C.46: v_2 as a function of p_T for π emitted from 30-40 % central Cu+Cu collisions at $\sqrt{s_{NN}} = 200$ GeV

p_T [GeV/c]	v_2	Statistical Error [%]	Systematic Error [%]
0.276	0.025	4.2	6.2
0.350	0.035	2.1	6.2
0.449	0.044	1.7	6.2
0.548	0.056	1.5	6.2
0.648	0.067	1.4	6.2
0.748	0.078	1.4	6.2
0.884	0.093	1.1	6.2
1.079	0.112	1.6	6.2
1.282	0.127	2.6	6.2
1.446	0.123	5.6	6.2
1.688	0.132	6.3	6.2
1.885	0.135	9.3	6.2
2.148	0.141	12.6	6.2
2.731	0.109	55.7	6.2

Table C.47: v_2 as a function of p_T for π emitted from 40-50 % central Cu+Cu collisions at $\sqrt{s_{NN}} = 200$ GeV

p_T [GeV/c]	v_2	Statistical Error [%]	Systematic Error [%]
0.276	0.026	6.1	6.8
0.350	0.033	3.3	6.8
0.449	0.046	2.5	6.8
0.548	0.055	2.3	6.8
0.648	0.062	2.4	6.8
0.748	0.078	2.2	6.8
0.884	0.092	1.8	6.8
1.079	0.111	2.5	6.8
1.282	0.126	4.0	6.8
1.446	0.138	7.8	6.8
1.688	0.151	8.6	6.8
1.884	0.140	14.1	6.8
2.147	0.191	14.6	6.8
2.735	0.178	53.9	6.8

Table C.48: v_2 as a function of p_T for K emitted from 0-10 % central Cu+Cu collisions at $\sqrt{s_{NN}} = 200$ GeV

p_T [GeV/c]	v_2	Statistical Error [%]	Systematic Error [%]
0.362	0.013	30.9	7.5
0.455	0.018	14.0	7.5
0.552	0.024	8.5	7.5
0.702	0.034	3.8	7.5
0.890	0.046	3.1	7.5
1.082	0.058	3.8	7.5
1.434	0.068	5.5	7.5
2.016	0.082	11.0	7.5

Table C.49: v_2 as a function of p_T for K emitted from 10-20 % central Cu+Cu collisions at $\sqrt{s_{NN}} = 200$ GeV

p_T [GeV/c]	v_2	Statistical Error [%]	Systematic Error [%]
0.362	0.021	19.1	7.0
0.455	0.026	9.8	7.0
0.552	0.031	6.8	7.0
0.702	0.046	3.0	7.0
0.890	0.064	2.4	7.0
1.082	0.076	3.0	7.0
1.435	0.095	4.1	7.0
2.020	0.116	7.9	7.0

Table C.50: v_2 as a function of p_T for K emitted from 20-30 % central Cu+Cu collisions at $\sqrt{s_{NN}} = 200$ GeV

p_T [GeV/c]	v_2	Statistical Error [%]	Systematic Error [%]
0.363	0.022	22.8	6.5
0.455	0.032	9.8	6.5
0.552	0.035	7.4	6.5
0.702	0.054	3.1	6.5
0.891	0.071	2.7	6.5
1.082	0.086	3.3	6.5
1.436	0.103	4.7	6.5
2.024	0.113	9.8	6.5

Table C.51: v_2 as a function of p_T for K emitted from 30-40 % central Cu+Cu collisions at $\sqrt{s_{NN}} = 200$ GeV

p_T [GeV/c]	v_2	Statistical Error [%]	Systematic Error [%]
0.363	0.024	28.4	6.9
0.455	0.023	18.9	6.9
0.552	0.038	9.4	6.9
0.702	0.054	4.4	6.9
0.891	0.076	3.4	6.9
1.082	0.090	4.3	6.9
1.437	0.114	5.9	6.9
2.031	0.145	10.3	6.9

Table C.52: v_2 as a function of p_T for K emitted from 40-50 % central Cu+Cu collisions at $\sqrt{s_{NN}} = 200$ GeV

p_T [GeV/c]	v_2	Statistical Error [%]	Systematic Error [%]
0.363	0.028	37.1	7.4
0.455	0.035	19.0	7.4
0.552	0.046	11.9	7.4
0.701	0.065	5.6	7.4
0.890	0.071	5.7	7.4
1.082	0.083	7.3	7.4
1.438	0.096	10.9	7.4
2.035	0.104	22.0	7.4

Table C.53: v_2 as a function of p_T for p emitted from 0-10 % central Cu+Cu collisions at $\sqrt{s_{NN}} = 200$ GeV

p_T [GeV/c]	v_2	Statistical Error [%]	Systematic Error [%]
0.555	0.011	21.0	6.6
0.652	0.019	10.2	6.6
0.751	0.022	8.3	6.6
0.899	0.033	3.8	6.6
1.097	0.048	2.8	6.6
1.292	0.061	2.6	6.6
1.488	0.076	2.8	6.6
1.685	0.080	4.0	6.6
1.883	0.094	5.4	6.6
2.201	0.100	7.4	6.6
2.816	0.101	12.2	6.6

Table C.54: v_2 as a function of p_T for p emitted from 10-20 % central Cu+Cu collisions at $\sqrt{s_{NN}} = 200$ GeV

p_T [GeV/c]	v_2	Statistical Error [%]	Systematic Error [%]
0.555	0.017	13.7	6.0
0.652	0.021	9.4	6.0
0.751	0.031	6.0	6.0
0.899	0.046	2.8	6.0
1.096	0.063	2.2	6.0
1.292	0.084	2.0	6.0
1.488	0.102	2.2	6.0
1.685	0.109	3.0	6.0
1.883	0.116	4.6	6.0
2.202	0.145	5.3	6.0
2.822	0.126	10.1	6.0

Table C.55: v_2 as a function of p_T for p emitted from 20-30 % central Cu+Cu collisions at $\sqrt{s_\mathrm{NN}} =$ 200 GeV

p_T [GeV/c]	v_2	Statistical Error [%]	Systematic Error [%]
0.555	0.021	13.2	5.5
0.652	0.031	7.6	5.5
0.750	0.042	5.3	5.5
0.898	0.055	2.9	5.5
1.096	0.078	2.2	5.5
1.292	0.097	2.1	5.5
1.488	0.115	2.4	5.5
1.685	0.130	3.2	5.5
1.883	0.143	4.6	5.5
2.201	0.142	6.9	5.5
2.828	0.177	8.9	5.5

Table C.56: v_2 as a function of p_T for p emitted from 30-40 % central Cu+Cu collisions at $\sqrt{s_\mathrm{NN}} =$ 200 GeV

p_T [GeV/c]	v_2	Statistical Error [%]	Systematic Error [%]
0.555	0.028	13.3	6.0
0.651	0.035	8.9	6.0
0.750	0.046	6.4	6.0
0.898	0.066	3.3	6.0
1.096	0.083	2.9	6.0
1.292	0.105	2.7	6.0
1.488	0.123	3.1	6.0
1.685	0.139	4.1	6.0
1.884	0.139	6.6	6.0
2.202	0.157	8.8	6.0
2.836	0.165	13.4	6.0

Table C.57: v_2 as a function of p_T for p emitted from 40-50 % central Cu+Cu collisions at $\sqrt{s_\text{NN}} = 200$ GeV

p_T [GeV/c]	v_2	Statistical Error [%]	Systematic Error [%]
0.555	0.031	17.5	6.5
0.651	0.036	13.0	6.5
0.750	0.050	9.0	6.5
0.897	0.063	5.2	6.5
1.095	0.087	4.2	6.5
1.292	0.113	4.0	6.5
1.488	0.132	4.6	6.5
1.685	0.138	6.5	6.5
1.883	0.137	10.6	6.5
2.201	0.149	14.7	6.5
2.842	0.137	25.3	6.5

C.2.2 Pion, Kaon and Proton v_2 in Au+Au Collisions at $\sqrt{s_{\mathrm{NN}}} = 62.4$ GeV

Table C.58: v_2 as a function of p_{T} for π emitted from 0-10 % central Au+Au collisions at $\sqrt{s_{\mathrm{NN}}} = 62.4$ GeV

p_{T} [GeV/c]	v_2	Statistical Error [%]	Systematic Error [%]
0.259	0.008	25.5	15.4
0.352	0.018	8.5	15.4
0.449	0.020	7.6	15.4
0.548	0.026	6.4	15.4
0.648	0.034	5.6	15.4
0.748	0.035	6.1	15.4
0.890	0.042	4.7	15.4
1.089	0.063	9.1	15.4
1.443	0.069	8.2	15.4
2.204	0.100	25.3	15.4

Table C.59: v_2 as a function of p_{T} for π emitted from 10-20 % central Au+Au collisions at $\sqrt{s_{\mathrm{NN}}} = 62.4$ GeV

p_{T} [GeV/c]	v_2	Statistical Error [%]	Systematic Error [%]
0.260	0.020	8.0	8.0
0.352	0.030	4.2	8.0
0.449	0.039	3.2	8.0
0.548	0.050	2.8	8.0
0.648	0.061	2.5	8.0
0.748	0.066	2.7	8.0
0.890	0.079	2.1	8.0
1.089	0.102	4.5	8.0
1.444	0.107	4.2	8.0
2.201	0.127	16.2	8.0

Table C.60: v_2 as a function of p_T for π emitted from 20-30 % central Au+Au collisions at $\sqrt{s_{NN}} =$ 62.4 GeV

p_T [GeV/c]	v_2	Statistical Error [%]	Systematic Error [%]
0.259	0.027	7.3	6.0
0.352	0.038	4.1	6.0
0.449	0.053	3.0	6.0
0.548	0.066	2.6	6.0
0.648	0.079	2.5	6.0
0.748	0.090	2.4	6.0
0.890	0.105	2.0	6.0
1.090	0.128	4.5	6.0
1.445	0.155	3.6	6.0
2.200	0.187	13.6	6.0

Table C.61: v_2 as a function of p_T for π emitted from 30-40 % central Au+Au collisions at $\sqrt{s_{NN}} =$ 62.4 GeV

p_T [GeV/c]	v_2	Statistical Error [%]	Systematic Error [%]
0.259	0.033	8.5	5.3
0.351	0.040	5.5	5.3
0.449	0.056	4.0	5.3
0.548	0.071	3.4	5.3
0.648	0.091	3.1	5.3
0.748	0.098	3.2	5.3
0.890	0.117	2.5	5.3
1.089	0.121	6.8	5.3
1.445	0.163	5.0	5.3
2.197	0.209	17.7	5.3

Table C.62: v_2 as a function of p_T for π emitted from 40-50 % central Au+Au collisions at $\sqrt{s_{NN}} =$ 62.4 GeV

p_T [GeV/c]	v_2	Statistical Error [%]	Systematic Error [%]
0.259	0.031	16.0	7.7
0.351	0.050	7.9	7.7
0.449	0.063	6.4	7.7
0.548	0.080	5.6	7.7
0.648	0.095	5.4	7.7
0.748	0.108	5.4	7.7
0.889	0.130	4.3	7.7
1.089	0.146	10.2	7.7
1.445	0.183	8.2	7.7
2.197	0.280	24.2	7.7

Table C.63: v_2 as a function of p_T for K emitted from 0-10 % central Au+Au collisions at $\sqrt{s_{NN}} = 62.4$ GeV

p_T [GeV/c]	v_2	Statistical Error [%]	Systematic Error [%]
0.426	0.011	70.1	23.4
0.606	0.018	27.0	23.4
0.750	0.024	26.3	23.4
0.898	0.037	12.7	23.4
1.089	0.050	11.0	23.4
1.475	0.047	22.1	23.4
2.216	0.107	34.9	23.4

Table C.64: v_2 as a function of p_T for K emitted from 10-20 % central Au+Au collisions at $\sqrt{s_{NN}} = 62.4$ GeV

p_T [GeV/c]	v_2	Statistical Error [%]	Systematic Error [%]
0.428	0.019	31.6	6.0
0.606	0.033	12.1	6.0
0.750	0.051	10.2	6.0
0.898	0.062	6.2	6.0
1.089	0.084	5.4	6.0
1.476	0.095	8.8	6.0
2.217	0.167	17.8	6.0

Table C.65: v_2 as a function of p_T for K emitted from 20-30 % central Au+Au collisions at $\sqrt{s_{NN}} = 62.4$ GeV

p_T [GeV/c]	v_2	Statistical Error [%]	Systematic Error [%]
0.429	0.017	45.0	17.4
0.606	0.054	9.2	17.4
0.750	0.067	9.8	17.4
0.897	0.086	5.6	17.4
1.089	0.104	5.5	17.4
1.477	0.144	7.4	17.4
2.216	0.161	22.8	17.4

Table C.66: v_2 as a function of p_T for K emitted from 30-40 % central Au+Au collisions at $\sqrt{s_{NN}} =$ 62.4 GeV

p_T [GeV/c]	v_2	Statistical Error [%]	Systematic Error [%]
0.429	0.031	34.9	17.0
0.606	0.057	12.6	17.0
0.750	0.072	13.0	17.0
0.897	0.096	7.3	17.0
1.089	0.118	7.1	17.0
1.476	0.126	12.3	17.0
2.227	0.161	32.9	17.0

Table C.67: v_2 as a function of p_T for K emitted from 40-50 % central Au+Au collisions at $\sqrt{s_{NN}} =$ 62.4 GeV

p_T [GeV/c]	v_2	Statistical Error [%]	Systematic Error [%]
0.430	0.046	41.8	38.9
0.605	0.059	21.9	38.9
0.750	0.084	20.4	38.9
0.897	0.121	10.7	38.9
1.089	0.166	9.4	38.9
1.476	0.154	18.9	38.9
2.222	0.220	44.5	38.9

Table C.68: v_2 as a function of p_T for p emitted from 0-10 % central Au+Au collisions at $\sqrt{s_{NN}} =$ 62.4 GeV

p_T [GeV/c]	v_2	Statistical Error [%]	Systematic Error [%]
0.614	0.009	56.8	39.3
0.751	0.012	53.1	39.3
0.899	0.024	18.1	39.3
1.097	0.036	12.7	39.3
1.494	0.058	13.0	39.3
2.362	0.110	16.9	39.3

Table C.69: v_2 as a function of p_T for p emitted from 10-20 % central Au+Au collisions at $\sqrt{s_{NN}} =$ 62.4 GeV

p_T [GeV/c]	v_2	Statistical Error [%]	Systematic Error [%]
0.614	0.019	21.7	13.1
0.751	0.040	12.5	13.1
0.899	0.052	6.7	13.1
1.097	0.069	5.4	13.1
1.493	0.107	5.8	13.1
2.361	0.174	8.7	13.1

Table C.70: v_2 as a function of p_T for p emitted from 20-30 % central Au+Au collisions at $\sqrt{s_{NN}} = 62.4$ GeV

p_T [GeV/c]	v_2	Statistical Error [%]	Systematic Error [%]
0.614	0.023	21.9	11.8
0.751	0.040	15.0	11.8
0.899	0.066	6.5	11.8
1.096	0.100	4.6	11.8
1.491	0.147	5.4	11.8
2.366	0.189	10.2	11.8

Table C.71: v_2 as a function of p_T for p emitted from 30-40 % central Au+Au collisions at $\sqrt{s_{NN}} = 62.4$ GeV

p_T [GeV/c]	v_2	Statistical Error [%]	Systematic Error [%]
0.613	0.028	25.2	14.5
0.751	0.065	13.1	14.5
0.898	0.080	7.6	14.5
1.096	0.102	6.5	14.5
1.486	0.179	6.5	14.5
2.365	0.173	16.9	14.5

Table C.72: v_2 as a function of p_T for p emitted from 40-50 % central Au+Au collisions at $\sqrt{s_{NN}} = 62.4$ GeV

p_T [GeV/c]	v_2	Statistical Error [%]	Systematic Error [%]
0.612	0.041	29.0	8.8
0.750	0.092	16.2	8.8
0.897	0.103	10.6	8.8
1.095	0.101	12.0	8.8
1.482	0.162	13.4	8.8
2.363	0.279	19.9	8.8

Table C.73: v_2 as a function of p_T for π^- emitted from 10-40 % central Au+Au collisions at $\sqrt{s_{NN}} = 62.4$ GeV

p_T [GeV/c]	v_2	Statistical Error [%]	Systematic Error [%]
0.259	0.025	7.1	7.2
0.352	0.034	3.9	7.2
0.450	0.047	2.8	7.2
0.549	0.059	2.4	7.2
0.648	0.074	2.1	7.2
0.748	0.078	2.3	7.2
0.890	0.093	1.7	7.2
1.089	0.109	4.4	7.2
1.446	0.130	3.6	7.2
2.199	0.161	13.2	7.2

Table C.74: v_2 as a function of p_T for K$^-$ emitted from 10-40 % central Au+Au collisions at $\sqrt{s_{NN}} = 62.4$ GeV

p_T [GeV/c]	v_2	Statistical Error [%]	Systematic Error [%]
0.427	0.019	33.7	20.6
0.606	0.042	9.9	20.6
0.750	0.064	8.6	20.6
0.897	0.071	5.6	20.6
1.089	0.089	5.4	20.6
1.478	0.112	8.6	20.6
2.218	0.198	16.8	20.6

Table C.75: v_2 as a function of p_T for $\bar{p}$ emitted from 10-40 % central Au+Au collisions at $\sqrt{s_{NN}} = 62.4$ GeV

p_T [GeV/c]	v_2	Statistical Error [%]	Systematic Error [%]
0.611	0.015	34.1	20.4
0.751	0.046	13.7	20.4
0.899	0.057	7.7	20.4
1.097	0.082	5.7	20.4
1.493	0.133	6.4	20.4
2.369	0.172	12.1	20.4

Table C.76: v_2 as a function of p_T for π^+ emitted from 10-40 % central Au+Au collisions at $\sqrt{s_{NN}} = 62.4$ GeV

p_T [GeV/c]	v_2	Statistical Error [%]	Systematic Error [%]
0.260	0.025	6.0	5.3
0.351	0.035	3.4	5.3
0.449	0.048	2.5	5.3
0.548	0.059	2.2	5.3
0.648	0.072	2.1	5.3
0.748	0.083	2.1	5.3
0.890	0.097	1.6	5.3
1.089	0.118	3.8	5.3
1.443	0.137	3.2	5.3
2.200	0.164	12.5	5.3

Table C.77: v_2 as a function of p_T for K^+ emitted from 10-40 % central Au+Au collisions at $\sqrt{s_{NN}} = 62.4$ GeV

p_T [GeV/c]	v_2	Statistical Error [%]	Systematic Error [%]
0.430	0.023	26.5	8.4
0.606	0.047	8.5	8.4
0.750	0.057	9.0	8.4
0.898	0.080	4.7	8.4
1.089	0.104	4.3	8.4
1.475	0.120	6.6	8.4
2.220	0.140	19.9	8.4

Table C.78: v_2 as a function of p_T for p emitted from 10-40 % central Au+Au collisions at $\sqrt{s_{NN}} = 62.4$ GeV

p_T [GeV/c]	v_2	Statistical Error [%]	Systematic Error [%]
0.615	0.026	13.9	9.2
0.751	0.045	9.4	9.2
0.899	0.065	4.6	9.2
1.096	0.087	3.7	9.2
1.490	0.134	4.0	9.2
2.361	0.181	7.3	9.2

Bibliography

[1] K.Yagi, T.Hatsuda, Y.Miake, **Quark-Gluon Plasma**, CAMBRIDGE (2006)

[2] J.C.Collins, M.J.Perry, Phys. Rev. Lett. **34**, 1353 (1975)

[3] E.V.Shuryak, Phys. Rep. **61**, 71 (1980)

[4] F.Karsch, in:Lecture Notes in Physics, **vol.583**, p.209 (2002)

[5] A. Adare *et al.*, (PHENIX Collaboration), Phys. Rev. Lett. **98**, 162301 (2007)

[6] K. Adcox *et al.* (PHENIX Collaboration), Nucl. Phys. **A757**, 184-283 (2005)

[7] S. S. Adler *et al.*, (PHENIX Collaboration), Phys. Rev. Lett. **91**, 182301 (2003)

[8] S.S. Adler *et al.*, (PHENIX Collaboration), Phys. Rev. Lett. **94**, 232302 (2005)

[9] J. Aichelin and K. Werner, Phys. Rev. **C79**, 064907 (2009)

[10] E.V. Shuryak, Nucl. Phys. **A750**, 64 (2005)

[11] U. Heinz *et al.*, Nucl. Phys. **A702**, 269 (2002)

[12] D. Teaney *et al.*, (2001) nucl-th/0110037

[13] P. Huvinen *et al.*, Phys. Lett. **B503**, 58 (2001)

[14] T. Hirano *et al.*, Nucl. Phys. **A743**, 305 (2004)

[15] T. Csorgo and B. Lorstad, Phys. Rev. **C54**, 1390 (1996)

[16] M. Csanad *et al.*, Eur. Phys. J. **A38**, 363-368 (2008)

[17] T. Hirano *et al.*, Phys. Lett. **B636**, 299 (2006)

[18] T. Hirano *et al.*, Phys. Rev. **C77**, 044909 (2008)

[19] K. Adcox *et al.*, Phys. Rev. **C69**, 024904 (2004)

[20] A. Adare *et al.*, Phys. Rev. Lett. **101**, 162301 (2008)

[21] P. F. Kolb and R. Rapp, Phys. Rev. **C67**, 044903 (2003)

[22] D. Teaney, J. Lauret, and E. V. Shuryak, Phys. Rev. Lett. **86**, 4783 (2001)

[23] E. Schnedermann, J. Sollfrank, and U. Heinz, Phys. Rev. **C48**, 2462 (1993)

[24] C. Adler *et al.*, (STAR Collaboration), Phys. Rev. Lett. **87**, 182301 (2001)

[25] J. D. Bjorken, Phys. Rev. **D27**, 140 (1983)

[26] P. F. Kolb, Heavy Ion Phys. **21**, 234 (2004)

[27] L. Ahle *et al.*, Phys. Lett. **B332**, 258 (1994)

[28] T. Alber *et al.*, Phys. Rev. Lett. **75**, 3814 (1995)

[29] K. Adkox, *et al.*, (PHENIX Collaboration), Phys. Rev. Lett. **87**, 052301 (2001)

[30] S. S. Adler *et al.*, (PHENIX Collaboration), Phys. Rev. **C71**, 034908 (2005)

[31] S. S. Adler *et al.*, (PHENIX Collaboration), Phys. Rev. **C71**, 049901 (2005)

[32] K. Guettler *et al.*, Phys. Rev. **D64**, 111 (1976)

[33] S. S. Adler *et al.*, Phys. Rev. **C69**, 034909 (2004)

[34] R.J. Fries, B. Muller, C. Nonaka, S.A. Bass, Phys. Rev. Lett. **90**, 202303 (2003)

[35] R.J. Fries, B. Muller, C. Nonaka, S.A. Bass, Phys. Rev. **C68**, 044902 (2003)

[36] G. Stefanek *et al.*, (NA49 Collaboration), Phys. Rev. **C75**, 044901 (2007)

[37] G. Stefanek *et al.*, (NA49 Collaboration), PoSCPOD2006, 030 (2006) nucl-ex/0611003

[38] B.I. Abelev *et al.*, (STAR Collaboration), Phys. Rev. **C75**, 054906 (2007).

[39] M. Shimomura *et al.*, (PHENIX Collaboration), Nucl. Phys. **A774**, 457-460 (2006)

[40] S.S. Adler *et al.*, (PHENIX Collaboration), Phys. Rev. **C69**, 034910 (2004)

[41] S.S. Adler *et al.*, (PHENIX Collaboration), Phys. Rev. Lett. **91**, 072301 (2003)

[42] S.S. Adler *et al.*, (PHENIX Collaboration), Phys. Rev. Lett. **91**, 072303 (2003)

[43] S.S. Adler *et al.*, (PHENIX Collaboration), Phys. Rev. Lett. **94**, 232301 (2005)

[44] S.S. Adler *et al.*, (PHENIX Collaboration), Phys. Rev. Lett. **91**, 241803 (2003)

[45] I. Vitev, Phys. Rev. Lett. **89**, 252301 (2002)

[46] X. Wang, Phys. Lett. **B595**, 165-170 (2004)

[47] K. Rajagopal, Acta Phys. Polon. **B31**, 3021 (2000)

[48] E. Laermann, O. Philipsen, Ann. Rev. Nucl. Part. Sci. **53**, 163 (2003)

[49] S. A. Voloshin, Nuclear Physics, **A715**, 379c (2003)

[50] Samuel S. M. Wong, Introductory Nuclear Physics second edition, JOHN WILEY & SONS Inc., (1998)

[51] M.Bleicher *et al.*, Phys. Lett. **B526**, 309 (2002)

[52] K. Adcox *et al.*, (PHENIX Collaboration), Nucl. Instrum. Meth. **A499**, 469-479 (2003)

[53] J.T. Mitchell *et al.*, (PHENIX Collaboration), Nucl. Instrum. Meth. **A482**, 491-512 (2002)

[54] A. Milov, Doctor thesis, Weizmann Institute, Rohovot Israel (2002)

[55] J. Jia, Doctor thesis, State University of New York at Stony Brook (2003)

[56] C. Adler *et al.*, Nucl. Instrum. Meth. **A470**, 488-499 (2001)

[57] S.S. Adler *et al.*, (PHENIX Collaboration), Phys. Rev. **C69**, 034910 (2004)

[58] K. Adcox *et al.*, (PHENIX Collaboration), Phys. Rev. Lett. **86**, 3500-3505 (2001)

[59] D.P. Morrison *et al.*, (PHENIX Collaboration), Nucl. Phys. **A638**, 565-570 (1998)

[60] L. McLerran, hep-ph/0202025 (2002)

[61] W.A. Zajc *et al.*, (PHENIX Collaboration), Nucl. Phys. **A698**, 39-53 (2002)

[62] K. Adcox *et al.*, (PHENIX Collaboration), Phys. Lett. **B561**, 82-92 (2003)

[63] M. Konno, Doctor thesis, University of Tsukuba (2007)

[64] H. Masui, Doctor thesis, University of Tsukuba (2007)

[65] A. Kiyomichi, Doctor thesis, University of Tsukuba (2005)

[66] N. Xu and M. Kaneta, Nucl. Phys. **A698**, 306c (2002)

[67] H. Masui and M. Shimomura,
https : //www.phenix.bnl.gov/WWW/p/draft/masui/2005/rpcalib/index.html

[68] S. Afanasiev *et al.*, (PHENIX Collaboration), Phys. Rev. **C80**, 024909 (2009)

[69] A. Taranenko *et al.*, PHENIX Analysis note 491, (2006)

[70] J. Jia, PHENIX Analysis note 119, (2002)

[71] H. Masui *et al.*, PHENIX Analysis note 541, (2006)

[72] M. Shimomura *et al.*, PHENIX Analysis note 473, (2005)

[73] A. Taranenko *et al.*, PHENIX Analysis note 441, (2005)

[74] S. Kelly *et al.*, PHENIX Analysis note 033, (2000)

[75] K. Reygers
https : //www.phenix.bnl.gov/WWW/p/draft/reygers/glauber/

[76] K. Reygers, PHENIX Analysis note 078, (2001)

[77] K. Reygers, PHENIX Analysis note 169, (2003)

[78] D. Morrison *et al.*, PHENIX Analysis note 290 (2004)

[79] A. M. Poskanzer *et al.*, Phys. Rev. **C58**, 1671 (1998)

[80] S. A. Voloshin, A. M. Poskanzer and R. Snellings (2008) nucl-ex/08092949
"Collective phenomena in non-central nuclear collisions"

[81] U. W. Heinz (2009) nucl-th/09014355
"Early collective expansion: Relativistic hydrodynamics and the transport properties of QCD matter"

[82] P. Sorensen (2009) nucl-ex/09050174
"Elliptic Flow: A Study of Space-Momentum Correlations In Relativistic Nuclear Collisions"

[83] I. Vitev *et al.*, Phys. Rev. Lett. **86**, 2537-2540 (2001)

[84] S. Manly *et al.*, Nucl. Phys. **A774**, 523-526 (2006)

[85] B. Alver *et al.*, Phys. Rev. Lett. **98**, 242302 (2007)